UCLouvain

Ecole polytechnique de Louvain
Institute of Mechanics, Materials
and Civil Engineering, (IMMC)

Multiscale thermo-mechanical modeling of semi-crystalline polymers. Application to additive manufacturing by selective laser sintering

Amine Bahloul

Thesis submitted in partial fulfillment of the requirements for the Ph.D
Degree in Engineering Sciences and technology

Thesis Committee

Advisors	Issam Doghri	*UCLouvain*
	Laurent Adam	*Hexagon*
Jury	Evelyne Van Ruymbeke	*UCLouvain*
	Stéphane Bordas	*U. Luxembourg*
	Hans Van Dommelen	*T.U. Eindhoven*
	Wim Van Paepegem	*U. Ghent*
Chairperson	Sandra Soares Frazao	*UCLouvain*

Louvain-la-Neuve, June 2022

REMERCIEMENTS

The research work carried out during these years of thesis would not have been possible without the support and understanding of many people, I would like to express my sincere thanks to them.

First and foremost, I would like to express my sincere gratitude to my advisors Mr. Issam Doghri, Professor at Université catholique de Louvain and Mr. Laurent Adam, Head of Research and Product Development - Digimat and MaterialCenter at Hexagon for the continuous support of my PhD study and related research, for their patience, motivation and immense knowledge. Their guidance helped me in all the time of research and writing of this thesis. I could not have imagined having a better advisors and mentor for my PhD study.

I would like to thank Mrs. Sandra Soares Frazao, Professor at Université catholique de Louvain, for chairing the jury. My sincere thanks also to Mrs. Evelyne Van Ruymbeke, Professor at Université catholique de Louvain, and to Mr. Stéphane Bordas, Professor at the University of Luxembourg, for accepting to be members of my support committee, as well as the other members of my thesis jury, Mr. Hans Van Dommelen, Professor at Eindhoven University of Technology and Mr. Wim Van Paepegem, Professor at Ghent University.

Thanks to Emmanuel Lacoste and Moncef Selmi, my office colleagues, for their help and relevant advice. Special thanks to Marc Duflot, without him the simulations of my RVE with the FFT method will not take place. Thanks also to Sylvain Mathieu who helped me to integrate my work into Digimat AM. I would like to thank all my colleagues in the R&D team, they have all given me help and advice.

This research was supported by the Luxembourg National Research Fund FNR in collaboration between e-Xstream Engineering sarl (part of Hexagon Manufacturing Intelligence) and Université catholique de Louvain. Without them, this work would not have been possible. I would like to thank all the parties who have contributed to this collaboration.

I deeply thank my parents, Jamel and Narjes for their unconditional trust, timely encouragement, and endless patience. It was their love that raised me up again when I got weary. I thank my wife Cyrine with love. She was my best friend and a wonderful companion, loved, supported, encouraged and helped me get through this period in the most positive way. My sisters, Amal and Eya, have also been generous with their love and encouragement. I also thank all my relatives and friends who accompanied, helped, and supported me throughout the completion of my PHD thesis.

Amine Bahloul

ACKNOWLEDGEMENTS

This research was supported by Luxembourg national research fund FNR with collaboration between e-Xstream engineering sarl (part of Hexagon Manufacturing Intelligence) and Université catholique de Louvain. The research project acronym is SIMAMPO, and aims at modeling the SLS (Selective Laser Sintering) process for polymer applications.

ABSTRACT

Semi-crystalline polymers exhibit performances that are highly dependent on their micro-structure as induced by the thermo-mechanical processes they are subjected to. In this thesis we developed a multiscale modeling and simulation framework able to predict the thermo-mechanical response of semi-crystalline polymers including crystallization and porosity evolution, with an application to additive manufacturing by selective laser sintering.

Firstly, an enhanced phase field model was developed for the numerical simulation of crystallization in semi-crystalline polymers [1]. The model is based on coupling the heat equation with the Allen-Cahn equation, which is derived from the Gibbs-Thomson solid-liquid interface equation. Starting from the nucleation of spherulites, existing phase field models can simulate their evolution in a surrounding liquid and separate the amorphous and crystalline phases. However, the predictions of the morphological characteristics of the spherulites remain qualitative only. Moreover, the predicted spherulite evolution as a function of crystallization temperature is not consistent with experimental results. In our work, existing phase field models were enhanced in order to obtain experimentally consistent results. We used spherulite growth, crystal morphology, and crystallinity degree in spherulite, as measures to determine the model accuracy. The model is numerically implemented using the finite difference method so that 2D and 3D simulation results are presented and compared to experimental data, illustrating the quantitative adequacy of the predictions with experimental evidence.

Secondly, full-field micromechanical simulations were conducted on the microstructures generated by the enhanced phase field model in order to predict the effective mechanical properties [2]. Care is taken to obtain Representative Volume Elements (RVEs) by computing the number of subcells in each spherulite and the number of spherulite nucleations in each RVE. An FFT solver was used to determine the thermo-mechanical properties for a range of crystallinity ratios. Validation against experimental data and comparison with simpler models was done.

Thirdly, we developed the constitutive laws enabling the prediction of the thermo-viscoelastic-viscoplastic behavior of semi-crystalline polymers. The crystalline lamellae follow an orthotropic elasto-viscoplastic model based on the activation of slip systems, while the amorphous phase is viscoelastic. Some material parameters were identified directly while others were reverse engineered from experimental measurements.

Finally, a mesoscale model was proposed for the density evolution of an initially low density polymer grain powder which becomes compacted after sintering. The approach is based on a generalized self-consistent model, the

analogy between linear elasticity and Newtonian fluid and the mass conservation equation. All the models have been implemented in a research version of the Digimat software [3].

Contents

Contents i

1 Introduction 1

2 Additive manufacturing processes and associated polymer materials 7
1 Introduction . . . 7
2 Additive manufacturing . . . 9
3 Polymers . . . 15
4 Conclusion . . . 34

3 Polymer behavior 35
1 Introduction . . . 35
2 Viscoelastic-viscoplastic material model . . . 36
3 Thermo-Viscoelastic-viscoplastic material model . . . 46
4 Extension of the TH-VE-VP model to include the effects of crystallization . . . 54
5 Conclusion . . . 57

4 Phase field model for polymer crystallization 59
1 Introduction . . . 59
2 Existing phase field models . . . 63
3 An enhanced phase field model . . . 69
4 Generalization to 3D simulations . . . 77
5 How to perform enhanced phase field model calibration for other semi-crystalline polymers . . . 79
6 Conclusion . . . 80

5 Full-field prediction of linear elastic and thermal properties of semi-crystalline polymers based on an enhanced phase field model 83
1 Introduction . . . 83

2 Micromechanical simulations based on an enhanced phase field model . . . 85
3 RVE simulations in 2D . . . 96
4 3D simulations . . . 100
5 Predicting polymer shrinkage during cooling . . . 103
6 Thermal conductivity prediction . . . 106
7 Composite inclusion model and simplified micromechanical models . . . 107
8 Conclusion . . . 115

6 Prediction of the nonlinear response by Full-field homogenization based on the phase field generated micro-structures 117
1 Introduction . . . 117
2 Crystalline phase . . . 118
3 Amorphous phase . . . 121
4 Results and discussion . . . 125
5 Conclusion . . . 126

7 Tentative direct numerical simulation (DNS) of porosity evolution in SLS process with a CFD software 129
1 Introduction . . . 129
2 Basic theory . . . 130
3 Model description . . . 132
4 Results and discussion . . . 134
5 Conclusion . . . 138

8 Mesoscale modeling of polymer powder densification due to thermal sintering 139
1 Introduction . . . 139
2 A model for the evolution of closed and spherical pores with a size distribution . . . 141
3 Modeling the sintering of powder grains . . . 152
4 Results and discussion . . . 155
5 Conclusion . . . 159

9 Conclusion 161

Bibliography 167

AppendixA Radial return algorithm for VE-VP materials 181

AppendixB Proof of crystal growth and heat equation 183
B.A Crystal growth equation . . . 183
B.B Heat transfer equation . . . 187

AppendixC Numerical formulation of the proposed enhanced phase field model **189**

AppendixD Functional derivative **193**

AppendixE Computation of the effective bulk modulus **195**

AppendixF Relation between the particle radius a and the sintering angle **197**

CHAPTER 1

Introduction

There are several 3D printing technologies in the industry, used in different sectors and for various applications. 3D printing belongs to the additive manufacturing (AM) family of processes. AM is gaining interest in the industry thanks to its ability to manufacture complex parts, with minimal material waste and limited costs when targetting small series. Among AM processes Selective Laser Sintering (SLS) is one of the most widely used for the AM of polymers parts.

From a high-level point of view, analysis of parts printed by SLS relies on several steps. First, a CAD model of the part is generated and cut into thin slices. The manufacturing simulation will be done layer by layer, starting from the deposited powder and the printing plate heated below the melting temperature of the polymer. The laser heats the surface of selected areas, causing the sintering and consolidation of the powder. After that, the printing

plate lowers and a new layer of powder is added. The steps are repeated until getting the complete solid part. After printing, the pieces are completely wrapped in the powder. This powder bin must be cooled before the part can be cleaned and post-treated.

Powder sintering technologies make it possible to manufacture objects in a wide range of materials, such as metals and polymer materials. For polymers, polyamide (PA) is generally the most used material but other materials can also be used such as polypropylene (PP), polyether ether ketone (PEEK), polyetherketoneketone (PEKK) and Polyaryletherketone (PAEK). It is also possible to add fibers or beads to the polymer powder thus improving the mechanical behavior of the parts.

During the manufacturing process, the selected polymer powder will sinter together, which will generate its condensation and the degree of cavities will be reduced. Then the material will be crystallized, which leads to inhomogeneity of the micro-structure in the part. This complex physical phenomenon will generate an unexpected warping in the part and the desired design will not be respected. In practice, to solve this problem, several prototypes are printed with different geometries or process parameters in order to optimize the process and obtain an acceptable result. Such iterative and experimental procedure can be cost and time expensive, and can be largely improved by numerical simulation. Figure 1.1 shows the progressive layer-by-layer build after finite element simulation of a printed part using SLS process, its final deformed shape can be obtained as well as residual stresses [4].

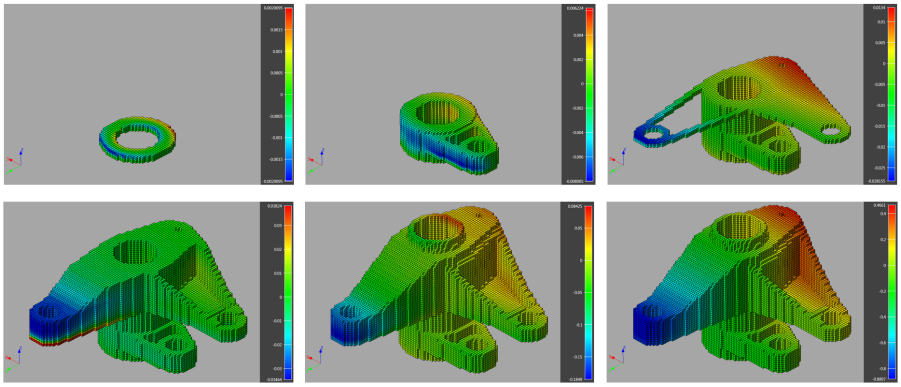

Figure 1.1: Layer-by-layer build of an aerospace rocker printed part and warpage prediction [4].

Most modeling efforts applied to SLS have focused on the generation of numerical models of CAD and finite element (FE), while contributions on ma-

terial modeling are simple and limited. Existing material models for SLS could be classified into two categories. First, simple models of solid materials, such as linear thermo-elasticity. Second, simple rheological models with fluid flows, of Newtonian type. Such models do not take into account the complexity of the behavior of the polymer, neither during the manufacturing phase nor in its final solid form.

In this research work, the developed material model includes crystallization kinetics. Crystallization in polymers is the rearrangement of molecular chains to form ordered regions. It occurs below the melting temperature and above the glass transition temperature. Molecular chains fold to form lamellae. These lamellae come from a single point called nucleation to give at the end a spherical structure called spherulite. There are three stages in crystallization. The first is nucleation, it is the creation of primary nuclei. Then, a period of rapid growth of spherulites is called primary crystallization. Finally, secondary crystallization is a slower crystallization period that occurs once the spherulites have come into contact. The crystallization can be modeled by the Kolmogorov model [5], which approximates the rate of crystal as a function of time and temperature. This model is little used in practice because it is too general, so other models were developed for the isothermal and non-isothermal conditions i.e. the Avrami model [6] for isothermal case and Nakamura model [7] for non-isothermal case. These two models can lead to good approximation of crystallisation kinetics, but they require noticeable experimental data for calibration. For more details, these semi-analytical models are presented in Chapter 2.

It is well known that all polymers have a response that depends on the strain rate and temperature. The literature contains many polymer models, such as Boyce et al. [8], Buckley et al. [9], Wu et al. [10], Govaert et al. [11], Anand et al. [12], Makradi et al. [13], Billon et al. [14], Drozdov et al. [15], etc. Although there are many constitutive models, most of them are either viscoelastic (VE) or elasto-viscoplastic (E-VP). In order to accurately simulate the behavior of the material during thermo-mechanical loading and unloading, a model recently developed by the team from UCLouvain (Doghri, Gudimetla, Krairi, Miled and others [16] [17]) was used. It is a combination of viscoelasticity and viscoplasticity, based on the thermodynamics of irreversible processes. In Chapter 3, the model will be presented. This model can be appropriate for polymers used in SLS, but it remains insufficient because during sintering the material will undergo a very important phenomenon which is the crystallization. Variation in crystallinity degree will lead to inhomogeneity of the material at the micro-scale, which will change the behavior from one region to another. For this reason, the model will be modified to take into account the crystallinity degree.

An enhanced phase field model is also proposed for the numerical simulation

of crystallization in semi-crystalline polymers. The model is based on coupling the heat equation with the Allen-Cahn [18] equation, which is derived from the Gibbs-Thomson solid-liquid interface equation. Starting from spherulite nucleation, existing phase field models can simulate their evolution in a surrounding liquid and separate the amorphous and crystalline phases. The nucleation is usually modeled by a semi-analytical model, assuming it as equal to a maximum nucleation rate multiplied by the nucleation probability (the probability being null at the melting temperature and maximum at the glass transition temperature). However, the predictions of the morphological characteristics of the spherulites remain qualitative only with such models. Moreover, the predicted spherulite evolution as a function of crystallization temperature is not consistent with experimental results. In this work, phase field models are enhanced in order to obtain experimentally consistent results. We used spherulite growth, crystal morphology, and crystallinity degree in spherulite, as measures to determine the model accuracy. We showed the importance of modeling the dependence of the model's parameters with respect to crystallization temperature, because, if assumed constants, the predicted results are not consistent with polymers physics. This topic will be detailed in Chapter 4.

After solidification, the value of the phase field variable in each subcell (2D pixel or 3D voxel or grid point used by the FFT solver) indicates whether the material is amorphous or crystalline. In Chapter 5, full-field micromechanical simulations are conducted on the micro-structures generated by the enhanced phase field model in order to predict the effective mechanical properties. A Fast Fourier Transform (FFT) method with periodic boundary conditions is used. Care is taken to obtain representative volume elements (RVEs) by computing the number of subcells in each spherulite and the number of spherulite nucleations in each RVE. Numerical FFT predictions of elastic properties for a range of crystallinity ratios are validated against experimental data and compared to simpler composite inclusion models.

In a second step the full-field micromechanical simulations are improved to take into account the viscoelastic-viscoplastic properties of the polymer. The amorphous phase can be modeled by a viscoelastic model because the random distribution of its chains gives it a rubbery behaviour. At high strain, plasticity can be produced in the amorphous phase. On the other hand, the crystalline phase is modeled by an elasto-viscoplastic model, because its structured chains give it a rigid elastic behavior. Its plasticity is obtained by sliding in the crystalline planes. The results of this subject are presented in Chapter 6.

In the SLS process, the whole grain powder is initially low density, and after sintering by laser, it will become compact. Knowing the degree of porosity evolution allows the calibration of the process parameters and the calculation of shrinkage due to densification. An attempt to model SLS processes for polymers application was carried out by the CFD method using direct numerical

simulation (DNS). Since the viscosity of the polymer is very high, the model was tested with a less viscous material in order to test it and understand its properties. The basic equations of the model are the mass conservation, Navier Stokes and the heat equations. The resolution of this problem is discussed in Chapter 7.

A mesoscale model is proposed for polymer powder densification due to thermal sintering. There are two main contributions. Firstly, we present a rigorous generalization of the Mackenzie and Shuttleworth model to predict the density evolution of a porous representative volume element containing multiple spherical cavities of various sizes. Secondly, we propose a novel development linking the evolution of the sintering angle in the two-grain models of Frenkel and Bellehumeur et al. to the density of a set of multiple interacting grains. The model was validated with experimental polyethylene densification data and compared with other existing models. The development of these models and the assumptions behind them will be discussed in Chapter 8.

The research work led to three scientific papers in peer-reviewed international journals, two published and one submitted. First, we published an article on phase field modeling titled "An enhanced phase field model for the numerical simulation of polymer crystallization" [1] which is actually the Chapter 4 of this report. Second, we published another article on multi-scale mechanical modeling titled "Linking a phase field model for polymer crystallization to full-field micromechanical simulations of semi-crystalline polymers" [2] which is actually Chapter 5. Finally, we recently submitted our third article in the Journal of Applied Mathematical Modeling titled "Mesoscale modeling of polymer powder densification due to thermal sintering" (ref: AMMOD-S-22-01750) which is Chapter 8.

CHAPTER 2

Additive manufacturing processes and associated polymer materials

1 | Introduction

Additive manufacturing is a technology that consists in manufacturing a part layer by layer. Each successive layer bonds to the previous layer of molten or sintered material. The part geometries are defined digitally by computer-aided design (CAD) software which is used to create geometry files (like .stl file) as well as a slicing in ultra-thin layers characterized by a defined thickness. In each layer, the path of the printing head or of a the laser beam is defined to optimize the printing speed, part performances, part weight or other part charateristics. After finishing the printing of the layers, a 3D object will be obtained. Unfortunately, the geometry obtained by such process is not exactly

the same as the initial part geometry, since the material will undergo shrinkage due to the change in temperature and crystallization (in case of semi-crystalline polymers) which will modify the shape of the part. In the case of additive manufacturing by laser applied to a powder (like SLS), there is additional shrinkage due to the densification of the powder.

The AM technology allows engineers to manufacture complex parts that are difficult or even impossible to manufacture in other ways. There are much less restrictions than with conventional processes and it is possible to create parts with greater design freedom. Assemblies that previously required multiple parts to be assembled and welded or brazed together can now be made into a single or limited number of parts, improving strength and durability.

Additive manufacturing is ideal for quickly prototyping. Parts are manufactured directly from a 3D designed one, which reduces cost and time. In addition, some modifications can be applied to the entire part almost without any disruption of the process. This technology also makes it possible to manufacture lightweight parts by mixing several materials together or building them architecturally while preserving their tenacity.

Additive manufacturing applies to a very wide range of materials, but in this work we will focus on polymers only. In this chapter the types of polymers, more specifically thermoplastics, studied in this research work will be defined. Their structural properties will be exposed, as well as their dependences on temperature.

A synthesis of the crystallization of semi-crystalline polymers and a state-of-the-art of how to model such phenomena is also presented in this section. The basic crystallization mechanisms will be described with their associated models. Like metals, the crystallization of polymers has a very important role in the definition of the thermal and mechanical properties of the material. Crystallization consists essentially of two major phenomena, one called nucleation and the other called growth.

A semi-analytical model to predict growth rate and nucleation based on the basic equation of thermodynamics will also be presented. Well known models like Kolmogorov, Avrami or Nakamura models will also be presented.

The chapter has the following outline. Section 2 contains a description of the additive manufacturing process, in particular selective laser sintering for polymers. Section 3 is devoted to polymers behavior. Their thermo-mechanical properties and dependences on crystallinity degree, as well as crystallization kinetics are discussed. Conclusions are drawn in section 4.

2 | Additive manufacturing

2.1 AM manufacturing processes

Additive manufacturing processes have evolved rapidly, several types of AM processes exist in the industry, such as Material extrusion, Material jetting, Binder jetting, Sheet lamination, Vat photopolymerization, Directed energy deposition and Powder bed fusion [19]. In this work, we will focus on Powder bed fusion. The object is obtained by the selective sintering or fusion of well-defined sections of a powder bed. Using a laser or an electron beam, the powdered material will melt/sinter together. Among this method are direct metal laser sintering (DMLS), electron beam melting (EBM), selective thermal sintering (SHS), selective laser melting (SLM) and selective laser sintering (SLS).

This work mainly aims to model the polymers behavior and the evolution of their micro-structure during the SLS manufacturing process. Process parameters play a very important role in the printed part and affect its properties. Among them, laser power, laser speed, hatch distance, layer thickness, printing chamber temperature, ... Appropriate calibration of these parameters is required, to obtain parts printed with minimal porosity and warp.

The semi-crystalline polymer has a relatively large temperature interval between the onset of melting at the melting temperature T_m and the onset of crystallization at the crystallization temperature T_c [20]. The polymer powder will melt by local heating to temperatures slightly above T_m using the laser beam [21]. Then the material remains hot between T_m and T_c until the cooling stage. This technique is used to reduce residual stresses and warping caused by layer recrystallization.

2.2 Quality and defects in AM for SLS process application

As with all other processes, every part produced by SLS has undergone post-printing quality control which is carried out on several aspects and scale. The defects classification can be decomposed into three categories, Macro-geometry, Micro-geometry and Micro-structural defects and inclusions.

- Macro-geometry.
  This defect category includes all volumetric defects. Such as shrinkage, warping and delamination. The Macro-geometry defects are depending on process parameters, when high power and low scan speed and hatch distance are applied. They also depend on process conditions, such as stop and start the printing. Design can affect them too, for example when the geometry is complex and it contains sharp edges, thin walls...

Finally, the Macro-geometry defects can be also affected by feedstock property.

- Micro-geometry.
  This defect category includes all defects that are easily noticeable to the eye and that are considered as surface defects. Such as rugosity. The Micro-geometry defects are depending on process parameters, when high or low energy density is applied. They also depend on process conditions, such as stop and start the printing. Design can affect them too, for example when the geometry is complex and contains many surface orientations. Finally, the Micro-geometry defects can be also affected by feedstock property characterized by the size and distribution of the powder.

- Micro-structural defects and inclusions.
  This defect category includes all Micro-structural defects. Such as the formation of pores with high or low energy density and the presence of impurities and lack of sintering in some region. Micro-structure defects depend on the process parameters, when high or low power density is applied. It also depends on the process conditions, such as the general pollution in the printing chamber. The design can also affect them, for example when the geometry is complex and contains a abrupt slice area change or existing of thin walls. Finally, micro-engineering defects can also be affected by the properties of feedstock represented by the powder quality.

Post-processing can be performed to reduce defects after printing such as stress release via thermal treatments and Hot Isostatic Pressing (HIP), which is one of the most effective treatment but fails to remove the bubbles containing trapped gases.

2.3 Powder properties effect on print quality

The SLS process applies to materials with very different properties. Further, the powders of the same material can also be different in their morphology which will influence the sintering. The properties of the powder strongly influence that of the part such as roughness, residual stresses, the presence of cracks and its mechanical behavior. The influence of powder properties and SLS process parameters on the properties of polymer parts produced by SLS is shown in Figure 2.1.

In SLS process, the materials must have a certain level of fluidity and compaction efficiency to allow the treatment of the unsintered powder, in particular during the deposition of the layers of powder. Efforts have been made to

understand the dynamic flow behavior of powders, all aimed at optimizing fluidity [22] [23] with methods such as the Revolution Powder Analyzer, dynamic particle flow can be studied under conditions that mimic those of the Roller (3DSystems) and Blade (EOS) [24] [25]. It is proven that powders composed of spherical particles offer the greatest flowability, closely followed by potato-shaped particles, which flow significantly better than irregular particles.

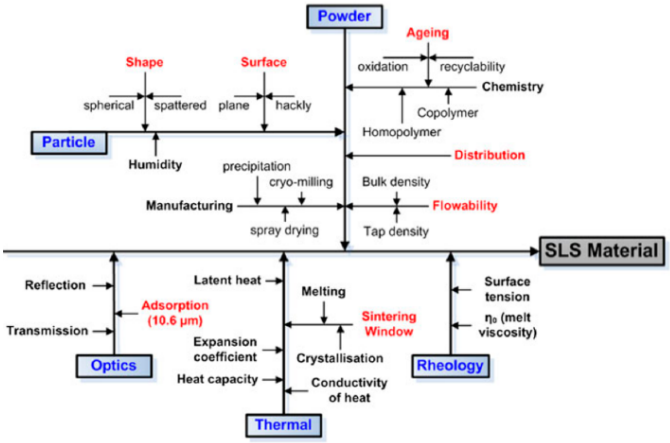

Figure 2.1: Powder parameters influencing the properties of polymer parts produced by SLS [21].

Sufficient absorption of laser radiation is one of the necessary powder characteristics to enable efficient energy absorption and sintering. The most important requirement for SLS is that crystallization of powder particles occurs uniformly in the same layer. Sintering phenomena depend on the powder properties and heating condition. Polymer powders sintering due to complete or partial fusion of powder particles is driven by capillary forces and depending on its viscosity, thus forming necks between adjacent powder particles. An increasingly dense part is usually obtained for the SLS process of polymers.

The thermal properties of semi-crystalline and amorphous polymers are different, so the method of processing them by SLS will be different. During melting and crystallization of a semi-crystalline polymer, its viscosity and density undergo a significant change within a narrow temperature range. Therefore, semi-crystalline powders are incorporated by local heating at temperatures slightly above T_m. The powder bed is then constantly kept at a temperature between T_m and T_c during the SLS process, in order to reduce residual stresses and warpage due to cooling process [21].

2.4 Fabrication of polymeric SLS powders

Excellent control of particle size distribution and morphology is required in the manufacture of powders for the SLS process. Most particle sizes are typically in the range of $60\mu m$ [21]. Several different methods are used to make SLS powders, the best known of which are precipitation and mechanical milling. The appropriate process selection depends on the material and the required powder properties. It is also common to combine two different types of powders or fillers to improve the mechanical properties of printed materials. Figure 2.2 shows the different powder manufacturing methods for the SLS process. The powder is produced in two ways either chemically based on a polymer solution or mechanically by cryogenic milling.

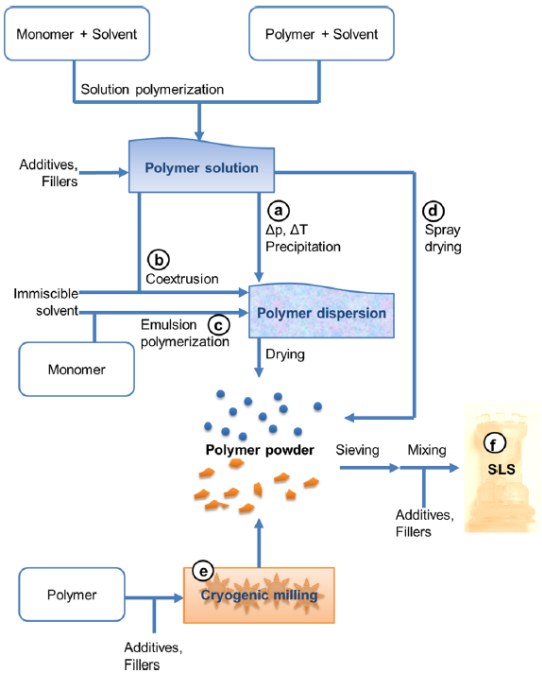

Figure 2.2: Fabrication of polymeric SLS powders: (a) precipitation from polymer solution; (b) coextrusion of polymer solution with immiscible solvent; (c) emulsion polymerization of water-insoluble monomers; (d) spray drying of polymer solution; (e) cryogenic milling of polymer powders; and (f) SLS processing of powders with controlled size distribution and formulated additives [19].

Some examples of the powders morphology made by different methods are shown in Figure 2.3. Spherical particles made by emulsion polymerization are

the most recommended in additive manufacturing. Moreover, in the theoretical part, all the models represent the powder particles by the spheres, so the choice of perfectly spherical particles makes the theory and reality coherent.

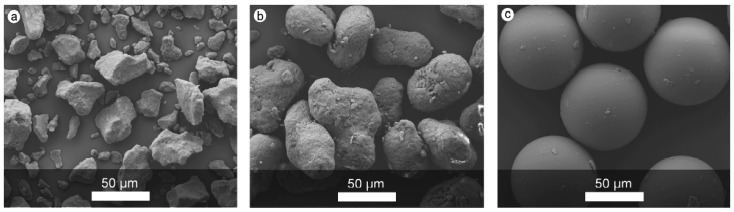

Figure 2.3: Morphology of commercial powders for laser sintering of polymers. (a) cryogenically ground rough particles of PA-11 powder (b) potato-shaped particles precipitated from an ethanol solution of PA-12 powder and (c) spherical particles produced by emulsion polymerization PS powder [19].

2.5 Range of compatible materials for SLS

In the SLS industry, there is a limited number of powders offered on a commercial basis (highlighted in blue in Figure 2.4). Researchers are still trying to find other usable materials (some examples are highlighted in orange). Polyamide PA12 is the most widely used material, there are also other types of polyamide such as PA11 and PA6. PEEK is also well known in additive manufacturing. HDPE and PP commodity polymers are also used in the SLS process.

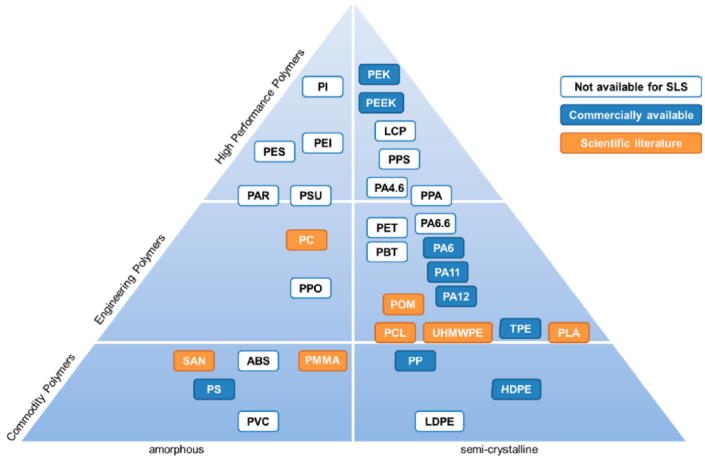

Figure 2.4: Pyramid of polymeric materials for SLS additive manufacturing [19].

2.6 Modeling challenge

In the literature, there are several methods for modeling the SLS process. Since polymer material undergoes will melt during the process, the SLS process can be modeled by fluid mechanics as used for the SLM model by Russel et al. [26] He et al. [27] or by thermo-mechanical coupling [27]. Simulations in fluid mechanics are carried out by solving the Navier Stokes equations coupled with the heat equation and the mass conservation. Since these simulations consume a huge CPU time, in practice the simulations are mainly done with solid mechanics. The thermal field plays a very important role in the sintering process, so to simulate quantitatively, it is necessary to ideally represent the lasing effect and apply the boundary conditions correctly. The interaction between the laser and the powder is a complex physical phenomena, which is represented in modeling by a volumetric source term included in the heat equation. The thermal problem includes also radiation, convection and conduction. The conductivity at the interface between the molten powder and the cold one must be taken into account. There are numerous formulations of the thermal problem, in 1D, 2D or 3D, as well as many numerical algorithms [28] [29] [30] [31], which are mainly based on finite element (FE) or finite differences. However, in the SLS process, the polymer material is heated, undergoes phase changes, softens or melts, hardens... This involves complex physical and chemical processes, which are both not completely understood and very hard to model. Most of the current literature deals only with the thermal problem (heat equation + BCs) and the physical and chemical processes are modeled indirectly in a very simplified and phenomenological way, for example by making the material parameters as linear functions of temperature. In a semi-crystalline polymer, the evolution of crystallinity degree must be predicted, since it significantly affects the behavior of polymers. As well as porosity. Indeed, when targeting high-performance parts, the porosity of the material must be controlled and minimized. It is well known that all polymers exhibit creep, relaxation, and a rate-dependent response, even at moderate temperatures. The literature contains many models for polymer mechanics, e.g. Boyce et al. [8], Buckley et al. [9], Wu et al. [10], Govaert et al. [11], Anand et al. [12], Makradi et al. [13], Billon et al. [14], Drozdov et al. [15], etc. Although many models of behavior exist, most of them are either viscoelastic (VE) or elasto-viscoplastic (E-VP), whereas the real behavior generally couples viscoelasticity and viscoplasticity (VE-VP). In order to accurately simulate both the behavior of the material when loaded and unloaded thermo-mechanically, we need a coupled (TH-VE-VP) model. Recently, the UCLouvain team [Doghri, Gudimetla, Krairi, Miled, et al.][17] [16] proposed a constitutive framework which couples viscoelasticity and viscoplasticity, relies on the thermodynamics of irreversible processes, is correctly formulated under finite transformations and is generic assuming isothermal conditions.

3 | Polymers

3.1 Polymer classification

A polymer is a macro-molecule composed of long sequences of molecules called monomers, each linked to the others by primary bonds, most often covalent bonds. From a structural point of view, organic polymers consist of long carbon chains on which are fixed atoms or groups of atoms such as hydrogen or alkyl groups. There are three polymer classification groups.

- Thermosetting polymer.
  Thermosets are formed of monomers or groups of monomers bonded to each other by a three-dimensional network of chemical bonds formed in the presence of heat and may be promoted by high pressure or in the presence of a catalyst. This operation is irreversible, so the melting point does not exist. Thermosets are rigid at the use temperature. Some examples of thermosetting materials: Phenoplasts, Aminoplasts.

- Elastomers.
  Known by the name rubber, are cross-linked amorphous polymers and are characterized by a glass transition temperature Tg, beyond it they have a low Young's modulus and high failure strain.

- Thermoplastics polymers.
  They consist of long chains that lose their rigidity when subjected to heat. This process is reversible and we can repeat this process many times without material degradation. Some examples of Thermoplastics materials Polyvinyl chloride (PVC), polyethylene (PE), polypropylene (PP or IPP), polystyrene (PS), polyamide (PA).

3.2 Semi-crystalline thermoplastics

Semi-crystalline thermoplastic is considered as a composite material because it decomposes into two phases, one called amorphous and the other crystalline.

The amorphous state is characterized by the random configuration of its chains, this structure gives the polymer a rubbery behavior. Plasticity can occur in the amorphous phase because unlike elastomers, it does not contain cross links between its chains. This state is also characterized by the existence of a glass transition temperature T_g, below this temperature the polymer becomes solid and rigid (vitreous state), and above this temperature, its stiffness modulus drops and it will be in a rubbery state.

The crystalline state is characterized by the regular configuration of its chains, this structure gives the polymer a high modulus. In this state, the melting temperature T_m exists and the stiffness is higher compared to the amorphous state, because the crystalline structure is very compact.

However, the presence of long atomic chains in the molten polymer prevents it from completely crystallizing. Therefore, two phases are present after cooling, one amorphous and the other crystalline. For this reason, the material is called semi-crystalline (Figure 2.5).

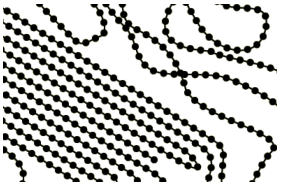

Figure 2.5: Schematization of a macro-molecular organization crystalline (left) and amorphous (right) [32].

The ability of a polymer to crystallize depends strongly on its tacticity. This property is evaluated according to the position of the groups attached with the carbons atoms(figure 2.6). The categories of polymers are as follows:

- Isotactic polymer.
  When the atom groups repeats itself in the same way.
- Syndiotactic polymer.
  When the atom groups are located in an alternating way.
- Atactic polymer.
  When the atom groups are randomly distributed

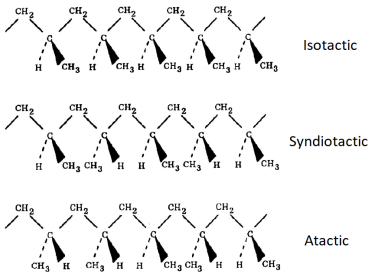

Figure 2.6: Polymer Tacticity [32].

In general, only the regular forms isotactic and syndiotactic can form crystals. The isotactic form will lead to higher crystallinity levels compared to the syndiotactic form. On the other hand, polymers whose configuration of the chains is irregular (atactic) generally tend to remain in the amorphous state, forming a glassy structure during cooling.

The physical properties of a semi-crystalline polymers are intermediate to those of a pure crystal and a pure amorphous (figure 2.7). In another way, the degree of crystallinity allows us to estimate the semi-crystalline properties by mixing the idealized properties of crystal and amorphous...

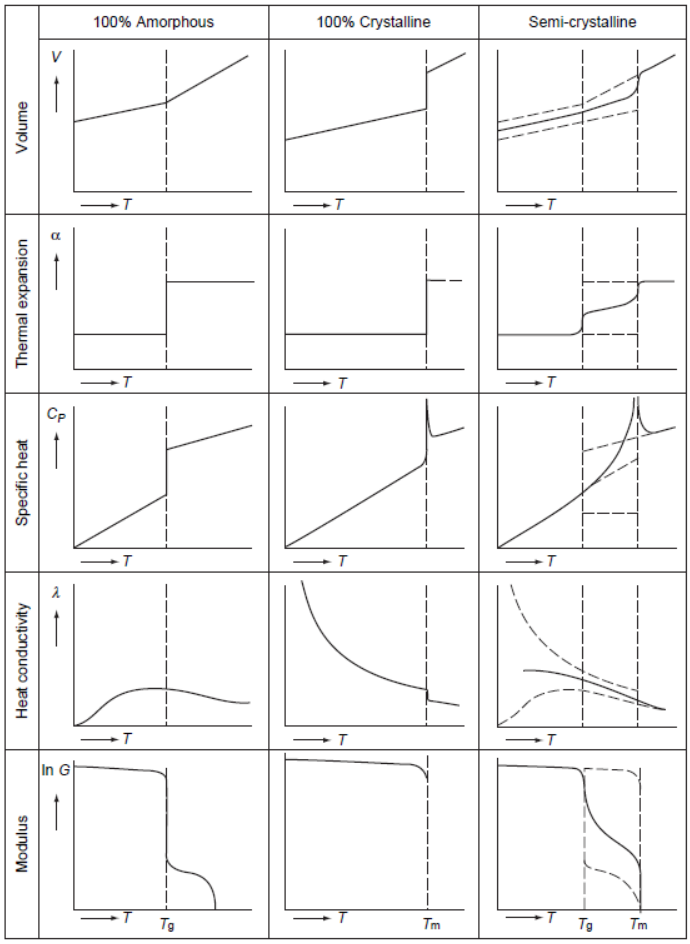

Figure 2.7: Evolution of some physical properties of thermoplastics in function of the temperature [33].

3.2.1 Glass transition temperature

Glass transition is a state transition phenomenon in a reversible manner, between the more brittle form and the molten or rubbery form of an amorphous material. This transition is characterized by a temperature called the glass transition temperature, above which the material becomes rubbery and below which the material becomes more brittle. Moreover, this temperature can be defined as transition barrier, under which the molecules exhibit low relative mobility. The glass transition temperature is represented by T_g and is a property of amorphous materials or the amorphous part of a semi-crystalline material.

3.2.2 Melting temperature

In physics and metallurgy, fusion is the transition of a substance from a solid state to a liquid state. For a pure substance, i.e. for a substance composed of atoms or molecules that are all identical, fusion takes place at a constant temperature called the melting point. This melting point or temperature depends on pressure. In the case of polymers, melting takes place only in the crystalline part because its amorphous phase is by default in the liquid state. It has been experimentally proven that the melting temperature varies with the crystallinity degree. Indeed, the temperature has a maximum value for a totally crystallized substance and the temperature decreases with the crystallinity degree.

3.2.3 Crystallization morphology

During crystallization, the molecular chains fold over them to form lamellae. If these lamellae grow in all direction from a point called nucleation, they form a category 1 spherulite (Figure (a) 2.8). If the first nucleation is a set of lamellae as thread-like fibers, the formed spherulite belongs to category 2 (Figure (b) 2.8). After a few moments of growth, this type of spherulite settles into a spherical growth pattern.

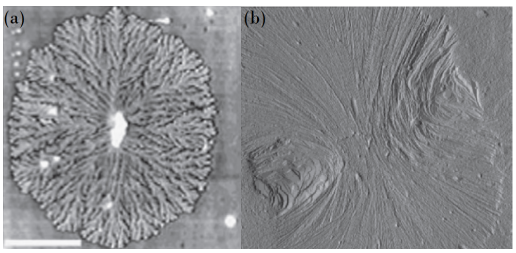

Figure 2.8: Spherulite category. (a) category 1. (b) category 2 [34].

Depending on the polymer nature and its crystallization temperature, the spherulite may have some anisotropy, Figure 2.9 shows the most known forms of anisotropy.

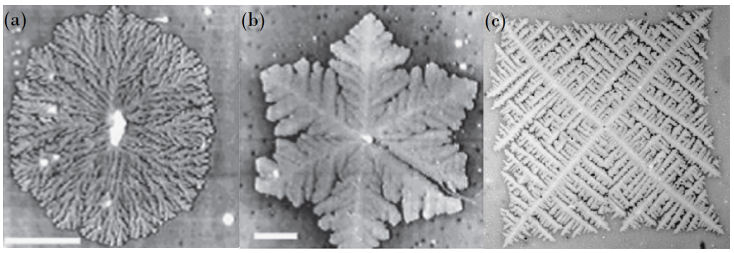

Figure 2.9: Spherulite anisotropy, (a) isotactic polystyrene without anisotropy at $T = 180\ ^{\circ}C$ [34],(b) isotactic polystyrene with anisotropy at $T = 205\ ^{\circ}C$ [34] and (c) methacrylate-polyethylene oxide with anisotropy [35].

Under non-static conditions, such as flow or the presence of pressure, the Spherulite may take other irregular shapes.

3.2.4 Thermal effect on the polymer

Polymers are like all materials whose structure strongly depends on the temperature at which they crystallize. Heat treatment is well known for carbon steels with which they improve their mechanical properties. For a steel, if we apply a very fast cooling, it will be harder and brittle according to the residual stress produced in it. For polymers, if we apply a very fast cooling, we get a softer structure because the crystallization degree is very low. It may also be noted that the nucleation number is very high at low temperature, whereas when at high temperature, a smaller amount can be found (see Figure (a) 2.10).

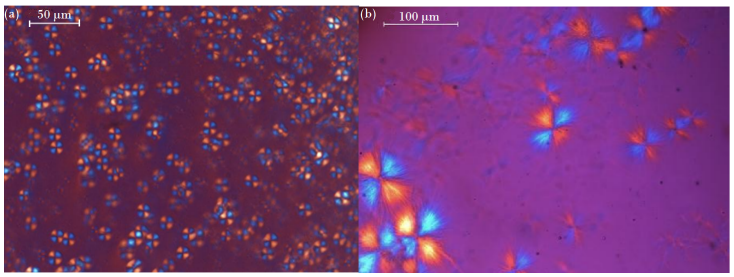

Figure 2.10: Thermal effect on the polymer PA66. (a) Fast cooling of PA66 in water. (b) PA66 crystallized at 257 $^{\circ}C$ [36].

A polymer can have a very compact structure with a very high crystallinity degree, this can only be obtained when the polymer crystallizes at a temperature close to that of the melting. This condition will lead to a very high crystallization time due to a low growth rate (Figure 2.11).

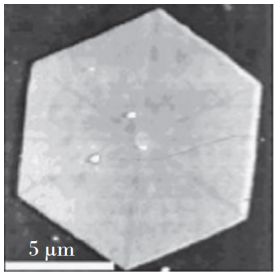

Figure 2.11: Isotactic polystyrene crystallisation at $T = 210\ ^{\circ}C$ take 4 hour [34].

In practice, it is not possible to wait days to perform crystallization process. For this reason, polymers generally have a low crystal content.

3.3 Thermodynamics

In this section, by using the basic equation of thermodynamics, we will model the two fundamental phenomena, growth and nucleation.

Nucleation is the appearance of small domains called nucleus of a new phase within or at the border of a homogeneous phase that has become unstable due to a change in temperature, pressure or its composition. Nucleation is the initial stage of a liquid-to-solid phase transition. The atoms or chains of atoms that need the least energy to move and create a solid region, will be the nucleus.

Growth is the step that comes after nucleation which consists in continuing the assembly of atoms or chains of atoms at the front of the nucleus in an ordered or disordered manner to form at the end a structure called spherulite.

3.3.1 Supercooling

Consider a polymeric liquid, the chemical potential per mole in the liquid phase is written as follow:

$$\mu_u^0 = \frac{\partial G}{\partial n_i} = h^l - Ts^l \tag{2.1}$$

where h^l is the enthalpy per mole, s^l is the entropy per mole, G is the Gibbs free energy and n_i is the mole's number. By analogy, chemical potential per mole in the crystalline phase is written as follows:

$$\mu_u^c = h^c - Ts^c \tag{2.2}$$

The equilibrium melting temperature T_m^0 is defined as the intersection point of the crystal and liquid chemical potential curves.

$$\mu_u^0 = \mu_u^c \quad \Rightarrow \quad T_m^0 = \frac{h^l - h^c}{s^l - s^c} = \frac{\Delta h}{\Delta s} \tag{2.3}$$

In a semi-crystalline polymer, the thermodynamic fusion temperature T_m is determined by the intersection of the chemical potential (or Gibbs free energy) curves of the perfect crystal and the amorphous material (see Figure 2.12).

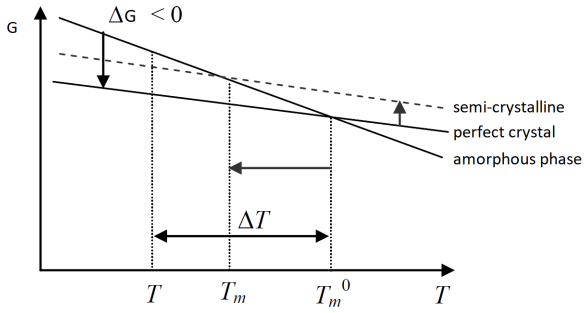

Figure 2.12: Gibbs free energy of a semi-crystalline polymer and thermodynamic melting temperature [37].

The polymers crystallize in thin layers, so surface effects are balanced by volume one. For these reasons, Gibb's free energy of semi-crystalline polymer is much higher than that of the perfect crystal (figure 2.12). As a result, the melting temperature T_m of a semi-crystalline polymer is less than the melting temperature T_m^0 of a perfect crystal.

For $T > T_m^0$, we have $\mu_u^0 < \mu_u^c$, so the liquid phase is stable. For $T < T_m^0$ the crystalline phase becomes more stable and the thermodynamic force given as follows:

$$\begin{aligned} -\Delta\mu_u &= \mu_u^0 - \mu_u^c = -(\Delta h - T\Delta s) \\ &= -\Delta h \left(1 - \frac{T}{T_m^0}\right) = -\Delta h \frac{\Delta T}{T_m^0} \end{aligned} \tag{2.4}$$

where $\Delta T = T_m^0 - T$ is the super-cooling.

3.3.2 Equilibrium crystal shape (Gibbs–Thompson Equation)

Consider a finite crystal as sketched in Figure 2.13. $L_i \mid i = 1..3$ are its size for each direction and σ_i are the surface free energy per unit area of surfaces perpendicular to the i^{th} axis.

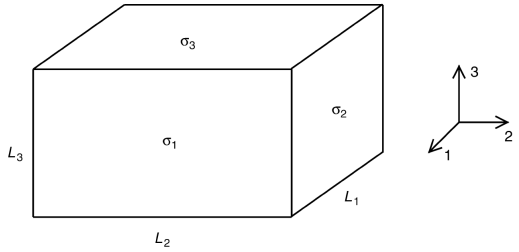

Figure 2.13: Sketch of a finite crystal.

The free energy of formation of this crystal from the pure melt is defined as follows:

$$\Delta G = -V\Delta\mu + 2\sigma_1 L_2 L_3 + 2\sigma_2 L_3 L_1 + 2\sigma_3 L_1 L_2 \tag{2.5}$$

where $\Delta\mu$ is the chemical potential per volume unit and $V = L_1 L_2 L_3$ is the volume of crystal. For the specific case of a lamella, we suppose that $L_3 = L$ (thickness), $\sigma_3 = \sigma_f$, $L_1 = L_2$ (lateral size) and $\sigma_1 = \sigma_2 = \sigma_l$. So the surface area $A = L_1 L_2$ is larger than lateral surface area $L_3 L_1 + L_2 L_3$. As consequence, the free energy of a lamella becomes as follow:

$$\Delta G = -AL\Delta\mu + 2A\sigma_f \tag{2.6}$$

Replacing $\Delta\mu$ with its expression (2.4), the free energy becomes as follows:

$$\Delta G = -AL\Delta H\frac{\Delta T}{T_m^0} + 2A\sigma_f \tag{2.7}$$

where $\Delta H = H^l - H^c$ is the latent heat of fusion per volume unit. At the melting temperature T_m of a lamella, ΔG will be equal to zero.

$$T_m = T_m^0\left(1 - \frac{2\sigma_f}{L\Delta H}\right) \tag{2.8}$$

3.3.3 Nucleation

When a liquid is subjected to a temperature below its melting temperature, small nuclei of different sizes and shapes are created. This phenomenon is called primary nucleation. These nuclei are stabilized when the free energy associated with their formation diminishes. For a spherical nucleus of radius r, the free energy of formation of a crystal from the liquid phase, is as expressed by:

$$\Delta G = -\frac{4}{3}\pi r^3 \Delta\mu + 4\pi r^2 \sigma \tag{2.9}$$

where σ is the interfacial tension at the spherical surface of the nucleus. Figure 2.14 shows that the free energy has a maximum for a value of r equal to the critical radius r_c. When the radius of nuclei exceeds this critical value, the nucleation will be stable and will continue to increase.

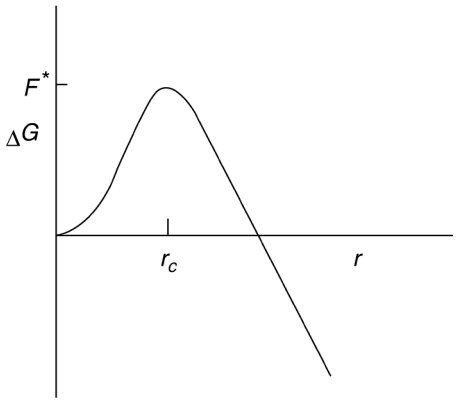

Figure 2.14: Free energy of a spherical germ formation [37].

The critical radius r_c is obtained from this condition:

$$\left(\frac{\partial \Delta G}{\partial r}\right)_{r=r_c} = 0 \tag{2.10}$$

The solution of equation (2.10) is written as follows:

$$r_c = \frac{2\sigma}{\Delta\mu} = \frac{2\sigma T_m^0}{\Delta H \Delta T} \tag{2.11}$$

We can also compute the critical free energy associated with the formation of nucleus of radius r_c.

$$F^* = \frac{16\pi}{3}\frac{\sigma^3}{(\Delta\mu)^2} = 16\pi 3\frac{\sigma^3(T_m^0)^2}{(\Delta H)^2(\Delta T)^2} \tag{2.12}$$

We then assume that $\dot{N}$ is the nucleation rate which is expressed as follows:

$$\dot{N} = \dot{N}_0 e^{-\frac{F^*}{kT}} \tag{2.13}$$

where k is Boltzmann's constant and $\dot{N}_0$ is called the nucleation rate prefactor. To calibrate the nucleation model, one can draw $log(\dot{N})$ as a function of $(T_m^0)^2/(T(\Delta T)^2)$, which is usually linear.

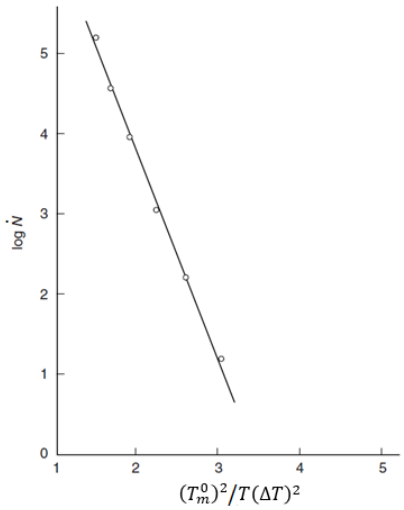

Figure 2.15: Dependence of nucleation rate on supercooling [37].

3.3.4 Secondary Nucleation and Growth

Lauritzen and Hoffman (LH) [38] proposed a model for crystal growth as a function of temperature. In the basic LH model, the first nucleation is associated with the creation of the first growth surface, where L_p is its lateral size. The second nucleation corresponds to the addition of polymer molecules to the growing front, which is considered as stem, where $V = Lab$ its volume, see sketch in figure 2.16.

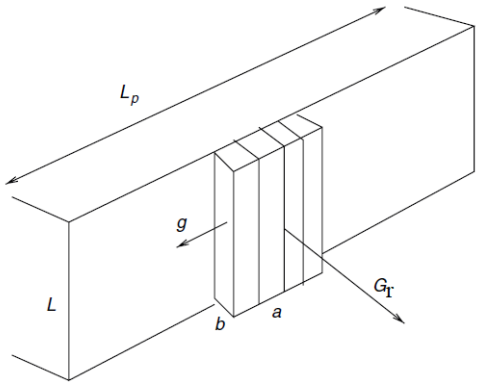

Figure 2.16: Lauritzen and Hoffman model of growth front [37].

There are two ways to attach the stems to the growth front. The first is to put the stem at the growth surface in the direction of growth rate G_r. The second is to add a stem in the direction of lateral rate g (figure 2.16). As a consequence, the stem formation is divided into three regimes:

- Regime I: if $g >> G_r$.
  All the substrate is covered with stems before adding stem in the growth direction. This regime exists essentially at high temperature. This explains the fact that there is a high crystalline amount in spherulite at high temperature.

- Regime II: if $g = G_r$.
  Stem growth occurs simultaneously in both directions. This regime occurs in medium temperature.

- Regime III: if $g << G_r$.
  The growth of the stem occurs essentially by deposition of new germs in the growth direction. This regime is obtained at low temperature.

The growth rate is proportional to two terms. The first corresponds to diffusion (or transport) of the macro-molecular chains in the liquid and the second to the deposit of germs on the surface of stem growth. Their expressions given by LH theory are as follows [39][38]:

$$G_r(T_c) = G_{ri} \underbrace{\exp\left[-\frac{U^*}{k(T_c - T_\infty)}\right]}_{\text{Diffusion term}} \underbrace{\exp\left[-\frac{K_{G_r}}{T_c \Delta T}\right]}_{\text{Germ deposit}} \tag{2.14}$$

With: $G_{r\ i}$ is the prefactor for each regime $i \mid i \in [I, II, III]$ and:

$$K_{G_r} = \begin{cases} 2K_{G_{r0}} & \text{in regimes } I \ \& \ III \\ K_{G_{r0}} & \text{in regime } II \end{cases} \Bigg| \ K_{G_{r0}} = \frac{2b\sigma_l\sigma_f T_m^0}{k\Delta H} \tag{2.15}$$

where U^* is the activation energy for transport of segments to the site of crystallization, k is Boltzmann's constant, $T_\infty < T_g$ is the temperature at which any motion is made impossible, its expression is $T_\infty = T_g - 30\ ^\circ C$ [38], $\Delta T = T_m^0 - T_c$ is the super-cooling and σ_l and σ_f are the free energies of the lateral and frontal surfaces of the stem, respectively. Applying the log operator to expression (2.14) leads to:

$$log(G_r) + \frac{U^*}{k(T - T_\infty)} = log(G_{r0}) - \frac{K_{G_r}}{T\Delta T} \tag{2.16}$$

It may be noted that there is a linear relation between $log(G_r) + \frac{U^*}{k(T-T_\infty)}$ and $\frac{1}{T\Delta T}$. Figure 2.17 shows the evolution of these three regimes.

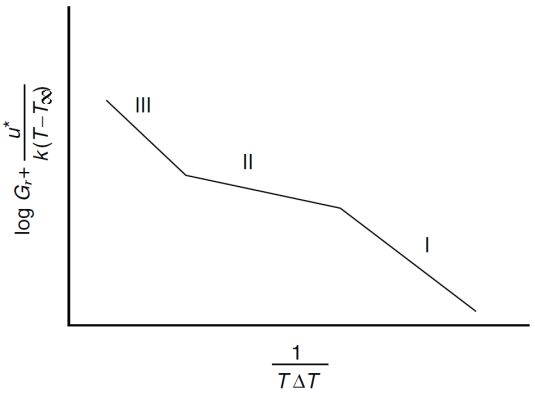

Figure 2.17: Three regimes in the Lauritzen and Hoffman model [37].

The slope of the curve in regime II should be exactly half that of regimes I and III, because in this theory $K_{G_r}^I = K_{G_r}^{III} = 2K_{G_r}^{II}$. The Hoffman-Lauritzen expression gives a bell-shaped curve for $G_r(T)$ (see Figure 2.18).

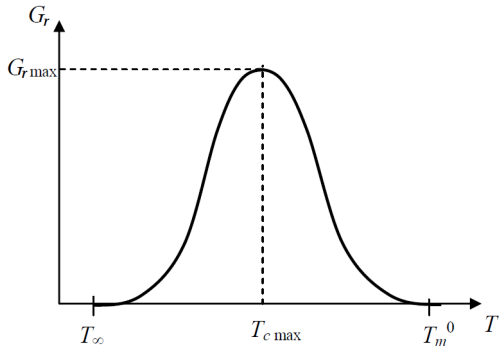

Figure 2.18: Crystalline growth rate according to the theory of Lauritzen and Hoffman.

If $T \approx T_\infty$ then the material is close to the vitreous state, and the diffusion of the stem is strongly restrained. If $T \approx T_m^0$ then the deposition of new stem on the substrate is very weak, and the growth term tends to 0.

3.4 Kinetics of isothermal crystallization

In this section, we will present semi-analytical models that predict the degree of crystallinity as a function of time and temperature.

3.4.1 Avrami's model [6]

The relative degree of crystallization is represented by a variable α_c which depends on time and temperature, and is defined as follows:

$$\alpha_c = \frac{x_c(t,T)}{x_\infty} \tag{2.17}$$

where x_c is the degree of crystallization and x_∞ the ultimate degree of crystallization. The Avrami's model is used for isothermal case i.e. when the crystallization temperature is constant. As consequence, nucleation and growth rate become constant.

Assuming a time interval $[0,t]$ and a current time τ, each new nucleus grows as a sphere of radius $r = G_r(t-\tau)$, where $G_r = \frac{dr}{dt}$ is the growth rate. So we can introduce the extended volume of the crystallized part in the time interval $[\tau, \tau + d\tau]$ as follows:

$$dV_c^e = \frac{4\pi}{3} r^3 V \dot{N} d\tau = \frac{4\pi}{3} G_r^3 (t-\tau)^3 V \dot{N} d\tau \tag{2.18}$$

where $\dot{N}$ is the nucleation rate per unit volume, V is total volume of substance and $dN = V\dot{N}d\tau$ is the number of new nucleus that appear in the time interval $[\tau, \tau + d\tau]$. Doing the time integral on $[0, t]$ of (2.18), we obtain,

$$V_c^e = \frac{\pi}{3} G_r^3 t^4 V \dot{N} \tag{2.19}$$

Since the new nucleus appears only in the amorphous phase, the real extended volume of the crystallized part in the time interval $[\tau, \tau + d\tau]$ should be written as follows:

$$dV_c = dV_c^e \left(1 - \frac{V_c}{V}\right) \tag{2.20}$$

The volume integral gives the following expression:

$$Ln(1-\alpha_c) = -\frac{V_c^e}{V} \tag{2.21}$$

Finally, we obtain Avrami's model:

$$\alpha_c = 1 - e^{-\frac{V_c^e}{V}} = 1 - e^{-\frac{\pi}{3} G_r^3 \dot{N} t^4} = \underbrace{1 - e^{-Kt^n}}_{\text{Generalized form}} \tag{2.22}$$

There is no physical interpretation of the variables n and K, n is called the Avrami exponent and depends on the dimension (1D, 2D or 3D) and material's characterization. For this reason, we'll determine it from experimental data. Generally it takes values between 1 and 4. K is called the isothermal crystallization rate and the unit of this quantity is $[1/s^n]$. There are another important formulation by applying twice the logarithm on Eq. (2.22) leading to:

$$Ln(-Ln(1-\alpha_c)) = Ln(K) + nLn(t) \tag{2.23}$$

This linear equation is very important. It will be used with experimental data to obtain more easily K and n values.

3.5 Kinetics of non-isothermal crystallization

3.5.1 Non-isothermal crystallization by Ozawa method

For transformation at a constant cooling rate, we can introduce the relationship between crystallization time t and crystallization temperature T.

$$t = \frac{|T - T_0|}{v_c} \tag{2.24}$$

where $v_c = |\frac{dT}{dt}|$ is the cooling rate, T_0 is the onset crystallization temperature and T is the crystallization temperature at time t. Ozawa considers that the process of non-isothermal crystallization is an infinitesimal accumulation of isothermal transformation [40]. Using (2.22) and (2.24), we can find the following expression.

$$\alpha_c = 1 - e^{-\frac{K(T_0 - T)^n}{v_c^n}} = 1 - e^{-\frac{\kappa}{v_c^n}} \tag{2.25}$$

where κ is the cooling function of non-isothermal crystallization.

3.5.2 Non-isothermal crystallization by modified Avrami method

Since Avrami's model parameters K and n are used only for the isothermal case, Jeziorny proposes an extension to non-isothermal case by modifying the expression of K [41] which becomes as follows:

$$Ln(K_c) = \frac{Ln(K)}{v_c} \tag{2.26}$$

where K_c is the crystallization rate modified by Jeziorny. The relative degree of crystallization equation becomes:

$$\alpha_c = 1 - e^{-K_c^{v_c} t^n} \tag{2.27}$$

In another way.

$$Ln(-Ln(1 - \alpha_c)) = v_c Ln(K_c) + nLn(t) \tag{2.28}$$

3.6 General model

Suppose that the nucleation rate $\dot{N}$ and the growth rate G_r are dependent on time, following the same methodology in the section 3.4.1 the equation (2.19) becomes:

$$V_c^e = \frac{4\pi}{3} V \int_0^t \dot{N}(\tau) \left(\int_\tau^t G_r(u) du \right)^3 d\tau \tag{2.29}$$

Using (2.21), we can deduce the Kolmogorov model [5].

$$\alpha_c = 1 - e^{-\frac{V_c^e}{V}} = 1 - e^{-\frac{4\pi}{3} \int_0^t \dot{N}(\tau) \left(\int_\tau^t G_r(u) du \right)^3 d\tau} \tag{2.30}$$

We can go back to Avrami's model if the following assumptions are used: Nucleation and growth rate depend only on temperature, so in isothermal case they are constant, $\dot{N} = cte$ and $G_r = cte$, we can write then.

$$\alpha_c = 1 - e^{-\frac{4\pi}{3} G_r^3 \dot{N} t^3} = 1 - e^{-Kt^n} \tag{2.31}$$

Later, Nakamura et al. [7] have generalized the isothermal model of Avrami to a non isothermal model. Based on the following assumptions: nucleation and growth rate are only thermo-dependent i.e. have the same dependence on temperature (isokinetic) and the growth rate is linear.

$$\frac{G_r(T)}{\dot{N}(T)} = cte \tag{2.32}$$

So, using the equation (2.30), we can deduce the Nakamura model.

$$\alpha_c = 1 - e^{-\left(\int_0^t \mathcal{K}(T) d\tau \right)^n} \tag{2.33}$$

where $\mathcal{K}$ is the non-isothermal crystallization rate. At a given temperature T, we can make a relation between Avrami and Nakamura parameters [42].

$$\mathcal{K}(T) = K(T)^{\frac{1}{n}} = Ln(2)^{\frac{1}{n}} \left(\frac{1}{t_{1/2}} \right) \tag{2.34}$$

The time $t_{1/2}$ can be calculated by Hoffman-Lauritzen theory [38], because the growth rate in Eq. (2.14) is proportional to the inverse of time.

$$\left(\frac{1}{t_{1/2}} \right) = K_0 exp \left(\frac{-U^*}{k(T - T_\infty)} \right) exp \left(\frac{-K_{G_r}}{T \Delta t} \right) \tag{2.35}$$

where K_0 is a temperature independent constant $[s^{-1}]$. There is another way to find $\mathcal{K}$ by using Weibull distribution law.

$$\mathcal{K} = \begin{cases} M\frac{k}{\lambda}\left(\frac{T-\theta}{\lambda}\right)^{k-1} exp\left(-\left(\frac{T-\theta}{\lambda}\right)^{k}\right) & if \quad T \geq \theta \\ 0 & else \end{cases} \tag{2.36}$$

where θ is the translation temperature, k is the shape parameter, λ is the scale parameter and M is the magnitude parameter. Nakamura et al. [7] offer another expression similar to that developed by the Hoffman-Lauritzen theory.

$$ln(K(T)) = A - \frac{B\ T}{(T - T_g - 51.6)^2} - \frac{C\ T_m}{T(T_m - T)} \tag{2.37}$$

where A, B and C are constants relevant to the polymer, T_m is the melting temperature and T_g is the glass transition temperature.

3.7 Crystallinity degree effect on polymer properties

In this section, simplified models to take into account the effect of crystallinity on the properties of polymers will be presented.

3.7.1 Crystallinity degree effect on density and specific heat

In any sample that has two phases, in our case amorphous and crystalline, it is possible to write the following equation:

$$m = m_a + m_c \tag{2.38}$$

where m is the total mass of the sample, m_a is the total mass of the amorphous phase and m_c is the total mass of the crystalline phase. Using the equation (2.38), it is possible to find a relation between the total density and that of each phase.

$$\begin{aligned} \rho V &= \rho_c V_c + \rho_a V_a \\ \rho &= \rho_c \tfrac{V_c}{V} + \rho_a \tfrac{V_a}{V} \\ \rho &= \rho_c x_c + \rho_a (1 - x_c) \end{aligned} \tag{2.39}$$

where V and ρ are respectively the total volume and the density of the sample, V_a and ρ_a are respectively the total volume and the density of the amorphous phase and V_c and ρ_c are respectively the total volume and the density of the crystalline phase.

Specific heat is the energy per mass unit and temperature. This energy is calculated by the contribution of two phases, amorphous and crystalline.

$$c_p m = c_{p_c} m_c + c_{p_a} m_a \tag{2.40}$$

where c_p is the specific heat of the sample per mass unit, c_{p_a} is the specific heat of the amorphous phase per mass unit and c_{p_c} is the specific heat of the crystalline phase per mass unit. By using the equation (2.39) we find the following expression:

$$C_p = C_{p_c} x_c + C_{p_a}(1 - x_c) \tag{2.41}$$

where C_p is the specific heat of the sample per volume unit, C_{p_a} is the specific heat of the amorphous phase per volume unit and C_{p_c} is the specific heat of the crystalline phase per volume unit.

3.7.2 Crystallinity degree effect on thermal conductivity

In this section, several theoretical and empirical models will be proposed to predict the effective thermal conductivity of two-phase mixtures.

For a simple case where the two phases are acting in parallel, the model equation can be written as follows:

$$k = k_c x_c + k_a(1 - x_c) \tag{2.42}$$

where k is the thermal conductivity of the sample, k_a is the thermal conductivity of the amorphous phase and k_c is the thermal conductivity of the crystalline phase.

For two phases acting in series, the model equation can be written as follows:

$$\frac{1}{k} = \frac{x_c}{k_c} + \frac{1 - x_c}{k_a} \tag{2.43}$$

It is well known that the structure of polymers is very complicated, so these simple models cannot give a good prediction. Then it is necessary to find other models. By the application of the potential theory, Maxwell [43] obtained an exact solution for the conductivity of spheres distributed in a random way and without interaction in a homogeneous medium. Considering that the spheres are constituted by the crystalline phase and the amorphous phase is homogeneous medium, this allows to derive a homogenization equation expressed as:

$$k = k_a \left[\frac{k_c + 2k_a + 2x_c(k_c - k_a)}{k_c + 2k_a - x_c(k_c - k_a)} \right] \tag{2.44}$$

Russell [44] proposed a model to predict the thermal conductivity of a porous material based on the thermal conductivities of its solid and porous components. In the case of two phases non-porous semi-crystalline polymers this leads to:

$$k = k_a \left[\frac{x_c^{2/3} + \frac{k_a}{k_c}(1 - x_c^{2/3})}{x_c^{2/3} - x_c + \frac{k_a}{k_c}(1 + x_c - x_c^{2/3})} \right] \tag{2.45}$$

3.7.3 Crystallinity degree effect on Young's modulus

Figure 2.19 shows the logarithm of experimental Young's modulus for PE, PET and PP as a function of crystallinity degree.

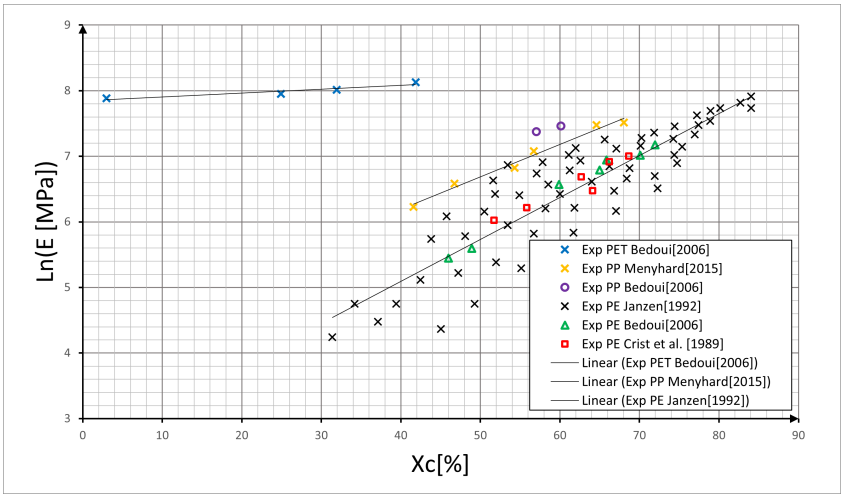

Figure 2.19: The logarithm of the experimental Young's modulus for PE, PET and PP as a function of crystallinity [45] [46] [47] [48].

From the figure, it is clear to see that the logarithm of Young's modulus scales linearly with crystallinity degree.

$$Ln(E) = Ax_c + B \tag{2.46}$$

where A and B are two material dependent parameters and it is possible to find them using these two conditions: $x_c = 0 \Rightarrow Ln(E) = Ln(E_a)$ and $x_c = 1 \Rightarrow Ln(E) = Ln(E_c)$. Hence the expression becomes.

$$Ln(E) = (Ln(E_c) - Ln(E_a))\, x_c + Ln(E_a) \tag{2.47}$$

where E_a is the Young's modulus of the amorphous phase and E_c is the Young's modulus of the crystalline phase.

4 | Conclusion

Today, additive manufacturing is no longer only used for prototyping, it is now possible to manufacture high-performance structural parts thanks to the rapid development of the underlying technology and knowlegde. The main problem with this process is that there is distortion along the printing leading to discrepancies between the part as design and the printed part. Therefore, there are many efforts to model this process with different methods despite its complexity. The origin of this shift is that the powdered material will go through different states of extension and thermal shrinkage accompanied by a shrinkage due to crystallization and porosity evolution.

For SLS (and other AM processes), most modeling efforts have been focused on the generation of CAD and finite element (FE) numerical models, while contributions on materials modeling are more limited and quite simple. The existing material models for SLS could be classified into two categories. First, simple models of solid materials, typically of linear thermoelasticity. Second, simple rheological fluid models, typically Newtonian flows. The former do not take into account the complexity of the behavior of the polymer, neither during the manufacturing stage nor in its final solid form. While the latter may be more or less appropriate during the fusing stage of the process, it is clearly not so for later stages of the printing process.

Polymers have a very complex behavior strongly dependent on temperature and crystallization. Indeed, polymers are semi-crystalline materials, so depending on its crystallinity degree all its thermal and mechanical parameters are affected. To predict quantitative simulations of polymer sintering, it is necessary to couple the thermal and mechanical field with the micro-structural evolution of the polymers which is represented by the crystallinity degree.

In this chapter, some semi-analytical laws taking into account the crystallinity degree have been proposed for thermal and mechanical properties. Since the polymers behavior is thermo-viscoelastic-viscoplastic, so taking into account the crystallinity degree effect on the Young's modulus only is not enough. Then, it is necessary to find another way to account for the crystallinity degree in this complex behavior.

CHAPTER 3

Polymer behavior

1 | Introduction

Semi-crystalline polymers consist of two phases called amorphous and crystalline. The amorphous phase consists of unorganized molecular chains. In modeling, this phase can be modeled by a viscoelastic (VE) or a viscoelastic-viscoplastic (VE-VP) behavior law in the isothermal case. On the other side, the crystalline phase consists of organized chains which makes it stiffer compared to the amorphous phase and its plastic deformation considered as a slip between the molecular chains. The most optimal model to use is therefore elasto-viscoplastic (E-VP) behavior law. Thus the homogeneous behavior of polymers could be VE-VP. Afterwards, we reviewed a VE-VP model developed by the a research team at UCLouvain [Doghri, Gudimetla, Krairi, Miled and others] [16].

The behavior of semi-crystalline polymers is largely influenced by temperature. As the temperature increases and exceeds the glass transition, the amorphous regions become mobile. As a result, the semi-crystalline polymer modulus declines, but it does not drop to zero like a completely amorphous polymer due to the presence of the crystalline regions. They preserve a low level of performance which is maintained until the temperature rises to its melting point. During manufacturing by the SLS process, the temperature varies between melting and printing chamber temperature, the application of thermo-viscoelastic-viscoplastic (TH-VE-VP) model will be mandatory. Afterwards, we also reviewed a TH-VE-VP model developed by the UCLouvain research team [Doghri, Gudimetla, Krairi, Miled and others] [17].

The first objective of this chapter is to review in detail the VE-VP and TH-VE-VP models and solve them numerically by implementing them in C++ code using solving methods such as "Radial return algorithm" (see appendix A). These models are implemented using the assumption of small deformation. The computational algorithms were inspired by I.Doghri's book [49].

The polymers behavior is also sensitive to the crystallinity degree. Since the polymer will melt during the SLS process, each region of the printed part will crystallize in a different way. For a predictive process simulation, the crystallinity degree effect must be added to the TH-VE-VP constitutive law previously developed. This will be the second objective of this chapter.

The chapter has the following outline. Section 2 describes the VE-VP model and the method of its implementation, while TH-VE-VP model was presented in section 3. The shift function method to account for the crystallinity degree is described in section 4. Conclusions are drawn in section 5.

2 | Viscoelastic-viscoplastic material model

2.1 Constitutive equation

We will assume an additive decomposition of the small strain tensor in two parts, the first is a viscoelastic strain ϵ^{ve} and the second is a viscoplastic strain ϵ^{vp}.

$$\epsilon = \epsilon^{ve} + \epsilon^{vp} \tag{3.1}$$

2.1.1 Linear viscoelastic part

Boltzmann proposed a linear viscoelastic model to express the evolution of Cauchy stress with the viscoelastic strain, accounting for the strain history.

$$\sigma(t) = \int_{-\infty}^{t} \boldsymbol{E}(t-\tau) : \frac{\partial \epsilon^{ve}}{\partial \tau} d\tau \tag{3.2}$$

where $\boldsymbol{E}(t)$ is the fourth-rank relaxation tensor. For an isotopic material, it will be as follows:

$$\boldsymbol{E}(t) = 2G(t)\boldsymbol{I}^{dev} + 3K(t)\boldsymbol{I}^{vol} \tag{3.3}$$

where $\boldsymbol{I}^{vol} = \frac{1}{3}\mathbf{1} \otimes \mathbf{1}$ and $\boldsymbol{I}^{dev} = \boldsymbol{I} - \boldsymbol{I}^{vol}$, $G(t)$ is the shear relaxation function and $K(t)$ the bulk relaxation function. We can use the Prony series to express $G(t)$ and $K(t)$.

$$G(t) = G_\infty + \sum_{i=1}^{I} G_i \exp(-\frac{t}{g_i}) \tag{3.4}$$

$$K(t) = K_\infty + \sum_{i=1}^{I} K_i \exp(-\frac{t}{k_i}) \tag{3.5}$$

where G_∞ is the long-term elastic shear modulus, K_∞ is the long-term elastic bulk modulus, g_i is the deviatoric relaxation times, k_i is the volumetric relaxation times and G_i and K_i are the corresponding modulus or weights of shear and bulk modulus respectively. The equations (3.2) and (3.3) give the following equations:

$$S(t) = 2G_\infty \xi^{ve}(t) + \sum_{i=1}^{I} S_i(t) \tag{3.6}$$

$$\sigma_H(t) = 3K_\infty \epsilon_H^{ve}(t) + \sum_{j=1}^{J} \sigma_{H_j}(t) \tag{3.7}$$

where $S(t)$ is the deviatoric part of the stress tensor, $\sigma_H(t)$ is the dilatational part of the stress tensor, $\xi^{ve}(t)$ is the deviatoric part of the strain tensor and $\epsilon_H^{ve}(t)$ is the dilatational part of the strain tensor.

$$S_i(t) = 2G_i \exp\left(-\frac{t}{g_i}\right) \int_{-\infty}^{t} \exp\left(\frac{\tau}{g_i}\right) \frac{\partial \xi^{ve}}{\partial \tau} d\tau \tag{3.8}$$

$$\sigma_{H_j}(t) = 3K_j \exp\left(-\frac{t}{k_j}\right) \int_{-\infty}^{t} \exp\left(\frac{\tau}{k_j}\right) \frac{\partial \epsilon_H^{ve}}{\partial \tau} d\tau \tag{3.9}$$

Numerical integration of the VE-VP model

We'll perform the numerical integration of equations (3.8) and (3.9) over a time step $[t_{n+1}, t_n]$ by writing these equations at time t_n and t_{n+1}:

$$S_i(t_n) = 2G_i \exp\left(-\frac{t_n}{g_i}\right) \int_{-\infty}^{t_n} \exp\left(\frac{\tau}{g_i}\right) \frac{\partial \xi^{ve}}{\partial \tau} d\tau \tag{3.10}$$

$$\sigma_{H_j}(t_n) = 3K_j \exp\left(-\frac{t_n}{k_j}\right) \int_{-\infty}^{t_n} \exp\left(\frac{\tau}{k_j}\right) \frac{\partial \epsilon_H^{ve}}{\partial \tau} d\tau \tag{3.11}$$

$$S_i(t_{n+1}) = 2G_i \exp\left(-\frac{t_{n+1}}{g_i}\right) \int_{-\infty}^{t_{n+1}} \exp\left(\frac{\tau}{g_i}\right) \frac{\partial \xi^{ve}}{\partial \tau} d\tau \tag{3.12}$$

$$\sigma_{H_j}(t_{n+1}) = 3K_j \exp\left(-\frac{t_{n+1}}{k_j}\right) \int_{-\infty}^{t_{n+1}} \exp\left(\frac{\tau}{k_j}\right) \frac{\partial \epsilon_H^{ve}}{\partial \tau} d\tau \tag{3.13}$$

If we multiply (3.10) and (3.11) by $\exp\left(-\frac{\Delta t}{g_i}\right)$ and we do the subtraction with (3.12) and (3.13), we find these expressions:

$$S_i(t_{n+1}) = \exp\left(-\frac{\Delta t}{g_i}\right) S_i(t_n) + 2G_i \int_{t_n}^{t_{n+1}} \exp\left(\frac{\tau - t_{n+1}}{g_i}\right) \frac{\partial \xi^{ve}}{\partial \tau} d\tau \tag{3.14}$$

$$\sigma_{H_j}(t_{n+1}) = \exp\left(-\frac{\Delta t}{k_j}\right) \sigma_{H_j}(t_n) + 3K_j \int_{t_n}^{t_{n+1}} \exp\left(\frac{\tau - t_{n+1}}{k_j}\right) \frac{\partial \epsilon_H^{ve}}{\partial \tau} d\tau \tag{3.15}$$

One of the methods to solve this problem is to take $\frac{\partial \epsilon^{ve}}{\partial \tau}(\tau)$ constant over the time interval i.e. $\forall \tau / t_n \leq \tau \leq t_{n+1}$, to simplify the integral calculation.

$$S_i(t_{n+1}) = \exp\left(-\frac{\Delta t}{g_i}\right) S_i(t_n) + 2G_i \left[1 - \exp\left(-\frac{\Delta t}{g_i}\right)\right] \frac{g_i}{\Delta t} \Delta \xi^{ve} \tag{3.16}$$

$$\sigma_{H_j}(t_{n+1}) = \exp\left(-\frac{\Delta t}{k_j}\right) \sigma_{H_j}(t_n) + 3K_j \left[1 - \exp\left(-\frac{\Delta t}{k_j}\right)\right] \frac{k_j}{\Delta t} \Delta \epsilon_H^{ve} \tag{3.17}$$

We insert the equation (3.16) into the equation (3.6) and the equation (3.17) into the equation (3.7), we find.

$$S(t_{n+1}) = 2G_\infty \xi^{ve}(t_n) + 2\tilde{G}\Delta\xi^{ve} + \sum_{i=1}^{I} \exp\left(-\frac{\Delta t}{g_i}\right) S_i(t_n) \tag{3.18}$$

$$\sigma_H(t_{n+1}) = 3K_\infty \epsilon_H^{ve}(t_n) + 3\tilde{K}\Delta\epsilon_H^{ve} + \sum_{j=1}^{J} \exp\left(-\frac{\Delta t}{k_j}\right) \sigma_{H_j}(t_n) \tag{3.19}$$

With:

$$\tilde{G} = G_\infty + \sum_{i=1}^{I} G_i \left[1 - \exp\left(-\frac{\Delta t}{g_i}\right)\right] \frac{g_i}{\Delta t} \tag{3.20}$$

$$\tilde{K} = K_\infty + \sum_{j=1}^{J} K_i \left[1 - \exp\left(-\frac{\Delta t}{k_j}\right)\right] \frac{k_j}{\Delta t} \tag{3.21}$$

We can deduce from equations(3.18) and (3.19) the following equation:

$$\begin{aligned}\sigma(t_{n+1}) =& \boldsymbol{E}_\infty : \epsilon^{ve}(t_n) + \tilde{\boldsymbol{E}} : \Delta\epsilon^{ve} + \sum_{i=1}^{I} \exp\left(-\frac{\Delta t}{g_i}\right) S_i(t_n) \\ &+ \sum_{j=1}^{J} \exp\left(-\frac{\Delta t}{k_j}\right) \sigma_{H_j}(t_n)\mathbf{1}\end{aligned} \tag{3.22}$$

where $\tilde{\boldsymbol{E}}(t) = 2\tilde{G}(t)\boldsymbol{I}^{dev} + 3\tilde{K}(t)\boldsymbol{I}^{vol}$

2.1.2 Viscoplastic part

We consider a J2 VP model with isotropic hardening [49], the yield function is given as follows:

$$f(\sigma_{eq}, p, \dot{\epsilon}) = \sigma_{eq} - (\sigma_y(\dot{\epsilon}) + R(p)) \tag{3.23}$$

where $\sigma_{eq} = \sqrt{\frac{3}{2} S : S}$ is the Von Mises equivalent stress, $R(p) = \kappa p^n$ is the hardening stress, κ is the hardening modulus, n is the hardening exponent, $p = \int_0^t \dot{p}(\tau) d\tau$ / $\dot{p} = \sqrt{\frac{2}{3} \dot{\epsilon}^{vp} : \dot{\epsilon}^{vp}}$ is the accumulated plastic strain, $\dot{\epsilon}^{vp} = \dot{p}\frac{\partial f}{\partial \sigma} = \dot{p}N$ is the VP strain rate and $N = \frac{3}{2}\frac{S}{\sigma_{eq}}$ is the normal to the surface of plasticity. To calculate $\dot{p}$ we will use the following equation:

$$\begin{cases} \dot{p} = 0 & if \quad f \leq 0 \\ \dot{p} = \dfrac{\sigma_y}{\eta}\left(\dfrac{f}{\sigma_y}\right)^m & if \quad f > 0 \end{cases} \tag{3.24}$$

where η is the viscoplastic modulus and m is the viscoplastic exponent. The viscoplastic strain and the accumulated plastic strain are calculated in each iteration by using an implicit method, assuming $\dot{p}$ constant over the time step and equal to $\dot{p}(t_{n+1})$. Their increments can be written as follows:

$$\Delta p \approx \dot{p}\Delta t \tag{3.25}$$

$$\Delta\epsilon^{vp} \approx \dot{\epsilon}(t_{n+1})\Delta t = \dot{p}(t_{n+1})N(t_{n+1})\Delta t = N(t_{n+1})\Delta p \tag{3.26}$$

In the return mapping algorithm (see appendix A), the viscoplastic correction is written as follows [49]:

$$\sigma(t_{n+1}) = \sigma^{pred}(t_{n+1}) - \tilde{E}\Delta\epsilon^{vp} \tag{3.27}$$

where σ^{pred} is the Cauchy stress calculated by a purely elastic strain using equation (3.22). Since $N = \frac{3}{2}\frac{S}{\sigma_{eq}}$ is deviatoric, the viscoplastic deformation increment is also deviatoric. So the viscoplastic correction can be written as follows:

$$\sigma(t_{n+1}) = \sigma^{pred}(t_{n+1}) - 2\tilde{G}N(t_{n+1})\Delta p \tag{3.28}$$

From equation (3.27) we can write:

$$S(t_{n+1}) = S^{pred}(t_{n+1}) - 2\tilde{G}\Delta\epsilon^{vp} \tag{3.29}$$

Using these two relations $N(t_{n+1}) = \frac{3}{2}\frac{S(t_{n+1})}{\sigma_{eq}(t_{n+1})}$ and $N^{pred}(t_{n+1}) = \frac{3}{2}\frac{S^{pred}(t_{n+1})}{\sigma_{eq}^{pred}(t_{n+1})}$ we can find.

$$N(t_{n+1})\sigma_{eq}(t_{n+1}) = N^{pred}(t_{n+1})\sigma_{eq}^{pred}(t_{n+1}) - 3\tilde{G}N(t_{n+1})\Delta p \tag{3.30}$$

The normal $N(t_{n+1})$ at the final plasticity surface is collinear to the normal of the preceding elastic surface $N^{pred}(t_{n+1})$. This implies that:

$$\sigma_{eq}(t_{n+1}) = \sigma_{eq}^{pred}(t_{n+1}) - 3\tilde{G}\Delta p \tag{3.31}$$

$$N(t_{n+1}) = N^{pred}(t_{n+1}) \tag{3.32}$$

So, to calculate Δp, we have to solve these two equations:

$$K_{\Delta p}(\Delta p, \sigma_{eq}) = \Delta p - \dot{p}\Delta t = 0 \tag{3.33}$$
$$K_{\sigma}(\Delta p, \sigma_{eq}) = \sigma_{eq}(t_{n+1}) + 3\tilde{G}\Delta p - \sigma_{eq}^{pred}(t_{n+1}) = 0 \tag{3.34}$$

These two equations are solved by Newton's method. The iteration index is omit for simplicity of notation. At each iteration, the corrections $C_{\Delta p}$ and C_{σ} are found [49].

$$K_{\Delta p}(\Delta p, \sigma_{eq}) + \left(1 + \frac{d\dot{p}}{df}\frac{dR}{dp}\Delta t\right) C_{\Delta p} - \left(\frac{d\dot{p}}{df}\Delta t\right) C_{\sigma} = 0 \tag{3.35}$$
$$K_{\sigma}(\Delta p, \sigma_{eq}) + 3\tilde{G}C_{\Delta p} + C_{\sigma} = 0 \tag{3.36}$$

With $\Delta p_{n+1} = \Delta p_n + C_{\Delta p}$ and $\sigma_{n+1}^{eq} = \sigma_n^{eq} + C_{\sigma}$. We have a system of two equations with two unknowns, we substitute the second expression in the first, we find.

$$C_{\Delta p} = -\frac{1}{h_v}\left(\frac{K_{\Delta p}}{\frac{d\dot{p}}{df}\Delta t} + K_{\sigma}\right) \tag{3.37}$$
$$C_{\sigma} = -K_{\sigma}(\Delta p_n, \sigma_n^{eq}) - 3\tilde{G}C_{\Delta p} \tag{3.38}$$

where $h_v = \frac{1}{\frac{d\dot{p}}{df}\Delta t} + 3\tilde{G} + \frac{dR}{dp}$. There is an other method to find Δp. In the plastic part we know that.

$$\Delta p \approx \dot{p}\Delta t = \frac{\sigma_y}{\eta}\left(\frac{f}{\sigma_y}\right)^m \Delta t \tag{3.39}$$

We can deduce the following expression:

$$f - \left(\eta\frac{\Delta p}{\Delta t}\sigma_y^{m-1}\right)^{\frac{1}{m}} = 0 \tag{3.40}$$

Replacing f by its value, we find:

$$\overline{f} = \sigma_{eq}^{pred} - 3\tilde{G}\Delta p - \sigma_y(\dot{\epsilon}) - R(p + \Delta p) - \left(\eta\frac{\Delta p}{\Delta t}\sigma_y^{m-1}\right)^{\frac{1}{m}} = 0 \tag{3.41}$$

So, to calculate Δp we solve by the Newton method the equation (3.41).

$$\begin{aligned}\Delta p_{n+1} &= \Delta p_n - \frac{\overline{f}}{\overline{f}'} \\ &= \Delta p_n + \frac{\sigma_{eq}^{pred} - 3\tilde{G}\Delta p_n - \sigma_y(\dot{\epsilon}) - R(p+\Delta p_n) - \left(\eta\frac{\Delta p_n}{\Delta t}\sigma_y^{m-1}\right)^{\frac{1}{m}}}{3\tilde{G} + R'(p+\Delta p_n) + \frac{1}{m}\left(\eta\frac{\Delta p_n^{1-m}}{\Delta t}\sigma_y^{m-1}\right)^{\frac{1}{m}}}\end{aligned} \tag{3.42}$$

To summarize, the box in appendix A contains the numerical resolution of the VE-VP model.

2.2 Result and discussion

In this section, we will compare the results of the VE-VP model with the experimental results. The material which we will adopt is high density polyethylene HDPE. The model parameters are given by B.Miled et al. (the tables 3.1 and 3.2) [16]. The experimental data is given by Zhang and Moore [50]. Since this model is already implemented in Digimat [3], the objective is to verify/validate the model with Digimat results and experimental data before extending it to the anisothermal case.

Figures 3.1 and 3.2 show a load-and-unload tensile test at two different strain rates. It can be noted that this model takes into account for strain rate dependency.

The difference in unloading between the experimental and the model curve can be explained by the fact that the real material exhibits nonlinear viscoelasticity and kinematic hardening. Whereas in the model we assume that the visco-elasticity is linear and we adopt an isotropic hardening.

Figures 3.1 and 3.2 show that in the case of uniaxial tensile test, the model is not sensitive to the increase in time step and it can predict the stress-strain curve even with large increments of time.

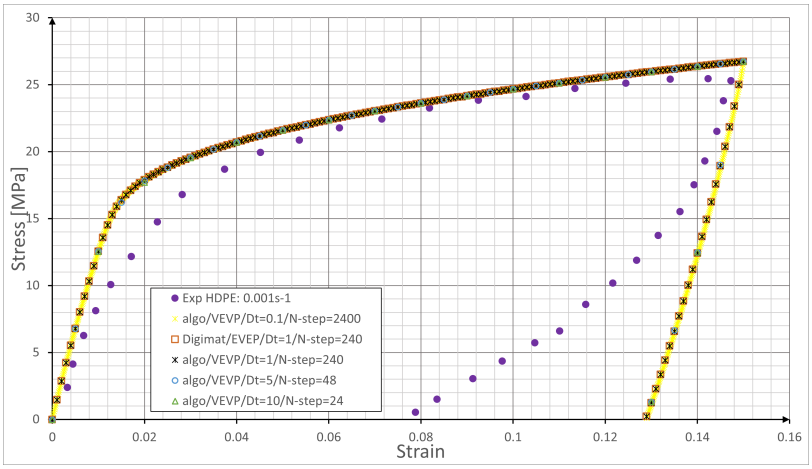

Figure 3.1: Uniaxial loading and unloading of HDPE under strain rate equals to $10^{-3}s^{-1}$. The used parameters are in Table 3.2.

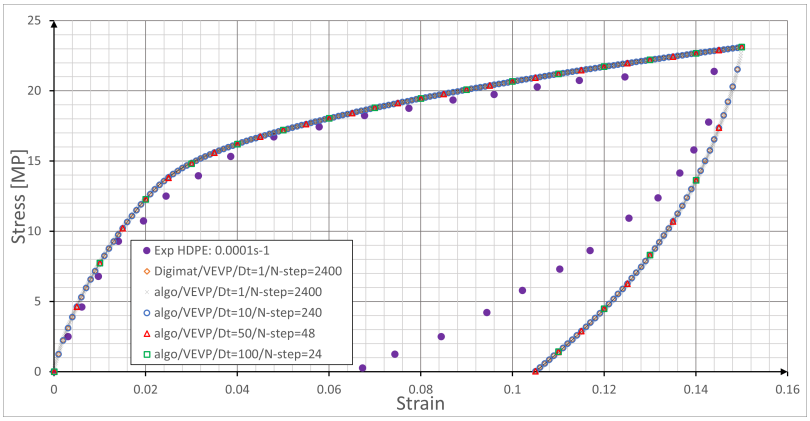

Figure 3.2: Uniaxial loading and unloading of HDPE under strain rate equal to $10^{-4}s^{-1}$. The used parameters are in Table 3.2.

The figure 3.3 shows an uniaxial loading–unloading cyclic test at a strain rate equals to $10^{-4}s^{-1}$. Even for cyclic loading and unloading, the model remains insensitive to time step and allows to use a big value of time steps.

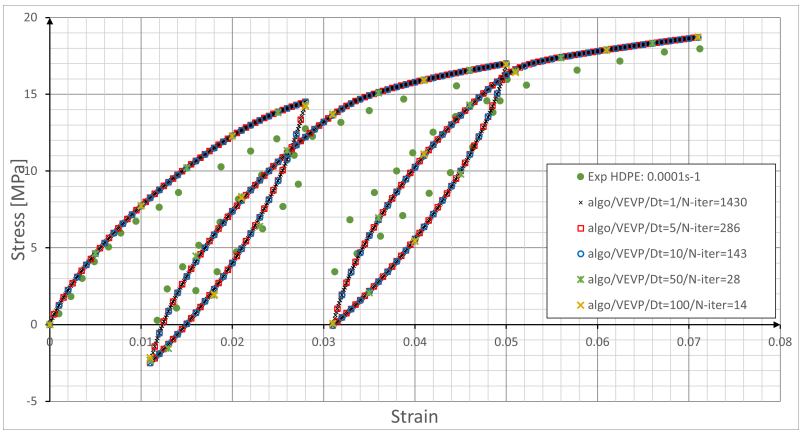

Figure 3.3: Uniaxial loading and unloading cycles of HDPE under strain rate equals to $10^{-4}s^{-1}$. The used parameters are in Table 3.2.

In case of shear, a three-phase test will be adopted for each phase and a strain rate is applied. The verification of model will be done with Digimat results because experimental data are not available.

The figures 3.4 and 3.5 show that as the strain rate increases, the stress level increases and when the strain is taken as constant, we see that the stress is released, it is the relaxation phenomenon.

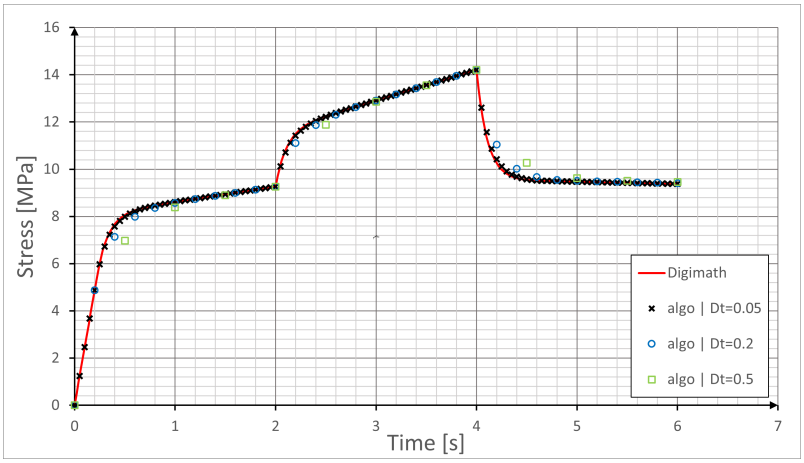

Figure 3.4: Shear test with different strain rate $\dot{\epsilon}_1 = 0.025s^{-1}$, $\dot{\epsilon}_2 = 0.05s^{-1}$ and $\dot{\epsilon}_3 = 0s^{-1}$ respectively for each phase. The used parameters are in Table 3.1.

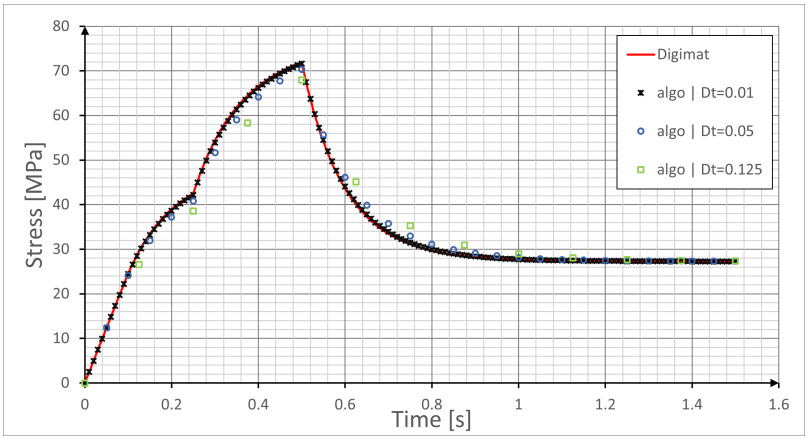

Figure 3.5: Shear test with different strain rate $\dot{\epsilon}_1 = 0.25s^{-1}$, $\dot{\epsilon}_2 = 0.5s^{-1}$ and $\dot{\epsilon}_3 = 0s^{-1}$ respectively for each phase. The used parameters are in Table 3.1.

Viscoelastic parameters	value	Viscoplastic parameters	value
G_0	$1000MPa$	κ	$80MPa$
G_1	$160MPa$	ν	$300MPa$
g_1	$10s$	σ_y	$40MPa$
G_2	$40MPa$	n	1
g_2	$0.1s$	m	1

Table 3.1: Material parameters for shear test with two relaxation times [16].

Viscoelastic parameters	value	Viscoplastic parameters	value
G_0	$577MPa$	κ	$28MPa$
K_0	$1250MPa$	ν	$106MPa$
G_1	$340MPa$	σ_y	$10MPa$
g_1	$110s$	n	0.39
G_2	$130MPa$	m	7
g_2	$10s$		
G_3	$25MPa$		
g_3	$5s$		
K_1	$404MPa$		
k_1	$15s$		
K_2	$369MPa$		
k_2	$5s$		
K_3	$115MPa$		
k_3	$3s$		

Table 3.2: Material parameters for HDPE [16].

3 | Thermo-Viscoelastic-viscoplastic material model

3.1 Constitutive equation

For the following TH-VE-VP model there are three parts of strain, the first is a viscoelastic strain ϵ^{ve}, the second is a viscoplastic strain ϵ^{vp} and the third is a thermal strain ϵ^{th}.

$$\epsilon = \epsilon^{ve} + \epsilon^{th} + \epsilon^{vp} \tag{3.43}$$

The expression of the thermal stress is defined as:

$$\epsilon^{th}(T) = (T - T_0)\alpha I = \theta\alpha I \tag{3.44}$$

where T is the absolute temperature of the current time, T_0 is the reference temperature and α is the thermal expansion coefficient. We will show in the next two paragraphs that in the TH-VE-VP model we can use the form of the stress expression given in the VE-VP model (Boltzmann's expression).

3.1.1 Helmholtz free energy

We consider that there are two parts of free energy: viscoelastic energy function Ψ^{ve} and hardening energy function Ψ^{h}.

$$\Psi = \Psi^{ve} + \Psi^{h} \tag{3.45}$$

We can write the expression of the free energy of hardening Ψ^{h} as:

$$\rho\Psi^{h} = \frac{3}{4}\frac{1}{C}\chi(t,T) : \chi(t,T) + \int_0^{p(t)} R(\xi,T)d\xi \tag{3.46}$$

where χ is the kinematic hardening stress, $R(p)$ is the isotropic hardening stress, χ and p are called internal variables, $\frac{2}{3}C\gamma = \chi = H\gamma$ such as H is the hardening modulus and γ such as $\dot{\gamma} = \lambda\left(\sqrt{\frac{3}{2}}\frac{s-\chi}{||s-\chi||} - \frac{3}{2}\frac{\gamma}{C}\chi\right)$ is the state variable. We introduce the thermo-viscoelastic strain:

$$\epsilon^{tve} = \epsilon^{ve} + \epsilon^{th} = \epsilon - \epsilon^{vp} \tag{3.47}$$

We can write the expression of viscoelastic free energy Ψ^{ve} as:

$$\begin{aligned}\rho\Psi^{ve} =&\rho\Psi_0^{ve} + \int_{-\infty}^{t} D(t-\tau) : \frac{\partial \epsilon^{tve}}{\partial \tau} d\tau - \int_{-\infty}^{t} \beta(t-\tau)\frac{\partial \theta}{\partial \tau} d\tau \\ &+ \frac{1}{2}\int_{-\infty}^{t}\int_{-\infty}^{t} \frac{\partial \epsilon^{tve}}{\partial \tau} : \boldsymbol{E}(t-\tau, t-\eta) : \frac{\partial \epsilon^{tve}}{\partial \eta} d\tau d\eta \\ &- \int_{-\infty}^{t}\int_{-\infty}^{t} \varphi(t-\tau, t-\eta) : \frac{\partial \epsilon^{tve}}{\partial \tau}\frac{\partial \theta}{\partial \eta} d\tau d\eta \\ &- \frac{1}{2}\int_{-\infty}^{t}\int_{-\infty}^{t} m(t-\tau, t-\eta)\frac{\partial \theta}{\partial \tau}\frac{\partial \theta}{\partial \eta} d\tau d\eta + O(\epsilon^3)\end{aligned} \tag{3.48}$$

where Ψ_0^{ve} is the mean free energy, $\boldsymbol{E}$, φ and m are the relaxation mechanical functions and $O(\epsilon^3)$ is a neglected terms. To ensure the continuity of mechanical relaxation functions, we adopt these properties: For $\tau_i < 0 \Rightarrow D_{ij}(\tau_1) = 0, \beta(\tau_1) = 0, \mathbb{C}^{ve}_{ijkl}(\tau_1, \tau_2) = 0, \varphi_{ij}(\tau_1, \tau_2) = 0$ and $m(\tau_1, \tau_2) = 0$.

3.1.2 Clausius-Duhem inequality

Using Clausius-Duhem inequality for the non-isothermal case, shows that the dissipation Φ must be non-negative.

$$\Phi = \sigma : \dot{\epsilon} - \rho(\dot{\Psi} + S\dot{T}) - \Delta T\frac{q}{T} \geq 0 \tag{3.49}$$

This dissipation can divide into two parts: the intrinsic dissipation $\Phi_1 = \sigma : \dot{\epsilon} - \rho(\dot{\Psi} + S\dot{T})$ and the heat dissipation $\Phi_2 = -\Delta T\frac{q}{T}$. Heat always flows spontaneously from hot to cold, therefore: $\Phi_2 = -\Delta T\frac{q}{T} \geq 0$, so, we can deduct $\Phi_1 = \sigma : \dot{\epsilon} - \rho(\dot{\Psi} + S\dot{T}) \geq 0$. Applying the time derivative to the equation (3.45) implies:

$$\rho\dot{\Psi} = \rho\dot{\Psi}^{ve} + \rho\dot{\Psi}^{h} \tag{3.50}$$

$$\rho\dot{\Psi}^{h} = \frac{3}{2}\frac{1}{C}\chi(t,T) : \frac{\partial \chi(t,T)}{\partial t} + R(p(t),T)\frac{\partial p(t)}{\partial t} \tag{3.51}$$

To calculate $\dot{\Psi}^{ve}$, we adapt these assumptions: $\boldsymbol{E}_{ijkl}(\tau,\eta) = \boldsymbol{E}_{klij}(\eta,\tau)$, $\varphi_{ij}(\tau,\eta) = \varphi_{ji}(\eta,\tau)$ and $m(\tau,\eta) = m(\eta,\tau)$.

$$\rho\dot{\Psi}^{ve} = \int_{-\infty}^{t} \frac{\partial D(t-\tau)}{\partial t} : \frac{\partial \epsilon^{tve}}{\partial \tau} d\tau + D(0) : \dot{\epsilon}^{tve}(t) - \int_{-\infty}^{t} \frac{\partial \beta(t-\tau)}{\partial t} \frac{\partial \theta}{\partial \tau} d\tau$$
$$- \beta(0)\dot{\theta}(t) + \frac{1}{2}\int_{-\infty}^{t}\int_{-\infty}^{t} \frac{\partial \epsilon^{tve}}{\partial \tau} : \frac{\partial \boldsymbol{E}(t-\tau, t-\eta)}{\partial t} : \frac{\partial \epsilon^{tve}}{\partial \eta} d\tau d\eta$$
$$+ \int_{-\infty}^{t} \boldsymbol{E}(t-\tau, 0) : \frac{\partial \epsilon^{tve}}{\partial \tau} d\tau : \dot{\epsilon}^{tve}(t) - \int_{-\infty}^{t}\int_{-\infty}^{t} \frac{\partial \varphi(t-\tau, t-\eta)}{\partial t} : \frac{\partial \epsilon^{tve}}{\partial \tau} \frac{\partial \theta}{\partial \eta} d\tau d\eta$$
$$- \int_{-\infty}^{t} \varphi(t-\tau, 0) : \frac{\partial \epsilon^{tve}(\tau)}{\partial \tau} d\tau \dot{\theta}(t) - \int_{-\infty}^{t} \varphi(0, t-\tau) \frac{\partial \theta(\tau)}{\partial \tau} d\tau : \dot{\epsilon}^{tve}(t)$$
$$- \frac{1}{2}\int_{-\infty}^{t}\int_{-\infty}^{t} \frac{\partial m(t-\tau, t-\eta)}{\partial t} \frac{\partial \theta}{\partial \tau} \frac{\partial \theta}{\partial \eta} d\tau d\eta - \int_{-\infty}^{t} m(t-\tau, 0) \frac{\partial \theta(\tau)}{\partial \eta} d\tau \dot{\theta}(t) \tag{3.52}$$

We replace $\rho\dot{\Psi}$ with its value in the Clausius-Duhem inequality and find

$$\left\{\sigma(t) - D(0) - \int_{-\infty}^{t} \boldsymbol{E}(t-\tau, 0) : \frac{\partial \epsilon^{tve}}{\partial \tau} d\tau + \int_{-\infty}^{t} \varphi(0, t-\tau) \frac{\partial \theta(\tau)}{\partial \tau} d\tau \right\} : \dot{\epsilon}^{tve}(t)$$
$$+ \left\{-\rho S(t) + \beta(0) + \int_{-\infty}^{t} m(t-\tau, 0) \frac{\partial \theta(\tau)}{\partial \eta} d\tau + \int_{-\infty}^{t} \varphi(t-\tau, 0) : \frac{\partial \epsilon^{tve}(\tau)}{\partial \tau} d\tau \right\} \dot{\theta}(t)$$
$$- \int_{-\infty}^{t} \frac{\partial D(t-\tau)}{\partial t} : \frac{\partial \epsilon^{tve}}{\partial \tau} d\tau + \int_{-\infty}^{t} \frac{\partial \beta(t-\tau)}{\partial t} \frac{\partial \theta}{\partial \tau} d\tau + \Lambda + \sigma : \dot{\epsilon}^{vp}(t) - R(p(t)) \frac{dp(t)}{dt}$$
$$- \frac{3}{2}\frac{1}{C}\chi(t, T) : \frac{\partial \chi(t, T)}{\partial t} - \Delta T \frac{q}{T} \geq 0 \tag{3.53}$$

where Λ is the dissipation term due to the time dependence of the relaxation functions and is given by:

$$\begin{aligned} \Lambda = &- \frac{1}{2}\int_{-\infty}^{t}\int_{-\infty}^{t} \frac{\partial \epsilon^{tve}}{\partial \tau} : \frac{\partial \boldsymbol{E}(t-\tau, t-\eta)}{\partial t} : \frac{\partial \epsilon^{tve}}{\partial \eta} d\tau d\eta \\ &+ \int_{-\infty}^{t}\int_{-\infty}^{t} \frac{\partial \varphi(t-\tau, t-\eta)}{\partial t} : \frac{\partial \epsilon^{tve}}{\partial \tau} \frac{\partial \theta}{\partial \eta} d\tau d\eta \\ &+ \frac{1}{2}\int_{-\infty}^{t}\int_{-\infty}^{t} \frac{\partial m(t-\tau, t-\eta)}{\partial t} \frac{\partial \theta}{\partial \tau} \frac{\partial \theta}{\partial \eta} d\tau d\eta \end{aligned} \tag{3.54}$$

Λ is a second order term and will be neglected. The equation (3.53) must be always positive whatever the value of $\dot{\epsilon}^{tve}(t)$, $\dot{\theta}(t)$, $\frac{\partial \epsilon^{tve}(t)}{\partial \tau}$ and $\frac{\partial \theta(t)}{\partial \tau}$ so we deduce these equations.

$$\sigma(t) = D(0) + \int_{-\infty}^{t} \boldsymbol{E}(t-\tau,0) : \frac{\partial \epsilon^{tve}}{\partial \tau} d\tau - \int_{-\infty}^{t} \varphi(0,t-\tau)\frac{\partial \theta(\tau)}{\partial \tau} d\tau \tag{3.55}$$

$$\rho S(t) = \beta(0) + \int_{-\infty}^{t} m(t-\tau,0)\frac{\partial \theta(\tau)}{\partial \eta} d\tau + \int_{-\infty}^{t} \varphi(t-\tau,0) : \frac{\partial \epsilon^{tve}(\tau)}{\partial \tau} d\tau \tag{3.56}$$

$$\frac{\partial D(t-\tau)}{\partial t} = 0 \tag{3.57}$$

$$\frac{\partial \beta(t-\tau)}{\partial t} = 0 \tag{3.58}$$

where $D(0)$ and $\beta(0)$ are the initial stress and initial entropy, respectively, and are assumed to be null. Finally we have:

$$\Phi = \sigma : \dot{\epsilon}^{vp} - R\dot{p} - \frac{3}{2}\frac{1}{C}\chi(t,T) : \dot{\chi}(t,T) - \Delta T \frac{q}{T} \geq 0 \tag{3.59}$$

If we replace ϵ^{tve} by its expression (3.47) and decompose the stress in hydraulic part and deviatoric part, we can simplify the equation (3.55):

$$s_{ij}(t) = \int_{-\infty}^{t} 2G(t-\tau)\frac{\partial \xi_{ij}^{ve}(\tau)}{\partial \tau} d\tau \tag{3.60}$$

$$\sigma_H(t) = \int_{-\infty}^{t} \left\{ 3K(t-\tau)\left(\frac{\partial \epsilon_H^{ve}(\tau)}{\partial \tau} + \alpha \frac{\partial \theta(\tau)}{\partial \tau} + \frac{\partial \alpha}{\partial \tau}\theta(\tau) \right) - \varphi(t-\tau)\frac{\partial \theta(\tau)}{\partial \tau} \right\} d\tau \tag{3.61}$$

We assume that the absolute value of $\frac{\partial \alpha}{\partial \tau}\theta(\tau)$ is negligible compared to that of $\alpha\frac{\partial \theta(\tau)}{\partial \tau}$ and we choosing $\varphi(t) = 3\alpha K(t)$, we can get these equations:

$$s_{ij}(t) = \int_{-\infty}^{t} 2G(t-\tau)\frac{\partial \xi_{ij}^{ve}(\tau)}{\partial \tau} d\tau \tag{3.62}$$

$$\sigma_H(t) = \int_{-\infty}^{t} 3K(t-\tau)\frac{\partial \epsilon_H^{ve}(\tau)}{\partial \tau} d\tau \tag{3.63}$$

We can notice that these equations are similar to those of the VE-VP equations developed in section 2.

3.2 Temperature influence on viscoelastic properties

In order to show the temperature dependence in the viscoelastic model, we adopt a change of variable. We assume that: $t \to \bar{t}$ and $\tau \to \bar{\tau}$, where $\bar{t}$ and $\bar{\tau}$ are reduced times and defined by R.A.Schapery [51]:

$$\bar{t} = \int_0^t \frac{d\xi}{a_T(T(\xi))}; \quad \bar{\tau} = \int_0^\tau \frac{d\xi}{a_T(T(\xi))} \tag{3.64}$$

where $a_T(T)$ is a temperature shift function. The equations (3.62) and (3.63) can be written as follows:

$$\sigma(t) = \int_{-\infty}^{\bar{t}} \boldsymbol{E}(\bar{t} - \bar{\tau}) : \frac{\partial \epsilon^{ve}(\bar{\tau})}{\partial \bar{\tau}} d\bar{\tau} \tag{3.65}$$

With:

$$\boldsymbol{E}(\bar{t}) = 2G(\bar{t})\boldsymbol{I}^{dev} + 3K(\bar{t})\boldsymbol{I}^{vol} \tag{3.66}$$

According to Schapery [51] the equation (3.65) can have the following form.

$$\sigma(t) = \int_{-\infty}^{t} \boldsymbol{E}(\bar{t} - \bar{\tau}) : \frac{\partial \epsilon^{ve}(\tau)}{\partial \tau} d\tau \tag{3.67}$$

The equation (3.67) can be obtained from equation (3.65), just by using this property:

$$\frac{\partial(..)}{\partial \tau} = \frac{\partial(..)}{\partial \bar{\tau}} \frac{\partial \bar{\tau}}{\partial \tau}; \quad \frac{\partial \bar{\tau}}{\partial \tau} = \frac{1}{a_T(T(t))} \tag{3.68}$$

Follow the same numerical method as developed in section 2. The equations (3.18), (3.19), (3.20) and (3.21) become:

$$S(t_{n+1}) = 2G_\infty \xi^{ve}(t_n) + 2\tilde{G}\Delta\xi^{ve} + \sum_{i=1}^{I} \exp\left(-\frac{\Delta\bar{t}}{g_i}\right) S_i(t_n) \tag{3.69}$$

$$\sigma_H(t_{n+1}) = 3K_\infty \epsilon_H^{ve}(t_n) + 3\tilde{K}\Delta\epsilon_H^{ve} + \sum_{j=1}^{J} \exp\left(-\frac{\Delta\bar{t}}{k_j}\right) \sigma_{H_j}(t_n) \tag{3.70}$$

With:

$$\tilde{G} = G_\infty + \sum_{i=1}^{I} G_i \left[1 - \exp\left(-\frac{\Delta\bar{t}}{g_i}\right)\right] \frac{g_i}{\Delta\bar{t}} \tag{3.71}$$

$$\tilde{K} = K_\infty + \sum_{j=1}^{J} K_i \left[1 - \exp\left(-\frac{\Delta\bar{t}}{k_j}\right)\right] \frac{k_j}{\Delta\bar{t}} \tag{3.72}$$

where $\Delta\bar{t} = \frac{\Delta t}{a_T(T(t))}$. In the literature, there are many expressions of the shift function, but in this work we will use the definition of Williams-Landel Ferry (WLF).

$$-\,log(a_T(T)) = -\frac{Ln(a_T(T))}{Ln(10)} = h(T) = \frac{C_1(T - T_{ref})}{C_2 + (T - T_{ref})} \tag{3.73}$$

where C_1 and C_2 are material parameters and T_{ref} is the reference temperature. If $T = T_{ref} - C_2$ the viscosity is assumed to be infinite, i.e, the material behavior becomes purely elastic. It's noted that the parameters of the Prony series are obtained at the temperature T_{ref}.

3.3 Temperature influence on viscoplastic properties

As in section 2, we'll here consider a J2 viscoplastic model with isotropic hardening [49]. We will keep the same methodology as that developed in section 2.1.2, except that we will modify the expressions of the yield stress and the isotropic hardening in order to take into account the effect of temperature. The new yield function is given as follows:

$$f(\sigma_{eq}, p, \dot{\epsilon}) = \sigma_{eq} - \Gamma(T, \beta_1)\sigma_y(\dot{\epsilon}) + \Gamma(T, \beta_2)R(p) \tag{3.74}$$

With:

$$\Gamma(T, \beta_i) = \exp(-\beta_i(T - T_{ref})) \quad | \quad i = 1..2 \tag{3.75}$$

And

$$R(p) = \kappa p^{n_1}(1 - \exp(-n_2 p)) \tag{3.76}$$

where $\beta_i \quad | \quad i = 1..2$, κ, n_1 and n_2 are material parameters and p is the accumulated plastic strain.

3.4 Result and discussion

In this section, we will compare the results of the TH-VE-VP model with the experimental results. The material we will adopt is polypropylene (PP 575P). Experimental data is provided from A.Krairi et al. work [17]. The model parameters are given by A.Krairi et al. (in the tables 3.3 and 3.4). The shear and bulk modulus G_i and K_i and their relaxation times g_i and k_i are obtained by the following relations:

$$\begin{cases} G_0 = \dfrac{E_0}{2(1+\nu)}; & G_i = \dfrac{E_i}{2(1+\nu)}; & g_i = \dfrac{\tau_i E_i}{G_i} \\ K_0 = \dfrac{E_0}{3(1-2\nu)}; & K_i = \dfrac{E_i}{3(1-2\nu)}; & k_i = \dfrac{\tau_i E_i}{K_i} \end{cases} \tag{3.77}$$

The instantaneous modulus E_0 is taken equal to 2000 MPa, the Poisson's ratio ν is assumed equal to 0.42, which is used only for identifying the model parameters, G_i and K_i. The parameters of the WLF shift function C_1 and C_2 are taken 61.22 and 178.5 $°C$ respectively.

Figures 3.6, 3.7 and 3.8 show a tensile test at different strain rates at $T = 23\ °C$, $T = 45\ °C$ and $T = 60\ °C$ respectively. It can be noted that this model takes into account the strain rate and temperature effects appropriately.

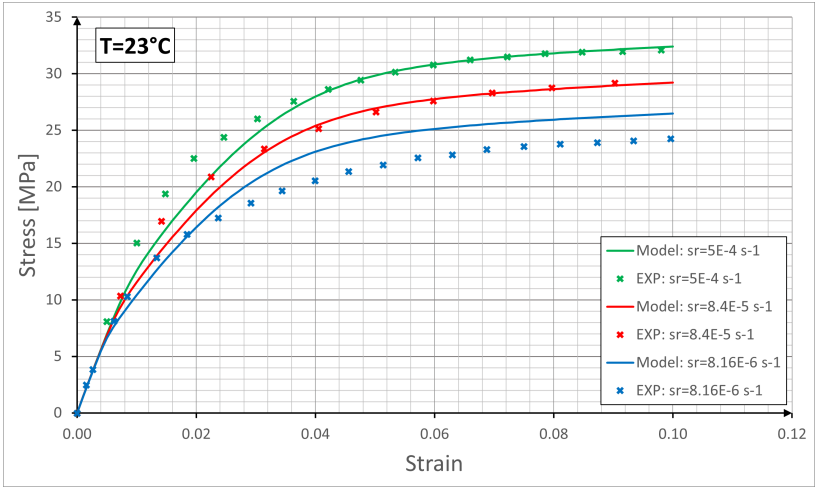

Figure 3.6: Tensile tests under different strain rates for Polypropylene PP at $T = 23\ °C$.

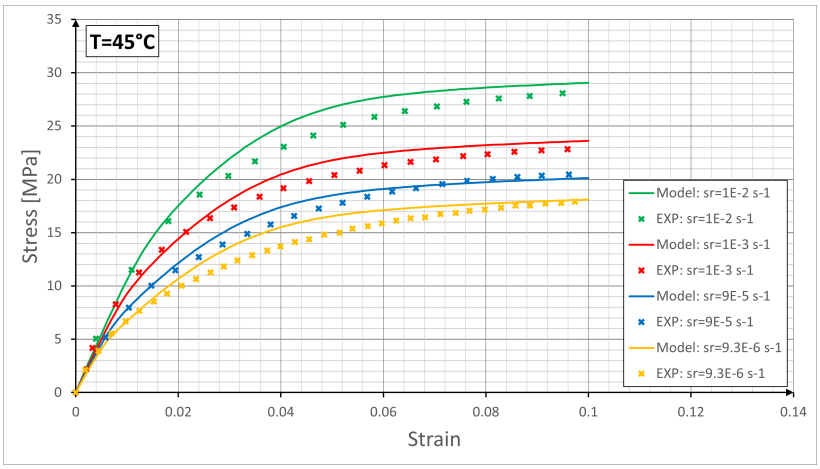

Figure 3.7: Tensile tests under different strain rates for Polypropylene PP at $T = 45\ ^{\circ}C$.

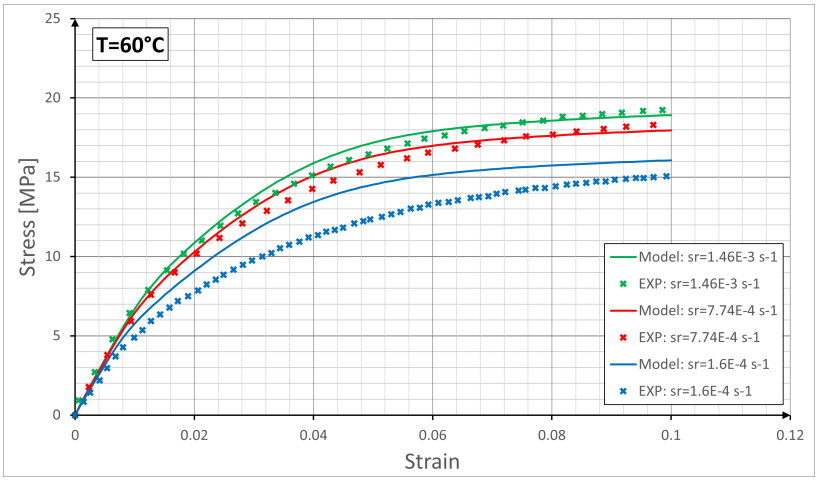

Figure 3.8: Tensile tests under different strain rates for Polypropylene PP at $T = 60\ ^{\circ}C$.

i	1	2	3	4	5	6	7	8	9	10
$log_{10}(\tau_i)$	-1.70	-0.55	0.59	1.73	2.88	4.02	5.17	6.31	7.46	8.60
$E_i[MPa]$	163	122	126	129	126	119	112	105	99	93.5
i	11	12	13	14	15	16	17	18	19	20
$log_{10}(\tau_i)$	9.74	10.9	12.0	13.1	14.3	15.5	16.6	17.8	18.9	20.0
$E_i[MPa]$	88.8	84.6	81.4	79.7	79.8	80.4	77.4	64.1	51.1	91.7

Table 3.3: Viscoelastic parameters for PP at $T = 23\ ^\circ C$ [17].

Viscoplastic parameters	
σ_y	3.5 MPa
T_{ref}	23 $^\circ C$
$\beta_1 = \beta_2$	0.018
κ	24 MPa
n_1	0.1
n_2	130
η	1.29 10^6 MPa
m	4.75

Table 3.4: Viscoplastic parameters for PP at $T = 23\ ^\circ C$ [17].

4 Extension of the TH-VE-VP model to include the effects of crystallization

As for temperature, it's possible to take into account the effect of crystallinity by using a shift function. The new shift function that contains the effect of temperature and crystallinity is defined as follows:

$$A_{sh} = a_T a_{X_c} \tag{3.78}$$

where a_T is defined in the eq. (3.73) and a_{X_c} is given as follow:

$$log(a_{X_c}(t)) = \frac{C_1^* \left(X_c(t) - X_{cref}\right)}{C_2^* + \left(X_c(t) - X_{cref}\right)} \tag{3.79}$$

where C_1^* and C_2^* are material parameters and X_{cref} is the reference crystallinity degree. For the viscoplastic part, the effect of crystallinity has been added using the shift function equation applied on the yield function which will become as follows:

$$f(\sigma_{eq}, p, \dot{\epsilon}) = \sigma_{eq} - \Gamma(X_c, \beta_{X_c})\Gamma(T, \beta_1)\sigma_y(\dot{\epsilon}) + \Gamma(X_c, \beta_{X_c})\Gamma(T, \beta_2)R(p) \tag{3.80}$$

With:

$$\Gamma(X_c, \beta_{X_c}) = exp(\beta_{X_c}(X_c - X_{c_{ref}})) \tag{3.81}$$

The parameters C_1^*, C_2^*, $X_{c_{ref}}$ and β_{X_c} are calibrated by Reverse Engineering method. They are provided with uniaxial tensile curves at temperature $T = 75\ °C$. Then they are validated with other uniaxial tensile curves at temperature $T = 25\ °C$. In this section, experimental data of PP tensile test are provided from Li et al. work [52].

Figures 3.9 and 3.10 show a tensile test with different crystallinity degree at $T = 25\ °C$ and $T = 75\ °C$ respectively, whereas figure 3.11 shows a tensile test with different temperature for $X_c = 50.68\%$. It can be noted that for low temperature and high crystallinity degree this model represents well the experimental results and it takes into account the evolution of the temperature as well as the variation of the crystallinity degree. This shift between the model and the experimental occurs when the temperature exceeds the crystallization temperature of the substance. In this context, the crystallinity degree will increase to find the new equilibrium state following the increase in temperature. The change in crystallinity degree will influence the behavior of the substance, therefore, to improve the model, it is necessary to find the new crystallinity degree and use it in the simulations.

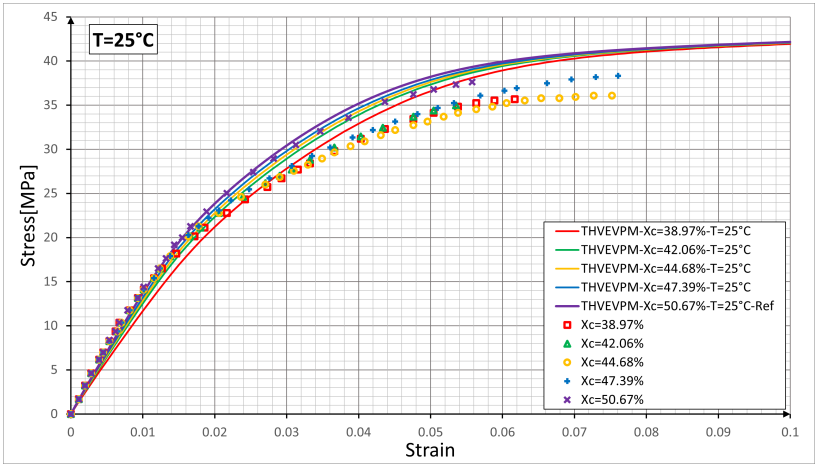

Figure 3.9: Tensile tests under different crystallinity degree for Polypropylene PP at $T = 25\ °C$.

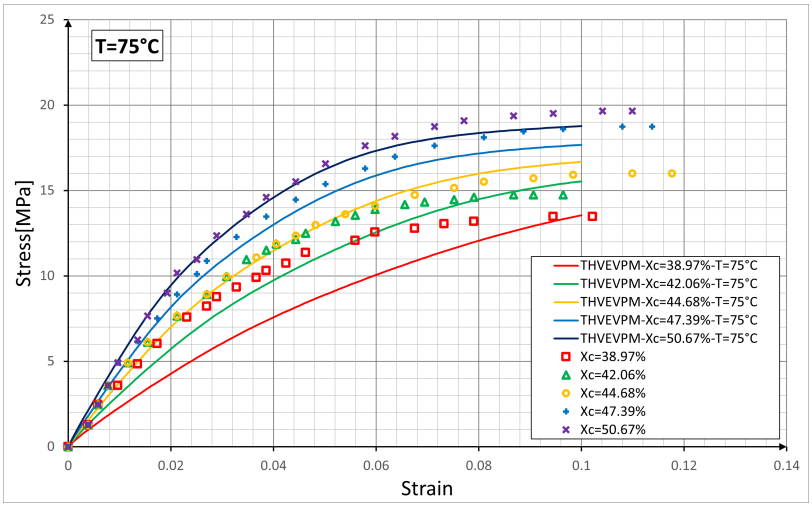

Figure 3.10: Tensile tests under different crystallinity degree for Polypropylene PP at $T = 75\ ^{\circ}C$.

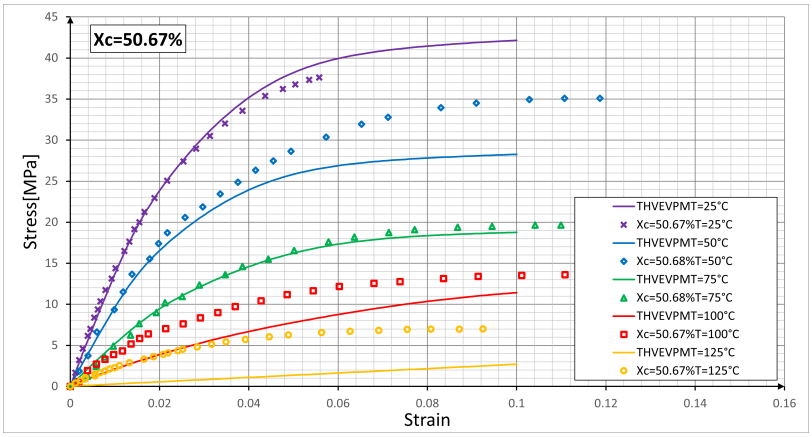

Figure 3.11: Tensile tests at different temperature for Polypropylene PP for $X_c = 50.67\%$.

5 | Conclusion

Polymers are known for their complexity and their combined viscoelastic and viscoplastic behaviors. This complexity is inherent to polymers and defined by their micro-structural constitution. Consitutive models for semi-crystalline polymers must capture temperature, strain or stress rate effects as well as well as the dependence with respect to micro-structure. Indeed, semi-crystalline polymers are composite materials consisting of two phases, amorphous and crystalline. The proportion of each phase has thus a significant effect on the thermo-mechanical behavior.

In the first section of this chapter, a VE-VP model has been presented with linear viscoelasticity and isotropic hardening. This model is applied at the macro scale where the material can be considered homogeneous.

In the next section, a TH-VE-VP model with linear thermo-viscoelasticity and thermo-viscoplasticity with isotropic hardening was presented. It's noted that this model does not include self-heating. This model is applied also at the macro-scale where the material can be considered homogeneous and isotropic. Except that it presents some differences with the experimental data at high temperature and low strain rate, it can well describe the dependence on the strain rate and the temperature.

In the SLS process, the material will undergo a phase change as crystallization will take place while cooling the material. Experience shows that as the crystallinity degree increases, the rigidity increases also and vice versa. In this context, the TH-VE-VP model has been improved to be crystallinity dependent. The model shows that it represents well the behavior of the material, except that it is necessary to update the crystallinity degree especially when the temperature exceeds the crystallization one.

CHAPTER 4

Phase field model for polymer crystallization

1 | Introduction

Polymeric materials are widely used in the industry, which explains the existence of several manufacturing processes, such as plastic injection moulding, plastic blowing, and more recently 3D printing, etc. Nowadays, the industry tends to digitize these processes, in order to provide information on the mechanical strength and final shape of the sample before starting production, the final aim being to optimize the process and reduce costs. In order to model the constitutive response of the polymers, a thermo-mechanical modeling based on viscoelasticity and / or viscoplasticity can be used, such as in [53] [54]. But such models remain insufficient because after melting, the material will undergo

a very important phenomenon which is crystallization. Variation in crystalline rate will lead to material inhomogeneity at the micro-scale, which will change the behavior from one region to another. So the objective of this study is to understand this phenomenon and to model it.

In the spherulite, there are two phases, amorphous and crystalline, the quantity of each state depends essentially on the crystallization temperature. The amorphous phase is characterized by the random configuration of molecular chains, this structure gives the polymer a soften behavior. This phase is also characterized by the existence of a glass transition temperature T_g, below which the polymer is solid and rigid (vitreous state), and above it, its stiffness modulus drops. It should be noted that the amorphous phase has no melting temperature. The crystalline phase is characterized by the regular configuration of molecular chains. This structure gives the polymer a rigid aspect. In this phase, the melting temperature T_m exists and the material is much more rigid than in the amorphous phase, because the crystalline structure is very compact.

After polymer melting, if the crystallisation temperature is slightly lower than the melting value, the molecular chains have the freedom to move but have difficulty establishing a link between them. As a result, the crystalline amount in the spherulite is very high while the growth is low. It should be noted that at macro-scale, the average crystalline amount is low because, at high temperature, the number of nucleations is low. When the temperature decreases, the molecular chains mobility decreases and the tendency to become attached to each other increases, as a consequence the crystal amount in the spherulite decreases (figure 4.1). The experiments observed in figure 4.1, are carried out in thin film whose thickness equals 11 μm. Experimentally, it can be shown that there is no crystallization at a temperature above the melting temperature because the tendency to create a link between the molecules is nil. After melting, if the temperature drops very quickly to the glass transition temperature, the polymer chains do not have time to move and form crystals, as consequence the sample will be totally amorphous.

Crystallization can be modeled by the Kolmogorov model [5], in order to calculate the probability (Poisson distribution) of existence of crystals as a function of nucleation and growth rate. In general, the temperature dependence of nucleation and growth rate should be evaluated separately. However, it is possible to establish a relationship between growth and nucleation by the isokinetic hypothesis, with the exception of polymers that crystallize very slowly. This is called the Nakamura model [7] which applies to non-isothermal cases. There is an extension to the isothermal case, assuming that nucleation and growth are constant during the process. This is called the Avrami model [6]. These two models can make a good approximation of the phenomenon, but they give only the normalized evolution of the degree of crystallization i.e.

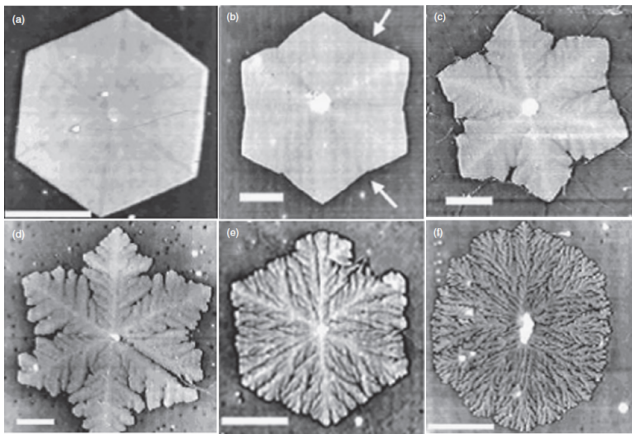

Figure 4.1: Experimental results [55] for isotactic polystyrene on the effect of crystallization temperature, (a) $T_c = 210\ ^\circ C$, 4 *hours*, (b) $T_c = 205\ ^\circ C$, 4 *hours*, (c) $T_c = 200\ ^\circ C$, 4 *hours*, (d) $T_c = 195\ ^\circ C$, 3 *hours*, (e) $T_c = 190\ ^\circ C$, 1 *hour* and (f) $T_c = 180\ ^\circ C$, 1 *hour*. Scale bars are 5 μm.

the evolution between the amorphous state, represented by (0), and the ultimate state of crystallization, represented by (1). Furthermore in multi-scale mechanical modeling, it is necessary to have access to the crystal amount in the structure, which is not possible with these models. To go further, a phase field model of crystallization has been developed, based on two equations, the Allen-Cahn equation [18] which expresses the growth law and the heat transfer which expresses the temperature evolution. With this equation system, crystal growth evolution can be simulated. The nucleation can be modeled by a semi-analytical model, assuming it equal to a maximum number of nucleations multiplied by the nucleation probability, the probability being null at the melting temperature and maximum at the glass transition temperature.

Kobayashi [56] is one of the first who developed the phase field model, in order to show series of numerical simulations of the formation of various dendritic patterns, but his model gives qualitative results. His work is based on a representative model in non-dimensional space and time. A serious concern with this model is that the evolution of crystal morphology as a function of temperature is not compatible with the physics of polymers. A few years later, Karma and Rappel [57] also used a non-dimensional space and time phase field model. Their results are coherent with the exact prediction of 1D analytical solution of solid-liquid interface evolution, but they did not test the influence of temperature on morphology and the crystallization degree for polymer. Xu et al. [58] make modifications to the phase field model essentially in the heat equation

by changing the expression of the dimensionless heat of fusion, which weakens the basic theory of the phase field. Consequently, they obtain an evolution of the morphology consistent with the experimental test given by Taguchi [55], but their simulation is not quantitative and the predicted growth rate is not correct. Hoffman-Lauritzen theory [39][38] shows that the spherulites growth is zero near the melting temperature T_m and that of the glass transition T_g. Except at T_m because it is considered as equilibrium temperature, the existing phase field model does not take into account the Hoffman-Lauritzen theory. Moreover, the crystal thickness is in the order of a few nm [59] especially when crystallization and melting temperatures are significantly apart. It should be noted that the representative volume elements (RVEs) of polymer substance is generated by a discretization into voxels, each voxel represents an element of the mesh (for more details on the numerical and the discretization method see appendix C). RVEs must present all micro-structural details. Generation of 3D RVEs for different heterogeneous materials are reviewed in S.Bargmann et al. work [60]. Therefore, for accurate numerical predictions, the micro-structure's mesh or grid must be very fine. With classical computer resources, it is not possible to do a simulation of a structure in mm by a mesh size in order of nm. In practice, the most used cell size is $0.1\mu m$, which allows to do simulation using large representative volume elements (RVEs). This value can satisfy simulations at very high temperatures close to T_m, but as soon as the temperature drops and the spherulite branches become very thin, the model loses its predictive potential. In addition, the phase field model requires that the temperature and the phase field variable evolve simultaneously. However, the polymer's heat diffusivity on the micoscopic scale gives an extremely rapid temperature evolution, whereas the phase evolution predicted by the equation is very slow. For this reason, most phase field models give very small times compared to the experimental observations. In conclusion, making fully quantitative predictions of crystal growth remains out of reach when using existing models.

The objective of this work is to modify a phase field model in order to obtain experimentally consistent results according to the crystallization temperature evolution and obtain accurate numerical predictions. We will target the following crystallization characteristics : growth rate, crystal morphology and crystalline rate in the spherulite. The chapter has the following outline. In section 2, there is a description of existing crystal growth models and explanations of what make them qualitative only. In section 3, the phase field model is modified in order to make it consistent with polymer physics, as illustrated by 2D simulations. 3D simulations are presented in section 4. Conclusions are drawn in section 6. Mathematical proofs behind the phase field model are given in Appendix B.

2 | Existing phase field models

2.1 Model description

Crystal evolution is controlled by two equations, the heat equation to control the temperature and check the equilibrium state (if the temperature equals the equilibrium value, there is no crystalline evolution) and the Allen-Cahn [18] equation which controls the crystalline phase evolution. In this equation system, there are two unknowns: a non-conserved phase field variable $\phi(X,t)$ and a temperature field $T(X,t)$ which both depend on space and time. ϕ is a non-dimensional variable that varies between 0 and 1, with $\phi = 1$ meaning solid phase and $\phi = 0$ designating liquid or amorphous phase. These two equations are interrelated and this relationship governs the growth and the morphology of the crystal. The equation system is as follows, the proof is given in Appendix B.

$$\begin{cases} \dfrac{\partial \phi}{\partial t} = -M \dfrac{\delta F(m(T),\phi)}{\delta \phi} \\ \dfrac{\partial T}{\partial t} = \alpha \nabla^2 T + K \dfrac{\partial \phi}{\partial t} \end{cases} \tag{4.1}$$

where M is a positive kinetic coefficient [18], $1/M$ can also be defined as the characteristic time of attachment of atoms at the interface according to Karma [57], F is the total free energy of the system, $\alpha = \frac{k_T}{\rho C_p}$ is the thermal diffusivity, $K = \frac{\Delta H}{C_p}$, ρ is the density, C_p is the specific heat at constant pressure, k_T is the thermal conductivity, ΔH is the latent heat and $m(T)$ is a function that depends on temperature and will be given later.

The total free energy of the system of melt and solidifying crystals is defined as the Cahn-Hilliard free energy [61].

$$F(\phi,T) = \int_V f_{loc} dV = \int_V f_{liq-sol}(\phi,T) + f_{grad}(\phi) dV \tag{4.2}$$

With:

$$f_{liq-sol}(\phi,T) = W \int_0^{\phi} \phi(1-\phi)(\frac{1}{2} - \phi - m(T)) d\phi \tag{4.3}$$

$$f_{grad}(\phi) = \frac{1}{2}\epsilon^2 (\nabla \phi)^2 \tag{4.4}$$

And

$$\frac{\delta F}{\delta \phi} = -\left[\nabla \cdot (\epsilon^2 \nabla \phi) - \frac{\partial f_{loc}}{\partial \phi}\right] \tag{4.5}$$

The local free energy f_{loc} is divided into two parts, one describing the local free energy $f_{liq-sol}$ and the other, the energy gradient f_{grad}. The local free energy is considered as a double-well potential for Gibbs free energy containing two equilibrium points in the liquid state and in the crystalline one. Since the amorphous phase has none, the melting temperature of a semi-crystalline material varies depending on the amount of crystalline phase. This property is added by changing T_m^0 by T_m in the crystal growth equation (see Appendix B), where T_m^0 is the equilibrium melting temperature and T_m is the melting temperature obtained at a specific crystallization temperature T_c. In order to add anisotropy to the crystalline form, the coefficient of energy gradient ϵ is taken not constant and is defined in 2D as follows [57].

$$\epsilon = \overline{\epsilon}\left[1 + \vartheta \cos(j(\theta - \theta_0))\right] \quad | \quad \theta = \arctan\left(\frac{\partial \phi / \partial y}{\partial \phi / \partial x}\right) \tag{4.6}$$

where $\overline{\epsilon}$ is the reference coefficient of energy gradient, ϑ is the strength of surface anisotropy, j is a form variable (when $j = 4$, the system represents a crystal structure with quadruple symmetry or when $j = 6$, the system represents a crystal structure which is six-fold symmetric), θ is the angle between the interface normal and the reference axis, and θ_0 is the spherulite orientation with respect to the horizontal axis, in this work $\theta_0 = 0$.

According to Kobayashi [56], we can add some noise at the interface to get a different growth morphology for each direction, which is more realistic. The noise function is equal to $a\phi(1-\phi)R_v$ with $R_v \in [-1/2, 1/2]$ being a random number.

As shown in Appendix B, equation 4.1 can be rewritten under the following dimensionless form.

$$\begin{cases} \tau^* \hat{\epsilon}^2 \dfrac{\partial \phi}{\partial \hat{t}} = \left[\begin{array}{l} \hat{\nabla} \cdot \left(\dfrac{1}{2}(\hat{\nabla}\phi)^2 \dfrac{\partial(\hat{\epsilon}^2)}{\partial \hat{\nabla}\phi}\right) + \hat{\nabla} \cdot \left(\hat{\epsilon}^2 \hat{\nabla}\phi\right) \\ - W\phi(\phi - 1)(\phi - 1/2 + m(\hat{T})) + a\phi(1-\phi)R_v \end{array}\right] \\ \dfrac{\partial \hat{T}}{\partial \hat{t}} = \hat{\nabla}^2 \hat{T} + \hat{K} \dfrac{\partial \phi}{\partial \hat{t}} \end{cases} \tag{4.7}$$

where $\hat{T} = \frac{T - T_c}{T_m - T_c}$ is the dimensionless temperature, $\tau^* = \frac{\alpha}{\epsilon^2 M}$ is the dimensionless diffusivity, $\hat{K} = \frac{K}{T_m - T_c}$ is the dimensionless latent heat, $d\hat{t} = \frac{dt}{\tau}$ is the dimensionless time step, $\hat{\epsilon} = \frac{\epsilon}{D}$ is proportional to the dimensionless interface

thickness, $d\hat{x} = \frac{dx}{D}$ is the dimensionless mesh size in X direction, $d\hat{y} = \frac{dy}{D}$ is the dimensionless mesh size in Y direction and $d\hat{z} = \frac{dz}{D}$ is the dimensionless mesh size in Z direction. D and $\tau = \frac{D^2}{\alpha}$ are characteristic length and time, respectively. In this work $d\hat{x} = d\hat{y} = d\hat{z} = 1$ and $d\hat{t} = 0.1$. $d\hat{t}$ is defined so that the explicit resolution does not diverge. T_m in the dimensionless latent heat expression can be estimated by Hoffman Weeks theory [62]: $T_m = T_m^0 \left(1 - \frac{1}{2\beta}\right) + \frac{1}{2\beta} T_c$.

2.2 Phase field model results and discussion

The resolution of the phase field model is based on the finite difference method. For efficiency, the implementation was done in C++ in a research version of the Digimat software [3]. The integration scheme is explicit with a stable time step computed according to the heat equation parameters. The numerical formulation is given in Appendix C.

The phase field model gives only the liquid-solid interface evolution, so it needs initial conditions. Since the simulations are performed at constant crystallization temperature T_c we consider that at time $t = 0$ there are N nucleations [63] which are circles in 2D and spheres in 3D placed in liquid at temperature T_c. Inside the nucleation, it is assumed that the temperature is equal to the equilibrium value and that the phase field parameter ϕ is equal to 1. While in the outside $\phi = 0$.

For now, we suppose 2D simulations, because the experimental observation (figure 4.1) is made on a thin film. The model also works in 3D, except for anisotropic spherulite, the anisotropy expression (4.6) has to be adapted accordingly.

Polymers are well known for their low crystal growth rate, mostly at high temperatures (figure 4.1), which gives a very low interface diffusivity. Theoretically, this phenomenon is controlled in the heat equation by $\hat{K}$ and in the growth equation by $m(T)$ which can be written in the dimensionless formulation as follows:

$$\begin{aligned} m(T_c, \hat{T}) &= \frac{\epsilon}{2k_{GT}}(T_m - T_c)(1 - \hat{T}) \\ &= \frac{\epsilon}{2d_0\hat{K}}(1 - \hat{T}) \end{aligned} \tag{4.8}$$

where $d_0 = k_{GT}\frac{C_p}{\Delta H} = \frac{\sigma T_m C_p}{\Delta H^2}$ is the capillary length and σ is the solid–liquid interface energy. At crystallisation temperature near to that of fusion, $m(T_c, \hat{T})$

becomes very small, this means that the energy barrier of the double-well potential is near to its maximum and that the interface evolution slow down (Figure 4.2).

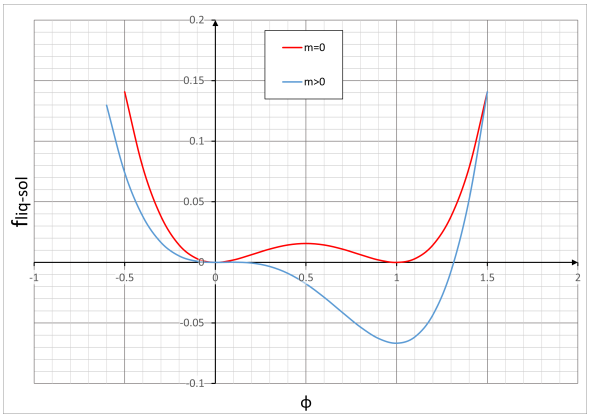

Figure 4.2: Effect of $m(T_c, \hat{T})$ on the double-well potential $f_{liq-sol}$ equation 4.3.

Kobayashi has simplified the expression of m and replaced it with the following expression which does not show the effect of the crystallization temperature:

$$m(\hat{T}) = \frac{\alpha_k}{\pi} \arctan(\gamma_k(1 - \hat{T})) \tag{4.9}$$

where $\alpha_k = 0.9$ and $\gamma_k = 10$[56]. Kobayashi shows that $m(T)$ should be such that $0 \leq m(T) < 1/2$, because if $m(T) > 1/2$ the double-well potential appearance will be lost. In addition, we only work with $T < T_m$ because we are interested in simulating a solidification process, which implies $m(T) > 0$. In order to compare the effect of the modification of $m(T_c, \hat{T})$, the parameters of the model will be fixed according to the non-dimensional values given by Kobayashi [56]. To operate the model, the non-dimensional parameter τ^* should be greater than or equal to 1 i.e. thermal and phase field diffusivities must be close to each other. For example, Kobayashi used $\tau^*\hat{\epsilon}^2/(d\hat{x})^2 = 1/3$ and $\hat{\epsilon}/d\hat{x} = 1/3$ which gives: $\tau^*\hat{\epsilon}^2 = 0.0003$ for $d\hat{x} = 0.03$[56]. So, as we use $d\hat{x} = 1$, it gives $\hat{\epsilon} = 1/3$ and $\tau^* = 3$. Karma and Rappel [57] also used $\tau^* \in [1, 13]$ [57]. Forcing phase field diffusivity to follow the thermal one causes incorrect simulation times, because physically the thermal diffusivity is very fast compared to the phase field one. To obtain a correct time, we can use the phase field diffusivity to calculate the characteristic time constant $\tau = \frac{D^2}{\epsilon M}$.

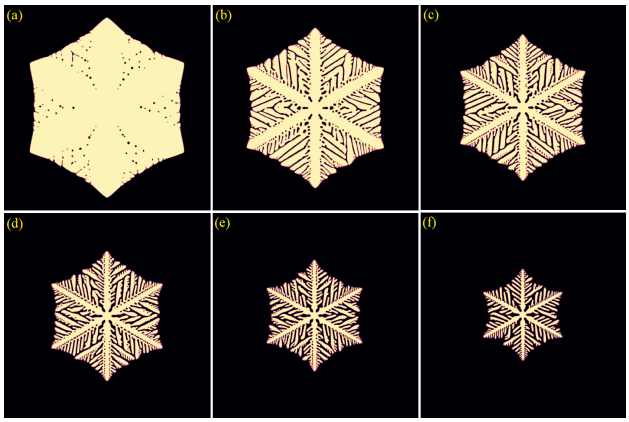

Figure 4.3: Predictions with Kobayashi's model [56] for isotactic polystyrene using $m(\hat{T}) = \alpha_k/\pi \arctan(\gamma_k(1-\hat{T}))$ and $K = 48.4\,^{\circ}K$ [58]: (a) $T_c = 180\,^{\circ}C \Leftrightarrow \hat{K} = 1.08$, (b) $T_c = 190\,^{\circ}C \Leftrightarrow \hat{K} = 1.28$, (c) $T_c = 195\,^{\circ}C \Leftrightarrow \hat{K} = 1.42$, (d) $T_c = 200\,^{\circ}C \Leftrightarrow \hat{K} = 1.59$, (e) $T_c = 205\,^{\circ}C \Leftrightarrow \hat{K} = 1.81$ and (f) $T_c = 210\,^{\circ}C \Leftrightarrow \hat{K} = 2.09$. Model parameters in table 4.1, only $W = 1$. Grid size $1000 \times 1000\ Pixel^2$.

For all the following simulations, the yellow color represents the crystalline region, the black color between the crystalline branches represents the amorphous phase and the rest (outside the spherulite) represents the liquid phase. Figures 4.3 and 4.4 show the effect of the modification of $m(T_c, \hat{T})$. Figure 4.3 represents Kobayashi model, comparing the results with those of experimental observation (Figure 4.1). It is clearly seen that when the temperature increases, the model predicts that the spherulites will have thinner branches and the crystal degree decreases, which is not physical. This problem is shown to be fixed in figure 4.4 thanks to the equation $m(T_c, \hat{T}) = \frac{\epsilon}{2d_0\hat{K}}(1-\hat{T})$. Unlike the Kobayashi model, there is a tendency to spread the crystalline branches as in the experimental observation of Figure 4.1. The branches are not able to emerge because as the temperature decrease, $\hat{K}$ decrease as well. Figure 4.3 shows that $\hat{K}$ has very important effect on branching mainly when it is bigger. If $\hat{K}$ tends to 0, spherulite growth "explodes" (Figure 4.5) and the growth continues without creating a crystal branch.

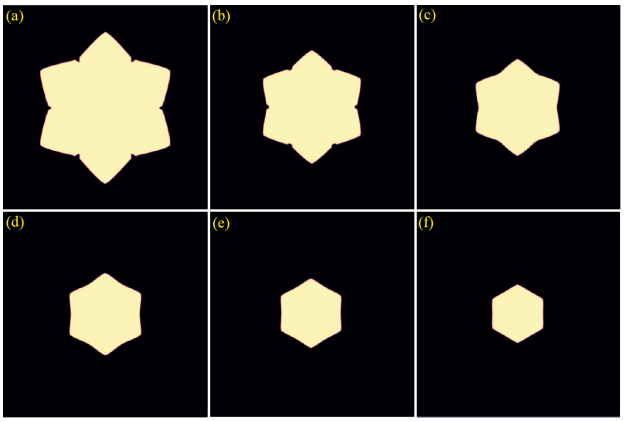

Figure 4.4: Predictions with Cahn-Allen model[18] for isotactic polystyrene using $m(T_c, \hat{T}) = \frac{\epsilon}{2d_0 K}(1 - \hat{T})$ and $K = 48.4\ ^\circ K$ [58]: (a) $T_c = 180\ ^\circ C \Leftrightarrow \hat{K} = 1.08$, (b) $T_c = 190\ ^\circ C \Leftrightarrow \hat{K} = 1.28$, (c) $T_c = 195\ ^\circ C \Leftrightarrow \hat{K} = 1.42$, (d) $T_c = 200\ ^\circ C \Leftrightarrow \hat{K} = 1.59$, (e) $T_c = 205\ ^\circ C \Leftrightarrow \hat{K} = 1.81$ and (f) $T_c = 210\ ^\circ C \Leftrightarrow \hat{K} = 2.09$. Model parameters in table 4.1, only $W = 1$. Grid size $500 \times 500\ Pixel^2$.

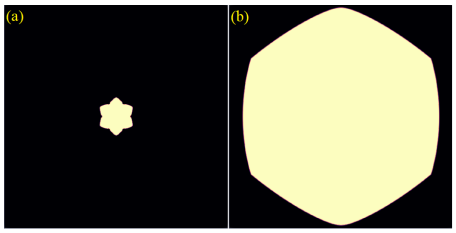

Figure 4.5: Predictions with Allen-Cahn model[18]:(a) $\hat{K} = 1.0$, (b)$\hat{K} = 0.5$. Model parameters in table 4.1, only $W = 1$. Grid size $500 \times 500\ Pixel^2$.

Experimentally, when the glass transition temperature is approached, the spherulite size and the crystallinity degree will be small simultaneously. It can therefore be seen that the phase field model can provide accurate predictions only close to the melting temperature.

Xu et al. [64][58] tried to improve the phase field model for polymers, mainly by changing the expression of the dimensionless latent heat $\hat{K}$ taken as $\hat{K} = K/T_m$, where T_m is obtained by Hoffman Weeks expression. This modifies the dependence of $\hat{K}$ as a function of the crystallization temperature T_c. The model thus loses a theoretical basis and the obtained simulations are

not accurate. Indeed, the time in the obtained simulations [58] for ITPS does not correspond to that of the experimental observation of Figure 4.1. The morphology evolution remained coherent but in a non quantitative way.

3 | An enhanced phase field model

In the phase field model, if we take all parameters constant and vary the non-dimensional parameter $\hat{K}$ (as in Kobayashi model 4.3), the spherulite will have a small size and a low crystallinity degree when $\hat{K}$ increases. Experimentally, this phenomenon can be observed between the maximum growth temperature $T_{c\ max}$ and the glass transition temperature T_g. But if we vary the dimensionless diffusivity $\tau^* = \frac{\alpha}{\epsilon^2 M}$, the spherulite will have a small size and a high crystallinity degree when τ^* increases. Experimentally, this phenomenon can be observed between $T_{c\ max}$ and melting temperature T_m (figure 4.1). In the proposed enhanced phase field model, we use the Kobayashi function $m(T)$ of eq. (4.9), but we give semi-analytical temperature-dependent expressions for parameters $\hat{K}$ and τ^* in order to correctly simulate the observed crystal growth phenomena.

3.1 Semi-analytical expression for interface mobility M between $T_{c\ max}$ and T_m

Since the phase field variation $\frac{\partial \phi}{\partial t}$ is proportional to the speed of propagation of the interface, then the evolution of $\frac{\partial \phi}{\partial t}$ and G_r Eq. (2.14) must be similar. The idea is to combine the Cahn-Allen equation with the growth equation developed by Lauritzen and Hoffman. In this context, we modify the expression of the dimensionless diffusivity τ^*.

$$\tau^*(T_c) = \tau_0^* / \mathcal{H}(T_c) \tag{4.10}$$

where $\tau_0^* = \tau^*(T_{c\ max})$ is the reference dimensionless diffusivity, The expression of $\mathcal{H}(T_c)$ is obtained by eq. (2.14) as follows:

$$\mathcal{H}(T_c) = G_r(T_c)/G_r(T_{c\ max}) \tag{4.11}$$

Since we modify the expression of τ^* only between $T_{c\ max}$ and T_m, it corresponds theoretically to regime I. For simplicity, the following expression will be used.

$$\mathcal{H}(T_c) = h_0 \exp\left[-\frac{h_1}{T_c - T_\infty}\right] \exp\left[-\frac{h_2}{T_m^0 - T_c}\right] \tag{4.12}$$

where h_1 and h_2 are parameters and h_0 is obtained such that $\mathcal{H}(T_{c\ mac}) = 1$ and $\frac{d\mathcal{H}}{dT_c}(T_c = T_{c\ mac}) = 0$.

$$h_0 = \exp\left[\frac{h_1 + h_2 + 2\sqrt{h_1 h_2}}{T_m^0 - T_\infty}\right] \tag{4.13}$$

As a result, the simplified Lauritzen and Hoffman expression gives a bell-shaped curve (see Figure 2.18). As we see in figure 2.18, the crystal growth rate evolution as a function of temperature is consistent with the experimental result, i.e. the growth rate is non-zero only between T_m^0 and T_∞ and there is no evolution outside this temperature range.

We assume that the model parameters will be calibrated at $T_{ref} = T_{c\ max}$ and the temperature dependence is taken only by $\mathcal{H}(T_c)$, so, $\hat{K}$ is assumed constant and calibrated at reference temperature $T_c = T_{ref}$ ($\hat{K}$ is fixed, since its variation can change the growth rate).

Figure 4.1 shows that the anisotropy changes with temperature. In the model, in order to have a continuous function, we express the surface anisotropy strength as follows:

$$\vartheta(T_c) = \vartheta_0 \left(\frac{\frac{2}{\pi}\arctan(\varpi(T_c - T_{crit})) + 1}{2}\right) \tag{4.14}$$

where ϑ_0 is the reference strength of surface anisotropy. Assume that the anisotropy begins to disappear at T_d and that there is no anisotropy after T_f, so ϖ calibrates the extension of the temperature domain $[T_d,\ T_f]$ and $T_{crit} = (T_d + T_f)/2$ is the critical temperature of change of anisotropy.

3.2 Semi-analytical expression for the dimensionless variable $\hat{K}$ between $T_{c\ max}$ and T_∞

Since we don't have a consistency with polymer physics at a temperature between the maximum growth temperature and the glass transition temperature, the model needs another correction. If we look at the behavior of the model, we can see that when we increase the non-dimensional variable $\hat{K}$ in the heat equation, the spherulite size decreases and the crystal amount also decreases (figure 4.4). In order to take advantage of this property, we take $\hat{K} \propto 1/\mathcal{H}(T_c)$. In this work we use the following function:

$$\hat{K}(T_c) = \begin{cases} \dfrac{\hat{K}_0}{\mathcal{H}(T_c)} & T_g \leq T_c \leq T_{c\ max} \\ \hat{K}_0 & T_{c\ max} < T_c \leq T_m^0 \end{cases} \tag{4.15}$$

where $\hat{K}_0$ is calibrated at $T_c = T_{c\ max}$ (temperature of maximum growth rate). It should be noted that $\tau^*(T_c)$ must be equal to τ_0^* at a temperature between the maximum growth temperature and the glass transition temperature and it takes the value of equation 4.10 at a temperature between the maximum growth temperature and the equilibrium melting temperature.

$$\tau^*(T_c) = \begin{cases} \dfrac{\tau_0^*}{\mathcal{H}(T_c)} & T_{c\ max} < T_c \leq T_m^0 \\ \tau_0^* & T_g \leq T_c \leq T_{c\ max} \end{cases} \tag{4.16}$$

After modification, the model equations (4.7) become:

$$\begin{cases} \tau^*(T_c)\hat{\epsilon}^2 \dfrac{\partial \phi}{\partial \hat{t}} = \begin{bmatrix} \hat{\nabla} \cdot \left(\dfrac{1}{2} (\hat{\nabla}\phi)^2 \dfrac{\partial(\hat{\epsilon}^2)}{\partial \hat{\nabla}\phi} \right) + \hat{\nabla} \cdot \left(\hat{\epsilon}^2 \hat{\nabla}\phi \right) \\ - W\phi(\phi - 1)(\phi - 1/2 + m(\hat{T})) \\ + a\phi(1-\phi)R_v \end{bmatrix} \\ \dfrac{\partial \hat{T}}{\partial \hat{t}} = \hat{\nabla}^2 \hat{T} + \hat{K}(T_c) \dfrac{\partial \phi}{\partial \hat{t}} \end{cases} \tag{4.17}$$

3.3 Results and discussion

Between temperatures $T_{c\ max}$ and T_m, the model calibration is done in two steps, the first consists in calibrating the function $\mathcal{H}(T_c)$. Figure 4.6 represents the fit of the function $\mathcal{H}(T_c)$ with the experimental data, which are given by Taguchi et al. [55] and Kathryn L. Beers et al. [65]. The second step is to calibrate $\hat{K}_0$ at the maximum growth temperature, which is taken equal to 180 °C, which controls the crystallinity degree. The other parameters of the phase field model are taken according to Kobayashi [56] (table 4.1). Among the non-dimensional parameters of the model, the only parameter which depends on the characteristic length D is $\hat{\epsilon} = \epsilon/D$. So, the variation of D will affect the numerical stability through $\hat{\epsilon}$. However, the characteristic length D must be less than the interface thickness 6ϵ to ensure numerical stability: $D \leq 6\epsilon$. Then the stability condition will be: $\hat{\epsilon} \geq \frac{1}{6}$. The idea in this work is therefore to fix $\hat{\epsilon}$ to ensure numerical stability, and the characteristic length D is fixed by comparing experimental observations with model predictions. In fact, the appropriate value of D will be taken by comparing two typical results with two different values of D (see Figures 4.7 and 4.8) with the experimental observation (see Figure 4.1). Then it will be possible to find approximately the interface thickness 6ϵ which is not available experimentally.

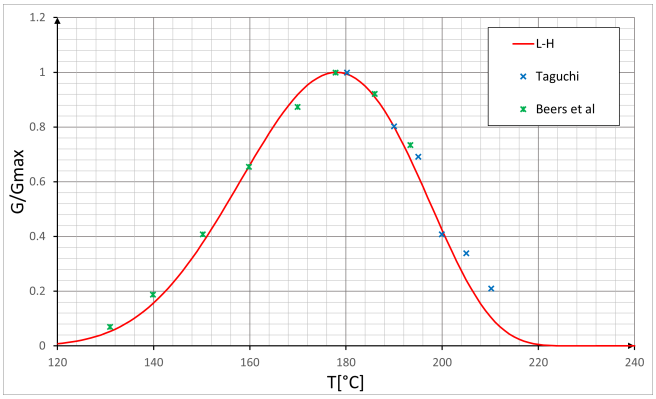

Figure 4.6: Calibration of the L-H function $\mathcal{H}(T_c)$, eq.4.12. Experimental results given by [55] [65].

Model parameters	value	Model parameters	value
$T_{c\ max}$	180 $^\circ C$ [55] [65]	$\Delta\hat{x}$	1.0
T_m^0	242 $^\circ C$ [55]	$\frac{\epsilon}{d_0}$	1.0
T_g	90 $^\circ C$ [55]	β	1.5 [58]
$\hat{\epsilon}$	0.333[56]	τ_0^*	3.0[56]
$\Delta\hat{t}$	0.1	ϑ_0	0.06[58]
$\hat{K}_0$	1.4	a	0.02
j	6	W	2 [66]
α_k	0.9 [56]	γ_k	10 [56]

Table 4.1: Model parameters for isotactic polystyrene ITPS.

Figure 4.7 shows the evolution of the crystal morphology according to temperature, now we can see that there is a consistency with experimental observations. The use of a large grid spacing can give good results at high temperature, but as soon as the temperature drops, crystals branch are observed to be thin and the model is thus inaccurate. If we reduce the grid spacing (figure 4.8), at high temperature, the crystal thickness becomes very small compared to the experimental observation. In addition, if we look at figure 4.9 we can see that the crystalline amount in the spherulite does not change with the change of space step (we do not consider the primary nucleation circle, only the ratio between the crystalline branch and the amorphous branch interests us). Moreover, by using a coarser mesh, the simulation time will be faster, in this case, we can easily make simulations on a larger scale. For these reasons, we will avoid reducing the mesh size. An interesting feature about this method is that we can assign a suitable value to the characteristic length D without knowing

the value of the interface thickness 6ϵ. There is indeed a mesh dependency, but the numerical stability is ensured.

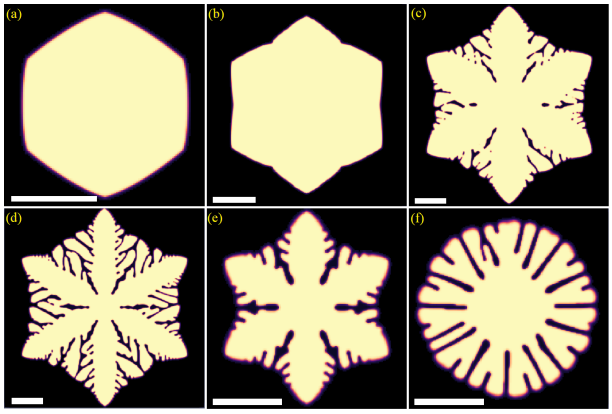

Figure 4.7: Simulation of changing the temperature effect for isotactic polystyrene with the proposed model of equation (4.17). Mesh size $D = 10^{-7}m$. (a) $T_c = 210\ ^\circ C$, 4 *hours*, (b) $T_c = 205\ ^\circ C$, 4 *hours*, (c) $T_c = 200\ ^\circ C$, 4 *hours*, (d) $T_c = 195\ ^\circ C$, 3 *hours*, (e) $T_c = 190\ ^\circ C$, 1 *hour* and (f) $T_c = 180\ ^\circ C$, 1 *hour*. Scale bars are 5 μm. Model parameters in table 4.1.

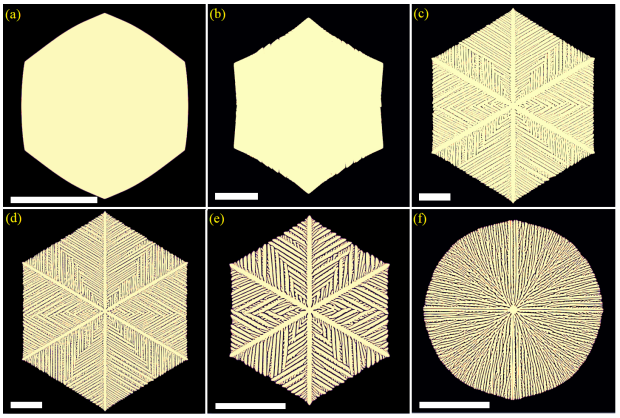

Figure 4.8: Simulation of changing the temperature effect for isotactic polystyrene with the proposed model of equation (4.17). Mesh size $D = 10^{-8}m$. (a) $T_c = 210\ ^\circ C$, 4 *hours*, (b) $T_c = 205\ ^\circ C$, 4 *hours*, (c) $T_c = 200\ ^\circ C$, 4 *hours*, (d) $T_c = 195\ ^\circ C$, 3 *hours*, (e) $T_c = 190\ ^\circ C$, 1 *hour* and (f) $T_c = 180\ ^\circ C$, 1 *hour*. Scale bars are 5 μm. Model parameters in table 4.1.

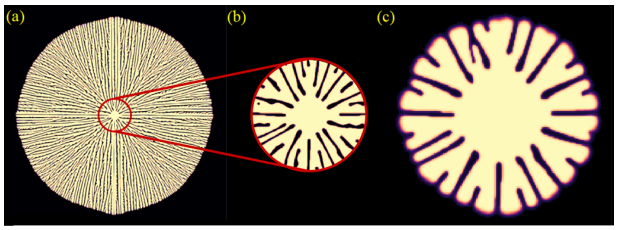

Figure 4.9: Simulations with the proposed model for $T_c = 180\ ^\circ C$ (a) crystal simulation with $D = 10^{-8}m$, (b) zoom on the crystal with $D = 10^{-8}m$ and (c) crystal simulation with $D = 10^{-7}m$.

Figure 4.10 shows the evolution of the crystal at temperatures below the maximum growth temperature $T_{c\ max}$. We can see that the result agrees with polymer physics.

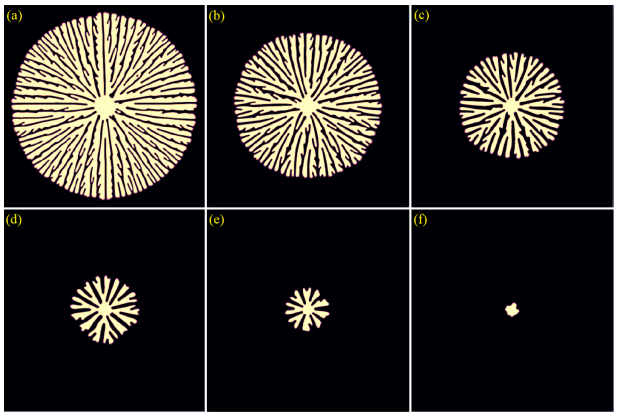

Figure 4.10: Simulations with the proposed model at time $t = 4h$ and film thickness 11 nm (a) $T_c = 170\ ^\circ C$, (b) $T_c = 165\ ^\circ C$, (c) $T_c = 160\ ^\circ C$, (d) $T_c = 155\ ^\circ C$, (e) $T_c = 150\ ^\circ C$ and (f) $T_c = 140\ ^\circ C$. Grid size $500 \times 500\ Pixel^2$. $(50 \times 50\ (\mu m)^2)$.

According to the experimental results, the maximum growth is given at $T_c = 180\ ^\circ C$ and is noted G_{max}. Figure 4.11 shows the comparison between phase field result, the L-H function $\mathcal{H}(T_c)$ and the experimental results given by Taguchi et al. [55] and Beers et al. [65]. This comparison shows that the phase field model is predictive with a certain error, which is concentrated according

to the figure between $T_{c\ max}$ and T_g. The phase field spherulite growth curve does not follow exactly the L-H curve (eq.4.12) because the evolution of the phase field variation $\frac{\partial \phi}{\partial t}$ is not linear as a function of τ^* and $\hat{K}$.

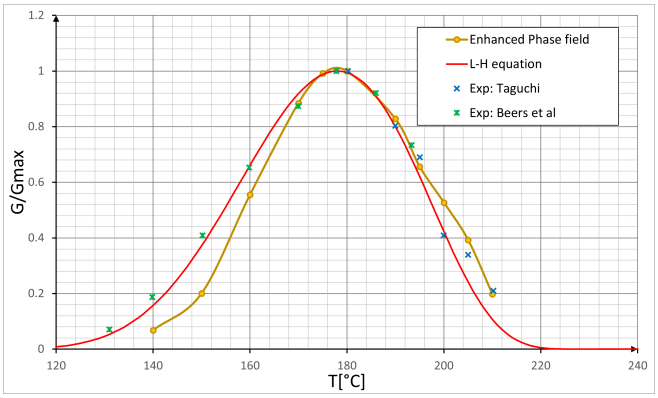

Figure 4.11: Spherulite growth given by phase field model compared to the L-H function $\mathcal{H}(T_c)$ (eq.4.12) and the experimental result given by [55] [65].

3.4 Virtual simulation of crystallization phenomena

Since we do not have experimental data on the number of nucleations for a film thickness equal to $11nm$ (the film is the sample used in the observation test), we will choose an approximate number at $T_c = 169\ ^\circ C$ according to the experimental observation given by Beers [65]. The nucleation position is taken random.

Figure 4.12 shows the evolution of crystal growth from multi-nucleation at $T_c = 169\ ^\circ C$. By calculating the average of the phase field variable ϕ, we can plot the crystal amount curve as a function of time (figure 4.13).

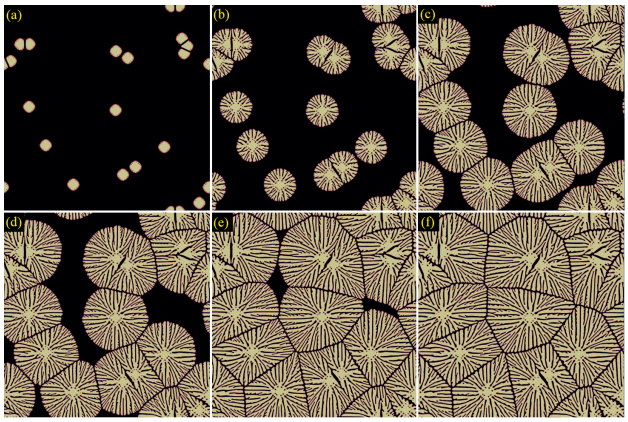

Figure 4.12: Simulation with the proposed model of isotactic polystyrene crystallization at $T_c = 169\ ^\circ C$, (a) $t = 26\ min$, (b) $t = 1\ h\ 18\ min$, (c) $t = 2\ h\ 10\ min$, (d) $t = 2\ h\ 36\ min$, (e) $t = 3\ h\ 28\ min$ and (f) $t = 4\ h\ 20\ min$. Grid size $1500 \times 1500\ Pixel^2$, $(150 \times 150\ (\mu m)^2)$, table 4.1.

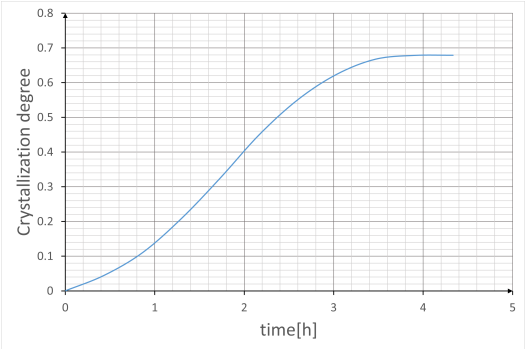

Figure 4.13: Simulation with the proposed model of crystallization degree as a function of time, in 2D for isotactic polystyrene at $T_c = 169\ ^\circ C$ (data in Table 4.1).

In figure 4.14, there are two images of a simulation and an experimental observation. It should be noted that we cannot make a direct comparison between these two images because they do not have the same film thickness, but we can see that there is a consistency between the simulation and the experimental result.

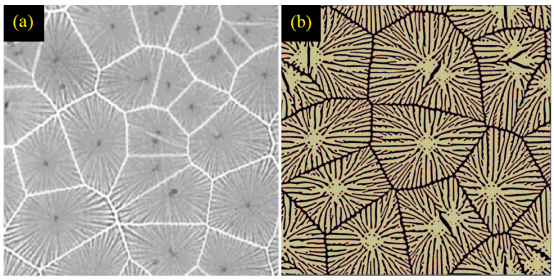

Figure 4.14: (a) experimental observation at $T_c = 169\ ^\circ C$ and film thickness equal to 60 nm [65], (b) numerical simulation with the proposed model at $T_c = 169\ ^\circ C$ and film thickness equal to 11 nm. $(150 \times 150\ (\mu m)^2)$.

4 | Generalization to 3D simulations

3D simulations are investigated by using equations (4.17). It is assumed that the crystallization temperature is uniform in the structure and the coefficient of energy gradient ϵ is taken constant. Figure 4.15 shows the morphology of a spherulite formed at temperature equal to 180 $^\circ C$.

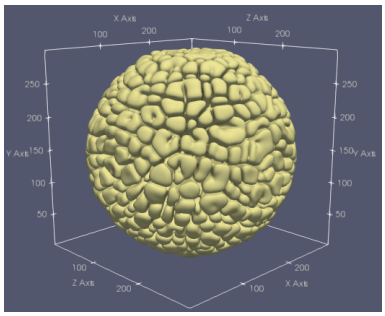

Figure 4.15: Simulation of 3D spherulite with the proposed model at $T_c = 180\ ^\circ C$. Grid size $300 \times 300 \times 300\ Pixel^3$, $(30 \times 30 \times 30\ (\mu m)^3)$.

Figures 4.16 and 4.17 show the crystal evolution simulation at temperature equal to 169 $^\circ C$ and RVE size equal to $50 \times 50 \times 50\ (\mu m)^3$. This 3D model does not take into account the film thickness change effect. For this reason, using thin-film polymer parameters makes this 3D representation qualitative. Indeed reducing the thickness of the film causes a difficulty for crystal propagation, because the film thickness will be comparable to that of the crystal (L in

figure 2.16). In addition, we used a large number of nucleations in a small RVE to reduce the simulation time, as a result the time scale in figure 4.13 is different from that time scale in figure 4.18, but we can see that the ultimate crystallization remains the same. It should be noted that the CPU time in the 2D simulation (figure 4.12) is 15 times faster than the 3D one (figure 4.16) on the same computer (16GB of RAM): 33 min in 2D and 8 h 25 min in 3D.

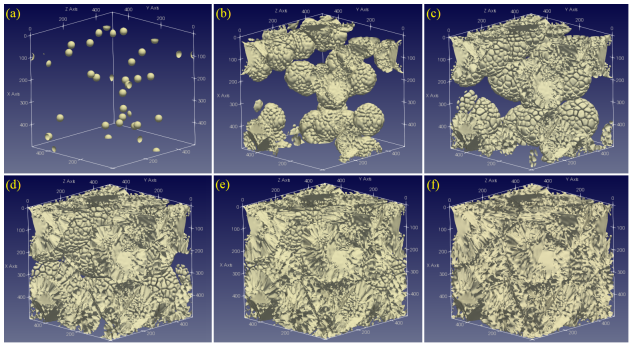

Figure 4.16: 3D simulation with the proposed model of isotactic polystyrene crystallization at $T_c = 169\ ^{\circ}C$, (a) at time $t = 10\ min\ 30\ s$, (b) at time $t = 1\ h\ 5\ min$, (c) at time $t = 1\ h\ 24\ min$, (d) at time $t = 1\ h\ 45\ min$, (e) at time $t = 2\ h\ 6\ min$, (f) at time $t = 3\ h\ 9\ min$. Grid size $500 \times 500 \times 500\ Pixel^3$, $(50 \times 50 \times 50\ (\mu m)^3)$. (evolution of the solid-liquid interface).

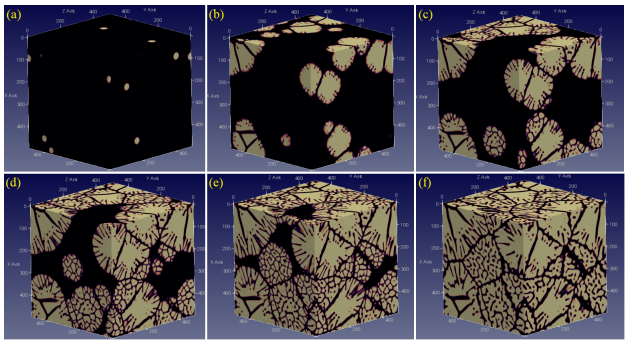

Figure 4.17: 3D simulation with the proposed model of isotactic polystyrene crystallization at $T_c = 169\ ^{\circ}C$, (a) at time $t = 10\ min\ 30\ s$, (b) at time $t = 1\ h\ 5\ min$, (c) at time $t = 1\ h\ 24\ min$, (d) at time $t = 1\ h\ 45\ min$, (e) at time $t = 2\ h\ 6\ min$, (f) at time $t = 3\ h\ 9\ min$. Grid size $500 \times 500 \times 500\ Pixel^3$, $(50 \times 50 \times 50\ (\mu m)^3)$. (spherulite evolution in the liquid phase).

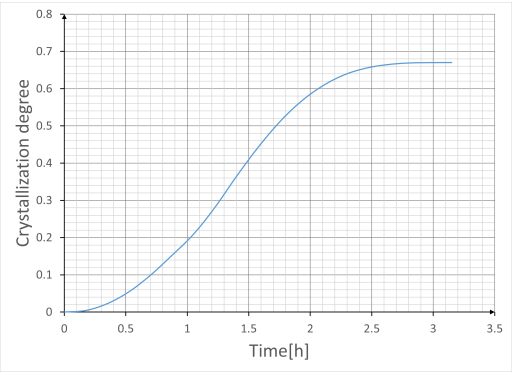

Figure 4.18: Simulation with the proposed model of crystallization degree as a function of time, in 3D for isotactic polystyrene at $T_c = 169\ ^\circ C$ (data in Table 4.1).

5 How to perform enhanced phase field model calibration for other semi-crystalline polymers

First, we start the calibration of the simplified equation of Lauritzen and Hoffman (4.12), in this equation we ha six unknown: T_m^0, $T_\infty = T_g - 30\ ^\circ C$, $T_{c\ mac}$, h_0, h_1 and h_2. By using the following relation, $\mathcal{H}(T_{c\ mac}) = 1$ and $\frac{d\mathcal{H}}{dT_c}(T_c = T_{c\ mac}) = 0$, we can reduce the number of unknowns to four. Characteristic growth temperatures (T_m^0, T_∞ and $T_{c\ mac}$) are generally available in the literature, if these values are fixed, only one unknown remains to be found. This unknown will be optioned by fitting the function (4.12) with the experimental spherulite growth curve like in figure 4.6.

The second step is the calibration of the phase field model parameters. Starting by j and ϑ (eq. (4.6)), these parameters are related to the anisotropy of spherulite, since anisotropy only occurs at high temperature near melting and when the polymer crystallizes into a thin film. In the general case, the polymer spherulite grows without any anisotropy, then we can take $\vartheta = 0$.

The noise parameter a is add to make realistic spherulite. Its value should be small but sufficient to break the spherulite symmetry, we take $a = 0.02$ (eq. (4.7)).

W (eq. (4.7)) is the energy barrier of the double-well free energy potential, we use the value that we found in the model proof in appendix B, $W = 2$.

For the Kobayashi's function (4.9) we will use the parameters used by Kobayashi, $\alpha_k = 0.9$ and $\gamma_k = 10$.

τ_0^* (eq. (4.7)) is the dimensionless diffusivity. For polymer, the growth rate of spherulites is usually low, therefore the value of τ_0^* is very large. Using a large value of τ_0^* results in the loss of coupling between the phase field and the heat equation. The coupling between these two equations is necessary to generate crystalline branched spherulites, to ensure this coupling we will use $\tau_0^* = 3$ as in Kobayashi's work.

$\hat{K}_0$ (eq. (4.15)) is linked to the crystallinity degree of the spherulite, so it will be calibrated at $T_{c\ mac}$ by using the experimental degree of crystallinity.

As discussed in section 3.3 to ensure numerical stability we take $\hat{\epsilon} = 0.333$ (eq. (4.7)), then D (eq. (4.7)) must be found by comparing the model result with the experimental observation as we did for ITPS or by finding the experimental value of the reference surface energy ϵ. Since we used a small value of τ_0^* in order to preserve the coupling between heat and phase field equation, the simulation time will be incorrect. Therefore, a correction on the simulation time is necessary. For the case of maximum growth, assume that the spherulite simulation takes a dimensionless time $\hat{t}_S$ which corresponding to experimental time t_E.Then the corrected characteristic time will be $\tau = \frac{t_E}{\hat{t}_S}$ (eq. (4.7)).

6 | Conclusion

Crystallization can be defined as the solid-liquid interface evolution in time and space. One of the best-known models in the literature is the phase field model which controls the interface evolution using the Allen-Cahn equation of crystal growth and the heat transfer equation.

However, as shown in Sect.2, existing phase field models only give a qualitative representation and can lead to non-physical results. This is the case for the well-known Kobayashi model [56], and also for the Xu et al. model [58], where the modifications made to the phase field model do not make it quantitative. In this study, we tried to improve this model by adding two semi-analytical expressions for the dimensionless diffusivity τ^* and $\hat{K}$, the dimensionless fraction between the latent heat of solidification and the specific heat at constant pressure. The dimensionless diffusivity τ^* and the expression of $\hat{K}$ are taken according to Lauritzen and Hoffman theory [39]. The proposed model in Sect. 3 is capable of quantitative prediction of growth, as shown in Figure 4.11. The given morphology is also close to experimental results (Figure 4.7), except those with temperature below 190 $°C$. It has been shown that simulations do not become quantitative when the grid spacing is too small. In some cases, the crystal branch becomes very thin compared to reality. As the change of mesh size does not modify the crystallinity degree in the spherulite, a coarse mesh was chosen which enables a significant gain in computation time.

Adding some approximations weakens the existing phase field theoretical model, but helps to obtain results which are more consistent with polymer physics (Figures 4.7, 4.11, 4.14). However, we cannot claim that the predictions are completely quantitative because the branch size is not respected for temperatures far from that of the fusion. In addition, the crystallization degree evolution is controlled proportionally with the growth rate by the functions $\tau^*(T_c)$ and $\hat{K}(T_c)$, but in reality each property can evolve independently.

CHAPTER 5

Full-field prediction of linear elastic and thermal properties of semi-crystalline polymers based on an enhanced phase field model

1 | Introduction

Polymeric materials are widely used in the industry, which explains the existence of several manufacturing processes, such as plastic injection moulding, plastic blowing, and more recently 3D printing, etc. Nowadays, the industry tends to digitize these processes, in order to provide information on the mechanical strength and final shape of the sample before starting production, the final aim being to optimize the process and reduce costs. In order to model

the constitutive response of polymers, a thermo-mechanical modeling based on viscoelasticity and / or viscoplasticity can be used, such as proposed in chapter 3. But such models remain insufficient because after melting, the material undergoes an important phenomenon which is crystallization when the temperature drops below the melting point. Spatial variation in crystallinity degree at micro-scale leads to material inhomogeneity, which changes the local material properties inside a given part from one region to another.

Semi-crystalline polymers contain two phases: amorphous and crystalline. At the micro-scale, polymer chains which do not present any order are considered as amorphous. This random arrangement of chains gives a rubbery appearance, whereas polymer chains that are periodically arranged are considered crystalline. The mechanical response depends on the crystallinity ratio and on the initial crystallographic orientation, as well as on the evolution of this micro-structure with the deformation.

In order to compute their effective properties, semi-crystalline polymers are considered as two-phase composite materials and homogenization models are used. Most of them rely on a composite inclusion model, consisting of an amorphous layer and a crystalline lamella linked together according to assumed interface conditions. The composite inclusion is homogenized, usually semi-analytically. Next, most models consider the representative volume element (RVE) as an aggregate of homogenized composite inclusions, and another homogenization is carried out after making an assumption on the orientation field. Usually, initially random orientation is considered.

The simplest mean-field model is the Voigt or Taylor model (Taylor[67]), which assumes uniform strain in the aggregate. However, this model generates excessively high stresses because the stiffness of the crystalline phase in the chain direction is much higher than the amorphous one. Another simple mean-field model is the Reuss or Sachs model (Sachs[68]), which supposes uniform stress in the aggregate. This model is recommended for polymers that are amorphous or have a low crystallinity degree. However, the model has been used by Lee et al. [69] and Nikolov et al. [70] for HDPE, which has a high crystallinity ratio, because it was found that the experimental response is closer to the Reuss estimate than to the Voigt one.

There are also hybrid inclusion models for lamellar composites, which were introduced by Lee et al.[69] and used by Van Dommelen et al. [71], and others. They represent an intermediate approach between the Voigt and Reuss models.

Still based on the composite inclusion model, there are also full-field models to homogenize the RVE, such as those of Van Dommelen et al. [72] or Uchida et al. [73]. They consist in giving each finite element (FE) an orientation and the homogenized properties of the underlying composite inclusion, applying boundary conditions and conducting a FE analysis. Oktay et al.[74] proposed

another full-field homogenization method which is based on a geometric model of spherulites.

The originality of the approach proposed in the present chapter is that full-field homogenization is not performed on assumed geometric representations of spherulites or RVEs, but on semi-crystalline micro-structures predicted by an enhanced phase field model for polymer crystallisation which was proposed in chapter 4. Crystallization is a very complex phenomenon which involves many physical parameters. However, if crystallization takes place in a free environment without constraint, spherulitic micro-structures will appear, of which the enhanced phase field model can predict representative images.

After solidification, the value of the phase field variable in each pixel or voxel indicates whether the material is amorphous or crystalline. Care is taken to define RVEs which are simulated with full-field Fast Fourier Transform (FFT) under periodic boundary conditions in order to predict the effective mechanical properties. Only elastic properties are reported but the procedure can be used to predict inelastic response.

The chapter has the following outline. Section 2 describes the procedure used to construct RVEs of the semi-crystalline micro-structures predicted by the enhanced phase field model. In section 3, full-field 2D simulations of RVEs are discussed, while 3D computations are presented in section 4. Numerical simulations of shrinkage are presented in section 5. In section 7, the composite inclusion model and several existing homogenization models are reviewed. A comparison between the predictions of some of those models and the proposed approach is presented in section 7.3. Conclusions are drawn in section 8.

2 | Micromechanical simulations based on an enhanced phase field model

In order to generate mechanical simulations, it is necessary to introduce a phase field and an orientation field. The former enables to distinguish between amorphous and crystalline phases, while the latter provides access to the local orientation of the crystalline lamellae.

In the literature, there are efforts to couple the orientation field with the phase field, e.g. Granasy et al. [35] [75] and Kobayashi et al. [76]. Similarly to the treatment of the phase field variable, a local free energy function is added which depends on the orientation field and its gradient. It should be noted that the phase field models of Kobayashi et al. and of Granasy et al. are different. The Kobayashi model consists in coupling the phase field variable with the temperature field while in the Granasy model, the phase field variable is coupled with the chemical composition field.

Kobayashi et al. were able to generate crystal orientation maps for solidification and coarsening processes, where each crystal grain has its own orientation. The work was initially in 2D, but it was later extended to 3D. Granasy et al. improved on the work of Kobayashi et al. and presented spherulite growth simulations associated with their local orientation fields. Three models were proposed [35].

In model A, the orientation field and the phase field are strongly coupled, so local free energy function for orientation is extended from that of Kobayashi et al.. The dendrites obtained by model A can transform into irregular dendrites or spherulites by the modification of the ratio of the phase-field and orientational mobilities or by increasing the number of single pixel-sized orientation-pinning. However, for the spherulites obtained by Model A, their orientation field does not follow the direction of the branches; subsequently these results cannot be representative of the polymer.

Model B is another model proposed by Granasy et al. which is similar to Model A except that a new unknown field has been added. Called the solid-solid phase field, it enables to distinguish two types of solids after crystallization, and it is generally used to model alloys or copolymers.

Model C is also an extension of model A, except that a new expression of the orientational free energy was added, which consists in setting a preference for crystallographic branching with fixed misorientations. This means that regions with a sufficiently large difference in orientation from a neighboring parent crystal will relax to finite misorientations. This model is managed by three parameters [75]: the thermodynamic driving force associated with supersaturation, the ratio of the phase-field and orientational mobilities and the depth of the metastable free energy cusp for branching. With an appropriate choice of these parameters, growth front nucleation can be recovered, with a random orientation of the new grains which have six well-defined orientations. Two types of spherulites are modeled, one is formed by a large kinetic anisotropy of two-fold symmetry (category 2) and the other is formed by four-fold symmetry (category 1). The simulations carried out by model C succeeded in representing the evolution of crystallography in polymers.

The modeling framework of Granasy et al. presents several advantages. Indeed, spherulites with complex anisotropies are generated, and the orientation of each anisotropic spherulite can be defined. Two categories of spherulites can be simulated, together with the orientation field corresponding to each crystalline branch. However, there are some drawbacks to the models of Granasy et al. There is no link between the modeling parameters and the physical characteristics of the polymer, so quantitative predictions cannot be generated. The reported simulations do not indicate the capability to predict spherulites with different degrees of crystallization. Regarding the orientation field, it has been experimentally proven that the polymer branches perform a spiral rotation

around their axis of propagation, whereas the Granasy et al. models do not take this phenomenon into account. Finally, branch growth is only simulated with six predefined orientations.

The numerical implementation of the enhanced phase field model, developed in chapter 4, relies on a finite difference scheme. Each volume element is discretized as a regular grid of small subcells, i.e. pixels in 2D and voxels in 3D, and periodic boundary conditions are applied. At the end of a phase field simulation, the material of each subcell is either crystalline (phase field variable $\phi = 1$) or amorphous ($\phi = 0$). As the mechanical simulations were made on isotropic spherulites, a simplified orientation model was chosen which allows to easily add spiral orientation to the branches. The crystalline orientation, which is not directly provided by the phase field model, is determined according to the orientation of each subcell relative to the center of the spherulite it belongs to. In other words, the orientation field is not coupled with the phase field model but is calculated separately. This is one main reason for which the computational cost is much more reduced then that of the Granasy et al. model.

In order to predict the effective mechanical properties, representative volume elements (RVEs) need to be determined, and this is done in two stages. First, the minimum number of subcells in a single spherulite is found. Next, the number of spherulites per RVE is fixed. Full-field simulations can be conducted with finite element analysis (FEA). However, in order to reduce computation time (by a factor of 10 at least) a Fast Fourier transform (FFT) method is used in this work with the Digimat-FFT software.

2.1 Micro-structures obtained from an enhanced phased field model

Supposing random nucleations as an initial condition, the enhanced phase field model can generate representative polymer micro-structures which take into account the interface between adjacent spherulites (see Figure 5.1). Experimental observation of crystallization in thin films shows that the phase field simulations are very close to reality (see Figure 5.2).

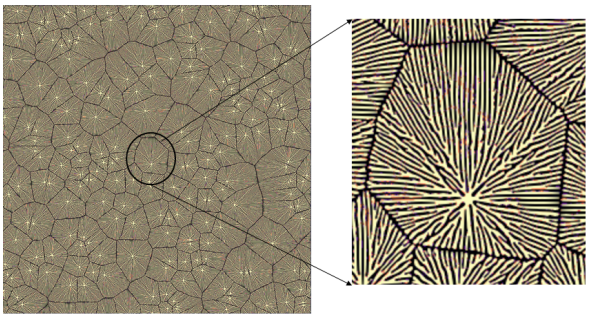

Figure 5.1: Micro-structures obtained from an enhanced phased field model.

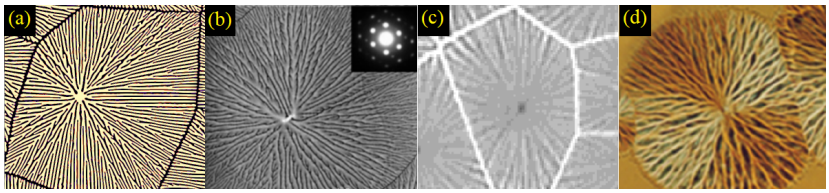

Figure 5.2: (a) Spherulite predicted by an enhanced phase field model, (b) AFM Spherulite image ($20\mu m \times 20\mu m$) in thin films of poly (ε-caprolactone) (PCL) crystallized for $24h$ at room temperature [77], (c) Optical microscope images of isotactic polystyrene (ipS) crystallization kinetics at $T_c = 169\ ^\circ C$ [78] and (d) PLM micrograph of poly(arylether ketone ketone) PEKK(70/30) (a 70/30 statistical copolymer of terephthalic and isophthalic linkages) crystallized isothermally from the melt at $280\ ^\circ C$ [79].

For the next sections, we will use polyethylene to perform mechanical simulations. As discussed in section 5, to generate a phase field simulation, it is necessary to calibrate the parameters of the simplified equation of Lauritzen and Hoffman (eq. (4.12)) and $\hat{K}_0$ (eq. (4.15)). The other parameters are assumed to be constant and their value is given in section 5. Lauritzen and Hoffman [39] give the parameters of equation (2.14) for HDPE: $U^* = 4120 cal/mol$, $T_g = -80\ ^\circ C$, $T_\infty = T_g - 51.6\ ^\circ C$, $T_m^0 = 146\ ^\circ C$, $K_{G_r} = 1.77710^{+5} K^2$ and $\log_{10}(G_{r\ i}\ cm/s) = 5.64$. Using these parameters, we can find the parameters of the simplified equation (4.12). At $T_{c\ mac} \approx 40\ ^\circ C$ the degree of crystallinity of HDPE is approximately equal to 60.5% according to S. Sommer et al. [80], using this information $\hat{K}_0 = 1.8$.

2.2 Orientation field model

To perform a mechanical simulation, it is necessary to define the orientation of the crystalline phase. Since this information is not provided directly by the phase field model, the orientation field is calculated separately and used later in full-field simulations. The spherical coordinates of each crystalline subcell with respect to the center of its spherulite are computed. Next, an additional rotation defined by an angle ω is applied in order to define the spiral shape of the crystalline branch (figure 5.3). Starting from the spherulite's center, and for three successive subcells, ω equals 0, $\frac{\pi}{4}$ and $\frac{\pi}{2}$, resp., and this process is repeated until the end of the spherulite.

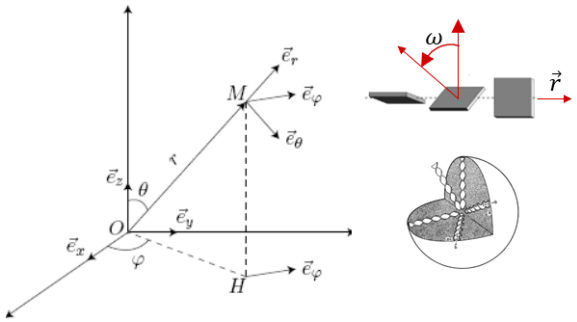

Figure 5.3: Orientation of the crystallographic directions.

The unit normal $\vec{n}$ to a crystalline lamella is defined in terms of two spherical basis vectors as follows (figure 5.3):

$$\vec{n} = \cos(\omega)\vec{e}_\theta + \sin(\omega)\vec{e}_\varphi \tag{5.1}$$

Therefore, the Cartesian components of $\vec{n}$ are

$$\begin{cases} x^* &= \cos(\omega)\cos(\theta)\cos(\varphi) - \sin(\omega)\sin(\varphi) \\ y^* &= \cos(\omega)\cos(\theta)\sin(\varphi) + \sin(\omega)\cos(\varphi) \\ z^* &= -\cos(\omega)\sin(\theta) \end{cases} \tag{5.2}$$

The orientation information is stored with only two angles θ^* and φ^* which are defined similarly to the classical relations between the spherical angles and the Cartesian coordinates, i.e.

$$\begin{cases} r^* &= \sqrt{(x^*)^2 + (y^*)^2 + (z^*)^2} = 1 \\ \theta^* &= \arccos(z^*/r^*) \\ \varphi^* &= \arctan(y^*/x^*) \end{cases} \tag{5.3}$$

2.3 Computing the number of subcells per spherulite

In order to obtain representative spherulites with the phase field model, the number of subcells needs to be sufficiently large. We distinguish between two cases, according to the crystallinity ratio $X_c = 100\%$ or $X_c < 100\%$. In the following simulations, we will use the mechanical properties of PE, whose properties are presented in the section 3.

The case $X_c = 100\%$ is not physical for semi-crystalline polymers and is not obtained by the phase field model. It is obtained by forcing the phase field variable to be equal to 1 for each subcell, thus representing a purely crystalline material. This fictitious case is however important for numerical computations. Indeed, running full-field mechanical simulations with a single phase ($X_c = 100\%$) is much more cheaper computationally than with a realistic two-phase material ($X_c < 100\%$). This is especially clear when finding the minimum number of spherulites in a RVE, where a large number of full-field simulations are needed, as explained in Sect. 2.4. Nevertheless, the minimum number of spherulites obtained when $X_c = 100\%$ is applicable to the case $X_c < 100\%$ because in the former case, there is a single anisotropic phase, while in the latter case the introduction of an isotropic amorphous phase reduces the degree of anisotropy. Another numerical advantage of the $X_c = 100\%$ simulations is that they enable to predict an effective isotropic Young's modulus for the crystalline phase (which is locally anisotropic) that is used in simple mean-field homogenization models such as Voigt, Reuss and their combinations.

2.3.1 Case of crystallinity ratio $X_c = 100\%$

For a crystallinity ratio $X_c = 100\%$ there is only one crystalline phase, and since its material is orthotropic, the orientation field must be used. The field φ^* is depicted in Figure 5.4 in the 2D simulations of a single spherulite with an increasing number of subcells.

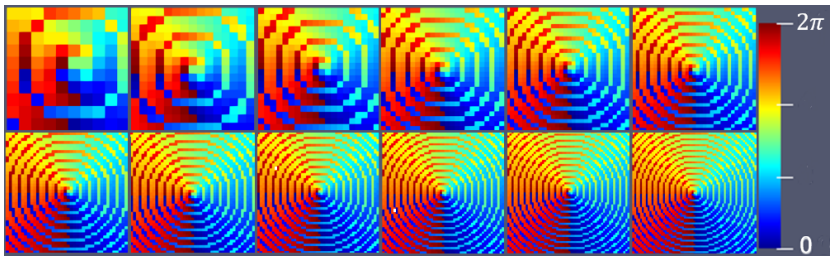

Figure 5.4: Orientation field φ^* in 2D simulations of a single crystalline spherulite ($X_c = 100\%$) with an increasing number of subcells (from left to right in each row). Square root of the number of subcells respectively: 10, 15, 20, 25, 30, 35, 40, 45, 50, 55, 60 and 65.

The number of lamellar twists in polymeric spherulites depends on the material properties and the crystallization conditions. And even within a RVE of a given micro-structure, the number of twists varies because the RVE's spherulites have different sizes. In this work, we propose a pragmatic approach to this complex problem.

Firstly, as already indicated, it is assumed that three successive subcells represent a lamellar twist. Therefore, the increase in the number of subcells leads to an increase in the number of lamellar twists. Secondly, we start by studying a single spherulite, and the number of subcells -and thus of lamellar twists- is increased until obtaining a converged prediction of the spherulite's apparent Young's modulus. The results are depicted in Fig. 5.5 which shows that 50×50 subcells are sufficient. Indeed, the relative errors compared to the case of 2000^2 subcells do not exceed 1.5% (Figure 5.6).

Thirdly, RVEs with multiple spherulites will be simulated in Sect. 2.4. The minimum number of twists found for a single spherulite is then considered as an initial guess of the average number per spherulite. Consequently, the number of lamellar twists will be different from one spherulite to another within a RVE, consistent with the fact that the spherulites have various sizes. The final number of spherulites in a RVE and the final number of subcells in the RVE will dictate the actual distribution of the number of lamellar twists in the spherulites.

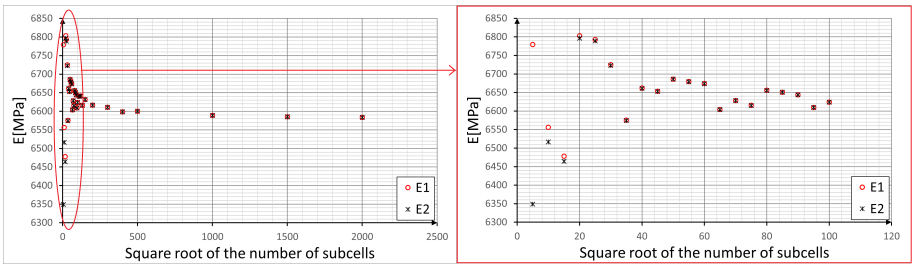

Figure 5.5: Convergence of apparent Young's moduli for a single crystalline spherulite ($X_c = 100\%$) with the square root of the number of subcells.

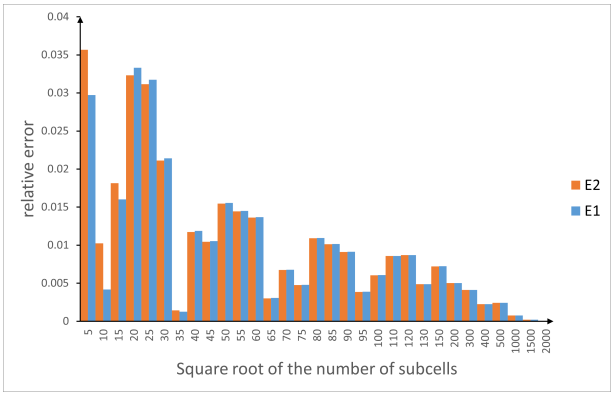

Figure 5.6: Relative errors in apparent Young's moduli for a single crystalline spherulite ($X_c = 100\%$) with respect to the results of a spherulite with 2000^2 subcells.

2.3.2 Case of crystallinity ratio $X_c < 100\%$

Polymers generally have very thin crystalline branches, e.g. a thickness of about 5 to 25 nm for polyethylene (Lee et al. [69], Keller et al. [81]). Therefore, in order to simulate actual spherulites, the subcell size should be about 1 nm or less. In addition, the size of polyethylene spherulites is between about 20 and 200μm (Butler and Donald [82], Bernard Lotz et al. [83]). Consequently, in order to represent a 20μm spherulite, we need 4×10^8 subcells in 2D, which is a very large number. The proposed method makes it possible to predict the mechanical behavior of semi-crystalline polymers by modeling representative spherulites which have crystalline branches thicker than the actual experimentally observed values. Keeping a given spherulite's size constant, the number

of subcells is increased (thus the subcell size is decreased) until the computed apparent Young's modulus converges within a small error, as shown in figure 5.8. This enables to conduct simulations with an optimal number of subcells.

The minimum number of subcells needed to simulate a single semi-crystalline spherulite (crystallinity ratio $X_c < 100\%$) is different from the previous case of $X_c = 100\%$. Figure 5.7 illustrates the case of $X_c = 69\%$ in 2D and shows for each number of subcells the spherulite's geometry and the equivalent strain and von Mises stress distributions obtained by full-field simulations. It is seen that when the number of subcells is not large enough, even the prediction of the spherulite's shape by the phase field model is not correct.

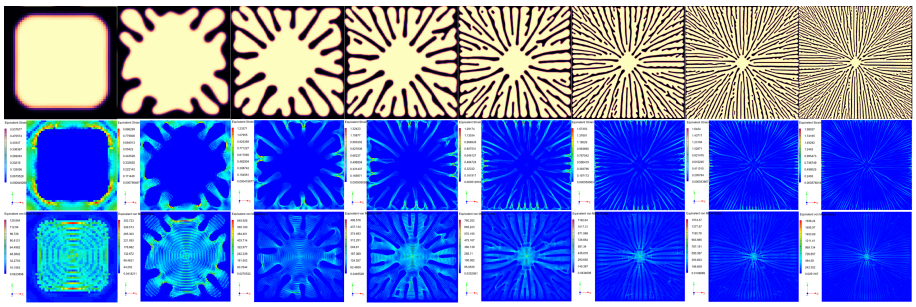

Figure 5.7: Simulations of a single semi-crystalline spherulite with crystallinity ratio $X_c = 69\%$ with increasing number of subcells from left to right. First row: phase field simulations of spherulite's geometry. Second row: equivalent strain distributions. Third row: equivalent Von mises stress distributions. Square root of the number of subcells respectively: 50, 100, 150, 200, 300, 500, 750 and 1000.

Figure 5.8 shows the apparent Young's moduli for a single semi-crystalline spherulite in 2D as a function of the square root of the number of subcells. The numerical spherulites are those of Fig. 5.7. The experimental Young's modulus in Fig. 5.8 was measured on a polymer sample. The apparent stiffness of a single spherulite must be larger than that of the experimentally-measured value because a single spherulite is not representative of the micro-structure. In subsequent sections, RVEs containing a sufficiently large number of spherulites and amorphous interphases between adjacent ones will be studied.

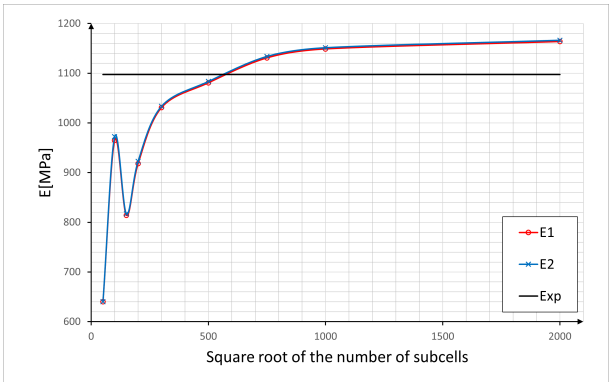

Figure 5.8: Convergence of apparent Young's moduli for a single semi-crystalline spherulite ($X_c = 69\%$) with the square root of the number of subcells (experimental Young's modulus for $X_c = 69\%$ from figure 5.15).

Figure 5.8 shows that a spherulite with 750^2 subcells is a good choice. Firstly, its apparent Young's modulus exceeds the experimental value. Secondly, the relative error in apparent stiffness with respect to that computed with 2000^2 subcells does not exceed 2.8%, as shown in Fig. 5.9. Recall however that for a crystalline spherulite ($X_c = 100\%$) a grid with 50^2 subcells was sufficient.

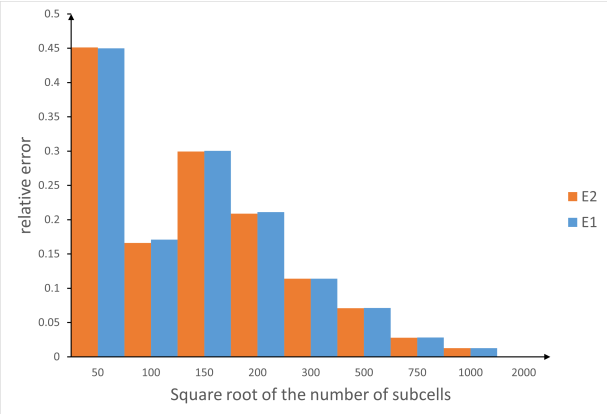

Figure 5.9: Relative errors in apparent Young's moduli for a single semi-crystalline spherulite ($X_c = 69\%$) with respect to the results of a spherulite with 2000^2 subcells.

2.4 Computing the number of spherulites per RVE

The RVE's size is determined from the number of spherulites it contains. The procedure is the following. For a given number M_s of spherulites, $N_r = 10$ realizations are created, each corresponding to an initially random distribution of M_s nucleations. For each realization ($i = 1$ to N_r), the enhanced phase field model runs to completion, and then full-field FFT simulations with periodic boundary conditions are carried out, leading to estimates of the effective Young's moduli $E_{1(i)}$ and $E_{2(i)}$. Next, the coefficient of variation CV of each modulus is computed. The CV, also called relative standard deviation, is a measure of relative dispersion which is often used in statistics. It is defined as the ratio between the standard deviation σ and the mean value μ,

$$CV = \frac{\sigma}{\mu}; \quad \mu = \frac{\sum_{i=1}^{N_r} x_i}{N_r}; \quad \sigma = \sqrt{\frac{\sum_{i=1}^{N_r} (x_i - \mu)^2}{N_r - 1}} \tag{5.4}$$

where x_i is a measurement value ($x_i = E_{1(i)}$ or $E_{2(i)}$). The procedure is repeated with an increased value of M_s until obtaining a low CV value. This is illustrated for purely crystalline spherulites ($X_c = 100\%$) in Fig. 5.10, which shows that the CV is around 0.008 for $M_s = 200$ spherulites. Therefore, based on this low CV value, the RVE's size is determined such that it contains 200 spherulites, and for $X_c = 100\%$, it was seen previously that accurate spherulite simulations are obtained with 50^2 subcells in each spherulite. Figure 5.11 shows the orientation angle φ^* field on such crystalline RVE. For semi-crystalline cases ($X_c < 100\%$) it was also found that RVEs in 2D should contain 200 spherulites.

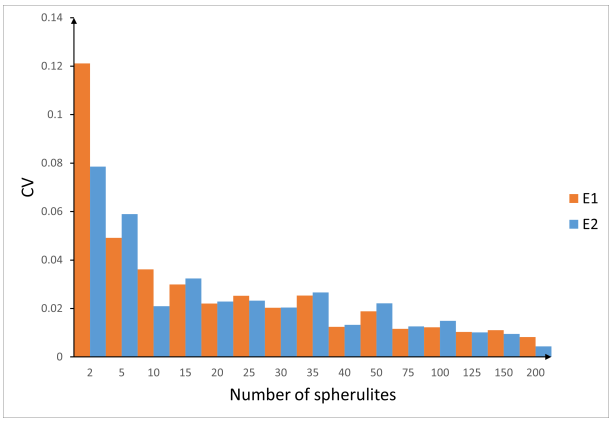

Figure 5.10: Coefficient of variation of effective Young's moduli as a function of the number of spherulites.

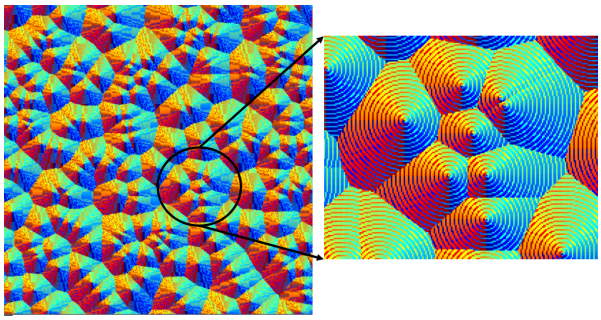

Figure 5.11: Orientation angle φ^* field of RVE.

3 | RVE simulations in 2D

The results of the previous sections showed that RVEs in 2D should contain 200 spherulites, with a discretization of 750^2 subcells in each spherulite. RVEs with a total number of 10607^2 subcells are represented in Fig. 5.12 for a crystallinity ratio $X_c = 64.05\%$ and in Fig. 5.13 for different values of X_c.

The micro-structures were obtained with the enhanced phase field model. However, the model has difficulty to generate an RVE with low values of X_c. Indeed, the crystalline amount in a spherulite is controlled by a non-dimensional variable $\hat{K}$ in the model, see equations (4.15) to (4.17), so that when $\hat{K}$ increases the crystallinity ratio decreases. The growth rate decreases drastically for $\hat{K} > 2$, as well as the ability to create branches. For $\hat{K} = 2$ the crystallinity degree is approximately $X_c = 50\%$. As $\hat{K}$ increases, the crystallinity degree remains practically constant, unable to get below $X_c = 45\%$ approximately, and when $\hat{K}$ is large enough, growth and branching stop.

Consequently, in order to obtain a RVE with crystallinity degree lower than 45%, we applied an erosion method, as in a RVE with $X_c = 30\%$ depicted in Fig. 5.13. In that case, the starting point was a RVE obtained for $X_c = 49\%$. The erosion method consisted then in reducing the size of the crystalline branches by eroding the subcells in the crystal-amorphous interphase until the desired final value of $X_c = 30\%$ was reached. A zoom on spherulites before ($X_c = 49\%$) and after ($X_c = 30\%$) erosion is shown in Fig. 5.14.

A lack of experimental data at low crystallinity values prevents from validating the erosion method. However the method is consistent with the phase field model, where the reduction of the crystallinity degree is driven by a thinning of the polymer branches.

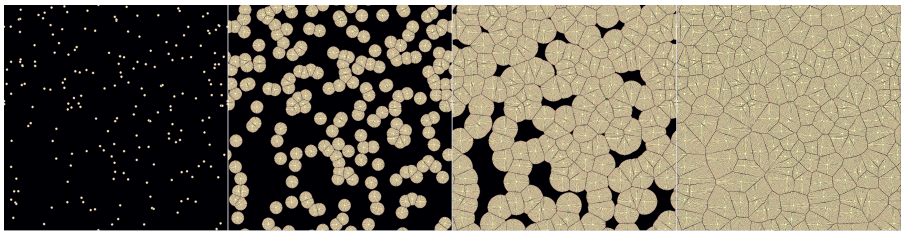

Figure 5.12: 2D phase field simulation for a RVE with 10607^2 subcells and crystallinity ratio $X_c = 64.05\%$.

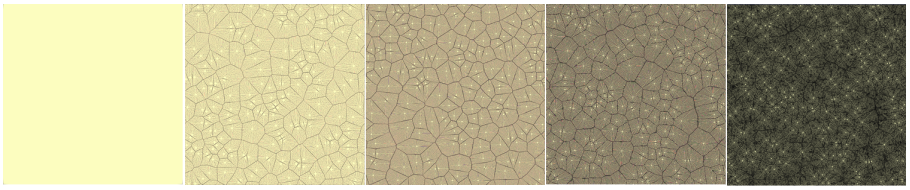

Figure 5.13: 2D phase field simulations of RVEs with 10607^2 subcells and decreasing crystallinity ratios; from left to right: $X_c = 100\%$, 84.6%, 64.05%, 49% and 30%.

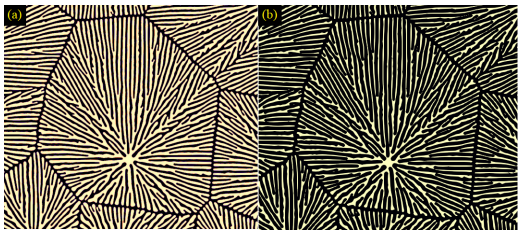

Figure 5.14: Zoom on RVE shown in Fig. 5.13: (a) before erosion ($X_c = 49\%$) and (b) after erosion ($X_c = 30\%$). Colours: black and yellow for amorphous and crystalline phases, resp.

Numerical simulations of RVEs subjected to macroscopic tension tests were carried out using Digimat-FFT, based on a full-field Fast Fourier Transform (FFT) method with periodic boundary conditions. The material properties of each phase were determined as follows.

For Polyethylene (PE) the elastic properties of the orthotropic crystalline phase were determined by Choy and Leung [84] who used an ultrasonic method

to measure the elastic constants of ultra-stretched high density PE with a stretching ratio up to $\lambda = 27$. Using the classical matrix storage convention for anisotropic materials, and designating the local polymer chain direction by index 3, the authors found the stiffness component value $C_{33} = 81$ GPa, which is smaller than the theoretical value, because the latter does not take into account material defects. The other stiffness components for the crystalline phase are: $C_{11} = C_{22} = 7$ GPa, $C_{12} = C_{23} = 3.8$ GPa, $C_{13} = 4.7$ GPa and $C_{44} = C_{55} = C_{66} = 1.6$ GPa.

The amorphous phase is isotropic and its Young's modulus E_a was computed as follows. From the experimental data of figure 5.15, a trend curve was determined whose expression is presented in the figure. This curve was extended to vanishingly small values of X_c. This enabled to have an estimate of $E_a = 12.66$ MPa. As for the Poisson's ratio, it was taken as $\nu_a = 0.499$ due to the quasi-incompressibility of the amorphous phase.

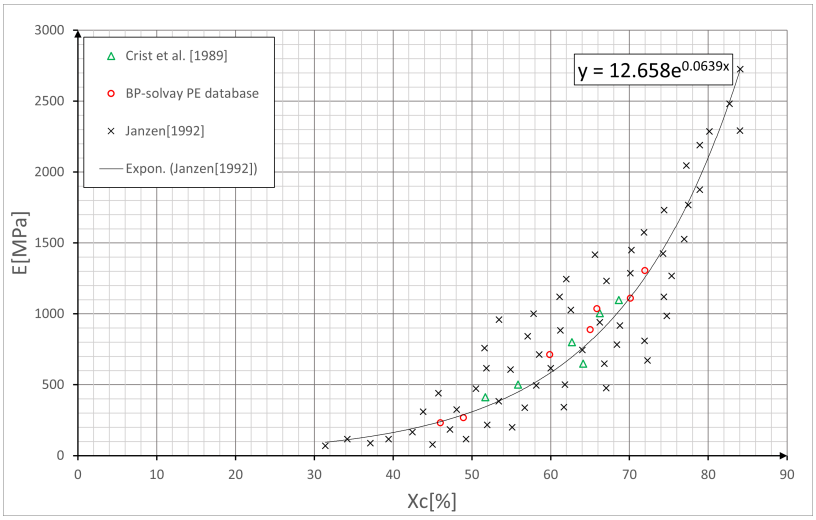

Figure 5.15: Experimental data of Young's modulus of Polyethylene as a function of the crystallinity ratio [47], [45] and [46].

The per-phase properties thus identified for the crystalline (C_{IJ}) and amorphous (E_a and ν_a) phases were used in all 2D simulations of RVEs with various crystallinity ratios X_c. Numerical simulations of tensile tests are presented in figures 5.16, which shows the maps of normalized equivalent strain and stress for each value of X_c. The ranges of values which are shown have been reduced except in the case of $X_c = 100\%$ in order to make the figures clearer.

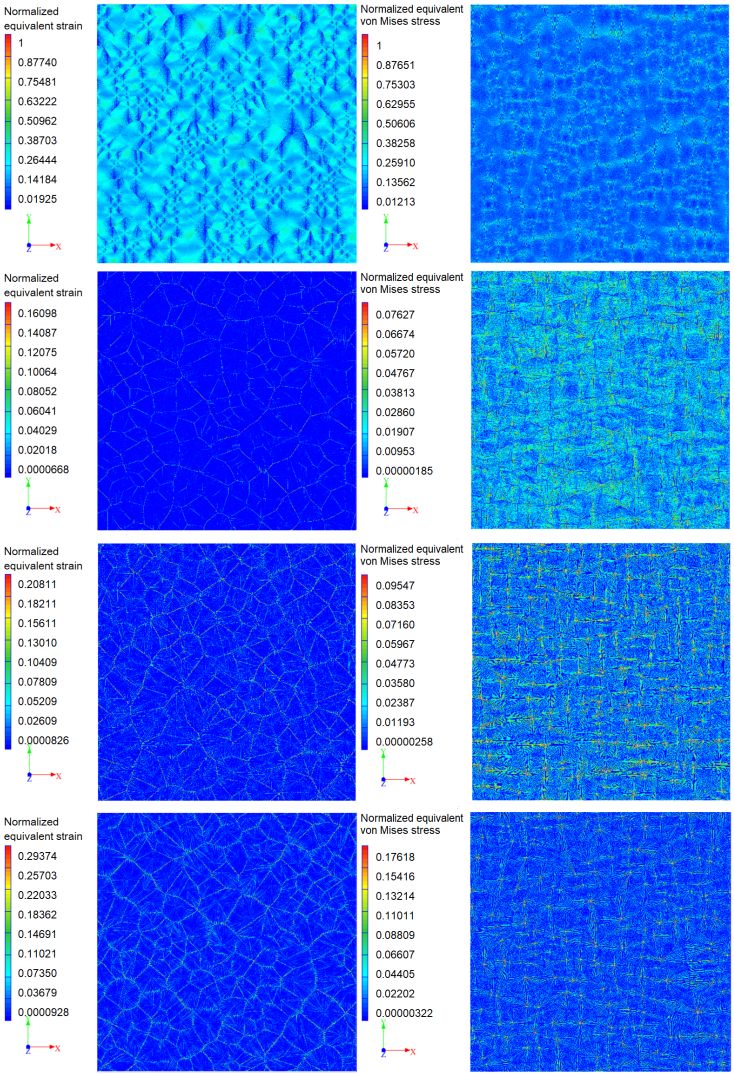

Figure 5.16: 2D FFT simulations of tensile tests of RVEs with 10607^2 subcells. From top to bottom, the crystallinity ratio is $X_c = 100\%$, 84.6%, 64.05% and 49%. For each row, maps of normalized equivalent strain and stress are shown.

The predictions of the effective Young's modulus of PE as a function of crystallinity ratio X_c are presented in Fig. 5.17, which shows a good agreement with experimental data for all X_c values, in particular for higher ones.

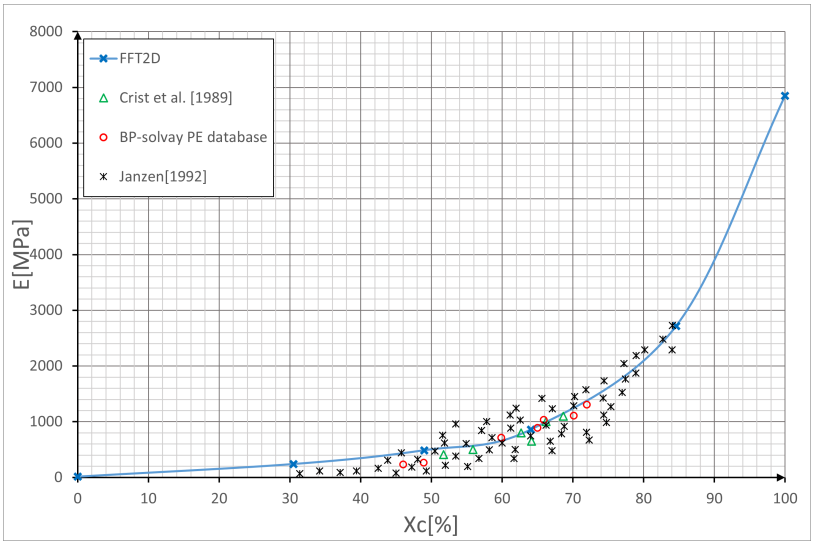

Figure 5.17: Young's modulus of Polyethylene as a function of the crystallinity ratio. Comparison between numerical 2D simulations of RVEs and experimental data.

The mean strain in all the RVEs is equal to the same imposed macro strain of 0.03. The strains in the amorphous phase exceed the mean value, and increase with an increasing crystallinity ratio. Inside the RVE, amorphous subcells will not witness the same level of strains, generally the amorphous inter-spherulite interphases are more stretched. Stresses in the crystalline phase subcells are high because their material is much stiffer than the amorphous one. Crystalline subcells are not subjected to the same stress levels, generally the stress is concentrated at spherulites' centers.

4 | 3D simulations

It was found that while in 2D a RVE has 10607^2 subcells, approximately 4386^3 subcells (voxels) are needed for a 3D RVE. This number is too large for numerical simulations with the enhanced phase field model on available computer resources, and smaller (statistical) volume elements (SVEs) had to be considered. A simulation with 1000^3 subcells is shown in Fig. 5.18. It was performed on a supercomputer with RAM 130 Go.

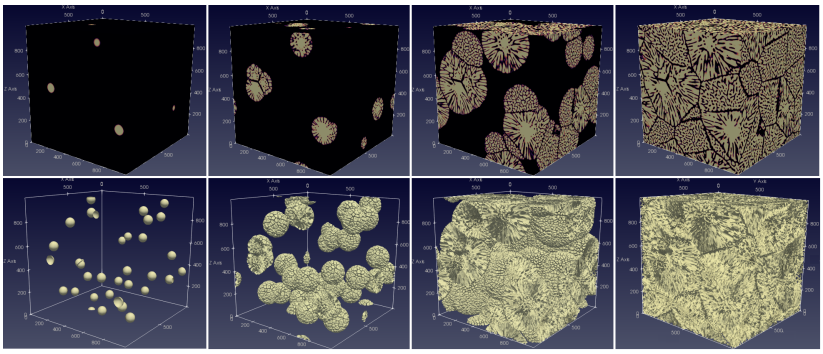

Figure 5.18: 3D phase field simulation on a SVE with 1000^3 subcells (voxels). Number of spherulites is 30 and $X_c = 59.7\%$.

In order to perform mechanical simulations with FFT, it was necessary to further reduce the volume size, because of the very large number of unknowns. For this reason, a pixelation method was adopted. It consists in gathering neighboring subcells and averaging their phase field variable. If the average is greater than 0.5, then the subcells are considered as belonging to the crystalline phase. This method reduces the number of subcells from 1000^3 to 500^3. Figure 5.19 shows the results of 3D FFT simulations of tensile tests on SVEs having different crystallinity ratios X_c.

Regarding the 3D simulations of Fig. 5.19, the comments are similar to those of the 2D case. The most stretched amorphous regions are located between the spherulites and the most stressed crystalline parts are in the centers of the spherulites.

Using the same properties for the crystalline and amorphous phases as those which were used for 2D RVEs, tensile tests on 3D SVEs were conducted for various values of X_c. The Young's moduli thus predicted are reported in Fig. 5.20 and compared to experimental data, and also to the previously obtained 2D results on RVEs. The figure shows that the 3D estimates are slightly higher than the 2D ones. The small discrepancy is mainly due to the fact that -as already mentioned- the 3D simulations were not obtained on RVEs but on smaller SVEs.

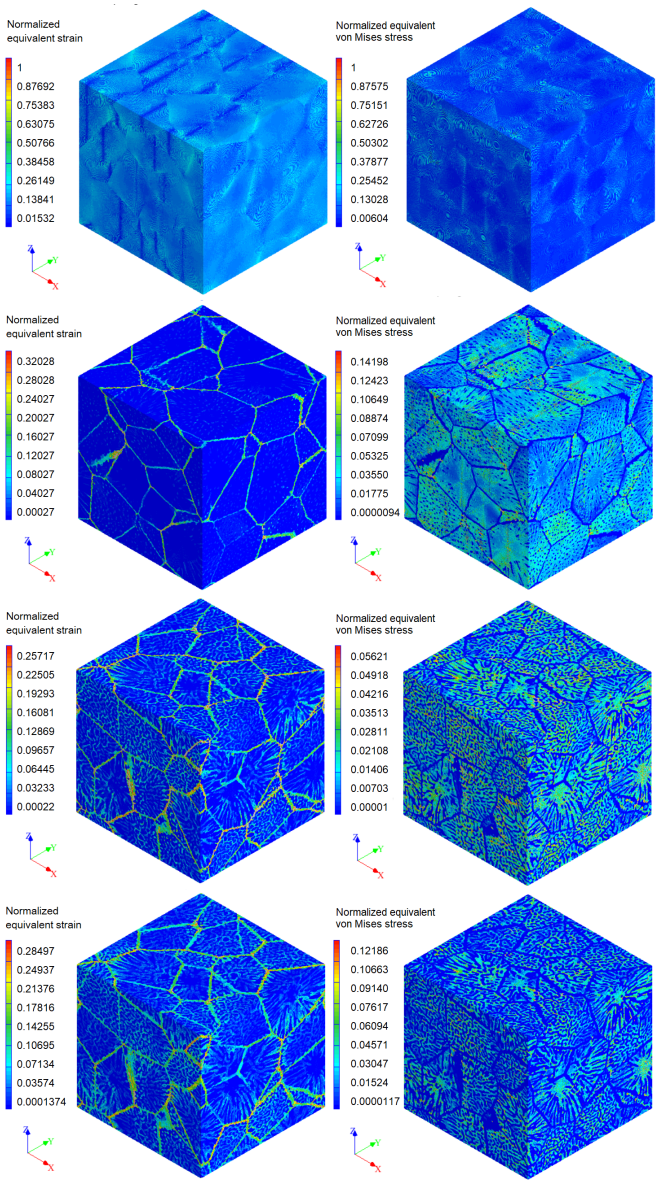

Figure 5.19: 3D FFT simulations of tensile tests on SVEs with 500^3 subcells. From top to bottom, the crystallinity ratio is $X_c = 100\%$, 83.3%, 59.7% and 46.9%. For each row, maps of equivalent normalized strain and stress are shown.

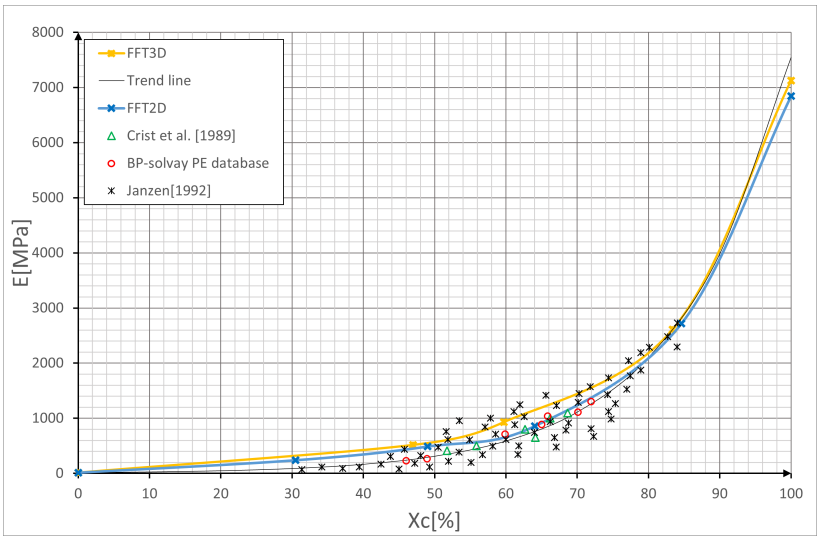

Figure 5.20: Young's modulus of Polyethylene as a function of the crystallinity ratio. Comparison between 3D (FFT3D) and 2D (FFT2D) numerical simulations and experimental data.

5 | Predicting polymer shrinkage during cooling

The enhanced phase field model is able to predict the shrinkage of polymers during cooling. There are two models of shrinkage, isothermal and non-isothermal, which are depicted in Fig. 5.21.

Isothermal shrinkage is due to crystallization under isothermal conditions, and is decomposed into two stages. The first is thermal shrinkage, which begins at the initial temperature T_0 and ends at the crystallization temperature T_c. The second stage is shrinkage due to crystallization and takes place at temperature T_c.

Non-isothermal crystallization causes a non-isothermal shrinkage which is decomposed into three stages. The first one is thermal shrinkage, which lasts from the initial temperature T_0 until the melting temperature T_m. The second stage combines thermal and crystal shrinkage from the melting temperature T_m until the crystallization temperature T_c. The last stage is a thermal shrinkage, from the crystallization temperature T_c until the final temperature T. However, unlike the first thermal shrinkage (from T_0 to T_m) which had a single phase, there are now two phases, amorphous and crystalline.

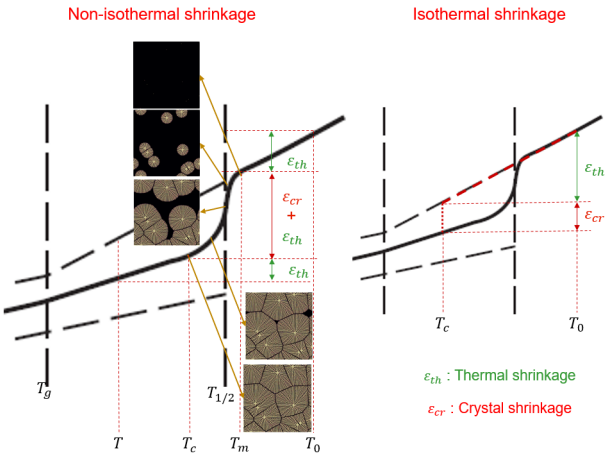

Figure 5.21: Illustration of isothermal shrinkage (right) and non-isothermal shrinkage (left).

Shrinkage is by definition the decrease in volume. Based on the density, it is possible to obtain the mean deformation in each phase β with the following equation (under infinitesimal strains):

$$\text{trace}(\epsilon^{\beta}) = \frac{dV_{\beta}}{dV_{\beta(0)}} - 1 = \frac{\rho_0}{\rho_{\beta}} - 1 \tag{5.5}$$

where $\beta = a, c$ defines the amorphous or crystalline phase, ρ_0 is the initial density at T_0 and ρ_{β} is the density of each phase. Using eq. (5.5) it is possible to estimate the local deformation of each element. Integrating these values in a FEA software enables shrinkage simulations. As the enhanced phase field model cannot generate spherulites with a crystallinity degree less than 45%, then quantitative simulation of PA12 would not be possible, because PA12 has a crystallinity degree lower than 50%. In this case the phase field model will be used as RVE or SVE generator.

Figure 5.22 illustrates an isothermal shrinkage for PA12 polymer at the crystallization temperature $T_c = 170\ ^{\circ}C$ and reference temperature of the liquid state $T_0 = 186\ ^{\circ}C$. The semi-analytical expression of the density of each phase is taken from the work of Amado and Wegener [42], as shown in the equations below.

$$\rho_c = 1010 - 0.688\ T\ \ [kg/m^3] \tag{5.6}$$

$$\rho_a = 961 - 0.616\ T\quad [kg/m^3] \tag{5.7}$$

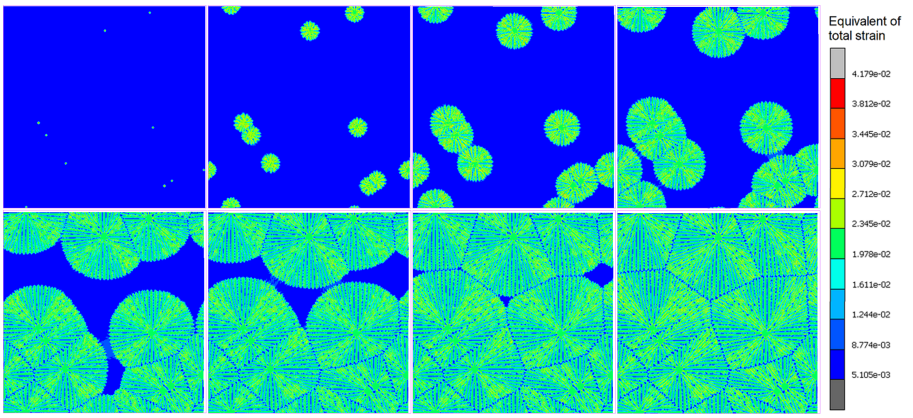

Figure 5.22: Crystal shrinkage simulation by finite elements on a SVE at $T_c = 170\ ^\circ C$.

The different stages of shrinkage are illustrated in Figure 5.23. Since the simulation is carried out at constant temperature, the material undergoes sudden thermal shrinkage with respect to the initial state (the purple frame in Fig. 5.23). After that, spherulites begin to appear, which causes further shrinkage due to the new crystalline phase. When the crystallization process is completed, the micro-structure will undergo both thermal and crystalline shrinkage (Fig. 5.23).

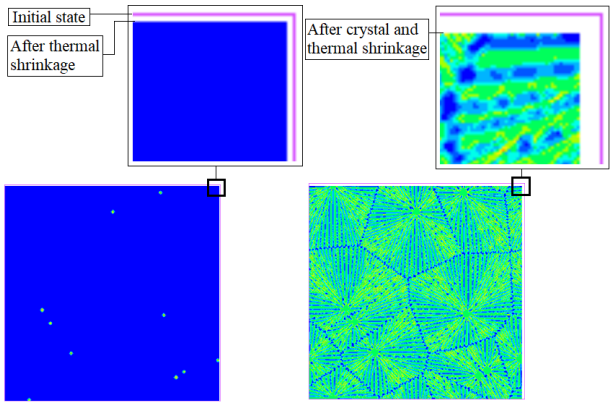

Figure 5.23: Illustration of the consecutive stages of thermal shrinkage (zoom on a small region of Fig. 5.22).

6 | Thermal conductivity prediction

As shown in section 3.7.2 of chapter 2, there are several simplified models to calculate the conductivity according to the crystallinity degree and the conductivity of each phase, but these models are based on a very strong geometric simplification, moreover one cannot select the perfect model between them.

The phase field model also makes it possible to determine the conductivity according to crystallinity degree by applying a simple thermal model. Indeed, the model consists in applying a temperature gradient to the RVE to generate a heat flux. The phase field model will help us distinguish between amorphous and crystalline phases. According to the properties of each phase an elementary flux will be generated and the global heat flux will be the volume average of all the elementary fluxes (see figure 5.24). If the elementary volume is constant for all the elements, the global heat flux will be the sum of all elementary fluxes divided by their number. The conductivity will be calculated by the following equation:

$$k = \frac{QL_x}{T_1 - T_2} \tag{5.8}$$

where $Q = \frac{1}{Ne}\sum_{i=1}^{Ne} Q_i$ is the global heat flux, Q_i is the elementary heat flux, L_x is the size of RVE and $(T_1 - T_2)/L_x$ is the temperature gradient.

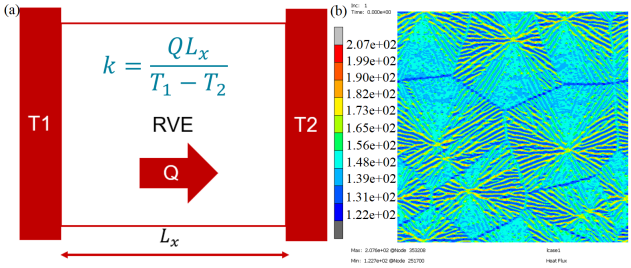

Figure 5.24: Computation of effective thermal conductivity, using $k_a = 0.2\ W/m/K$ and $k_c = 0.28\ W/m/K$. (a) illustration of the model boundary condition and (b) the heat flux $[W/m^2]$ on RVE with $X_c = 49\%$.

Figure 5.25 shows the results obtained using the phase field model and other mean field models. A comparison of these models makes it possible to observe that the Maxwell (Eq. (2.44)) and Russell (Eq. (2.45)) models are the most suitable for polymer modeling, because they give results close to those based on the phase field model.

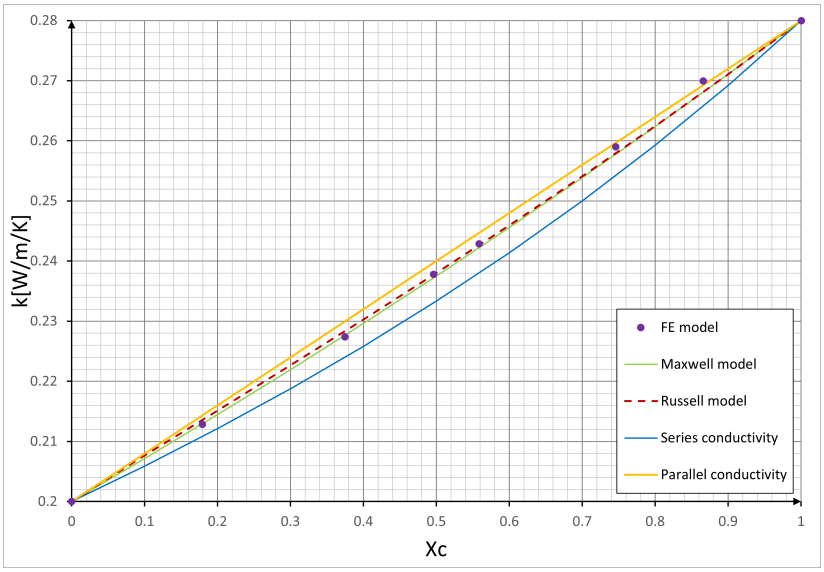

Figure 5.25: Compare full field model based on phase field with another mean field model.

7 | Composite inclusion model and simplified micromechanical models

In order to predict the mechanical properties of solid semi-crystalline polymers, there are simplified micromechanical models in the literature which are based on the composite inclusion model. These models are summarized in the following subsections before a comparison of their predictions against those obtained with the present proposal, i.e. full field FFT predictions based on the enhanced phase field model

7.1 Composite inclusion model

The composite inclusion model is depicted in Fig. 5.26 and was investigated by Lee et al. [69] and several other authors (e.g., Van Dommelen et al. [71], Nikolov et al. [70]). Each inclusion is made of a crystalline lamella which deforms plastically by crystallographic sliding, and an amorphous layer for which several constitutive models have been proposed. Typical amorphous material models are an elasto-viscoplastic power law with a back-stress tensor

to take account of the hardening induced by molecular chains rearrangement, or a nonlinear viscoelastic model.

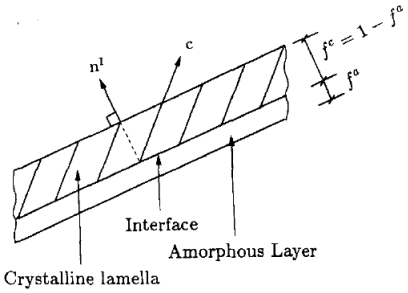

Figure 5.26: Schematic representation of a composite inclusion [69].

The mechanical properties of each phase are coupled with those of the inclusion by using the following equations:

$$F^I = f^c F^c + f^a F^a \tag{5.9}$$

$$\sigma^I = f^c \sigma^c + f^a \sigma^a \tag{5.10}$$

where f^a and $f^c = 1 - f^a$ are respectively the volume fractions of amorphous and crystalline phases, F^I and σ^I are respectively the volumes averages over the inclusion domain of the deformation gradient and the Cauchy stress, resp., and (F^a, σ^a) and (F^c, σ^c) designate similar averages over the amorphous and crystalline subdomains, resp. Note that rigorously, under finite transformation, the volumes averages of the deformation gradient and the Cauchy stress should be taken with respect to the reference and current configurations, respectively, and care should be taken with the volume fractions. However, this article is restricted to the small perturbation hypothesis.

A perfect interface is supposed between the crystalline lamella and the amorphous layer. A unit vector normal to the interface is designated by $e_3 = n^I$, while e_1 and e_2 are the other basis vectors in the interface plane. The interface kinematic compatibility condition can be written as:

$$F^I_{11} = F^c_{11} = F^a_{11} \tag{5.11}$$

$$F^I_{22} = F^c_{22} = F^a_{22} \tag{5.12}$$

$$F^I_{12} = F^c_{12} = F^a_{12} \tag{5.13}$$

$$F^I_{21} = F^c_{21} = F^a_{21} \tag{5.14}$$

Traction equilibrium across the interface can be expressed as follows:

$$\sigma^I_{33} = \sigma^c_{33} = \sigma^a_{33} \tag{5.15}$$
$$\sigma^I_{13} = \sigma^c_{13} = \sigma^a_{13} \tag{5.16}$$
$$\sigma^I_{23} = \sigma^c_{23} = \sigma^a_{23} \tag{5.17}$$

7.2 Aggregate of oriented composite inclusions

After homogenizing a composite inclusion, an orthotropic material is obtained. At a larger (mesoscopic) scale, the polymer material is seen as an aggregate of homogenized composite inclusions having different orientations. Several models exist to homogenize the aggregate; they can be classified into mean-field or full-field models.

7.2.1 Mean-field homogenization models

Mean-field models are based on assumed interaction laws. For the aggregate of composite inclusions, there are the simple Voigt and Reuss models, and hybrid models which are intermediate between Voigt and Reuss schemes.

Voigt model

The simple Voigt model assumes a uniform deformation gradient in the aggregate of homogenized inclusions (Taylor [67]),

$$\bar{F} = F^I_i \ ; \ i = 1 \dots N^I \tag{5.18}$$

where N^I is the number of inclusions. The mesoscopic stress tensor is obtained as the volume average of the stress over all inclusions,

$$\bar{\sigma} = < \sigma^I_i > \tag{5.19}$$

The Voigt model predicts excessively high stresses because the stiffness contrast between the crystalline and amorphous phases inside each inclusion is very large.

Reuss model

The simple Reuss model assumes that the Cauchy stress is uniform inside the aggregate of homogenized inclusions (Sachs [68]),

$$\bar{\sigma} = \sigma_i^I; \;\; i = 1 \dots N^I \tag{5.20}$$

The mesoscopic deformation gradient is obtained as the volume average of the deformation gradient over all inclusions,

$$\bar{F} = \left(\frac{\bar{J}}{J_\Sigma} \right)^{1/3} < F_i^I > \tag{5.21}$$

With:

$$\bar{J} = \det(\bar{F}) = < J_i^I > \;\; | \;\; J_i^I = \det(F_i^I) \;\; \text{and} \;\; J_\Sigma = \det(< F_i^I >) \tag{5.22}$$

The scaling factor $\left(\frac{\bar{J}}{J_\Sigma}\right)^{1/3}$ is used to assure volumetric consistency. The Reuss model is recommended for polymers with low crystallinity ratio. However, it has been used by Lee et al. [69] and Nikolov et al. [70] for HDPE, which has a high crystallinity ratio. Indeed, it was found experimentally that the response of polymers is closer to the Reuss estimate than to the Voigt one.

Hybrid $\hat{U}$-inclusion model

There are hybrid inclusion models which were introduced by Lee et al. [69] and Van Dommelen et al. [71]. They represent an intermediate approach between the Voigt and Reuss models.

Both hybrid models designated by $\hat{U}$ and $\hat{\sigma}$, resp., used the following fourth-order subspace projection tensors, obtained according to the orientation of the amorphous/crystalline interface.

$${}^4\mathcal{P}_n^{I^i} = \sum_{j=1}^{3} e_j^{I^i} \otimes n^{I^i} \otimes n^{I^i} \otimes e_j^{I^i} \tag{5.23}$$

$${}^4\mathcal{P}_X^{I^i} = {}^4\mathcal{I} - {}^4\mathcal{P}_n^{I^i} \tag{5.24}$$

where ${}^4\mathcal{I}$ is the fourth-order identity tensor and n^{I^i} is the unit normal of the interface in the current configuration. In the reference configuration the subspace projection tensors will be called ${}^4\mathcal{P}_{n_0}^{I^i}$ and ${}^4\mathcal{P}_{X_0}^{I^i}$ respectively.

The $\hat{U}$-inclusion model is based on a Reuss assumption applied to the ${}^4\mathcal{P}_X^{I^i}$ subspace projection of the mesoscopic Cauchy stress tensor with that of the homogenized inclusion,

$$ {}^4\mathcal{P}_X^{I^i} : \sigma_i^I = {}^4\mathcal{P}_X^{I^i} : \bar{\sigma} \quad | \quad i = 1 \dots N^I \tag{5.25} $$

Moreover, six auxiliary deformation-like unknowns are introduced. Then, the subspace projection ${}^4\mathcal{P}_{n_0}^{I^i}$ of the the mesoscopic stretch of inclusion is assumed equal to the corresponding subspace projection of $\hat{U}$,

$$ {}^4\mathcal{P}_{n_0}^{I^i} : U_i^I = {}^4\mathcal{P}_{n_0}^{I^i} : \hat{U} \quad \text{and} \quad R_i^I = \bar{R} \quad | \quad i = 1 \dots N^I \tag{5.26} $$

Hybrid $\hat{\sigma}$-inclusion model

The $\hat{\sigma}$-inclusion model is based on a Voigt assumption applied to the ${}^4\mathcal{P}_{n_0}^{I^i}$ subspace projection of the mesoscopic corresponding right stretch tensor with that of the homogenized inclusion,

$$ {}^4\mathcal{P}_{n_0}^{I^i} : U_i^I = {}^4\mathcal{P}_{n_0}^{I^i} : \bar{U} \quad \text{and} \quad R_i^I = \bar{R} \quad | \quad i = 1 \dots N^I \tag{5.27} $$

Moreover, an auxiliary unknown symmetric stress tensor $\hat{\sigma}$, is introduced. Then, the subspace projection ${}^4\mathcal{P}_X^{I^i}$ of the mesoscopic Cauchy stress of inclusion is assumed equal to the corresponding subspace projection of $\hat{\sigma}$,

$$ {}^4\mathcal{P}_X^{I^i} : \sigma_i^I = {}^4\mathcal{P}_X^{I^i} : \hat{\sigma} \quad | \quad i = 1 \dots N^I \tag{5.28} $$

7.2.2 Full-field homogenization models

Several full-field homogenization models at mesoscale are available in the literature, some of the most interesting ones are considered hereafter. The model proposed by Van Dommelen et al. [72] consists in conducting a (semi)analytical homogenization of the composite inclusion first. As a result, a homogenized orthotropic inclusion is obtained. Next, full-field FEA simulations are carried out on mesoscale RVEs, taking into account the orientation of a composite inclusion in each element. Two types of RVEs are defined according to the orientation texture. A plane strain RVE (Figure 5.27) is based on an irregular distribution of spherulite centers, each spherulite containing an isotropic orientation distribution of composite inclusions. Periodic boundary conditions are applied to this RVE. An axisymmetric RVE (Figure 5.28) is made of a spherulite of center C_1. Anti-symmetry conditions with respect to point M are applied.

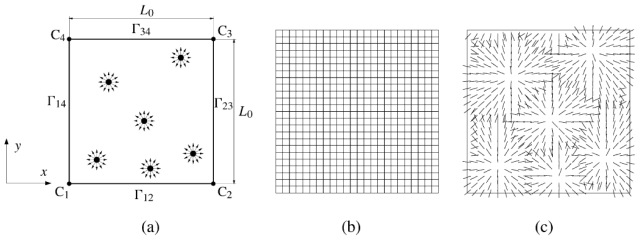

Figure 5.27: Schematic visualization of the plane strain RVE of Van Dommelen et al. [72]. (a) irregular distribution of spherulite centers, (b) finite element mesh and (c) local material orientations.

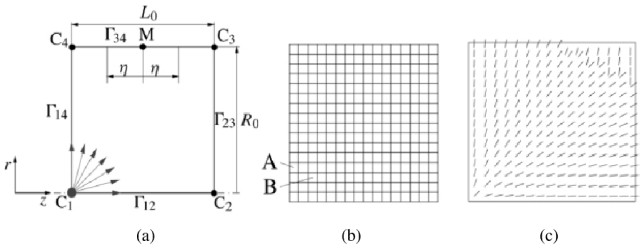

Figure 5.28: Schematic visualization of the axisymmetric RVE of van Dommelen et al. [72]. (a) staggered array of spherulites, (b) finite element mesh and (c) local material orientations .

A second model was proposed by Uchida and Tada [73] and is depicted in Figure 5.29. The macroscale is modeled by FEA, and each macroscopic integration point is seen as the center of a spherulite at mesoscale. The mesoscale problem is also solved by FEA. Each element at mesoscale is seen as a homogenized composite inclusion, whose orientation is obtained by connecting each mesoscale element to the spherulite's center. At micro-scale, each composite inclusion is made of an amorphous layer and a crystalline lamellae, and is homogenized with a (semi)analytical model.

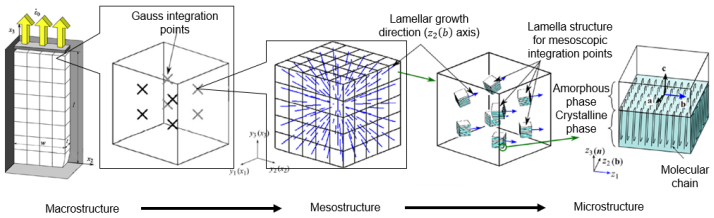

Figure 5.29: Schematic illustration of Uchida and Tada model [73].

A third model was proposed by Oktay and Gurses [74] for thin layer spherulites and is depiced in Figure 5.30. Accordingly, each spherulite is modeled by a volume element which is partitioned into slices. Each slice is considered amorphous or crystalline, each pair of neighboring slices should not have the same type of material, and the problem is solved by FEA.

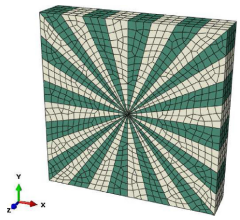

Figure 5.30: Finite element spherulite structure model of Oktay and Gurses [74].

7.3 Comparison between the predictions of various micromechanical models

Figure 5.31 shows the predictions with several micromechanical models of the Young's modulus of the PE material considered earlier. There is the proposed full-field FFT model based on the enhanced phase field model simulations (this is designated by FFT2D in the figure). There is also the full-field irregular plane strain RVE proposed by Van Dommelen et al. [72] and based on the composite inclusion model (designated by 2DINCM). In addition, there are several simple models. These are the models of Reuss, Voigt, and two combinations of them:

- Reuss(Voigt/Reuss): this a Reuss-type mixture rule applied on a mean of Voigt and Reuss compliance estimates,

- Voigt(Voigt/Reuss): a Voigt-type mixture rule applied on a mean of Voigt and Reuss stiffness estimates.

The estimates of the simple models are given by the following equations:

$$E = \left[(1 - X_c)\frac{1}{E^a} + X_c\frac{1}{E^c}\right]^{-1} \quad \{Reuss\} \tag{5.29}$$

$$E = (1 - X_c)E^a + X_c E^c \quad \{Voigt\} \tag{5.30}$$

$$E = 2\left[\begin{array}{c}(1 - X_c)\frac{1}{E^a} + X_c\frac{1}{E^c} \\ +\left[(1 - X_c)E^a + X_c E^c\right]^{-1}\end{array}\right]^{-1} \quad \{Reuss(Voigt/Reuss)\} \tag{5.31}$$

$$E = \left[\begin{array}{c}(1 - X_c)E^a + X_c E^c \\ +\left[(1 - X_c)\frac{1}{E^a} + X_c\frac{1}{E^c}\right]^{-1}\end{array}\right]/2 \quad \{Voigt(Voigt/Reuss)\} \tag{5.32}$$

From the results shown in Fig. 5.31, several remarks can be made. The simple models lead to very inaccurate estimates, except for the Reuss and Reuss-type models at low crystallinity ratios X_c. The proposed approach (labeled FFT2D) gives accurate predictions at all values of X_c. The Van Dommelen et al. model (2DINCM) gives acceptable predictions for X_c between 50% and 80%, approximately, and loses accuracy outside this range, in particular for $X_c > 80\%$. Compared to our FFT2D estimates, those of 2DINCM are higher for $X_c < 70\%$ and lower for $X_c > 70\%$. This shift at $X_c < 70\%$ is due to the fact that in our model, the crystalline branches of the spherulite are totally immersed in the amorphous phase, while in the 2DINCM model the micro-scale is represented by a sandwich inclusion made up of two layers, amorphous and crystalline. In order to reproduce a situation comparable to our proposal, it is necessary for the inclusion to become a crystalline fragment surrounded by an amorphous phase on all sides except in the direction of branch axis. For $X_c > 70\%$ the difference between the FFT2D and 2DINCM estimates is very large. This can be explained by the fact that in the phase field model if X_c becomes large, small bonds between the crystalline branches start to be created, which will increase the stiffness of the micro-structure. As illustrated in Fig. 5.32, the micro-structure representation by the proposed phase field model at high X_c values becomes similar to that of the paracrystallinity model, which according to Van Krevelen [33], represents well the micro-structure at high crystallinity ratios.

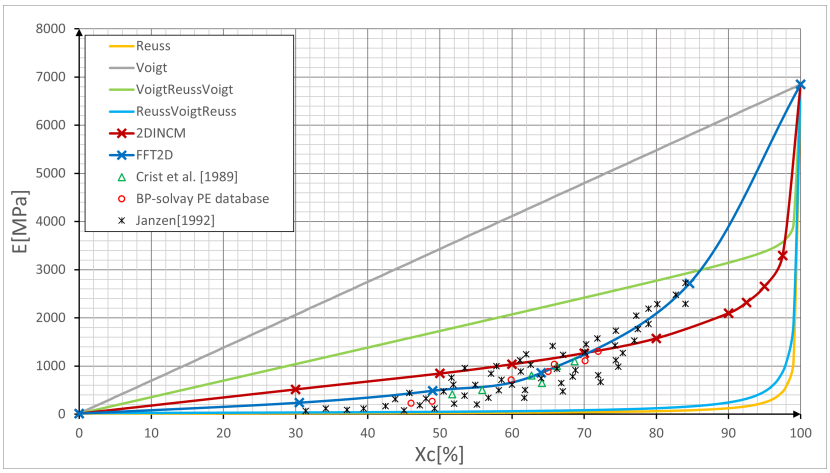

Figure 5.31: Young's modulus of Polyethylene as a function of the crystallinity ratio. Comparison between experimental data, the proposed phase field based FFT model (FFT2D), a composite inclusion based plane strain RVE model (2DINCM) and 4 simple models.

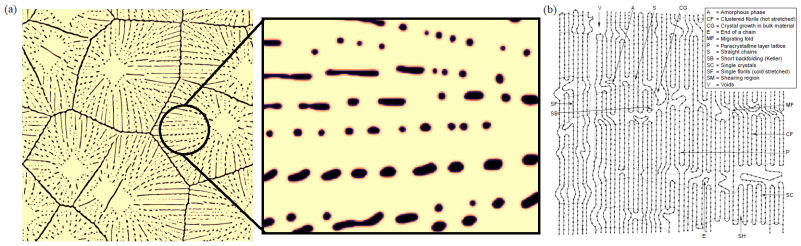

Figure 5.32: (a) Left and middle (zoom) figures: Micro-structure representation at $X_c = 86\%$ with the proposed enhanced phase field model. (b) Schematic representation with the paracrystallinity model (after Hosemann, 1962) [33].

8 | Conclusion

A full-field micromechanical modeling approach for semi-crystalline polymers was proposed. After solidification, the value of the phase field variable in each subcell (2D pixel or 3D voxel) indicates whether the material is amorphous or crystalline. The mechanical simulations are obtained with a Fast Fourier

Transform (FFT) method and periodic boundary conditions. The approach was numerically implemented in a research version of the Digimat software.

The enhanced phase field model was taken to obtain representative volume elements (RVEs). First, the minimum number of subcells in a spherulite is determined, for different values of the crystallinity ratio X_c. Next, the minimum number of spherulites in a RVE is computed. For a given number M_s of spherulites, 10 realizations are created, each corresponding to initially randomly distributed M_s spherulite nucleation sites. After solidification, FFT simulations enable to compute estimates of the elastic moduli and their coefficients of variation (CV) over the 10 realizations. The procedure is repeated with increasing M_s until obtaining low CV values.

Numerical 2D predictions of the Young's modulus of PE compare remarkably well with experimental data for a whole range of X_c values. Similar observations hold for 3D simulations. The model is also able to simulate thermal shrinkage during cooling. The numerical results provide useful information on this phenomenon. The conductivity of the RVE can be obtained when a temperature gradient is applied to it in a thermal simulation.

Several micromechanical models for solid semi-crystalline polymers based on the composite inclusion concept were also reviewed. The Young's modulus predictions were compared against the experimental results on PE. It was found that the simple models (Voigt, Reuss, and two combinations of them) lead to very inaccurate estimates, except for the Reuss and Reuss-type models at low X_c values. The full-field plane strain RVE of Van Dommelen et al. [72] gives acceptable predictions for X_c between 50% and 80%, but loses accuracy outside this range, in particular for $X_c > 80\%$. However, our proposed approach gives accurate predictions at all values of X_c. It appears that the micro-structure predicted by the proposed enhanced phase field model at high X_c values is similar to that of the paracrystallinity model, which is a good representation of the micro-structure at high X_c ([33]).

CHAPTER 6

Prediction of the nonlinear response by Full-field homogenization based on the phase field generated micro-structures

1 | Introduction

Polymers are considered as composite materials, containing two different phases, amorphous and crystalline. At the micro-scale, polymer chains which do not respect any order are considered as amorphous. This random arrangement of chains gives a rubbery behavior. Whereas, polymer chains that are periodically arranged are considered crystalline. The elastic behavior depends on the crystallinity degree and on the initial crystallographic orientation, as well as on the evolution of this micro-structure with monotonic deformation. As the micro-structure of the polymer contains two materials with two very different

behaviors, a homogenization model must be set up. In the literature, there are various models. Starting from the nanometric scale, several works consider an inclusion containing a crystalline layer and another amorphous one to represent the nanostructure of the polymer (Lee et al. [69], Uchida et al. [73], Van Dommelen el al. [71], Nikolov et al. [70], ...). Here the homogenization is done by the stress equilibrium and strain compatibility equations at the amorphous-crystal interface. At the micro-scale, the crystal branches which are produced by a single nucleation point create a sperulite, for this micro-structure there are two possibilities: either to apply mean field (Lee et al. [69], Nikolov et al. [70]) or full field methods (Uchida et al. [73], Van Dommelen el al. [72]).

Full field homogenization is the best way to generate quantitative results. Based on the phase field model, representative polymer micro-structures can be generated. By indicating the mechanical property of each phase, virtual micromechanical simulations can be generated from the finite element method or FFT (Fast Fourier Transform). Generally, the FFT method is the most used because it is the fastest.

The most used model for the crystalline phase is an elasto-viscoplastic model, whose plasticity is activated according to crystalline slip systems. The amorphous phase can be represented by a nonlinear viscoelastic model as in the works of (Dahoun et al. [85], Nikolov et al. [70] ...) or by a elastic viscoplastic model as in the works of (Lee et al. [69], Uchida et al. [73], Van Dommelen el al. [71], ...). The choice of the behavior model depends on the glass transition temperature of the polymer. However, the amorphous phase of polymers with a higher glass transition temperature like nylon, must be modeled as elasto-viscoplastic. There are works that use it regardless of the value of the glass transition. For example, many authors use an elasto viscoplastic model for high density polyethylene HDPE, while its glass transition temperature is equal to $-70\ ^{\circ}C$ (Lee et al. [69], Van Dommelen et al. [71], Nicolov et al. [86]).

The chapter has the following outline. Section 2 contain a description of the crystalline phase properties, while amorphous phase properties are presented in section 3. Results and discussion are presented in section 4. Conclusions are drawn in section 5.

2 | Crystalline phase

To understand the mechanical behavior of the crystalline phase, it is necessary to understand its structure at the nanometric scale. During crystallization, polymer chains reassemble each other like a bundle to form a polymer crystal. Figure 6.1 shows polyethylene lamellar single crystals, which have orthotropic elastic behavior. When the stress exceeds a certain threshold called yield stress, a slip between the chains occurs, this means that the polymer single crystals has plasticized.

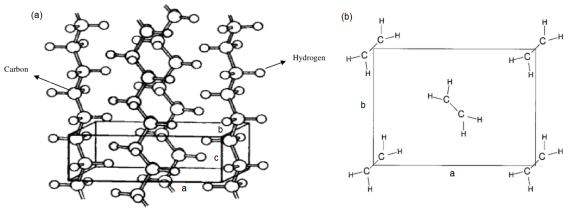

Figure 6.1: (a) Perspective view of the orthorhombic crystal structure of polyethylene [87] (b) projection view.

The most used behavior law of a rate-dependent crystal plasticity is an elastoviscoplastic model. The constitutive model is based on the assumption that the total strain is subdivided into elastic E and viscoplastic VP parts.

$$\varepsilon_c = \varepsilon_c^e + \varepsilon_c^{vp} \tag{6.1}$$

where ε_c is the total strain, ε_c^e is the elastic strain and ε_c^{vp} is the viscoplastic strain or the irreversible one. The Cauchy stress σ_c is related to the elastic strain by Hooke's law.

$$\sigma_c = \mathbf{C}_c : \varepsilon_c^e \tag{6.2}$$

where $\mathbf{C}_c$ is Hooke's operator and σ_c is the Cauchy stress tensor. The irreversible deformation is formulated based on the crystalline plasticity theory which is composed of the contributions of all the N_s distinct slip systems.

$$\dot{\varepsilon}_c^{vp} = \sum_{i=1}^{N_s} \dot{\gamma}_i R^i \tag{6.3}$$

where $\dot{\gamma}_i$ is the shear strain rate and R^i is Schmid's tensor defined as follows:

$$\left\{ \begin{array}{lcl} R^i & = & \frac{1}{2}\left(n^i \bigotimes m^i + m^i \bigotimes n^i\right) \\ tr(R^i) & = & 0 \end{array} \right. \tag{6.4}$$

where n^i is the normal to a slip plane and m^i is the slip direction. The shear strain rate $\dot{\gamma}_i$ is defined by viscoplastic power law relation.

$$\dot{\gamma}_i = \dot{\gamma}_0 sign(\tau_i) \left| \frac{\tau_i}{\tau_i^0} \right|^{1/m} \tag{6.5}$$

where τ_i^0 is the resistance to shear associated with the ith slip system, $\dot{\gamma}_0$ is the reference shear rate, m is the strain rate sensitivity and τ_i is the resolved shear stress associated with the ith slip system.

$$\tau_i = \sigma_c : R^i = (\sigma_c.n^i).m^i \tag{6.6}$$

Crystallographic slip in polymer crystals can occur either by fine slip, which means a small amount of slip has occurred over a large number of planes or by coarse slip meaning larger amounts of slip have occurred on fewer planes.

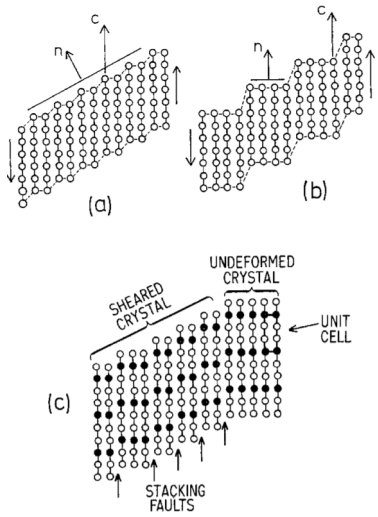

Figure 6.2: Schematic diagrams illustrating different degrees of fineness of slip. (a) Fine slip (b) Coarser slip and (c) Shearing of a lattice that has a large lattice vector in the chain direction by fine slip of partial dislocations [88].

For fine slip, a displacement of a lattice vector has occurred on all other lattice planes in the crystal. The direction n is the normal to the surface of the crystal which has rotated with respect to the chain axis c during the deformation. Whereas for a coarser slip, the same total shear was produced by a displacement of two lattice vectors on every fourth plane. Figure 6.3 shows slip planes and their normal for polyethylene.

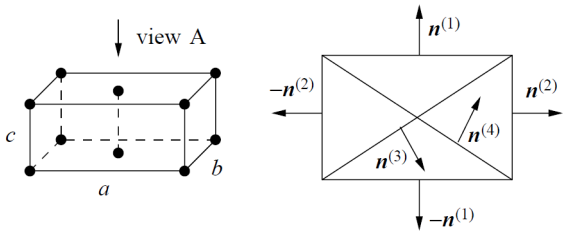

Figure 6.3: Slip systems in crystalline phase: right: view "A" of the slip planes and their normal directions. Left: orthorhombic crystal [70].

2.1 Crystalline parameters

As in chapter 5 we will validate the model by using polyethylene. The elastic stiffness matrix is taken from chapter 5.

$$\begin{bmatrix} 7 & 3.8 & 4.7 & 0 & 0 & 0 \\ 3.8 & 7 & 3.8 & 0 & 0 & 0 \\ 4.7 & 3.8 & 81 & 0 & 0 & 0 \\ 0 & 0 & 0 & 1.6 & 0 & 0 \\ 0 & 0 & 0 & 0 & 1.6 & 0 \\ 0 & 0 & 0 & 0 & 0 & 1.6 \end{bmatrix} [GPa] \tag{6.7}$$

The viscoplastic properties will be calibrated by reverse engineering in section 4. The resistance to shear associated with ith slip system τ_i^0 is given in the table 6.1.

Slip system	$\tau_i^0[MPa]$
(100)[001]	8
(010)[001]	20
{110}[001]	20
(100)[010]	13.3
(010)[100]	20
$\{110\}\langle 1\bar{1}0\rangle$	17.6

Table 6.1: Slip systems and corresponding resistances for HDPE [69].

3 | Amorphous phase

It is well known that all polymers have a response that depends on the strain rate and the temperature. The literature contains many polymer models, such

as Boyce et al. [8], Buckley et al. [9], Wu et al. [10], Govaert et al. [11], Anand et al. [12], Makradi et al. [13], Billon et al. [14], Drozdov et al. [15], etc. Although there are many constitutive models, most of them are either viscoelastic (VE) or elasto-viscoplastic (E-VP). However, the behavior of semi-crystalline polymers usually combines viscoelasticity and viscoplasticity (VE-VP). Since the crystalline phase is E-VP, to have a final VE-VP response, the amorphous phase must be VE or VE-VP. The rubbery behavior of amorphous phase makes plasticity appear only for large strains loading, because there are no cross-links between the molecular chains. By using small deformation loading, a VE law for the amorphous phase is enough. However, the introduction of crystal plasticity at the crystal phase requires the use of large strain hypothesis. The constitutive model is based only on viscoelastic strain ϵ_a^{ve}. A linear VE model, to express the Cauchy stress while taking into account the dependence on the history of the viscoelastic strain, can be written in the following integral form.

$$\sigma(t)_a = \int_{-\infty}^{t} \boldsymbol{E_a}(t-\tau) : \frac{\partial \epsilon_a^{ve}}{\partial \tau} d\tau \tag{6.8}$$

For an isotopic material, we have:

$$\boldsymbol{E_a}(t) = 2G_a(t)\boldsymbol{I}^{dev} + 3K_a(t)\boldsymbol{I}^{vol} \tag{6.9}$$

where $\boldsymbol{I}^{vol} = \frac{1}{3}\mathbf{1} \otimes \mathbf{1}$, $\boldsymbol{I}^{dev} = \boldsymbol{I} - \boldsymbol{I}^{vol}$, $G_a(t)$ is the shear relaxation functions and $K_a(t)$ the bulk relaxation functions. Both are expressed in terms of Prony series.

$$G_a(t) = G_\infty + \sum_{i=1}^{I} G_i \exp\left(-\frac{t}{g_i}\right) \tag{6.10}$$

$$K_a(t) = K_\infty + \sum_{i=1}^{I} K_i \exp\left(-\frac{t}{k_i}\right) \tag{6.11}$$

where G_∞ is the long-term elastic shear modulus, K_∞ is the long-term elastic bulk modulus, g_i are the deviatoric relaxation times, k_i are the volumetric relaxation times, G_i and K_i the corresponding moduli or weights.

Figure 6.4 shows the change in the loss factor ($\tan(\gamma)$) as a function of the temperature at 1 Hz for different crystallinity rates for two different polymer materials. The loss factor is important in the amorphous phase and degrades in the presence of crystallinity, which confirms the choice, elasto-viscoplastic for the crystalline phase and viscoelastic for the amorphous phase.

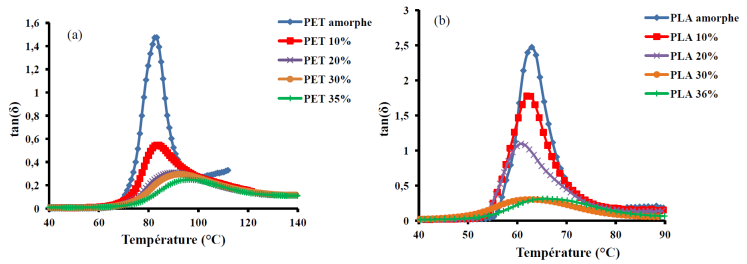

Figure 6.4: The loss factor ($\tan(\gamma)$) curves as a function of the temperature of (a) PET and (b) PLA at 1 Hz for different crystallinity rates [89].

3.1 Amorphous parameters

The calibration of the Prony series is usually done by a DMA test, but when there is a composite material like the polymer containing two phases, it is not possible to assign the global Prony series corresponding to the polymer to the local series corresponding to the amorphous phase. As there is no scientific method to solve this problem, a manual adaptation of the parameters was made in order to obtain an adequate result. The method consists of starting the calibration in the linear regime in order to reduce the number of parameters to be calibrated. In this case the crystalline phase will be represented by an orthotropic elastic tensor and the amorphous phase by a linear viscoelastic law. For simplicity, the Prony series of the amorphous phase contains only two relaxation times.

The calibration is done in two steps, the first is to calibrate the initial Young's modulus using the curve that has the highest strain rate for each crystallinity degree. The initial bulk and shear moduli will be interpreted taking into account that the amorphous phase is incompressible. The second step is to calibrate the parameters of Prony series. The calibration is done with the tensile curves of the lowest crystallinity degree, because the effect of the amorphous phase is dominant. The curves in Figures 6.5 and 6.6 show the results of the VE model after calibration.

The model curves shown in Figure 6.5 are only representative before 1% strain because the plastification start in crystalline phase. We represented this phase by a simple elastic model to reduce the parameters to be calibrated and to focus only on the calibration of amorphous phase, so what interests us in these simulations is the initial slope of the curves.

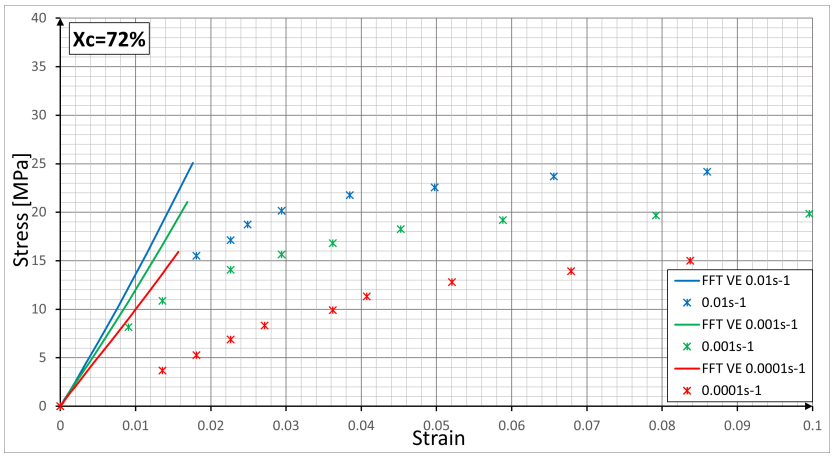

Figure 6.5: Tensile test of PE for $Xc = 72\%$ at different stress rates. VE model compared to experimental data.

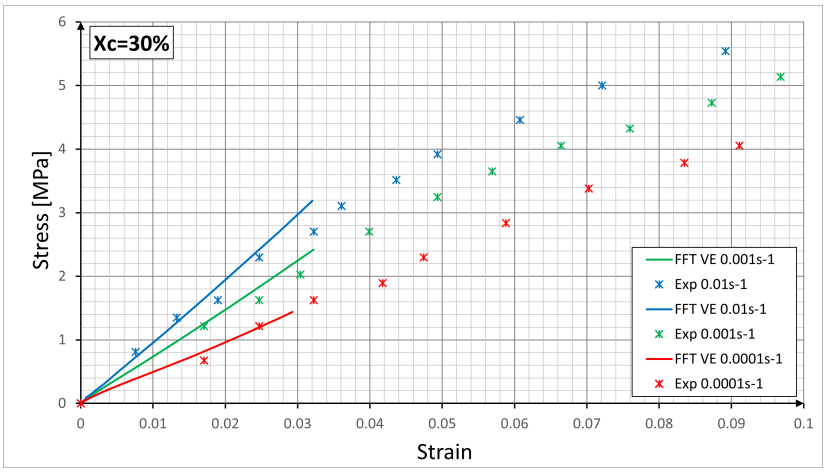

Figure 6.6: Tensile test of PE for $Xc = 30\%$ at different stress rates. VE model compared to experimental data.

In the table 6.2 a comparison is made between the parameters of the Prony series macro of polymer and micro of amorphous phase. The macro parameters are fitted by Digimat MX using the experimental tensile curves. While the parameters of the amorphous phase are obtained manually by preserving the

relaxation times of the maco properties and modifying the weights and initial moduli.

Model parameters	VE parameters of polymer for $X_c = 30\%$	VE parameters of amorphous phase
$G_0[MPa]$	37.33	5.0167
$K_0[MPa]$	80.874	500
G_1/G_0	0.1511	0.3511
$g_1[s]$	1.0233	1.0233
K_1/K_0	0.1511	0.3511
$k_1[s]$	1.0233	1.0233
G_2/G_0	0.35157	0.35157
$g_2[s]$	31.623	31.623
K_2/K_0	0.35157	0.35157
$k_2[s]$	31.623	31.623

Table 6.2: Comparison between the VE parameters of polymer and amorphous phase.

4 | Results and discussion

In chapter 5, linear elastic properties were predicted by FFT full-field homogenization based on the micro-structures predicted by the enhanced phase field model of chapter 4. Here we use the same procedure to simulate nonlinear virtual tests of uniaxial tension of PE. The simulations are made with finite strain context, because crystal plasticity is only valid in large deformations in Digimat. The reference plastic strain rate is calibrated using the experimental curves presenting the greatest degree of crystallization, because at this stage the effect of the crystalline phase is most dominant, ($m = 0.1, \dot{\gamma}_0 = 0.2\ s^{-1}$). After calibration, applying a constant strain rate loading generates the simulations shown in Figures 6.7 and 6.8. The experimental curves of HDPE and LLDPE are brought from work of G. Ayoub et al.[90]. Where HDPE is associated to crystallinity degree $X_c = 72\%$ and LLDPE is associated to crystallinity degree $X_c = 30\%$. The results displayed in the figure show the effect of crystallinity and strain rate on the stress-strain curve. The obtained results are acceptable, with the exception of the small shift presented in the curve of figure 6.7. The main cause of this shift is the difficulty of calibrating the parameters of each phase. For the homogeneous case, there are experimental methods to find the parameters of the model, while for the case of a composite it is difficult to extract the parameters of each phase through the global response.

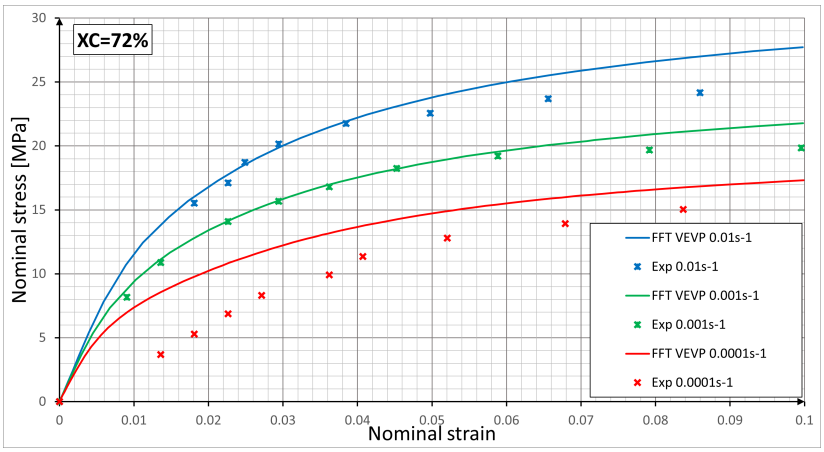

Figure 6.7: Tensile test of PE for $Xc = 72\%$ at different stress rates. VE-VP model compared to experimental data.

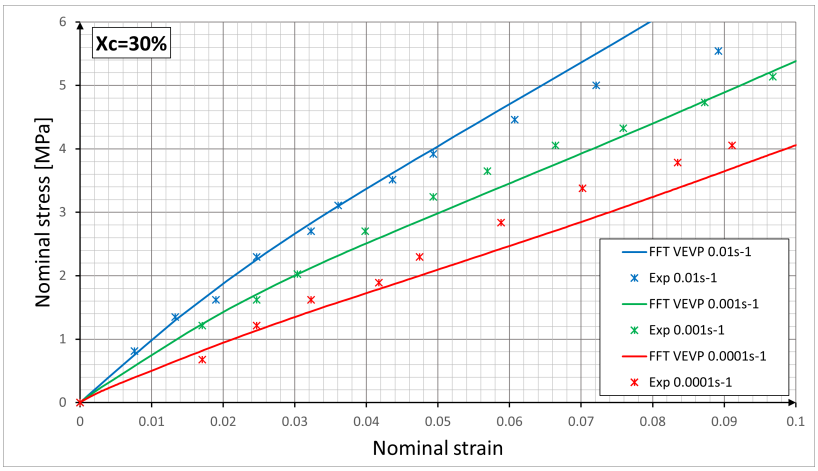

Figure 6.8: Tensile test of PE for $Xc = 30\%$ at different stress rates. VE-VP model compared to experimental data.

5 | Conclusion

The present work is aimed at coupling viscoelastic-viscoplastic modeling using full field homogenization for isotropic polymer RVEs. The polymer is decom-

posed into amorphous and crystalline phases. The total strain of crystalline phase is supposed to be the sum of elastic and viscoplastic parts, whereas the total strain of amorphous phase is supposed to be only viscoelastic. In the linear VE model for the amorphous phase, the stress is related to the history of viscoelastic strains by using Boltzmann's hereditary integral.

The model makes it possible to analyze the effect of the evolution of the crystallinity degree and also of the change in loading speed, for either stress or strain rate. The results obtained are satisfying. However, the methodology to identify the viscoelastic parameters of the model needs to be improved. The model will be more predictive when the temperature dependence is added.

CHAPTER 7

Tentative direct numerical simulation (DNS) of porosity evolution in SLS process with a CFD software

1 | Introduction

Selective laser sintering (SLS) is an additive manufacturing process for fabrication of three-dimensional (3D) parts with complex geometries. In SLS, laser beam energy is employed to sintering powder grains together. The polymer powder will melt by local heating to temperatures slightly above T_m [21]. By adjusting process parameters such as laser intensity and printing speed, the porosity in final part can be controlled.

Powder fusion and matter flow to form a solid structure are a very complex phenomena. In 3D printing, this stage is very important, and it requires

an understanding of the printed material properties, mainly the evolution of shrinkage due to porosity. To understand this phenomenon and calculate the porosity evolution, relying on experimental results would be very costly. The most optimal method is to use numerical modeling. Modeling SLS process for polymer application is not an easy task, because it is a coupled thermo-mechanical problem with phase change from solid to liquid and then from liquid to solid.

There are several efforts in literature to generate realistic simulations of the powder melting process by laser such as Russell et al.[26], He et al.[91] and Tan et al.[92]. Russell et al. provided a model based on the Smooth Particle Hydrodynamics (SPH) method that can accurately resolve thermal, mechanical, and material fields. They validated their model by comparison with a laser spot welding experiment. Their model allowed them to generate simulations with different values of laser intensities. And they found that increasing the laser power led to an increase in the surface roughness of the track. Their model needs several improvements, such as finding a more sophisticated formalism to calculate the effect of surface tension forces, accounting for rigid body motion of unmelted particles, and generating simulations of 3D domains on reasonable time scales. For the same target, He et al. proposed a multi-physics model by using PFC3D software and ANSYS Fluent. They made analyzes of the thermal field in multiple tracks and layers during the process. They are also examined the effects of scanning spacing and laser power on the shape of the remolten region and pore defect. Similarly, Tan et al. provided simulations using OpenFOAM software.

Based on scFLOW of Hexagon M.I, simulations with thermo-mechanical coupling were generated within fluid mechanics framework. The equations which govern the problem are presented with the boundary conditions and the model parameters.

The chapter has the following outline. Section 2 contains a description of the basic equations which are necessary to solve the problem of sintering by CFD method, while the model description is presented in section 3. Results and discussion are presented in section 4. Conclusions are drawn in section 5.

2 | Basic theory

Converting micro-scale material powder into a continuous solid track using a laser source is the basic definition of the SLS process for polymer application. A diagram of a typical process of creating a melt track is shown in Figure 7.1. The laser beam is applied to a section of deposited powder particles, heating them to their melting point and forming a weld pool and which penetrates into the previous layer. The laser is then advanced in an imposed direction. As the

laser source passes, the liquid weld pool cools by thermal conduction in the substrate and convection across the surface, eventually solidifying. Voids can be created if vapor is trapped in the molten bath during solidification.

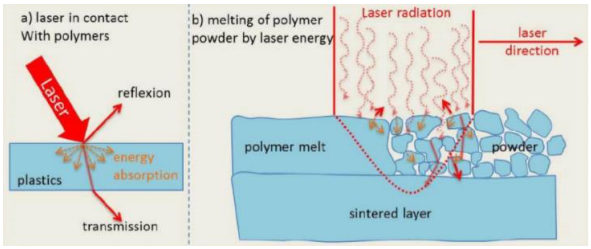

Figure 7.1: Laser sintering processing [93].

To model SLS process, a transient thermo-mechanical coupling which takes into account the change of state, is necessary. In this work we will use Cradle CFD scFLOW developed by Hexagon M.I. Cradle CFD is a series of practical, state-of-the-art CFD simulation and visualization software. It has been in use for diverse applications, such as Automotive, Aerospace, Electronics, Building and Architecture, Civil Engineering, Fans, Machinery, and Marine developments, to solve thermal and fluid problems. scFLOW solution will be used for incompressible fluids. It should be noted that polymers in the liquid state are incompressible. The basic equations used by scFLOW for this study are represented as follows [94].

- Mass conservation equation:

$$\frac{\partial u_i}{\partial x_i} = 0 \tag{7.1}$$

  where x_i are Cartesian coordinates and u_i is the flow velocity in x_i direction.

- Momentum conservation equation or Navier–Stokes equation:

$$\frac{\partial \rho u_i}{\partial t} + \frac{\partial u_j \rho u_i}{\partial x_j} = -\frac{\partial p}{\partial x_i} + \frac{\partial}{\partial x_j}\mu\frac{\partial \rho u_i}{\partial x_j} - \rho g_i \beta (T - T_0) \tag{7.2}$$

  where t is time, ρ is the density, p is the pressure, μ is the viscosity, g_i is the gravity, β is the thermal expansion coefficient, T is the actual temperature and T_0 is the reference temperature.

- Energy conservation equation or heat equation:

$$\frac{\partial \rho C_p T}{\partial t} + \frac{\partial u_j \rho C_p T}{\partial x_j} = \frac{\partial}{\partial x_j} K \frac{\partial T}{\partial x_j} + \dot{q} + \rho L \frac{\partial f_s}{\partial t} \tag{7.3}$$

  where C_p is the specific heat at constant pressure, K is the thermal conductivity, $\dot{q}$ is the heat source, L is the latent heat and f_s is the solid volume fraction.

In scFLOW, the phase change from liquid to solid or from solid to liquid can be calculated by using solidification/melting analysis. The volume of the phase generally varies through the phase change but the volume variation is ignored in the solidification/melting analysis of scFLOW. In solidification/melting analysis, the solid phase in an element is represented as a solid volume fraction (phase field variable) f_s. When the solid volume fraction in an element is 1, the element is filled with solid phase and when the solid volume fraction is 0, the element is filled with a liquid phase. In solidification/melting analysis of scFLOW, the solid regions (for $f_s = 1$) are assumed fixed, i.e. their velocity is zero.

3 | Model description

The model consists of three parts, the domain considered as incompressible air to represent the SLS chamber, a support where the powder is placed and the powder grains Figure 7.2.

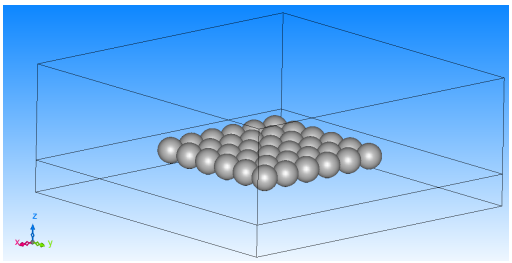

Figure 7.2: Model description, domain is the upper parallelepiped, the support is the parallelepiped at the bottom. The powder grains are shown.

Initially, it should be indicated that the domain is a gas and that the support and the powder grains are solid with volume fraction f_s equal to 1. It is also necessary to indicate the initial temperature of the support and the powder.

Free slip wall stress boundary is applied to the domain surface. A constant temperature is applied to the top of the domain, which represents the printing chamber temperature in the SLS process. The laser beam is represented by the Goldak Model, Figure 7.3. Goldak et al. developed a model representing the heat applied in arc welding processes. By analogy, the Goldak heat source will be applied to the powder. It's written as follows:

$$q = \begin{cases} q_f = \dfrac{2I\eta\alpha f_f}{V_f} \exp\left(-2\begin{pmatrix}(x-x_0)^2/c_f^2 + (y-y_0)^2/a^2 \\ +(z-z_0)^2/b^2\end{pmatrix}\right) & x > 0 \\ q_r = \dfrac{2I\eta\alpha f_r}{V_r} \exp\left(-2\begin{pmatrix}(x-x_0)^2/c_r^2 + (y-y_0)^2/a^2 \\ +(z-z_0)^2/b^2\end{pmatrix}\right) & x \leq 0 \end{cases} \tag{7.4}$$

where I is the laser power, η is the material absorption, α is the laser efficiency, c_f is the forward dimension of heat source, c_r rearward dimension of heat source, a is the width of heat source, f_f is the forward fractional factors of the heat, f_r is the rearward fractional factors of the heat with $f_f + f_r = 2$, V_f is the forward volume, V_r is the rearward volume and x_0, y_0 and z_0 are the initial position (See Figure 7.3).

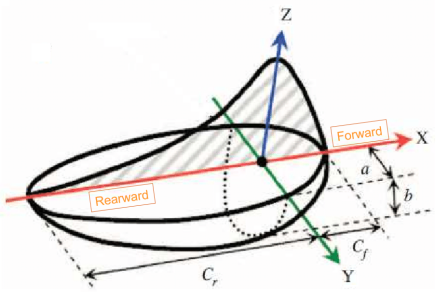

Figure 7.3: Goldak heat source.

Since the polymers have a very high viscosity, the simulations require a big number of time iteration to visualize the flow after melting. In addition, it was noted that when the viscosity increases, the time step must be reduced in order to avoid the divergence of simulations. For these reasons, the material used in the following simulations is aluminum which has a very small viscosity after its melting temperature. The objective will therefore be to test the DNS model and its attributes. The powder properties in its liquid and solid state, as well as the properties of gas within the SLS chamber are given in the table 7.1.

Model parameters			
Parameters	Air(incompressible) for domain	Liquid state for support and powder	Solid state for support and powder
Density $[kg/m^3]$	0.674851917	2369	2770
viscosity$[Pa.s]$	2.80813 10^{-05}	0.0029	–
Specific heat capacity$[J/(kgK)]$	1007	1084	880
Thermal conductivity $[W/(mK)]$	0.045750858	103.4	120
Thermal expansion $[1/K]$	0.001911498	1.82 10^{-05}	–
Surface tension $[N/m]$	0	0.88	–

Table 7.1: Model parameters from Cradle database.

4 | Results and discussion

To specify a motion to the laser beam, the initial coordinates corresponding to the chosen direction much be modified. In this study the initial coordinate x_0 will be modified, it is changed by the following equation.

$$x = x_0 + vt \tag{7.5}$$

where v is the speed of heat source. Figure 7.4 shows different captures of the molten powder flow when the laser beam is advancing. To get a clearer representation, figure 7.5 shows a sectional view in the XY plane. For all the following simulations, the violet color represents the solid phase, the purple color represents the liquid phase, and the multicolored line represents the liquid-solid interface. As soon as the laser is applied, the material undergoes a phase transformation. Unlike the solid phase, the liquid phase flows and fills the voids. Sometimes air bubbles remain trapped in the fluid, after cooling they will transform into porosity. As the intensity of the laser decreases or the speed of the heat source increases the porosity degree becomes very high. This model gives also an important information about the roughness of the printed part surface.

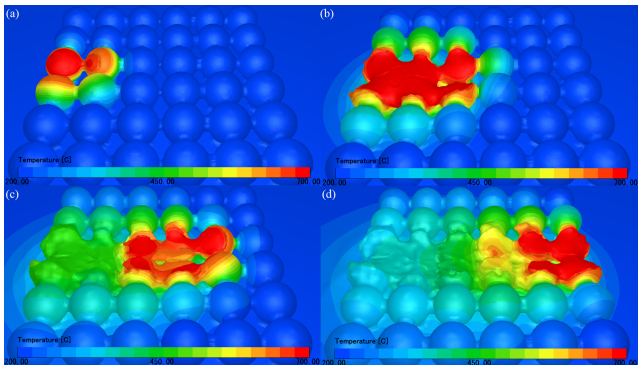

Figure 7.4: Modeling SLS for the first layer.

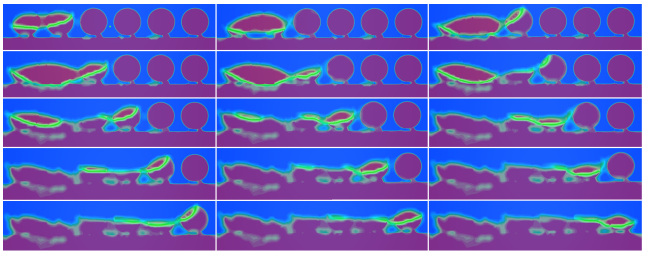

Figure 7.5: 2D cut of the first layer in XY plane.

Adding a second layer is a very important step in computing the porosity degree. A single layer is not enough, it is necessary to print a larger volume to clearly see the porosity distribution. Figures 7.6 and 7.7 show different captures of the molten powder flow as the laser beam advances, in 3D representation and in 2D section view in the XY plane respectively.

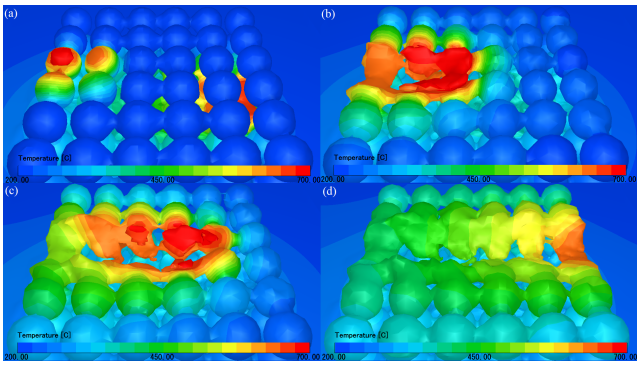

Figure 7.6: Modeling SLS for the second layer.

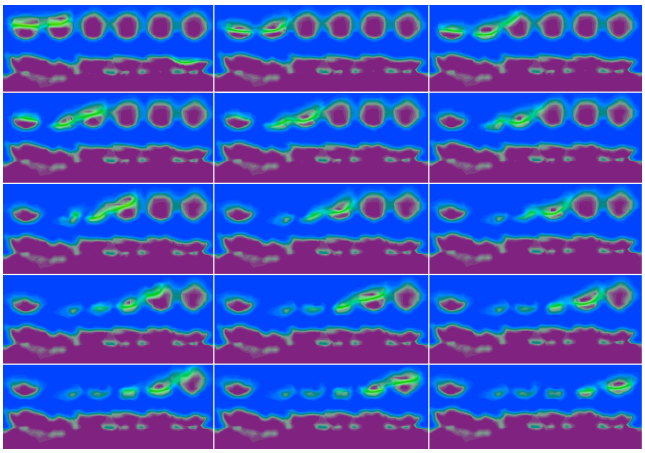

Figure 7.7: 2D cut of the second layer in XY plane.

It is clearly observed in figure 7.7 that there is a big gap between the first melted layer and the second unmelted layer. This gap can be noticed from figure 7.8, which shows that the second layer does not take into account the gravity. Physically, the grains of the second layer must touch those of the first one by gravity. Whereas Cradle prevents the movement of solid regions, that is one of the major problems of these simulations.

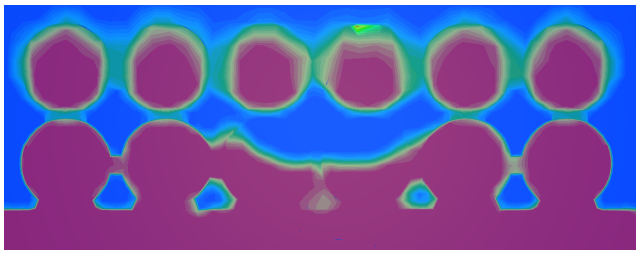

Figure 7.8: 2D cut of the second layer in ZY plane.

When the grains melt, they do not flow to the first layer but are welded with the adjacent unmelted grains (from the same layer) which prevents them from moving, as shown the figure 7.6. This renders the simulation not representative and the obtained results are not physical. There is another drawback that should be mentioned, when the mesh is not fine enough and the distance between two grains very small, strong connections between the grains can be occur, Figure 7.9. To avoid them, it is necessary to increase the distance between the grains, or to further refine the mesh.

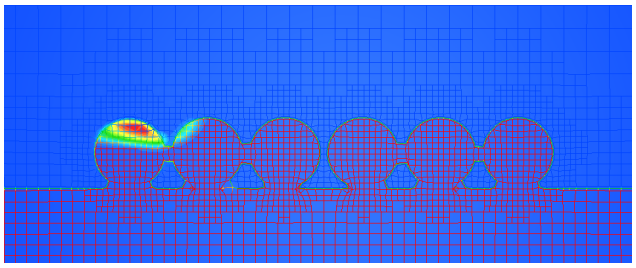

Figure 7.9: Adaptive mesh in 2D cut of the first layer in ZY plane.

Cradle scFLOW employs 'Finite Volume Method' for CFD problem resolution. Each element is a part of flow/thermal field, thus fluid or heat flows in and out between neighbor elements. This flow between the elements is called 'Numerical flow', which is computed based on the governing equations with discretized data on each element. If the numerical flux is determined for each face of all elements, time and spatial variation of data can be found in each element, then, data can be updated along the time and spatial variation. To reduce the calculation time, the elements are made by the use of the octree method which makes adaptive mesh on the part.

There is a lot of challenge to get a physical simulation of SLS process. The model remains functional using polymer properties, but the large required number of time iterations makes the generation of simulations to observe the evolution of molten polymer during SLS process quasi-impossible. However, it is possible to add temperature dependence for each parameter, this can improve the results, especially since the temperature variation interval is very wide.

5 | Conclusion

The Direct Numerical Simulation (DNS) of SLS process for polymer application by CFD is very interesting. DNS makes it possible to predict thermal shrinkage and porosity, it is also possible to predict the final roughness of the printed part. However defects in the model destroy its predictability. Therefore to have a quantitative model, it is necessary to solve the gravity and mesh problems. Moreover, using the polymers properties is a very big challenge because simulation time will be unacceptable. It should be noted that the parameters used in the current model are for testing the model only. In fact, we avoided using the polymers properties because they have a high viscosity, which leads to using a small time step to avoid divergence. In addition, the relaxation time of polymers is very large due to its high viscosity, thus making the simulation time very long.

While it was not possible to making a predictive DNS model, in the next chapter we present a simpler semi-analytical model able to predict porosity evolution due to thermal sintering.

CHAPTER 8

Mesoscale modeling of polymer powder densification due to thermal sintering

1 | Introduction

Making a homogeneous polymeric substance from powder grains exists in several manufacturing processes, such as rotational molding, selective laser sintering (SLS), powder coating and cold compression molding. In the case of SLS, the laser will heat the polymer grains until they exceed the melting temperature. The grains that touch each other will go into a step called creating the neck. The contact radius between the grains will grow over time until closed pores are created. These pores will shrink thanks to the pressure generated by the surface tension until the compressed gas inside the pore stops this evolution when it reaches a critical pressure. In this process, the viscosity and the surface

tension have a very important effect on the evolution time. If the viscosity is low, the densification process evolves rapidly and slows down as it increases. Surface tension has the opposite effect, that is, if it is low, the densification process evolves slowly and accelerates as it increases.

There are direct numerical simulation methods of the sintering phenomenon, by coupling the Navier-Stokes, the mass conservation and the heat equations. In this context, we can cite the works of Russell et al.[26], He et al.[91] and Tan et al.[92] who proposed different numerical methods to generate realistic simulations of the powder melting process by laser. There are other models using molecular dynamics simulations, limited to the sintering of nanoparticles because for the case of big particles the simulation time becomes very large. In this context, we can cite the works of Yang et al.[95], Sestito et al.[96] and Seong et al.[97]. Although these simulations are rich and insightful, this type of modeling remains unusable in practice for a large domain because the computational cost is too high.

In the literature, there are several efforts to simulate the sintering of grains using analytical equations which relate their physical properties to their geometric evolution. Most of these models focus on sintering of a pair of interacting grains. The two grains are represented by two spheres that touch and join until they form a large sphere whose volume is equal to the sum of the initial volumes of the two spheres. The sintering modeling history begins with Frenkel [98] who found a simplified expression for the evolution of the sintering angle θ (see figure 8.4). This expression was found by writing the balance between the work of internal and external forces. This model was corrected by Eshelby [99] and modified by Pokluda et al. [100] to predict the complete coalescence of two spheres. Then, an extension to the case of a non-Newtonian viscoelastic material has been proposed by Bellehumeur et al. [101].

Mackenzie and Shuttleworth [102] proposed a model used for a rapid increase in density during sintering of powder substances. The theory assumes that the pores between the grains are represented by equal size spheres and that evolution is driven by the pressure of surface tension. The model is based on supposing that each spherical pore is coated with the actual Newtonian fluid material and that this hollow sphere is embedded in an infinite medium having the effective properties of the porous material. Mackenzie [103] gave a detailed proof of the model by applying the analogy between linear elasticity and Newtonian viscosity. Mackenzie and Shuttleworth also proposed a generalization of the model to a distribution of pore sizes. Unlike two-grain models, the Mackenzie and Shuttleworth model represents a granular substance, and is thus more adequate for the simulation of sintering of grain sets. In this context, Scherer [104] proposed a model which represents a granular substance and called it the cylinder model. It consists of cylinders in a cubic network which represents the granular structure of the cubic stack. The relative density variation of the sub-

stance is affected by the variation of the cylinder radius. The evolution in this model is also driven by the surface tension pressure applied to the surface of the cylinder. Kontopoulou and Vlachopoulos [105] proposed a model of bubble dissolution in molten polymers, similar to that of Mackenzie and Shuttleworth except that it considers a single porosity in an infinite medium and uses the equation of conservation of momentum to solve this problem. An equation is found which relates the pressure inside the bubble to its rate of dissolution.

It has been shown experimentally that the two-grain models cannot simulate the evolution of the sintering of a set of grains. Indeed, the stacking mode and the number of additional grains have a very important effect on the sintering speed. Asgarpour et al. [106] made a correction to the Bellehumeur et al. model and added an additional parameter which defines the positions of three grains in contact. However, their correction is not based on a physical law but on an empirical calibration. They also discovered experimentally that the effect of non-neighboring grains on the sintering rate is negligible. In sintering modeling, there are ideas for interconnecting existing models. In fact, since the Frenkel or Bellehmeur et al. models are especially created to simulate the beginning of sintering, while the Mackenzie and Shuttleworth or Kontopoulou and Vlachopoulos models represent the final stage of sintering, there are works that consider that there are two stages of sintering, one called the open-pore stage and the other called the closed-pore stage and to solve this problem they linked these two types of models e.g., Wadsworth et al. [107], Asgarpour et al.[108], Kontopoulou and Vlachopoulos [109] and Mokrane et al.[110].

In this work, first we present a rigorous generalization of the Mackenzie and Shuttleworth model to predict the density evolution of a porous substance containing cavities with a size distrbution. Next, we propose a novel development linking the evolution of the sintering angle in the two-grain models of Frenkel and Bellehumeur et al. to the density of a set of multiple interaction grains. The article has the following outline. In section 2, there is a detailed description of our proposed model for the densification of a porous substance with a size distribution of spherical cavities. In section 3.1, there is a description of some existing models of sintering. In section 3.2, we establish a novel relation between the sintering angle θ and the relative density for a set of interacting grains. Model simulations are presented and compared to experimental data and some existing models in section 4. Conclusions are drawn in section 5. Appendices E and F contain further modeling details.

2 | A model for the evolution of closed and spherical pores with a size distribution

The densification of a substance created by powder grains stacked randomly is a difficult problem to solve analytically using fluid mechanics. Some modeling

assumptions render the problem more tractable. Initially, the spaces between the grains have a disordered shape, moreover they are linked to each other (open porosities). However, the system evolves and those spaces will close and become spherical. We consider the second case when the pores are closed spheres and model the resulting representative volume element (RVE) see figure 8.1. It should be noted that the RVE contains viscous fluid, but in our simplified approach, we will solve the problem in elasticity and we will then apply the analogy between linear elasticity and Newtonian fluid.

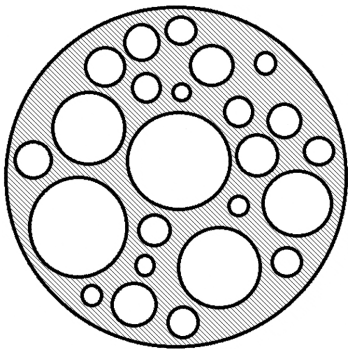

Figure 8.1: Representative volume element (RVE) of the substance when the pores are closed.

We suppose that there is a large number n_p of pores in the RVE, a_i represents the i^{th} pore radius. Inspired by the generalized self-consistent (GSC) model of Christensen and Lo in linear elasticity [111], we suppose that each pore is coated by the actual material until a radius r_i, and that each such hollow sphere is embedded in a large ("infinite") domain of radius $R >> r_i$ whose fictitious material has the RVE's effective porperties, see Figure 8.2. Also, we make the following GSC hypothesis regarding the inner (a_i) and outer (r_i) radii of each hollow sphere:

$$\frac{a_i^3}{r_i^3} = 1 - \rho \quad \forall \quad i \in [1; n_p] \tag{8.1}$$

where ρ is the nominal density of the grain powder in the RVE. The original Mackenzie and Shuttleworth model also adopts the hypothesis of Figure 8.2, but it supposes equal-size pores ($a_i = a$, $\forall i$). Because of isotropy the actual material is characterized by a shear modulus μ_m and a bulk modulus k_m, while the equivalent homogeneous continuum is characterized by μ and k.

Figure 8.2: Model used for the RVE of Figure 8.1.

The hypothesis of slow steady motion will be made, which enables to use the analogy between linear elasticity and Newtonian fluid. In this context, the displacement of substance generated by the pressures applied in the porosity will be replaced by the velocity and its shear modulus will be replaced by the viscosity. Finally, the actual material in the fluid state will be considered as incompressible.

2.1 Linear elastic analogy

Following GSC, the problem to be solved for any cavity $i \in [1; n_p]$ is depicted in Figure 8.2. A pressure P is applied to the outer radius R, while an internal pressure $\mathcal{P}_i$ is applied at the cavity's radius a_i. Using spherical symmetries, the radial displacement field (figure 8.2) can be expressed as follows [112].

$$\begin{cases} u_i(r) = \dfrac{r}{3k}\dfrac{\mathcal{P}_{m|i}r_i^3 - PR^3}{R^3 - r_i^3} + \dfrac{R^3 r_i^3}{4\mu r^2}\dfrac{\mathcal{P}_{m|i} - P}{R^3 - r_i^3} & For \quad r_i \leq r \leq R \\ u_i(r) = \dfrac{r}{3k_m}\dfrac{\mathcal{P}_i a_i^3 - \mathcal{P}_{m|i}r_i^3}{r_i^3 - a_i^3} + \dfrac{a_i^3 r_i^3}{4\mu_m r^2}\dfrac{\mathcal{P}_i - \mathcal{P}_{m|i}}{r_i^3 - a_i^3} & For \quad a_i \leq r \leq r_i \end{cases} \tag{8.2}$$

where $\mathcal{P}_{m|i}$ is the interface pressure at $r = r_i$, which is obtained by the displacement continuity condition at $r = r_i$. After regrouping the pressure terms, the continuity equation becomes as follows:

$$\begin{aligned} &\mathcal{P}_{m|i}\left[\frac{1}{3k_m}\frac{r_i^3}{r_i^3 - a_i^3} + \frac{1}{4\mu_m}\frac{a_i^3}{r_i^3 - a_i^3} + \frac{1}{3k}\frac{r_i^3}{R^3 - r_i^3} + \frac{1}{4\mu}\frac{R^3}{R^3 - r_i^3}\right] \\ &= P\left[\frac{1}{3k} + \frac{1}{4\mu}\right]\frac{R^3}{R^3 - r_i^3} + \mathcal{P}_i\left[\frac{1}{3k_m} + \frac{1}{4\mu_m}\right]\frac{a_i^3}{r_i^3 - a_i^3} \end{aligned} \tag{8.3}$$

Using the GSC modeling assumptions, the continuity equation becomes as follows:

$$\begin{aligned}&\mathcal{P}_{m|i}\left[\frac{1}{3k_m}\frac{1}{\rho}+\frac{1}{4\mu_m}\frac{1-\rho}{\rho}+\frac{1}{4\mu}\right]\\&=P\left[\frac{1}{3k}+\frac{1}{4\mu}\right]+\mathcal{P}_i\left[\frac{1}{3k_m}+\frac{1}{4\mu_m}\right]\frac{1-\rho}{\rho}\end{aligned}\tag{8.4}$$

The GSC model [113] gives estimates of the effective shear (μ) and bulk (k) moduli of the equivalent homogeneous continuum. The estimate of k is given as follows (see also appendix E):

$$k=\frac{4k_m\mu_m\rho}{4\mu_m+3k_m\left(1-\rho\right)}\tag{8.5}$$

However, it will be seen that in the displacement equation (8.15), μ will be eliminated, therefore its expression is not needed.

The displacement at $r=R$ due to each pore is given by eq. (8.2) and rewritten as:

$$u_i(R)=-\frac{RP}{3k}+R\left(\mathcal{P}_{m|i}-P\right)\left[\frac{1}{3k}+\frac{1}{4\mu}\right]\frac{r_i^3}{R^3-r_i^3}\tag{8.6}$$

Assuming that there are n_p pores, the total displacement at $r=R$ due to all cavities in Figure 8.1 is the sum of all local displacements generated by each one, this is called the superposition theorem. It should be noted that the displacement $\left(-\frac{RP}{3k}\right)$ is not considered in the superposition because it is a global one applied to all the pores. Therefore,

$$u(R)=-\frac{RP}{3k}+n_pR\left[\frac{1}{3k}+\frac{1}{4\mu}\right]\left\langle\left(\mathcal{P}_{m|i}-P\right)\frac{r_i^3}{R^3-r_i^3}\right\rangle\tag{8.7}$$

where the notation $\langle-\rangle$ designates the average,

$$\langle-\rangle=\frac{1}{n_p}\sum_{i=1}^{n_p}(-)\tag{8.8}$$

It is possible to relate n_p and R via this relation:

$$\frac{n_p}{R^3}\left\langle r_i^3\right\rangle=1\tag{8.9}$$

Using equation (8.9) and (8.1), a term appearing in eq. (8.7) can be rewritten as follows:

$$n_p \frac{r_i^3}{R^3 - r_i^3} \approx \frac{r_i^3}{\langle r_i^3 \rangle} = \frac{a_i^3}{\langle a_i^3 \rangle} = \alpha_i \tag{8.10}$$

Consequently, equation (8.7) becomes:

$$\begin{aligned} u(R) = &- RP \left(\frac{1}{3k} + \left[\frac{1}{3k} + \frac{1}{4\mu} \right] \langle \alpha_i \rangle \right) \\ &+ R \left[\frac{1}{3k} + \frac{1}{4\mu} \right] \langle \mathcal{P}_{m|i} \alpha_i \rangle \end{aligned} \tag{8.11}$$

Now, let's use the continuity equation (8.4) to replace $\mathcal{P}_{m|i}$ with its expression in terms of P and $\mathcal{P}_i$.

$$\begin{aligned} u(R) = &- RP \left(\frac{1}{3k} + \left[\begin{array}{l} \left[\frac{1}{3k} + \frac{1}{4\mu} \right] \langle \alpha_i \rangle \\ \left(1 - \left[\frac{1}{3k} + \frac{1}{4\mu} \right] \left[\frac{1}{3k_m} \frac{1}{\rho} + \frac{1}{4\mu_m} \frac{1-\rho}{\rho} + \frac{1}{4\mu} \right]^{-1} \right) \end{array} \right] \right) \\ &+ R \left[\begin{array}{l} \left[\frac{1}{3k} + \frac{1}{4\mu} \right] \left[\frac{1}{3k_m} \frac{1}{\rho} + \frac{1}{4\mu_m} \frac{1-\rho}{\rho} + \frac{1}{4\mu} \right]^{-1} \\ \left[\frac{1}{3k_m} + \frac{1}{4\mu_m} \right] \frac{1-\rho}{\rho} \langle \mathcal{P}_i \alpha_i \rangle \end{array} \right] \end{aligned} \tag{8.12}$$

The effective bulk modulus k - eq. (8.5) - gives the following identity:

$$\frac{1}{3k} = \frac{1}{3k_m \rho} + \frac{1}{4\mu_m} \frac{1-\rho}{\rho} \tag{8.13}$$

Thus, equation 8.12 becomes much simpler:

$$u(R) = -RP \left(\frac{1}{3k} \right) + R \left[\frac{1}{3k_m} + \frac{1}{4\mu_m} \right] \frac{1-\rho}{\rho} \langle \mathcal{P}_i \alpha_i \rangle \tag{8.14}$$

It is seen that the effective shear modulus μ is not needed anymore. Using the incompressibility hypothesis ($k_m \to \infty$), equation (8.12) will be written as follows:

$$u(R) = -R\frac{1}{4\mu_m}\frac{1-\rho}{\rho}\left(P - \langle \mathcal{P}_i \alpha_i \rangle\right) \tag{8.15}$$

Finally, consider a solid sphere made of the equivalent homogeneous medium. The sphere is subjected to a pressure P at its surface ($r = R$). The displacement $\mathcal{U}(R)$ at ($r = R$) should be the same as $u(R)$ of eq. (8.15). And since the displacement field in the solid sphere is $\vec{\mathcal{U}}(r) = A\ r\vec{e}_r$, where $\vec{e}_r$ is the radial unit vector in spherical coordinates, then A is equal to the factor which multiples R in equation (8.15).

2.2 Newtonian fluid and density evolution for closed porosity

The analogy between elasticity and Newtonian fluid consists in replacing displacement $\vec{\mathcal{U}}(r)$ by velocity $\vec{v}$ and shear modulus μ_m by viscosity η. Consider the homogeneous equivalent fluid medium. Using the incompressibility of the actual material in the original porous medium, the mass conservation equation can be written as:

$$\frac{1}{\rho}\frac{d\rho}{dt} = -\nabla.\left(\vec{v}(r)\right) \tag{8.16}$$

where $\vec{v}(r)$ is the radial velocity field in the homogenized medium. Following the end of section 2.1, the previous equation becomes:

$$\frac{d\rho}{dt} = \frac{3}{4\eta}\left(1-\rho\right)\left(P - \langle \mathcal{P}_i \alpha_i \rangle\right) = \frac{3}{4\eta}\left(1-\rho\right)\langle (P - \mathcal{P}_i)\alpha_i \rangle \tag{8.17}$$

In equation (8.17) we used the property $\langle \alpha_i \rangle = 1$. The pressure P is used when the process is under pressure or when we want to take into account the compressed gas inside the pores. Physically, if the substance is not subjected to an imposed pressure, it remains subjected to atmospheric pressure. In addition, in reality the pores are not empty and they usually contain air, so we must also add the effect of atmospheric pressure inside them. First, suppose that the gas inside the porosity does not compress during the process. Using the Laplace pressure formula [114], the pressure expression becomes:

$$\begin{aligned} P &= 2\frac{\Gamma}{R} + P_a \approx P_a \\ \mathcal{P}_i &= -2\frac{\Gamma}{a_i} + P_a \end{aligned} \tag{8.18}$$

where Γ is the surface tension, P_a is the atmospheric pressure and $2\frac{\Gamma}{R} << P_a$, because radius R is large. The sign in front of the surface tension pressure

is obtained according to the curvature direction. Putting equation (8.18) in (8.17).

$$\frac{d\rho}{dt} = \frac{3\Gamma}{2\eta}(1-\rho)\left\langle \frac{\alpha_i}{a_i} \right\rangle \tag{8.19}$$

Physically, if the porosity is closed, the gas will be trapped inside and compressed according to the reduction of the porosity radius during the densification process. The expression which defines the evolution of the pressure caused by the change in volume can be calculated by the ideal gas equation,

$$P_c = P_0 \frac{V_0}{V}\frac{T}{T_0} = P_0 \frac{a_{i|0}^3}{a_i^3}\frac{T}{T_0} \tag{8.20}$$

where P_0, V_0 and T_0 are the initial pressure, volume and temperature of gas inside the pores and P_c, V and T are their current values. Assume that the pressure P is equal to the initial pressure of the environment at T_0 which is the atmospheric one ($P = P_0 = P_a$) and that the temperature does not change ($T = T_0$). Therefore,

$$\begin{aligned} \frac{d\rho}{dt} &= \frac{3}{4\eta}(1-\rho)\left\langle \left(P_0 + 2\frac{\Gamma}{a_i} - P_c\right)\alpha_i \right\rangle \\ &= \frac{3}{4\eta}(1-\rho)\left\langle P_a\left(1 - \frac{a_{i|0}^3}{a_i^3}\right)\alpha_i + 2\frac{\Gamma}{a_i}\alpha_i \right\rangle \end{aligned} \tag{8.21}$$

In equations (8.19) or (8.21), the unknowns are ρ and a_i, $i \in [1; n_p]$ so to solve this problem we need additional equations. Let's find a geometric relation that connects these unknowns. The total volume of pores V_p is such that:

$$\frac{V_p}{V_m} = \frac{4\pi}{3V_m}\sum_{i=1}^{n_p} a_i^3 = \frac{1-\rho}{\rho} \tag{8.22}$$

where V_m is the total volume of actual material, $V_m/V = \rho$, $V_p/V = 1-\rho$ and $V = \frac{4}{3}\pi R^3$ is the total volume. Using the incompressibility of the actual material and the GSC assumptions (8.1) and (8.9), the total time derivative of equation (8.22), is written as follows:

$$\frac{d\rho}{dt} = -3\rho(1-\rho)\frac{\langle a_i^2 \dot{a}_i \rangle}{\langle a_i^3 \rangle} \tag{8.23}$$

where $\dot{a}_i = \frac{da_i}{dt}$. Combining equations (8.17) and (8.23), and using the expression of α_i in eq. (8.10), it follows that:

$$\left\langle a_i^2 \dot{a}_i + \frac{a_i^3}{4\eta\rho}(P - \mathcal{P}_i) \right\rangle = 0 \tag{8.24}$$

Equation (8.24) has to be satisfied in average only. However, in order to close the problem, we impose a stronger condition, to be satisfied for each cavity, that the expression between the angle brackets is zero,

$$\dot{a}_i = -\frac{a_i}{4\eta\rho}(P - \mathcal{P}_i) \quad \forall i \in [1; n_p] \tag{8.25}$$

2.3 Link with existing closed porosity models

To deduce the Mackenzie model from the proposed more general model, we must add its additional hypotheses. Firstly, it considers that the external pressure applied to the substance is zero ($P = 0$), secondly, it uses a stack of pores with uniform radius ($a_i = a \quad \forall i \in [1; n_p] \Rightarrow \alpha_i = 1$) and finally it uses the Laplace pressure, or capillary pressure inside the pores,

$$\mathcal{P}_i = -2\frac{\Gamma}{a} \tag{8.26}$$

where Γ is the surface tension. Equation (8.17) becomes:

$$\frac{d\rho}{dt} = \frac{3\Gamma}{2\eta a}(1 - \rho) \tag{8.27}$$

Mackenzie [103] proposed the following expression when there is a distribution of pore sizes,

$$\frac{d\rho}{dt} = \frac{\Gamma}{2\eta}(1 - \rho)\frac{4\pi \int f(a)a^2 da}{\frac{4\pi}{3}\int f(a)a^3 da} \tag{8.28}$$

where $f(a)da$ is the proportion of holes with radii lying in the range $[a, a + da]$. $\int f(a)a^3 da$ is another way of writing the volume average of pores, which verifies the equation $\int f(a)da = 1$. We can justify this assumption using our model. Indeed, with $P = 0$ and $\mathcal{P}_i = -\frac{2\Gamma}{a_i}$, eq. (8.17) becomes:

$$\begin{aligned} \frac{d\rho}{dt} &= \frac{3\Gamma}{2\eta}(1 - \rho)\left\langle \frac{1}{a_i}\alpha_i \right\rangle \\ &= \frac{\Gamma}{2\eta}(1 - \rho)\frac{4\pi \left\langle a_i^2 \right\rangle}{\frac{4\pi}{3}\left\langle a_i^3 \right\rangle} \end{aligned} \tag{8.29}$$

which is equivalent to eq. (8.28).

Taking the case of identical porosity ($a_i = a \ \forall \ i \in [1; n_p]$) and assuming $P = P_{ex}$ and $\mathcal{P}_i = -2\frac{\Gamma}{a_i} + P_{in}$, where P_{ex} represents the pressure outside the substance and P_{in} the gas pressure inside the bubble, the radius evolution following equation (8.25) becomes:

$$\frac{da}{dt} = \frac{1}{4\eta\rho}\left((P_{in} - P_{ex})a - 2\Gamma\right) \tag{8.30}$$

This is similar to the expression found by Kontopoulou and Vlachopoulos [105], except that we have an additional term ρ next to the viscosity η. This represents the effect of neighboring cavities, because we consider an "infinite" porous medium, whereas in the Kontopoulou and Vlachopoulos work [105], they consider a single cavity in a infinite medium.

2.4 Open porosity case

The surface tension pressure $\mathcal{P}$ during the first sintering phase depends on the radius of the grains and the number of grains surrounding a pore. Then the powder particles join together and the pores between them become almost spherical (Figure 8.3). At this moment the surface tension pressure $\mathcal{P}$ becomes dependent on the equivalent pore radius. According to Mackenzie and Shuttleworth [102], if the density increase is rapid during sintering, then it can be assumed that the pressure $\mathcal{P}$ depends on the equivalent pore radius, even in the first sintering phase.

Basically, the sintering process consists of three steps. First the powder particles fuse together and the pores between them become almost spherical (from figure 8.3 (a) to (b)). After that, the pores continue to shrink until they close and become completely spherical (from figure 8.3 (b) to (c)). And finally the pores dissolve in the molten polymer (from figure 8.3 (c) to the equilibrium). Note that not all pores will go into the third sintering step, only some will close. In addition, the pores that will go into the third sintering step do not disappear completely, they shrink until they can no longer shrink when the sum of the pressures inside the pore becomes equal to the outside pressure. The arrows in the cavities shown in Figure 8.3 indicate the direction of surface tension pressure according to the curvature direction.

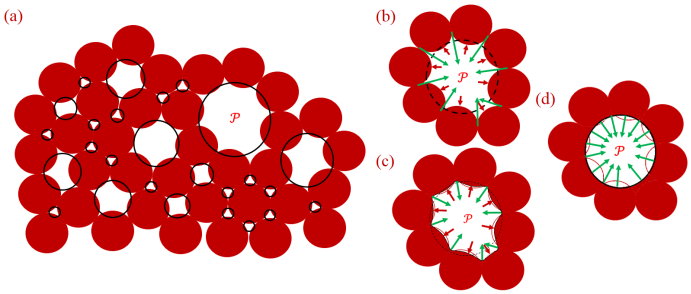

Figure 8.3: Open porosity case, 2D representation. (a) Set of grains before sintering, (b) representation of porosity and pressure in the initial state, (c) representation of pore and pressure in the intermediate state when the porosity becomes quasi-spherical and (d) representation of the pore and the pressure in the final state when the porosity becomes spherical

In reality, the material that covers a fictitious pore is not the actual material because the porosity is open, i.e. there are connections between pores. Considering that the volume fraction of connections between the pores is low compared to that of the fictitious pores, it is possible to assume that the volume fraction of the real pores is equal to that of the fictitious ones. In this case, it is possible to consider the material which covers the fictitious pores as the actual material. To take into account the fact that the pores are actually open, the gas inside the pores is supposed to be incompressible. In this case we use equation (8.19). In the case of closed pores, the compressibility of the gas inside must be considered. In this case we use equation (8.21).

2.5 Initial cavity size distribution

Let's consider that the initial volume V_0 of the substance contains n_p pores with a size distribution. Geometrically we can obtain a relation between pore's initial radius a_i ($i \in [1..n_p]$) and the volume V_0.

$$a_{i|0} = \sqrt[3]{\beta_i \left(1 - \rho_0\right) \frac{3}{4\pi} V_0} \tag{8.31}$$

where ρ_0 is the initial relative density of the sample and β_i is the weight of each radius a_i, with all the weights such that.

$$\sum_{i}^{n_p} \beta_i = 1 \tag{8.32}$$

In the case where the pores are identical, β_i becomes equal to $\frac{1}{n_p}$. Physically β_i has a minimum value, which is calculated from the approximate radius of the hexagonal stack.

$$\beta_{min} = \frac{\frac{4\pi}{3} a_{min}^3}{(1-\rho_0)\, V_0} \tag{8.33}$$

with:

$$a_{min} = \sqrt[3]{\frac{n_{H|g}}{n_{H|p}} \frac{1-\rho_{H|0}}{\rho_{H|0}}} r_g = \sqrt[3]{\frac{3\sqrt{2}-\pi}{2\pi}} r_g \tag{8.34}$$

where $n_{H|g} = 6$ is the number of grains in the elementary hexagonal prism of the hexagon stack, $n_{H|p} = 12$ is the number of pores in the elementary hexagonal prism and r_g is the grain radius. Equation (8.34) was obtained by using eq. (8.22). If the number of grains n_g is known, it is possible to obtain β_{min} as a function of n_g by taking $V_0 = \frac{n_g \frac{4\pi}{3} r_g^3}{\rho_0}$ and using equations (8.33) and (8.34),

$$\beta_{min} = \frac{\rho_0 \left(3\sqrt{2}-\pi\right)}{2\pi \left(1-\rho_0\right) n_g} \tag{8.35}$$

Mathematically, it is possible to determine the maximum value of β_i using equation (8.32). β_i will have a maximum value when there is only one big pore and all the other pores have the smallest radius.

$$\beta_{max} = 1 - (n_p - 1)\, \beta_{min} \tag{8.36}$$

The stacking in the real case can never be compact and orderly, since the relative density of the granular material often does not exceed 50%. Usually there are large cavities in the grain sets which can prove the initial low relative density. The cavity when it exists will slow down the densification process. Therefore, it is very important to consider this geometric effect in modeling. Our model allows to choose a distribution of initial pore sizes. Physically, the cavities size is a random which depends on the stacking mode. Sometimes, in a manufacturing process like SLS, the whole powder will be pressed by a roller to make it more compact, thus reducing the cavity sizes.

3 | Modeling the sintering of powder grains

3.1 Review of existing sintering models

Frenkel's model [98] is the first which gives a simple solution of the two-grain sintering problem (Figure 8.4). It is based on the balance between the work of external forces generated by surface tension and the work of internal forces generated by the stresses. After Eshelby's correction [99], Frenkel's model becomes:

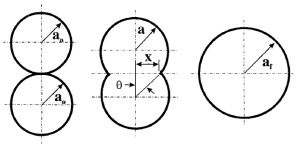

Figure 8.4: Sintering sequence for two spheres [101].

$$\theta = \sqrt{\frac{\Gamma}{\eta a_0} t} \tag{8.37}$$

where θ is the sintering angle (see figure 8.4), Γ is the surface tension, η is the viscosity, a_0 is the initial radius of the sphere before sintering starts and t is time. The Frenkel model is based on the analogy between Newtonian fluid and linear elasticity and is limited to small variations of the angle θ. Years later, Bellehumeur et al. [101] proposed a general model that allows large variations in the sintering angle and they also made an extension to viscoelastic materials,

$$8\left(b\lambda K_1 \frac{\partial\theta}{\partial t}\right)^2 + \left(2b\lambda K_1 + \frac{\eta a_0}{\Gamma}\frac{K_1^2}{K_2}\right)\frac{\partial\theta}{\partial t} - 1 = 0 \tag{8.38}$$

where b corresponds to the upper ($b = -1$), lower ($b = 1$) and corotational ($b = 0$) derivatives in convected Maxwell constitutive equation [115], λ is a material relaxation time and K_1 and K_2 are given by the following expressions.

$$\begin{aligned} K_1 &= \frac{\sin\theta}{(1+\cos\theta)(2-\cos\theta)} \\ K_2 &= \frac{2^{-\frac{5}{3}}\cos\theta\sin\theta}{(1+\cos\theta)^{\frac{4}{3}}(2-\cos\theta)^{\frac{5}{3}}} \end{aligned} \tag{8.39}$$

It is possible to retrieve Frenkel's model from that of Bellehumeur et al. if the relaxation time λ is zero, i.e. a Newtonian fluid and the sintering angle theta is small ($\cos(\theta) \approx 1$ and $\sin(\theta) \approx \theta$).

3.2 A model relating the sintering angle and the relative density

The models of Frenkel and Bellehumeur only provide the sintering angle of a pair of grains as a function of time. To make them useful for calculating the density evolution of a set of powder grains, it is necessary to create a relation between the density and the sintering angle θ. Geometrically it is possible to obtain such a relation, if we assume that the angle θ is the same for all pairs of interacting grains. Let's consider a regular stack of grains, for example the hexagonal stack in figure 8.5. It can be shown that this type of stack can be represented by an elementary hexagonal prism whose volume can be expressed as a function of θ.

$$V = \frac{3\sqrt{3}}{2} l^2 h = 24\sqrt{2}\left(a\cos\left(\theta\right)\right)^3 \tag{8.40}$$

where $l = 2\ a\ \cos\left(\theta\right)$ is the hexagon base length and $h = 2\left(2\sqrt{\frac{2}{3}}\ a\ \cos\left(\theta\right)\right) = 4\sqrt{\frac{2}{3}}\ a\ \cos\left(\theta\right)$ is the height of the prism.

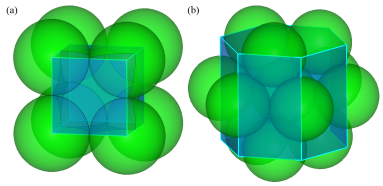

Figure 8.5: (a) Cubic stack and (b) hexagonal stack.

The relative density ρ is the fraction between the real volume of material inside the elementary hexagonal prism V_m and the total volume V.

$$\rho = \frac{V_m}{V} = \frac{\rho_{H|0} V_0}{V} = \rho_{H|0} \frac{a_0^3}{\left(a\cos\left(\theta\right)\right)^3} \tag{8.41}$$

where $\rho_{H|0} \approx 0.74$ is the initial relative density of hexagonal stack and V_0 is the initial total volume of hexagonal prism. Assuming that there is no diffusion between grains and that the material is incompressible, as a consequence the volume of grains is conserved and it remains equal to its initial value. Using this assumption, geometrically, it is possible to derive a relation between a and a_0 (see appendix F).

$$a = a_0 \left(\frac{1}{1 - 3\left(1 - \cos\theta\right)^2 \left(2 + \cos\theta\right)} \right)^{1/3} \tag{8.42}$$

Using this previous relation, the relative density expression (8.41) becomes.

$$\rho = \rho_{H|0} \frac{1 - 3\left(1 - \cos\theta\right)^2 \left(2 + \cos\theta\right)}{\left(\cos\theta\right)^3} \tag{8.43}$$

Using the same methodology to obtain a relation between ρ and θ of the cubic stack of figure 8.5, it is found that:

$$\rho = \rho_{C|0} \frac{1 - \frac{3}{2}\left(1 - \cos\theta\right)^2 \left(2 + \cos\theta\right)}{\left(\cos\theta\right)^3} \tag{8.44}$$

where $\rho_{C|0} \approx 0.52$ is the initial relative density of cubic stack. It is seen that equations (8.43) and (8.44) are similar, but each equation is only used for a specific grain stack. In the general case the set of grains will have an irregular stacking and its initial relative density ρ_0 is different from that of cubic or hexagonal stacks. From these two studied cases, we postulate a general relation between the density and the sintering angle θ,

$$\rho = \rho_0 \frac{1 - \delta\left(1 - \cos\theta\right)^2 \left(2 + \cos\theta\right)}{\left(\cos\theta\right)^3} \tag{8.45}$$

where δ is a correction parameter which varies according to ρ_0 and its expression can be found by using the following procedure.

According to the cases of cubic and hexagonal stacking, the derivative of the relative density with respect to θ is zero when θ is equal to θ_f.

$$\begin{aligned} &\frac{d\rho}{d\theta}|_{\theta=\theta_f} = \rho_0 \frac{3\left(2\delta\cos(\theta_f) - 2\delta + 1\right)\sin(\theta_f)}{(\cos\theta_f)^4} = 0 \\ &\Rightarrow \delta = \frac{1}{2 - 2\cos(\theta_f)} \end{aligned} \tag{8.46}$$

where θ_f is the final sintering angle and is obtained when $\rho = 1$ from equation (8.45). After solving the equation, its expression will be found.

$$\theta_f = \cos^{-1}\left(\frac{\rho_0}{4} + \sqrt{\frac{\rho_0^2}{16} + \frac{\rho_0}{2}} \right) \tag{8.47}$$

Finally, the expression of δ is as follows:

$$\delta = \frac{1}{2 - \frac{\rho_0}{2} - \sqrt{\frac{\rho_0^2}{4} + 2\rho_0}} \tag{8.48}$$

Equation (8.45) can now be coupled with the sintering models of Frenkel and Bellehumeur et al. Since the Frenkel model is based on the assumption that the angle θ is small, then it is possible to use the relation $\cos(\theta) = 1 - \frac{\theta^2}{2}$. Using also equations (8.45) and (8.37), it is then possible to relate the relative density to the physical properties of the material and to time.

$$\rho = \rho_0 \frac{1 - \delta\left(\frac{\Gamma}{2\eta a_0}t\right)^2\left(3 - \frac{\Gamma}{2\eta a_0}t\right)}{\left(1 - \frac{\Gamma}{2\eta a_0}t\right)^3} \tag{8.49}$$

4 | Results and discussion

The validation of the model is carried out using the experimental results of Kontopoulou and Vlachopoulos [109] (See table 8.1). Their experiment consisted in taking a sample of $0.7g$ of polymer and heating it until the desired sintering temperature is reached. At a chosen time, they stop the process by immersing the sample in water and they measure the density with an electronic density meter MD-200s. This method is repeated at different process end times in order to obtain a curve of the density evolution during sintering as a function of time. The initial volume of the sample V_0, before sintering begins, can be calculated from the initial density and mass, assuming that the mass is conserved.

Physical Property	EBA	EVA-1	EVA-2
Average particle diameter $[m]$	4.10^{-4}	4.10^{-4}	4.10^{-4}
Real material density $[kg/m^3]$	924	927	942
Surface tension $[N/m]$	0.03	0.03	0.03
Viscosity $[Pa.s]$	58000 at $T = 105\ ^\circ C$	36000 at $T = 105\ ^\circ C$	16900 at $T = 105\ ^\circ C$
Number of bubbles per mm^3	2.75 ± 0.24	2.62 ± 0.24	3.465 ± 0.116

Table 8.1: Model parameters [109].

Given that the initial relative density of the material to be modeled is approximately 36%, this means that there are large cavities in the material. Since it is not possible to obtain the experimental size distribution, we make a random distribution of the cavity sizes. The values of the weights β_i must respect

the limits given in equations (8.36) and (8.35) respectively. As the distribution is random, sometimes large cavities can be found which may not exist in the actual stack. Moreover, the existence of large cavities slows down the evolution of the density considerably since they take a long time to disappear. To avoid this problem, we will modify the value of β_{max}, in order to get a cavity size interval which is consistent with the actual stacking.

Figures 8.6, 8.7 and 8.8 represent the experimental curves of densification of polyethylene copolymer solution, our model and other existing models. The Frenkel model curves are obtained by our proposed equation (8.49). Bellehumeur model curves are obtained by solving equation (8.38) to get the sintering angle as a function of time, after that we use our proposed equation (8.45) which relates the relative density and the sintering angle.

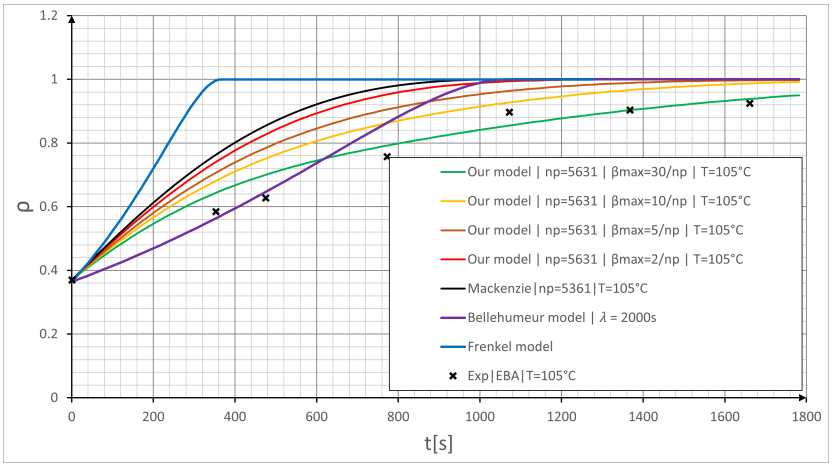

Figure 8.6: Densification model curves of polyethylenes copolymer EBA at $T = 105\ ^{\circ}C$ compared with experimental data [109] and other existing models.

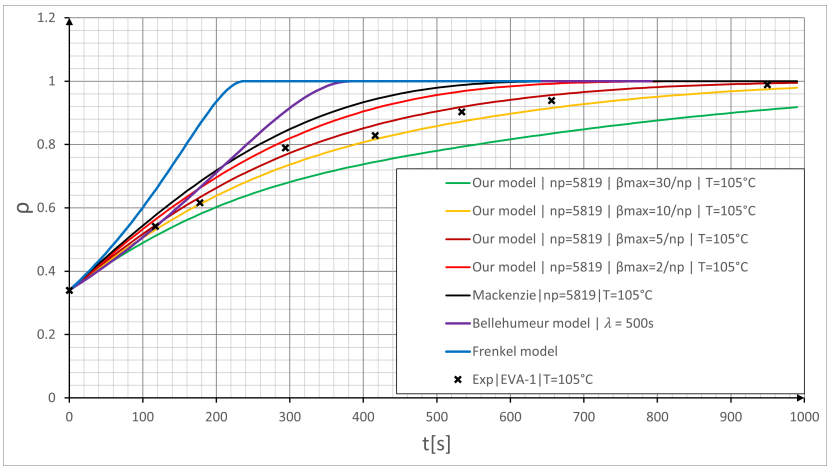

Figure 8.7: Densification model curves of polyethylenes copolymer EVA-1 at $T = 105\ ^{\circ}C$ compared with experimental data [109] and other existing models.

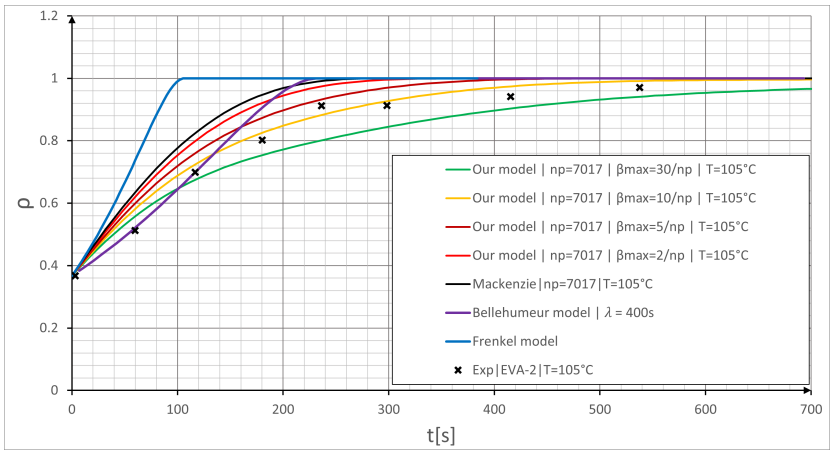

Figure 8.8: Densification model curves of polyethylenes copolymer EVA-2 at $T = 105\ ^{\circ}C$ compared with experimental data [109] and other existing models.

The Frenkel model [98] is based on the assumption that the sintering angle is small, which is not valid at the end of the sintering process, because the angle becomes very large. This can justify the divergence from the experimental

results. In addition, this model does not take into account the effect of the presence of large cavities.

The Bellehumeur model [101] includes viscoelastity in the polymer behavior, this can explain the slowing down of the densification processes in the experimental results. Indeed, according to a specific relaxation time, the material will act with delay in the presence of the surface tension pressure. The results of this model are better than Frenkel's, but compared to the experimental results, the shape of the curve is not the same. In fact, the Bellehumeur model is based on the balance between external and internal works, where the driven external force is obtained by the surface tension pressure applied to the grain, which is calculated based on the grain radius, but as the material becomes dense and the pores become almost spherical, the surface tension pressure becomes dependent on the porosity geometry and not on the grain geometry. This can justify that the Bellehumeur model initially gives good predictions and then it deviates from the experimental results when the relative density exceeds a certain threshold. This also applies to the Frenkel model.

Basically, the powder sintering phenomenon depends on the viscosity, the surface tension and the stacking mode of the grains. Polymers are viscoelastic materials and this behavior persists even after melting, especially when the temperature is not far from the melting point. Therefore, it is necessary to take into account the material relaxation during this process. In our model, we justify the slowness of the densification process in the experimental results by the presence of different pore sizes in the substance. Indeed, in the real representation of the granular material (see figure 8.3) we can justify the presence of large cavities, which have a very important effect in the densification because they can modify the speed of the process. Practically all the parameters of the model are specified from experimental data [109] and the size of the cavities is taken randomly. However, there is no information about the sizes of the cavities and whether there are big cavities. The solution we have adopted is to choose different limit values of weight β_{max} and compare their results with the experimental curves (see Figures 8.6, 8.7 and 8.8). We can see that each time we allow the existence of large cavities, the evolution of density will be slower. The common value of β_{max} which gives adequate results is ten times higher than the nominal value of $\beta_i = \frac{1}{n_p}$ (see Figure 8.9). After having fixed the value of β_{max}, Figure 8.9 shows that the model gives a good prediction of the evolution of the density during sintering except for the EBA where there is a small shift. This shift can be explained by the fact that the EBA copolymer has a high viscosity compared to EVA-1 and EVA-2. When the viscosity becomes very high its effect on the evolution of the density becomes more remarkable. In future work, it is preferable to consider this effect by extending the model to the non-Newtonian case.

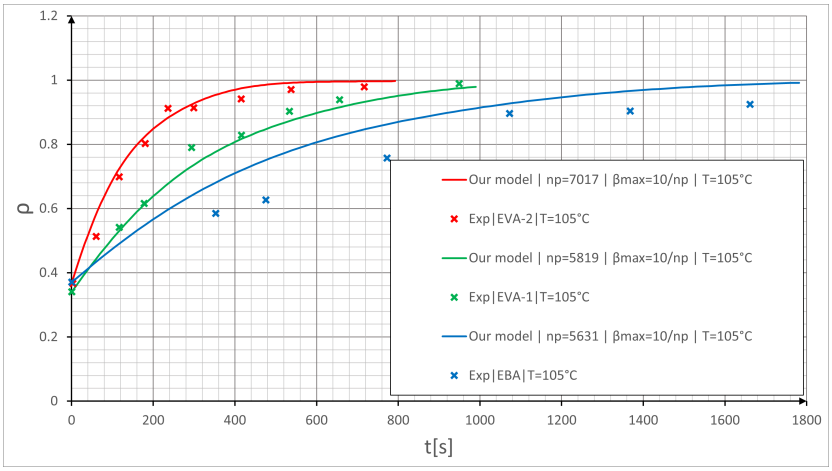

Figure 8.9: Densification model curves of polyethylenes copolymer with taking into account the gas compressibility at $T = 105\ ^{\circ}C$ compared with experimental data [109].

5 | Conclusion

A modeling approach for polymer densification has been proposed. In our first contribution, a generalization of the Mackenzie and Shuttleworth model to predict the density evolution of a porous representative volume element containing multiple spherical cavities of various sizes was developed.

Care was taken to obtain the density evolution based on time and physical parameters. Our proposed approach is based on generalized self-consistent model, the analogy between linear elasticity and Newtonian fluid and the mass conservation equation. The boundary conditions are an external pressure applied to the substance and other internal pressures applied in each pore. Depending on these pressures, two different simulations are generated, for open pores when the gas inside the pores is not compressing and for closed pores case when the gas inside the pores compresses. The closed pores evolution stops when the gas pressure reaches a critical value. The first stage of sintering which consists in creating the neck between powder grains was neglected in the modeling, because it is assumed that the polymer sinter quickly. The modeling is limited to the remaining two stages, namely the open and closed cavity stages.

Sintering models for polymers based on a two-grain concept were reviewed. In our second contribution, we proposed a theory which makes the link between

the sintering angle obtained by these models and the density based on a generalization of regular packing structures such as cubic and hexagonal. When linked with the Frenkel model, the proposal provides a direct relation between the evolution of density, material properties and time.

The proposed modeling approach was implemented in a research version of the Digimat software [3]. The density evolutions were compared against the experimental results on PE copolymers. It was found that the simple (Frenkel) model leads to very inaccurate estimates. Whereas the Bellehumeur model, after taking into account the visco-elasticity of the polymer, gives initially acceptable predictions, but it diverges form experimental data when the material becomes dense. The curves of the Mackenzie model are similar in shape to the experimental one, and the divergence between them can be explained by the fact that the material has a viscoelastic behavior and there are large cavities in the material. However, our proposed approach gives accurate predictions.

In order to improve the predictions, some issues should be addressed in future work, such as including viscoelastic effects and modeling the first sintering stage.

CHAPTER 9

Conclusion

The selective laser sintering (SLS) process is ideal for manufacturing geometrically complicated parts. With the development of printing machine precision and quality control procedures, the process has become a tool for manufacturing mechanical parts and not only for prototyping. Despite progress in the sintering process, the complexity of physical printing phenomena makes it very difficult to obtain a part identical to the designed one. This discrepancy is mainly explained by three types of shrinkage: thermal shrinkage, shrinkage due to crystalline phase evolution and shrinkage due to densification. One solution in order to obtain compatible parts is to fabricate several prototypes and make corrections to the designed geometry until the printed part becomes identical to the desired one. The disadvantage of this method is that it is very expensive. Numerical simulation represents an optimal solution, especially with the progress of processors technology. The simulation time is decreasing drastically.

The challenge of the simulation is to correctly model the physical problem of sintering which is very complex. The change of material state and the evolution of the properties make the task of modeling very hard.

Polymers are semi-crystalline materials because they do not fully crystallize. Their physical properties are between those of the crystalline phase and the amorphous one. Since the crystallinity ratio changes during crystallization, the physical properties also change. Experimentally, crystals can take many forms, depending on the nature of the polymer, the thermal conditions and the material flow. Generally, the polymers have a spherulite form at a temperature away from the melting temperature because the growth is very fast. Under static conditions, crystallization depends only on time and temperature, but under dynamic conditions it also depends on pressure and flow. Considering that in the SLS process, there is no external pressure or flow, we can suppose static conditions.

In the research reported here, several topics have been addressed in order to model the thermo-mechanical behavior of semi-crystalline polymers during and after a SLS process.

Semi-analytical models have been proposed in order to relate the mechanical and thermal properties of a polymer to its degree of crystallization. Experimentally, we can prove for several polymers that the Logarithm of Young's modulus evolves linearly with the crystallinity degree. In the literature, there are several conductivity models. To select one of them, a comparison with experimental data or with a full-field simulation is necessary. For density and specific heat, it is possible to use a simple model such as Voigt. Detailed descriptions of the thermo-viscoelastic-viscoplastic models were presented. It is possible to add the effect of crystallinity via a shift function similarly to the one used for temperature effect. The obtained results are excellent except when the temperature becomes very high and exceeds the temperature at which the polymer has crystallized, because in this case the crystallinity degree increases slightly.

There are many semi-analytical models to model the evolution of the crystallinity degree. They are essentially based on the Kolmogorov model. In a particular case, under isothermal conditions, the general model will be the Avrami model, but in the non-isothermal case and by using the isokinetic condition, the model will be Nakamura's. The crystallization phenomena being very important, the idea was to look for another more sophisticated model and which gives more information. Crystallization can be defined as the solid-liquid interface evolution in time and space. One of the best-known models in the literature is the phase field model that controls the solid-liquid interface using the Allen-Cahn equation of crystal growth and the heat transfer equation.

Since their creation, phase field models only give a qualitative representation and even non-physical results. An enhanced phase field model for the numerical

simulation of polymer crystallization was proposed in order to obtain results consistent with polymer physics. The enhancement technique was performed by coupling the Lauritzen and Hoffman equation for crystal growth with the phase field model via two parameters, τ^* and $\hat{K}$. The enhanced phase field model was able to predict growth quantitatively. Moreover, the spherulites morphology also became close to the experimental results. The proposed model was used to generate RVEs conforming to polymer theory which were then used for mechanical and thermal simulations.

Next, a full-field micromechanical modeling approach for semi-crystalline polymers was proposed. Using the enhanced phase field model, the value of the phase field variable in each sub-cell (2D pixel or 3D voxel) indicates whether the material is amorphous or crystalline. In order to obtain representative volume elements (RVEs), first, the minimum number of subcells in a spherulite is determined. Next, the minimum number of spherulites in an RVE is computed. The mechanical simulations are obtained with a Fast Fourier Transform (FFT) method and periodic boundary conditions. 2D and 3D numerical predictions of Young's modulus of PE are generated and compared with experimental data for a range of crystallinity (X_c) values. Finite element simulations of thermal shrinkage can also be performed. The conductivity of the RVE can be obtained when a temperature gradient is applied to it in a thermal simulation. The material description was later extended to a more realistic viscoelastic-viscoplastic model. The crystalline lamellae follow an orthotropic viscoplastic model based on the activation of slip systems, while the amorphous phase is viscoelastic. Some properties can be identified directly while others are calibrated by a reverse engineering method. The model gives accurate predictions at all values of X_c compared to the experimental results of PE.

A Direct Numerical Simulation (DNS) of SLS process by CFD was carried out. Potentially, heat shrinkage, final printed part roughness and porosity could be predicted and visualized. However, some major shortcomings of the model like the mesh and gravity problems prevented it from being predictive. In addition the model was evaluated using Aluminum properties from Cradle database. It is possible to use the properties of a polymer except that the simulation time will be unbearable. In fact, polymers have a very high viscosity, so to avoid divergence of the numerical simulations, it is necessary to use small time steps. Moreover, simulations require a lot of time because high viscosity slows down the movement of materials. There are many challenges to be overcome for CFD simulation, polymer sintering to become possible and useful.

A polymer densification modeling approach based on a generalization of the Mackenzie and Shuttleworth model has been proposed. The model aims to predict the evolution of the density of a porous medium containing several spherical cavities of different sizes. The theory is based on generalized self-

consistent model, the analogy between linear elasticity and Newtonian fluid and the mass conservation equation. The modeling was developed for cavities covered by the actual material and was extended for the case of open cavities by modifying the expression of the pressure boundary conditions. The first step of sintering which is the creation of the neck between the grains has been neglected in the modeling, because it is assumed that the polymer sinters quickly. In this field we made another contribution, which is the link between the sintering angle obtained by Frenkel and Bellehumeur two-grain models and the density evolution. We can interpret a direct relation between the density evolution, material properties and time by coupling with the Frenkel model. Compared to the experimental results of PE copolymers, our proposed approach gives accurate predictions.

In summary, the most original contributions of the thesis are the following:

- Added crystallinity effect to a thermo-viscoelastic-viscoplastic model via a shift function.

- Developed an enhanced phase field model to predict polymer crystallization consistent with polymer physics.

- Performed 2D and 3D simulations to compute the mechanical and thermal properties of RVEs generated by the enhanced phase field model.

- Developed a model which relates powder densification due to sintering to material properties and time by predicting the density evolution of a porous medium containing multiple spherical cavities of various sizes.

The contributions made during the thesis can help to stimulate the warpage between designed and printed parts. Indeed, in the SLS process, the powders will undergo three types of shrinkage which will then generate residual stresses in the part: thermal shrinkage, shrinkage due to crystallization and shrinkage due to powder densification. The thermal shrinkage can be calculated by the value of the coefficients of thermal expansion (CTE) of each phase or by knowing the evolution of the density according to the temperature of each phase. Shrinkage due to crystallization can be calculated by simulation with the phase field model. Shrinkage due to powder densification can be calculated using the densification model.

During SLS simulations, it is not possible to generate phase field simulations to know the homogenized properties of each finite element or pixel/voxel of an actual part. In this context, we propose a simplified relation to take into account the effect of crystallinity on polymer properties. The phase field model can be used to calibrate the parameters of these models. For instance, the phase field model was used to compute thermal conductivity and also the elastic Poisson's ratio, the conductivity model was chosen using the phase field model, also for the expression of the Poisson's ratio for an elastic model. The densification model has a very important role in SLS simulations, because it is not only used to calculate the evolution of density and shrinkage, but it can be used for other things, like calibration of process parameters. If we display for each finite element or pixel/voxel their relative density, we can detect printing defects on the part, such as the lack of adhesion between the layers.

In future work, the research presented here can be improved along several directions, which are outlined hereafter.

The crystalline phase being orthotropic, to make mechanical simulations it is necessary to introduce the orientation in each element. In our model we use an algorithm in which we define the orientation of each element from its position and the sperulite center to which it belongs. This method is limited to the case of spherical spherulites only, for any anisotropy or a specific form of spherulite this method does not work. To solve this problem it is necessary to couple the orientation variable with the phase field model.

The phase field model enables to simulate only the growth of the spherulites. In order to model crystallization phenomena more completely it must be coupled with a nucleation model.

The improved phase field model does not generate spherulites with a crystallinity degree below 50%. Predictability only remains valid for degrees above 50%. For low degrees, the erosion method was used to generate RVEs. Improvements are required on this side to have a predictive model even with low degrees of crystallinity.

The method for calibrating the parameters of each phase should be improved, especially for the amorphous phase, since its parameters are not fully available in the literature.

The RVEs obtained by enhanced phase field model gave adequate results compared to the PE tensile tests, but it's still recommended to validate the predictions with another type of polymer.

The densification model was obtained rigorously from fundamental equations. Molten polymers being viscoelastic materials, an extension of the model to non-Newtonian fluids is recommended.

For certain cases where the viscosity is very high, the initial sintering step will no longer be negligible. So coupling our powder densification model with the sintering model of Bellehumeur et al. should be explored.

Bibliography

[1] A. Bahloul, I. Doghri, L. Adam, An enhanced phase field model for the numerical simulation of polymer crystallization, polymer crystallization 3 (2020) e10144. doi:https://doi.org/10.1002/pcr2.10144.

[2] A. Bahloul, I. Doghri, L. Adam, Linking a phase field model for polymer crystallization to full-field micromechanical simulations of semi-crystalline polymers, Computational Materials Science 199 (2021) 110685. doi:https://doi.org/10.1016/j.commatsci.2021.110685.

[3] Digimat, the nonlinear multiscale material and process modeling platform, version 2019.1, October 2019, e-Xstream engineering part of Hexagon Manufacturing Intelligence.

[4] L. Adam, O. Lietaer, S. Mathieu, I. Doghri, Numerical simulation of additive manufacturing of polymers and polymer-based composites, in: K. Friedrich, R. Walter, C. Soutis, S. G. Advani, I. H. B. Fiedler (Eds.), Structure and Properties of Additive Manufactured Polymer Components, Woodhead Publishing Series in Composites Science and Engineering, Woodhead Publishing, 2020, pp. 115–146. doi:https://doi.org/10.1016/B978-0-12-819535-2.00005-3.

[5] A. Kolmogorov, Statistics crystallization processes in metals, Izvestia Akademii Nauk SSSR 1 (1937) 355–359. doi:https://www.bibsonomy.org/bibtex/224fd6d8e53caf97b0510736ae99e5e63/peter.ralph.

[6] M. Avrami, Kinetics of phase change. i general theory, The Journal of Chemical Physics 7 (1939) 1103. doi:https://doi.org/10.1063/1.1750380.

[7] K. Nakamura, T. Watanabe, K. Katayama, T. Amano, Some aspects of nonisothermal crystallization of polymers. i. relationship between crystallization temperature, crystallinity, and cooling conditions, Journal of Applied Polymer Science 16 (1972) 1077–1091. doi:https://doi.org/10.1002/app.1972.070160503.

[8] M. C. Boyce, D. M. Parks, A. S. Argon, Large inelastic deformation of glassy polymers. part i: rate dependent constitutive model, Mechanics of Materials 7 (1) (1988) 15–33. doi:https://doi.org/10.1016/0167-6636(88)90003-8.

[9] C. Buckley, D. Jones, Glass-rubber constitutive model for amorphous polymers near the glass transition, Polymer 36 (17) (1995) 3301–3312. doi:https://doi.org/10.1016/0032-3861(95)99429-X.

[10] P. Wu, E. Van Der Giessen, On improved network models for rubber elasticity and their applications to orientation hardening in glassy polymers, Journal of the Mechanics and Physics of Solids 41 (3) (1993) 427–456. doi:https://doi.org/10.1016/0022-5096(93)90043-F.

[11] L. E. Govaert, P. Timmermans, W. Brekelmans, The Influence of Intrinsic Strain Softening on Strain Localization in Polycarbonate: Modeling and Experimental Validation , Journal of Engineering Materials and Technology 122 (2) (1999) 177–185. doi:https://doi.org/10.1115/1.482784.

[12] L. Anand, M. E. Gurtin, A theory of amorphous solids undergoing large deformations, with application to polymeric glasses, International Journal of Solids and Structures 40 (6) (2003) 1465–1487. doi:https://doi.org/10.1016/S0020-7683(02)00651-0.

[13] A. Makradi, S. Ahzi, R. Gregory, D. Edie, A two-phase self-consistent model for the deformation and phase transformation behavior of polymers above the glass transition temperature: application to pet, International Journal of Plasticity 21 (4) (2005) 741–758. doi:https://doi.org/10.1016/j.ijplas.2004.04.012.

[14] N. Billon, New constitutive modeling for time-dependent mechanical behavior of polymers close to glass transition: Fundamentals and experimental validation, Journal of Applied Polymer Science 125 (2012) 4390–4401.

[15] A. Drozdov, J. Christiansen, Cyclic viscoplasticity of high-density polyethylene: Experiments and modeling, Computational Materials Science 39 (2) (2007) 465–480. doi:https://doi.org/10.1016/j.commatsci.2006.07.014.

[16] B. Miled, I. Doghri, L. Delannay, Coupled viscoelastic–viscoplastic modeling of homogeneous and isotropic polymers: Numerical algorithm and analytical solutions, Computer Methods in Applied Mechanics and Engineering 200 (2011) 3381–3394. doi:https://doi.org/10.1016/j.cma.2011.08.015.

[17] A. Krairi, I. Doghri, J. Schalnat, G. Robert, W. V. Paepegem, Thermo-mechanical coupling of a viscoelastic-viscoplastic model for thermoplastic polymers: Thermodynamical derivation and experimental assessment, International Journal of Plasticity 115 (2019) 154–177. doi:https://doi.org/10.1016/j.ijplas.2018.11.016.

[18] J. Cahn, S. Allen, A microscopic theory for domain wall motion and its experimental verification in fe-al alloy domain growth kinetics, In Journal of Physics Colloquium C7 38 (1977) C7–51. doi:https://hal.archives-ouvertes.fr/jpa-00217210.

[19] S. C. Ligon, R. Liska, J. Stampfl, M. Gurr, R. Mülhaupt, Polymers for 3d printing and customized additive manufacturing, Chemical Reviews 117 (15) (2017) 10212–10290. doi:10.1021/acs.chemrev.7b00074.

[20] S. Dadbakhsh, L. Verbelen, O. Verkinderen, D. Strobbe, P. Van Puyvelde, J.-P. Kruth, Effect of pa12 powder reuse on coalescence behaviour and microstructure of sls parts, European Polymer Journal 92 (2017) 250–262. doi:https://doi.org/10.1016/j.eurpolymj.2017.05.014.

[21] M. Schmid, A. Amado, K. Wegener, Materials perspective of polymers for additive manufacturing with selective laser sintering, Journal of Materials Research 29 (2014) 1824–1832. doi:https://doi.org/10.1557/jmr.2014.138.

[22] R. G. Kleijnen, M. Schmid, W. Konrad, Production and processing of a spherical polybutylene terephthalate powder for laser sintering, Applied Sciences 9 (7) (2019). doi:https://doi.org/10.3390/app9071308.

[23] M. Krantz, H. Zhang, J. Zhu, Characterization of powder flow: Static and dynamic testing, Powder Technology 194 (3) (2009) 239–245. doi:https://doi.org/10.1016/j.powtec.2009.05.001.

[24] G. Lumay, F. Boschini, K. Traina, S. Bontempi, J.-C. Remy, R. Cloots, N. Vandewalle, Measuring the flowing properties of powders and grains, Powder Technology 224 (2012) 19–27. doi:https://doi.org/10.1016/j.powtec.2012.02.015.

[25] R. Freeman, Measuring the flow properties of consolidated, conditioned and aerated powders — a comparative study using a powder rheometer and a rotational shear cell, Powder Technology 174 (1) (2007) 25–33, special Edition from the PSA2005 Conference. doi:https://doi.org/10.1016/j.powtec.2006.10.016.

[26] M. Russell, A. Souto-Iglesias, T. Zohdi, Numerical simulation of laser fusion additive manufacturing processes using the sph method, Computer

Methods in Applied Mechanics and Engineering 341 (2018) 163–187. doi:https://doi.org/10.1016/j.cma.2018.06.033.

[27] P. Tan, F. Shen, B. Li, K. Zhou, A thermo-metallurgical-mechanical model for selective laser melting of ti6al4v, Materials & Design 168 (2019) 107642. doi:https://doi.org/10.1016/j.matdes.2019.107642.

[28] T. Zohdi, Modeling and simulation of laser processing of particulate-functionalized materials, Archives of Computational Methods in Engineering 24 (2017) 89–113. doi:https://doi.org/10.1007/s11831-015-9160-1.

[29] I. Kovaleva, S. Grigoriev, A. Gusarov, Non-disturbing boundary conditions for modeling of laser material processing, Physics Procedia 56 (2014) 421–428, 8th International Conference on Laser Assisted Net Shape Engineering LANE 2014. doi:https://doi.org/10.1016/j.phpro.2014.08.145.

[30] L. Dong, A. Makradi, S. Ahzi, Y. Remond, Three-dimensional transient finite element analysis of the selective laser sintering process, Journal of Materials Processing Technology 209 (2) (2009) 700–706. doi:https://doi.org/10.1016/j.jmatprotec.2008.02.040.

[31] K. Zeng, D. Pal, B. Stucker, A review of thermal analysis methods in laser sintering and selective laser melting, in: 2012 International Solid Freeform Fabrication Symposium, University of Texas at Austin, 2012. doi:http://dx.doi.org/10.26153/tsw/15390.

[32] M. Zinet, Modélisation de la cristallisation des polymères dans les procédés de plasturgie : quantification des effets thermiques et rhéologiques., Ph.D. thesis, Lyon, France (2010).

[33] D. V. Krevelen, K. T. Nijenhuis, Properties of Polymers: Their Correlation with Chemical Structure; their Numerical Estimation and Prediction from Additive Group Contributions, Elsevier Science, 2009. doi:ISBN:978-0-08-054819-7.

[34] B. Crist, Chapter 3: Structure of Polycrystalline Aggregates, Handbook of Polymer Crystallization, 2013. doi:https://doi.org/10.1002/9781118541838.ch3.

[35] L. Gránásy, T. Pusztai, T. Borzsonyi, Phase field theory of nucleation and polycrystalline pattern formation, Edited by Michael Rieth and Wolfram Schommers (American Scientific Publishers, Stevenson Ranch, CAL) 9 (2006) 525–572. doi:https://arxiv.org/abs/cond-mat/0703676.

[36] E. L. Freire, Effets de vitesse et de transcristallinité dans l'analyse de la cristallisation de polyamides 66 d'architectures différentes., Ph.D. thesis, Paris, France (2016).

[37] M. Muthukumar, Nucleation in Polymer Crystallization, Advances in Chemical Physics„ 2004. doi:https://doi.org/10.1002/0471484237.ch1.

[38] J. D. Hoffman, J. I. Lauritzen, Crystallization of bulk polymers with chain folding: Theory of growth of lamellar spherulites, Journal of Research of the National Bureau of Standards-A. Physics and Chemistry 65A (1961) 297–336. doi:http://dx.doi.org/10.6028/jres.065A.035.

[39] J. D. Hoffman, L. J. Frolen, G. S. Ross, J. I. Lauritzen, On the growth rate of spherulites and axialites from the melt in polyethylene fractions: Regime i and regime ii crystallization, Journal of Research of the National Bureau of Standards-A. Physics and Chemistry 79A (1972). doi:https://doi.org/10.6028/jres.079a.026.

[40] T. Ozawa, Kinetics of non-isothermal crystallization, Polymer 12 (1971) 150–158. doi:https://doi.org/10.1016/0032-3861(71)90041-3.

[41] A. Jeziorny, Parameters characterizing the kinetics of the non-isothermal crystallization of poly(ethylene terephthalate) determined by d.s.c., Polymer 19 (1978) 1142–1144. doi:https://doi.org/10.1016/0032-3861(78)90060-5.

[42] F. Amado, M. Schmid, L. G., K. Wegener, Characterization and modeling of non-isothermal crystallization of polyamide 12 and co-polypropylene during the sls process, in: 5th International Polymers & Moulds Innovations Conference, 2012, pp. 207–216.

[43] J. C. Maxwell, A treatise on electricity and magnetism, Vol. 1, Clarendon press, 1873.

[44] H. Russell, Principles of heat flow in porous insulators, Journal of American Ceramic Society 18 (1935) 1–5. doi:https://doi.org/10.1111/j.1151-2916.1935.tb19340.x.

[45] F. Bédoui, J. Diani, G. Régnier, W. Seiler, Micromechanical modeling of isotropic elastic behavior of semicrystalline polymers, Acta Materialia 54 (2006) 1513 – 1523. doi:https://doi.org/10.1016/j.actamat.2005.11.028.

[46] J. Janzen, Elastic moduli of semicrystalline polyethylenes compared with theoretical micromechanical models for composites, Polymer Engineering

& Science 32 (1992) 1242–1254. doi:https://doi.org/10.1002/pen.760321710.

[47] C. Buckley, F. Christopher, H. Paul, Mechanical properties of model polyethylenes: tensile elastic modulus and yield stress, Macromolecules 22 (1989) 1709–1718. doi:https://doi.org/10.1021/ma00194a035.

[48] A. Menyhárd, P. Suba, Z. László, H. M. Fekete, A. Mester, Z. Horváth, G. Vörös, J. Varga, J. Móczó, Direct correlation between modulus and the crystalline structure in isotactic polypropylene, eXPRESS Polymer Letters 9 (2015) 308–320. doi:http://dx.doi.org/10.3144/expresspolymlett.2015.28.

[49] I. Doghri, Mechanics of deformable solids: linear, nonlinear, analytical and computational aspects, Springer Science & Business Media, 2013.

[50] C. Zhang, I. D. Moore, Nonlinear mechanical response of high density polyethylene. part ii: Uniaxial constitutive modeling, Polymer engineering and science 37 (1997) 414–420. doi:https://doi.org/10.1002/pen.11684.

[51] R. Schapery, On the characterization of nonlinear viscoelastic materials, Polymer engineering and science 9 (1969) 295–310. doi:https://doi.org/10.1002/pen.760090410.

[52] J. Li, Z. Zhu, T. Li, X. Peng, S. Jiang, L.-S. Turng, Quantification of the young's modulus for polypropylene: Influence of initial crystallinity and service temperature, Journal of Applied Polymer Science 137 (2019) 48581. doi:https://doi.org/10.1002/app.48581.

[53] H. Meijer, L. Govaert, Mechanical performance of polymer systems: The relation between structure and properties, Elsevier 30 (2005) 915–938. doi:https://doi.org/10.1016/j.progpolymsci.2005.06.009.

[54] M. C. Boyce, D. M. Parks, A. S. Argon, Large inelastic deformation of glassy polymers, Mechanics of Materials 7 7 (1988) 15–33. doi:https://doi.org/10.1016/0167-6636(88)90003-8.

[55] K. Taguchi, H. Miyaji, K. Izumi, A. Hoshino, Y. Miyamoto, R. Kokawa, Growth shape of isotactic polystyrene crystals in thin films, Polymer 42 (2001) 7443–7447. doi:https://doi.org/10.1016/S0032-3861(01)00215-4.

[56] R. Kobayashi, Modeling and numerical simulations of dendritic crystal growth, In Physica D 63 (1993) 410–423. doi:https://doi.org/10.1016/0167-2789(93)90120-P.

[57] A. Karma, W.-J. Rappel, Quantitative phase-field modeling of dendritic growth in two and three dimensions, Physical review E 57 (1998) 4323–4349. doi:https://doi.org/10.1103/PhysRevE.57.4323.

[58] H. Xu, R. Matkar, T. Kyu, Phase-field modeling on morphological landscape of isotactic polystyrene single crystals, Physical review E 72 (2005). doi:https://doi.org/10.1103/PhysRevE.72.011804.

[59] A. Keller, M. Hikosaka, S. Rastogi, A. Toda, The size factor in phase transitions: Its role in polymer crystal formation and wider implications, Philosophical Transactions of the Royal Society of London 348 (1994) 3–17. doi:https://doi.org/10.1098/rsta.1994.0077.

[60] S. Bargmann, B. Klusemann, J. Markmann, J. E. Schnabel, K. Schneider, C. Soyarslan, J. Wilmers, Generation of 3d representative volume elements for heterogeneous materials: A review, Progress in Materials Science 96 (2018) 322–384. doi:https://doi.org/10.1016/j.pmatsci.2018.02.003.

[61] J. Cahn, J. Hilliard, Free energy of a nonuniform system. i. interfacial free energy, The Journal of Chemical Physics 28 (1958) 258–267. doi:https://doi.org/10.1063/1.1744102.

[62] J. D. Hoffman, J. J. Weeks, Melting process and the equilibrium melting temperature of polychlorotrifluoroethylene, Journal of Research of the National Bureau of Standards-A, Physics and Chemistry 66A (1962). doi:https://doi.org/10.6028/jres.066a.003.

[63] Y. Tong, Y. Lin, S. Wang, M. Song, A study of crystallisation of poly (ethylene oxide) and polypropylene on graphene surface, The International Journal for the Science and Technology of Polymers 73 (2015) 52–61. doi:https://doi.org/10.1016/j.polymer.2015.07.025.

[64] H. Xu, W. Keawwattana, T. Kyu, Effect of thermal transport on spatiotemporal emergence of lamellar branching morphology during polymer spherulitic growth, The Journal of Chemical Physics 123 (2005). doi:https://doi.org/10.1063/1.2036976.

[65] K. L. Beers, J. F. Douglas, E. J. Amis, A. Karim, Combinatorial measurements of crystallization growth rate and morphology in thin films of isotactic polystyrene, Langmuir 19 (2003) 3935–3940. doi:https://pubs.acs.org/doi/abs/10.1021/la026751r.

[66] C. Beckermann, H. Diepers, I. Steinbach, A. Karma, X. Tong, Modeling melt convection in phase-field simulations of solidification, In Journal of Computational Physics 154 (1999) 468–496. doi:https://doi.org/10.1006/jcph.1999.6323.

[67] G. Taylor, Plastic strain in metals, Journal of the Institute of Metals 62 (1938) 307–324. doi:http://pajarito.materials.cmu.edu/rollett/27750/Taylor_1938.pdf.

[68] G. Sachs, Zur ableitung einer flieβbedingung. in: Mitteilungen der deutschen materialprüfungsanstalten, Springer, Berlin, Heidelberg 72 (1928) 734–736. doi:https://doi.org/10.1007/978-3-642-92045-5_12.

[69] B. Lee, A. Argon, D. Parks, S. Ahzi, Z. Bartczak, Simulation of large strain plastic deformation and texture evolution in high density polyethylene, Polymer 34 (1993) 3555–3575. doi:https://doi.org/10.1016/S0032-3861(03)00558-5.

[70] S. Nikolov, I. Doghri, O. Pierard, L. Zealouk, A. Goldberg, Multi-scale constitutive modeling of the small deformations of semi-crystalline polymers, Journal of the Mechanics and Physics of Solids 50 (2002) 2275–2302. doi:https://doi.org/10.1016/S0022-5096(02)00036-4.

[71] J. van Dommelen, D. Parks, M. Boyce, W. Brekelmans, F. Baaijens, Micromechanical modeling of the elasto-viscoplastic behavior of semi-crystalline polymers, Journal of the Mechanics and Physics of Solids 51 (2003) 519–541. doi:https://doi.org/10.1016/S0022-5096(02)00063-7.

[72] J. van Dommelen, D. Parks, M. Boyce, W. Brekelmans, F. Baaijens, Micromechanical modeling of intraspherulitic deformation of semicrystalline polymers, Polymer 44 (2003) 6089–6101. doi:https://doi.org/10.1016/S0032-3861(03)00558-5.

[73] M. Uchida, N. Tada, Micro-, meso- to macroscopic modeling of deformation behavior of semi-crystalline polymer, International Journal of Plasticity 49 (2013) 164–184. doi:https://doi.org/10.1016/j.ijplas.2013.03.007.

[74] H. E. Oktay, E. Gurses, Modeling of spherulite microstructures in semicrystalline polymers, International Journal of Plasticity 90 (2015) 83–101. doi:https://doi.org/10.1016/j.mechmat.2015.04.010.

[75] L. Gránásy, T. Pusztai, J. F. Douglas, Insights into Polymer Crystallization from Phase-Field Theory, Springer Berlin Heidelberg, Berlin, Heidelberg, 2014, pp. 1–35. doi:10.1007/978-3-642-37179-0_30-1.
URL https://doi.org/10.1007/978-3-642-37179-0_30-1

[76] R. Kobayashi, J. Warren, W. Carter, Vector-valued phase field model for crystallization and grain boundary formation, Physica D: Nonlinear Phenomena 119 (1998) 415–423. doi:https://doi.org/10.1016/S0167-2789(98)00026-8.

[77] C. Yu, Q. Xie, Y. Bao, G. Shan, P. Pan, Crystalline and spherulitic morphology of polymers crystallized in confined systems, Crystals 7(5) (2017) 147. doi:https://doi.org/10.3390/cryst7050147.

[78] K. Taguchi, H. Miyaji, K. Izumi, A. Hoshino, Y. Miyamoto, R. Kokawa, Growth shape of isotactic polystyrene crystals in thin films, polymer 42 (2001) 7443–7447. doi:https://doi.org/10.1016/S0032-3861(01)00215-4.

[79] C. Buckley, J. M.Schultz, Polymer spherulites: A critical review, Progress in Polymer Science 56 (2016) 1–63. doi:https://doi.org/10.1016/j.progpolymsci.2015.11.006.

[80] S. Sommer, T. Raidt, B. M. Fischer, F. Katzenberg, J. C. Tiller, M. Koch, Thz-spectroscopy on high density polyethylene with different crystallinity, Journal of Infrared, Millimeter, and Terahertz Waves 37 (2016) 189–197. doi:https://doi.org/10.1007/s10762-015-0219-8.

[81] A. Keller, M. Hikosaka, S. Rastogi, A. Toda, P. J. Barham, G. Goldbeck-Wood, The size factor in phase transitions: its role in polymer crystal formation and wider implications, Transactions of the Royal Society of London. Series A: Physical and Engineering Sciences 348 (1994) 3–17. doi:https://doi.org/10.1098/rsta.1994.0077.

[82] M. Butler, A. Donald, Deformation of spherulitic polyethylene thin films, Journal of Materials Science 32 (1997) 3675–3685. doi:https://doi.org/10.1023/A:1018642732686.

[83] B. Lotz, S. Z.D.Cheng, A critical assessment of unbalanced surface stresses as the mechanical origin of twisting and scrolling of polymer crystals, Polymer 46 (2005) 577–610. doi:https://doi.org/10.1016/j.polymer.2004.07.042.

[84] C. Choy, W. Leung, Elastic moduli of ultradrawn polyethylene, Journal of Polymer Science: Polymer Physics Edition 23 (9) (1985) 1759–1780. doi:https://doi.org/10.1002/pol.1985.180230903.

[85] A. Dahouh, G. Canova, A. Molinari, The modelling of large strain textures and stress-strain relations of polyethylene, Textures and Microstructures 14 (1991) 347–354. doi:http://downloads.hindawi.com/archive/1991/736469.pdf.

[86] S. Nikolov, R. Lebensohn, D. Raabe, Self-consistent modeling of large plastic deformation, texture and morphology evolution in semi-crystalline polymers, Journal of the Mechanics and Physics of Solids 54 (2005) 1350–1375. doi:https://doi.org/10.1016/j.jmps.2006.01.008.

[87] W.-F. Su, Principles of polymer design and synthesis, Vol. 82, Springer, 2013.

[88] P. Bowden, R. Young, Deformation mechanisms in crystalline polymers, Journal of materials science 9 (1974) 2034–2051. doi:https://doi.org/10.1007/BF00540553.

[89] T. L. Nguyen, Approche multi-échelles dans les matériaux polymères : de la caractérisation nanométrique aux effets d'échelles, Theses, Université de Technologie de Compiègne (2014).
URL https://tel.archives-ouvertes.fr/tel-01127516

[90] G. Ayoub, F. Zaïri, C. Fréderix, J. Gloaguen, M. Naït-Abdelaziz, R. Seguela, J. Lefebvre, Effects of crystal content on the mechanical behaviour of polyethylene under finite strains: Experiments and constitutive modelling, International Journal of Plasticity 27 (4) (2011) 492–511. doi:https://doi.org/10.1016/j.ijplas.2010.07.005.

[91] Q. He, H. Xia, J. Liu, X. Ao, S. Lin, Modeling and numerical studies of selective laser melting: Multiphase flow, solidification and heat transfer, Materials and Design 196 (2020) 109115. doi:https://doi.org/10.1016/j.matdes.2020.109115.

[92] T. J. Lun, T. Chao, W. C. How, Thermal fluid modelling of selective laser melting. proceedings of the 3rd international conference on progress in additive manufacturing, Nanyang Technological University Pro-AM 2018 (2018) 557-562. doi:https://doi.org/10.25341/D43S3S.

[93] M. Schmid, K. Wegener, Additive manufacturing: Polymers applicable for laser sintering (ls), Procedia Engineering 1 149 (2016) 457–464. doi:https://doi.org/10.1016/j.proeng.2016.06.692.

[94] scFLOW ©2020 Software Cradle. Hexagon M.I product.

[95] L. Yang, X. Gan, C. Xu, L. Lang, Z. Jian, S. Xiao, H. Deng, X. Li, Z. Tian, W. Hu, Molecular dynamics simulation of alloying during sintering of li and pb metallic nanoparticles, Computational Materials Science 156 (2019) 47–55. doi:https://doi.org/10.1016/j.commatsci.2018.09.032.

[96] J. M. Sestito, F. Abdeljawad, T. A. Harris, Y. Wang, A. Roach, An atomistic simulation study of nanoscale sintering: The role of grain boundary misorientation, Computational Materials Science 165 (2019) 180–189. doi:https://doi.org/10.1016/j.commatsci.2019.04.015.

[97] S. Yujin, S. Hwang, S. J. Kim, S. Kim, S.-G. Kim, H. J. Kim, S. J. Park, Atomistic simulation of sintering mechanism for copper nano-powders, Journal of Korean Powder Metallurgy Institute 22 (2015) 247–253. doi:http://dx.doi.org/10.4150/KPMI.2015.22.4.247.

[98] J. Frenkel, Viscous flow of crystalline bodies under the action of surface tension, Journal of Physics 9 5 (1945) 385–391. doi:https://www.scienceopen.com/document?vid=f06230b7-a32d-474e-974d-b1fb9a2ae914.

[99] J. Eshelby, Discussion of 'seminar on the kinetics of sintering', Metallurgical Transactions 185 (1949) 796–813.

[100] O. Pokluda, C. T. Bellehumeur, J. Vlachopoulos, Modification of Frenkel's model for sintering, American Institute of Chemical Engineers journal 43 (1997) 3253–3256. doi:https://doi.org/10.1002/aic.690431213.

[101] C. T. Bellehumeur, M. Kontopoulou, J. Vlachopoulos, The role of viscoelasticity in polymer sintering, Rheologica acta 37 (1998) 270–278. doi:DOI:10.1007/s003970050114.

[102] J. Mackenzie, R. Shuttleworth, A phenomenological theory of sintering, Proceedings of the Physical Society. Section B 62 (12) (1949) 833. doi:https://doi.org/10.1088/0370-1301/62/12/310.

[103] J. Mackenzie, The elastic constants of a solid containing spherical holes, Proceedings of the Physical Society. Section B 63 (1) (1950) 2. doi:https://doi.org/10.1088/0370-1301/63/1/302.

[104] G. W. Scherer, Viscous sintering of a bimodal pore-size distribution, Journal of the American Ceramic Society 67 (11) (1984) 709–715. doi:https://doi.org/10.1111/j.1151-2916.1984.tb19506.x.

[105] M. Kontopoulou, J. Vlachopoulos, Bubble dissolution in molten polymers and its role in rotational molding, Polymer Engineering and Science 39 (7) (1999) 1189–1198. doi:https://doi.org/10.1002/pen.11505.

[106] M. Asgarpour, F. Bakir, S. Khelladi, A. Khelladi, A. Tcharkhtchi, Characterization and modeling of sintering of polymer particles, Journal of Applied Polymer Science 119 (5) (2011) 2784–2792. doi:https://doi.org/10.1002/app.32924.

[107] F. B. Wadsworth, J. Vasseur, E. W. Llewellin, J. Schauroth, K. J. Dobson, B. Scheu, D. B. Dingwell, Sintering of viscous droplets under surface tension, Proceedings of the Royal Society A: Mathematical, Physical and Engineering Sciences 472 (2188) (2016) 1364–5021. doi:https://doi.org/10.1098/rspa.2015.0780.

[108] M. Asgarpour, F. Bakir, S. Khelladi, A. Khavandi, A. Tcharkhtchi, 3D Model for Powder Compact Densification in Rotational Molding, Polymer Engineering and Science 52 (9) (2012) 2033–2040. doi:https://doi.org/10.1002/pen.23133.

[109] M. Kontopoulou, J. Vlachopoulos, Melting and densification of thermoplastic powders, Polymer Engineering and Science 41 (2) (2001) 155–169. doi:https://doi.org/10.1002/pen.10718.

[110] A. Mokrane, M. Boutaous, S. Xin, Process of selective laser sintering of polymer powders: Modeling, simulation, and validation, Comptes Rendus Mécanique 346 (11) (2018) 1087–1103. doi:https://doi.org/10.1016/j.crme.2018.08.002.

[111] R. Christensen, K. Lo, Solutions for effective shear properties in three phase sphere and cylinder models, Journal of the Mechanics and Physics of Solids 27 (4) (1979) 315–330. doi:https://doi.org/10.1016/0022-5096(79)90032-2.

[112] A. Love, A Treatise on the Mathematical Theory of Elasticity, Dover Books on Engineering Series, Dover Publications, 1944.
URL https://books.google.fr/books?id=z8rCbeD_MrYC

[113] R. Christensen, Two theoretical elasticity micromechanics models, Journal of Elasticity 50 (1) (1998) 15–25. doi:https://doi.org/10.1023/A:1007497600857.

[114] J. C. Maxwell, J. Strutt, Capillary action. encyclopaedia britannica (1876).

[115] D. Joseph, Fluid Dynamics of Viscoelastic Liquids, Applied Mathematical Sciences, Springer New York, 2013.
URL https://books.google.fr/books?id=4IDkBwAAQBAJ

[116] N. Valizadeh, T. Rabczuk, Isogeometric analysis for phase-field models of geometric pdes and high-order pdes on stationary and evolving surfaces, Computer Methods in Applied Mechanics and Engineering, (2019), 351, 599–642. doi:https://doi.org/10.1016/j.cma.2019.03.043.

[117] H. Gomez, V. M. Calo, Y. Bazilevs, T. J. Hughes, Isogeometric analysis of the cahn-hilliard phase-field model, Computer Methods in Applied Mechanics and Engineering, (2008), 197, 4333–4352. doi:https://doi.org/10.1016/j.cma.2008.05.003.

[118] R. Sanal. Numerical Simulation of Dendritic crystal growth using phase field method and investigating the effects of different physical parameter on the growth of the dendrite, Computer Methods in Applied Mechanics and Engineering. **2014**. arXiv:1412.3197.

APPENDIX

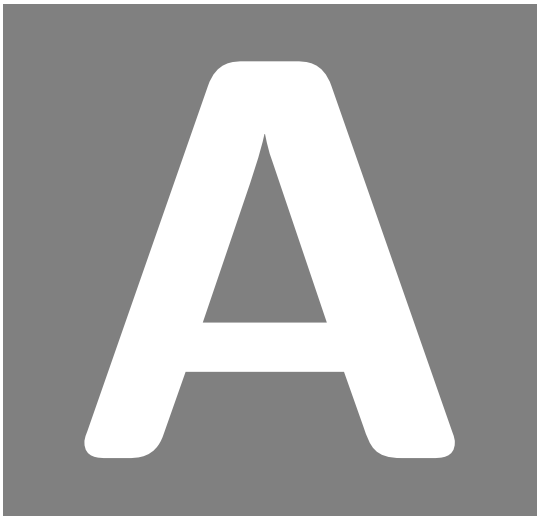

Radial return algorithm for VE-VP materials

Begin algorithm

We give the time increment Δt.
We calculate the strain increment $\Delta\epsilon$ from the strain rate $\dot{\epsilon}$.
Initialization of $\epsilon^{ve}(t_0)$, $S_i(t_0)$, $\sigma_{H_j}(t_0)$ and $\Delta\epsilon^{vp} = 0$.

$$\sigma(t_{n+1}) = E_\infty : \epsilon^{ve}(t_n) + \tilde{E} : \Delta\epsilon + \sum_{i=1}^{I} exp\left(-\frac{\Delta t}{g_i}\right) S_i(t_n) + \sum_{j=1}^{J} exp\left(-\frac{\Delta t}{k_j}\right) \sigma_{H_j}(t_n)\mathbf{1}$$

$S(t_{n+1}) = 2G_\infty \xi^{ve}(t_n) + 2\tilde{G}\Delta\xi + \sum_{i=1}^{I} exp\left(-\frac{\Delta t}{g_i}\right) S_i(t_n)$

$\sigma_{eq}(t_{n+1}) = \sqrt{\frac{3}{2} S(t_{n+1}) : S(t_{n+1})}$

$f(\sigma_{eq}, p, \dot{\epsilon}) = \sigma_{eq} - (\sigma_y(\dot{\epsilon}) + R(p))$

$\Delta p = 0$
if $f(\sigma_{eq}, p, \dot{\epsilon}) > 0$
  while $(|f(\sigma_{eq}, p, \Delta p, \dot{\epsilon})| > 1.E^{-6} \;\; \& \;\; N_{iter} < N_{IterMax})$
    if $(p < 1.E^{-18})$
      $p = 1.E^{-18}$
    end if

    if $(\Delta p < 1.E^{-18})$
      $\Delta p = 1.E^{-18}$
    end if

    $f'(\Delta p(t_n)) = -3\tilde{G} - R'(p(t_n) - \Delta p(t_n)) - \frac{1}{m}\left(\eta \frac{\Delta p^{1-m}(t_n)}{\Delta t} \sigma_y^{m-1}\right)^{\frac{1}{m}}$
    $\Delta p(t_{n+1}) = \Delta p(t_n) - \frac{f(\Delta p(t_n))}{f'(\Delta p(t_n))}$
    $f(\Delta p(t_{n+1})) = \sigma_{eq} - 3\tilde{G}\Delta p(t_{n+1}) - \sigma_y(\dot{\epsilon}) - R(p(t_{n+1}) + \Delta p(t_{n+1})) -$
    $\left(\eta \frac{\Delta p(t_{n+1})}{\Delta t} \sigma_y^{m-1}\right)^{\frac{1}{m}}$
    $N_{iter} + +$
  end while

  $N = \frac{3}{2} \frac{S}{\sigma_{eq}(t_{n+1})}$
  $\sigma(t_{n+1}) = \sigma(t_{n+1}) - \tilde{E}\Delta p N$
  $\Delta\epsilon^{vp} = \Delta p N$
  $\Delta\epsilon^{ve} = \Delta\epsilon - \Delta\epsilon^{vp}$
  $\epsilon^{vp}(t_{n+1}) = \epsilon^{vp}(t_n) + \Delta\epsilon^{vp}$
end if

$S_i(t_{n+1}) = exp\left(-\frac{\Delta t}{g_i}\right) S_i(t_n) + 2G_i \left[1 - exp\left(-\frac{\Delta t}{g_i}\right)\right] \frac{g_i}{\Delta t} \Delta\xi^{ve}$
$\sigma_{H_j}(t_{n+1}) = exp\left(-\frac{\Delta t}{k_j}\right) \sigma_{H_j}(t_n) + 3K_j \left[1 - exp\left(-\frac{\Delta t}{k_j}\right)\right] \frac{k_j}{\Delta t} \Delta\epsilon_H^{ve}$

End algorithm

APPENDIX

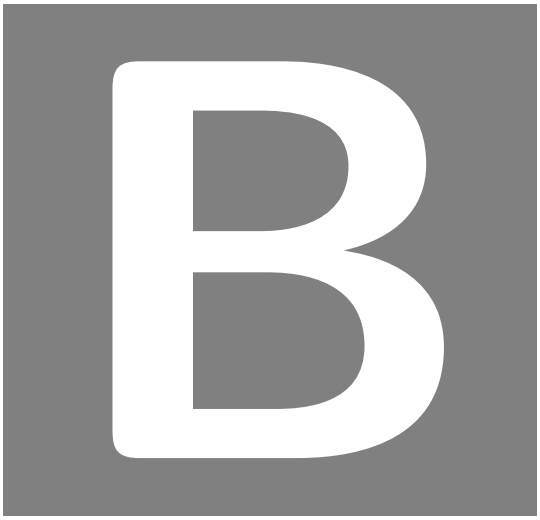

Proof of crystal growth and heat equation

B.A | Crystal growth equation

The phase field equation is given by the Gibbs-Thomson relation, which describes the thermal influence on the liquid-solid interface evolution. The equation can be expressed as follows [66] [64].

$$\frac{v_n}{\mu_k} = T_m^0 - T - k_{GT}\kappa \tag{B.1}$$

where μ_k is the kinetic coefficient, k_{GT} is the Gibbs-Thomson coefficient, v_n is the velocity of the interface, κ is the interface curvature gradient and T_m^0 is the equilibrium melting temperature.

The normal to the interface is defined as $\vec{n} = -\frac{\nabla\phi}{|\nabla\phi|}$(see figure B.1). Assume that $\phi(x,t)$ is a smooth Level Set function. Using the Level Set advection equation, we can write.

$$v_n = \vec{v}.\vec{n} = \frac{\partial x}{\partial t} \cdot \left(-\frac{\partial\phi/\partial x}{|\nabla\phi|}\right) = \frac{\partial\phi/\partial t}{|\nabla\phi|} \tag{B.2}$$

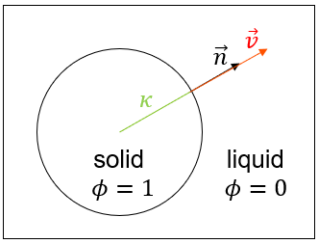

Figure B.1: Solid-liquid interface representation.

By definition, the (total) curvature of the interface is given as:

$$\kappa = \nabla \cdot \vec{n} = -\frac{1}{|\nabla\phi|}\left[\nabla^2\phi - \frac{(\nabla\phi)\cdot\nabla|\nabla\phi|}{|\nabla\phi|}\right] \tag{B.3}$$

By substituting (B.2) and (B.3) in (B.1) we find.

$$\frac{\partial\phi}{\partial t} = v_n|\nabla\phi| = \mu_k k_{GT}\left[\nabla^2\phi - \frac{(\nabla\phi)\cdot\nabla|\nabla\phi|}{|\nabla\phi|}\right] + \mu_k(T_m^0 - T)|\nabla\phi| \tag{B.4}$$

In the Gibbs-Thomson equation T_m^0 is considered as an equilibrium temperature T_e, i.e. there is no evolution at this temperature. For polymer material, at each crystallization temperature there is a specific crystallizable volume, since the amorphous phase has no melting temperature, the melting point of the polymer changes depending on its crystallization rate. Moreover, the crystallisation is an exothermic process, using a perfect system without heat dissipation, the crystal will release its melting temperature. As a result, for polymer, the equilibrium temperature T_e is equal to T_m.

At equilibrium, $T = T_m$ and $\frac{\partial\phi}{\partial t} = 0$, equation (B.4) does not have a unique solution in the stationary case, for example it depends on the initial profile. If

a double-well potential is used for the local free energy, then the profile of the phase-field for the steady state solution is given by:

$$\phi = \frac{1}{2}\left(1 - \tanh\left(\frac{r}{2\delta}\right)\right) \tag{B.5}$$

where 6δ is the interface thickness and r is the coordinate normal to the interface. According to Beckermann et al. [66], this is the most commonly used profile for a double-well free energy potential. Actually, depending on the choice of potential for the local free energy, the profile of the phase-field for the steady-state solution can be obtained through formal asymptotic analysis, and no assumption is needed.

Since evolution exists only in the normal direction of the interface, using (B.5), we can calculate:

$$|\nabla\phi| = \left|\frac{\partial\phi}{\partial r}\right| = \frac{\phi(1-\phi)}{\delta} \tag{B.6}$$

$$\frac{(\nabla\phi)\cdot\nabla|\nabla\phi|}{|\nabla\phi|} = \nabla^2\phi = \frac{\partial^2\phi}{\partial r^2} = \frac{\phi(1-\phi)(1-2\phi)}{\delta^2} \tag{B.7}$$

Equation (B.4) becomes:

$$\begin{aligned}\frac{\partial\phi}{\partial t} &= \mu_k k_{GT}\left[\nabla^2\phi - \frac{\phi(1-\phi)(1-2\phi)}{\delta^2}\right] + \mu_k(T_m - T)\frac{\phi(1-\phi)}{\delta} \\ &= \mu_k k_{GT}\left[\nabla^2\phi - \frac{2}{\delta^2}\phi(1-\phi)(-\frac{\delta}{2k_{GT}}(T_m - T) + \frac{1}{2} - \phi)\right] \\ &= \mu_k k_{GT}\left[\nabla^2\phi - \frac{2}{\delta^2}\phi(1-\phi)(-m(T) + \frac{1}{2} - \phi)\right]\end{aligned} \tag{B.8}$$

In equation (B.8), the term $\mu_k k_{GT}$ has dimension $[m^2/s]$ and it represents the phase field diffusivity. Multiplying the diffusivity by $\frac{1}{\delta^2}$ we obtain the phase field mobility called M $[s^{-1}]$, is also defined as a positive kinetic coefficient according to Allen-Cahn [18], $1/M$ can be defined as a characteristic time of attachment of atoms at the interface according to Karma [57]. Taking $\epsilon^2 = \delta^2$ $[m^2]$, ϵ is called the reference surface energy according to Cahn-Hilliard theory. To generalize the equation we replace a factor 2 with W which represents the energy barrier for second nucleation. Assume that $m(T) = \frac{\delta}{2k_{GT}}(T_m - T) = \gamma(T_m - T)$. After these approximations, equation (B.8) becomes:

$$\frac{\partial \phi}{\partial t} = M\left[\epsilon^2 \nabla^2 \phi - W\phi(1-\phi)(-m(T) + \frac{1}{2} - \phi)\right] \tag{B.9}$$

Which can be rewritten as follows by using the functional derivative formula:

$$\frac{\partial \phi}{\partial t} = M\left[\nabla \cdot (\epsilon^2 \nabla \phi) - \frac{\partial f_{loc}}{\partial \phi}\right] = -M\frac{\delta F}{\delta \phi} \tag{B.10}$$

Equation (B.10) is the actual Allen-Cahn [18] equation, where the total free energy F of the system of melt and solidifying crystals is defined as the Cahn-Hilliard free energy:

$$F(\phi, T) = \int_V f_{loc} dV = \int_V \left[f_{liq-sol}(\phi, T) + f_{grad}(\phi)\right] dV \tag{B.11}$$

With:

$$f_{liq-sol}(\phi, T) = W \int_0^{\phi} \phi(1-\phi)(-m(T) + \frac{1}{2} - \phi) d\phi \tag{B.12}$$

And

$$f_{grad}(\phi) = \frac{1}{2}\epsilon^2 (\nabla \phi)^2 \tag{B.13}$$

If we consider that the coefficient of energy gradient ϵ is not a constant, then equation (B.10) becomes:

$$\frac{\partial \phi}{\partial t} = M\begin{bmatrix} \nabla \cdot \left(\frac{1}{2}(\nabla \phi)^2 \frac{\partial(\epsilon^2)}{\partial \nabla \phi}\right) + \nabla \cdot \left(\epsilon^2 \nabla \phi\right) \\ - W\phi(\phi - 1)(\phi - 1/2 + m(T)) \end{bmatrix} \tag{B.14}$$

For two-dimensional model, it is assumed that the coefficient of energy gradient ϵ is expressed as follows [57]:

$$\epsilon = \bar{\epsilon}\left[1 + \vartheta \cos(j(\theta - \theta_0))\right] \quad | \quad \theta = \arctan\left(\frac{\partial \phi / \partial y}{\partial \phi / \partial x}\right) \tag{B.15}$$

where $\bar{\epsilon}$ is the reference coefficient of energy gradient, ϑ is the strength of surface anisotropy, j is a shape parameter, θ is the angle between the interface normal and the reference axis and θ_0 is the spherulite orientation with respect to the horizontal axis, in this $\theta_0 = 0$. Equation (B.14) becomes.

$$\begin{aligned}\frac{1}{M}\frac{\partial\phi}{\partial t} = &-\frac{\partial}{\partial x}\left(\epsilon\epsilon'\frac{\partial\phi}{\partial y}\right)+\frac{\partial}{\partial y}\left(\epsilon\epsilon'\frac{\partial\phi}{\partial x}\right)\\ &+\frac{\partial\epsilon^2}{\partial x}\frac{\partial\phi}{\partial x}+\frac{\partial\epsilon^2}{\partial y}\frac{\partial\phi}{\partial y}+\epsilon^2\left(\frac{\partial^2\phi}{\partial x^2}+\frac{\partial^2\phi}{\partial y^2}\right)\\ &-W\phi(\phi-1)(\phi-1/2+m(T))\end{aligned} \tag{B.16}$$

where $\epsilon' = \partial\epsilon/\partial\theta$.

B.B | Heat transfer equation

Suppose that we have two states (1 and 2). The enthalpy of the pure two phase body is determined as follows:

$$H = \phi_1 H_1 + \phi_2 H_2 \tag{B.17}$$

where H_i is the enthalpy of the pure body in state i and ϕ_i is the volume fraction of phase i. Assume $\phi = \phi_2$.

The enthalpy of change of state from phase 2 to phase 1 at temperature T $\Delta H_{2\to1}$ also called latent heat, can be expressed as follows:

$$\Delta H_{2\to1} = H_1 - H_2 \tag{B.18}$$

Suppose that state 1 is liquid and 2 is solid. Using (B.17) and (B.18) we obtain:

$$H = H_1 - \phi\Delta H_{2\to1} = \rho C_p T - \rho L_f \phi \tag{B.19}$$

where $\rho L_f = \Delta H_{2\to1}$, L_f is the latent heat of fusion and C_p is the specific heat at constant pressure. The heat transfer equation can be written as follows:

$$\frac{\partial H}{\partial t} = -\nabla.\vec{J} \tag{B.20}$$

where $\vec{J} = -k_T\nabla T$ is the heat flow and k_T is the thermal conductivity. Finally we get:

$$\rho C_p\frac{\partial T}{\partial t} = k_T\nabla^2 T + \rho L_f\frac{\partial\phi}{\partial t} \tag{B.21}$$

Then we can write the equation system:

$$\begin{cases} \dfrac{\partial \phi}{\partial t} = -M \dfrac{\delta F(m(T), \phi)}{\delta \phi} \\ \dfrac{\partial T}{\partial t} = \alpha \nabla^2 T + K \dfrac{\partial \phi}{\partial t} \end{cases} \tag{B.22}$$

where $\alpha = \frac{k_T}{\rho C_p}$ and $K = \frac{\Delta H_{2\to 1}}{\rho C_p}$.

APPENDIX C

Numerical formulation of the proposed enhanced phase field model

In this Appendix, details are given about the finite difference method which was used to implement the proposed enhanced phase field model. Other methods exist in the literature, such as the variational formulations proposed by Valizadeh et al. [116] and Gomez et al. [117] for the Cahn-Hilliard model and based on isogeometric analysis.

Spatial discretization

The spatial gradient of the phase field variable is discretized as follows:

$$\nabla\phi(x,y,z) \approx \left\{ \begin{array}{l} \dfrac{\phi(x+\Delta x,y,z)-\phi(x-\Delta x,y,z)}{2\Delta x} \\ \dfrac{\phi(x,y+\Delta y,z)-\phi(x,y-\Delta y,z)}{2\Delta y} \\ \dfrac{\phi(x,y,z+\Delta z)-\phi(x,y,z-\Delta z)}{2\Delta z} \end{array} \right\} \tag{C.1}$$

The spatial Laplacian of the phase field variable is classically discretized as follows:

$$\nabla^2\phi(x,y,z) \approx \left[\begin{array}{l} \dfrac{\phi(x+\Delta x,y,z)+\phi(x-\Delta x,y,z)-2\phi(x,y,z)}{(\Delta x)^2} \\ + \dfrac{\phi(x,y+\Delta y,z)+\phi(x,y-\Delta y,z)-2\phi(x,y,z)}{(\Delta y)^2} \\ + \dfrac{\phi(x,y,z+\Delta z)+\phi(x,y,z-\Delta z)-2\phi(x,y,z)}{(\Delta z)^2} \end{array} \right] \tag{C.2}$$

However, the use of this classical expression generates an incorrect propagation of the interface and a distorted spherulite shape, as illustrated in figure C.1(a).

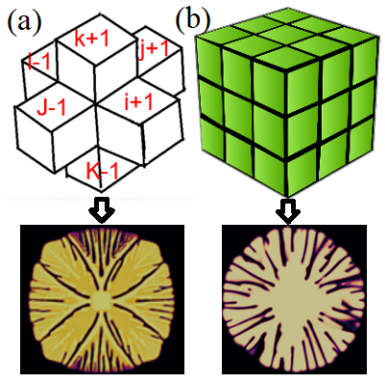

Figure C.1: Influence on spherulite growth of the discretization of the spatial Laplacian operator using: (a) classical equation C.2 and (b) modified equation C.3.

Therefore, we used a different discrete Laplacian expression. In order to motivate it, we assume for simplicity that $\Delta x = \Delta y = \Delta z = h$ and rewrite the classical expression as follows:

$$h^2\nabla^2\phi(x,y,z) \approx \phi(x+h,y,z)+\phi(x-h,y,z)+\phi(x,y+h,z)+\phi(x,y-h,z)+ \phi(x,y,z+h)+\phi(x,y,z-h)-6\phi(x,y,z)$$

We modify the classical formula so that it takes into account all the neighbors of a given element. This method is inspired by the work of Sanal [118]. Accordingly, the Laplacian of the phase field variable is computed as follows:

$$3h^2\nabla^2\phi(x,y,z) \approx \left[\begin{array}{l} \phi(x+h,y,z)+\phi(x-h,y,z) \\ +\phi(x,y+h,z)+\phi(x,y-h,z) \\ +\phi(x,y,z+h)+\phi(x,y,z-h) \\ +\phi(x+h,y+h,z)+\phi(x-h,y-h,z) \\ +\phi(x,y+h,z+h)+\phi(x,y-h,z-h) \\ +\phi(x+h,y,z+h)+\phi(x-h,y,z-h) \\ +\phi(x+h,y-h,z)+\phi(x-h,y+h,z) \\ +\phi(x,y+h,z-h)+\phi(x,y-h,z+h) \\ +\phi(x+h,y,z-h)+\phi(x-h,y,z+h) \\ +\phi(x+h,y+h,z+h)+\phi(x-h,y-h,z-h) \\ +\phi(x+h,y-h,z-h)+\phi(x-h,y+h,z+h) \\ +\phi(x+h,y+h,z-h)+\phi(x-h,y-h,z+h) \\ +\phi(x-h,y+h,z-h)+\phi(x+h,y-h,z+h) \\ -26\phi(x,y,z) \end{array}\right] \tag{C.3}$$

The two equations C.1 and C.3 are also used for the gradient and the Laplacian of the temperature field $T(x,y,z)$.

Time discretization

The time derivatives of the phase field and temperature variables at a given position (x,y,z) are approximated by the following discrete expressions:

$$\frac{\partial\phi}{\partial t}(t) \approx \frac{\phi(t+\Delta t)-\phi(t)}{\Delta t} \equiv \frac{\Delta\phi}{\Delta t} \tag{C.4}$$

$$\frac{\partial T}{\partial t}(t) \approx \frac{T(t+\Delta t)-T(t)}{\Delta t} \equiv \frac{\Delta T}{\Delta t} \tag{C.5}$$

However, in the heat equation (B.21), and following Kobayashi[56], the discrete expression of the time derivative of the phase field variable is taken as follows:

$$\frac{\partial \phi}{\partial t}(t) \approx (1-\beta)\frac{\phi(t+\Delta t)-\phi(t)}{\Delta t} + \beta\frac{\phi(t)-\phi(t-\Delta t)}{\Delta t} \tag{C.6}$$

where $\beta \in [0;1]$ is an integration parameter; in this work we take $\beta = 0.5$. The discrete expressions of $\nabla^2\phi$, $\nabla^2 T$, $\frac{\partial \phi}{\partial t}$ and $\frac{\partial T}{\partial t}$ are replaced in eqs. (4.17) of the enhanced phase field model.

Boundary conditions

Conditions of periodic continuity are imposed on the border of the computational domain for both the temperature and the phase field variables. They can be illustrated with the simple 1D example with n_x elements depicted in Fig. C.2. The discrete spatial partial derivative $\phi_{,x} \approx \frac{\phi(n_x+1)-\phi(n_x-1)}{2\Delta x}$ becomes $\phi_{,x} \approx \frac{\phi(1)-\phi(n_x-1)}{2\Delta x}$ because by periodicity $\phi(n_x+1) = \phi(1)$.

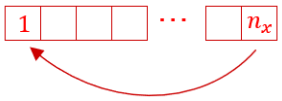

Figure C.2: Illustration of periodic continuity conditions in 1D.

APPENDIX

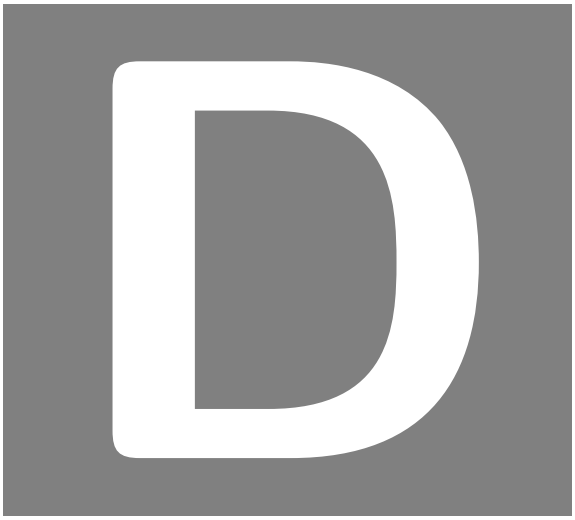

Functional derivative

For continuous functional F, its functional derivative (or variational derivative), denoted $\delta F/\delta\phi$, is defined by:

$$\int_V \frac{\delta F}{\delta \phi}(V)\rho(V)dV = \lim_{\epsilon \to 0}\frac{F(\phi + \epsilon\rho) - F(\phi)}{\epsilon} = \left[\frac{d}{d\epsilon}F(\phi + \epsilon\rho)\right]_{\epsilon=0} \tag{D.1}$$

where ρ is an arbitrary function. The quantity $\epsilon\rho$ is called the variation of ϕ. Suppose that $F(\phi) = \int_V f(V, \phi(V), \nabla\phi(V))dV$

$$\begin{aligned}
\int_V \frac{\delta F}{\delta \phi}(V)\rho(V)dV &= \left[\frac{d}{d\epsilon}\int_V f(V,\phi(V)+\epsilon\rho(V),\nabla\phi(V)+\epsilon\nabla\rho(V))dV\right]_{\epsilon=0} \\
&= \left[\int_V \left(\frac{\partial f}{\partial \phi}\rho(V)+\frac{\partial f}{\partial \nabla\phi}\nabla\rho(V)\right)dV\right] \\
&= \left[\int_V \left(\frac{\partial f}{\partial \phi}\rho(V)-\left(\nabla\frac{\partial f}{\partial \nabla\phi}\right)\rho(V)+\nabla\left(\frac{\partial f}{\partial \nabla\phi}\rho(V)\right)\right)dV\right] \\
&= \left[\int_V \left(\frac{\partial f}{\partial \phi}\rho(V)-\left(\nabla\frac{\partial f}{\partial \nabla\phi}\right)\rho(V)\right)dV\right] \\
&= \left[\int_V \left(\left(\frac{\partial f}{\partial \phi}-\nabla\frac{\partial f}{\partial \nabla\phi}\right)\rho(V)\right)dV\right]
\end{aligned} \tag{D.2}$$

The second line is obtained by using the formula of the total derivative. The fourth line was obtained by using the divergence theorem and the condition that $\rho = 0$ at the boundary of the integration region.
Finally, according to the localization theorem, equation (D.2) should be valid $\forall$ volume V and $\forall\rho(V) \mid \rho(V) = 0$ on ∂V, therefore:

$$\frac{\delta F}{\delta \phi} = \frac{\partial f}{\partial \phi} - \nabla\frac{\partial f}{\partial \nabla\phi} \tag{D.3}$$

APPENDIX E

Computation of the effective bulk modulus

To obtain the homogenized bulk modulus k, the pressure inside the porosity must be null ($\mathcal{P}_i = 0$). Using the continuity equation (8.3), the following equation is obtained:

$$\frac{\mathcal{P}_{m|i}}{P} = \frac{\left[\frac{1}{3k} + \frac{1}{4\mu}\right]}{\left[\frac{r_i^3}{3k_m R^3}\frac{R^3 - r_i^3}{r_i^3 - a_i^3} + \frac{a_i^3}{4\mu_m R^3}\frac{R^3 - r_i^3}{r_i^3 - a_i^3} + \frac{r_i^3}{3kR^3} + \frac{1}{4\mu}\right]} \tag{E.1}$$

Using the infinite medium hypothesis, the term $\frac{r_i^3}{R^3}$ can be neglected ($\frac{r_i^3}{R^3} \approx 0$), $\frac{\mathcal{P}_{m|i}}{P}$ becomes:

$$\frac{\mathcal{P}_{m|i}}{P} = \frac{4\mu + 3k}{\left[\left(\frac{4\mu_m + 3k_m \frac{a_i^3}{r_i^3}}{k_m\mu_m - k_m\mu_m \frac{a_i^3}{r_i^3}}\right) k\mu + 3k\right]} \tag{E.2}$$

Using equation (8.2), the displacement at the edge ($r = R$) corresponding to the i^{th} porosity can be written as follows:

$$\frac{u_i(R)}{R} = -\frac{P}{3k} + \left(\mathcal{P}_{m|i} - P\right)\left[\frac{1}{3k} + \frac{1}{4\mu}\right]\frac{r_i^3}{R^3 - r_i^3} \tag{E.3}$$

Let's consider the "equivalent" solid sphere with properties μ, k and radius R subjected to a pressure P. According to Love [112], the displacement in the edge ($r = R$) is given as:

$$U = -\frac{PR}{3k} \tag{E.4}$$

The equivalence between the heterogeneous porous medium and the homogeneous solid sphere implies that the displacement in equation (E.3) must be equal to that in equation (E.4).

$$U = u_i(R) \implies R\left(\mathcal{P}_{m|i} - P\right)\left[\frac{1}{3k} + \frac{1}{4\mu}\right]\frac{r_i^3}{R^3 - r_i^3} = 0 \implies \mathcal{P}_{m|i} = P \tag{E.5}$$

Using equations (E.2) and (E.5) and replacing the geometric parameters by using relation (8.1), it follows that:

$$k = \frac{4k_m\mu_m\rho}{4\mu_m + 3k_m\left(1 - \rho\right)} \tag{E.6}$$

This is exactly the estimate given by the GSC model [113].

APPENDIX F

Relation between the particle radius a and the sintering angle

Figure F.1 shows the state of the contact interface between two grains before and after sintering.

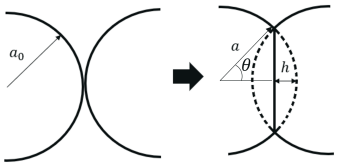

Figure F.1: Representation of the connection between two-grain of powder.

The grain volume after sintering is equal to that of a sphere with radius a subtracted by the volume of the ball cap with height h and multiplied by the number of contacts with all adjacent grains N_c.

$$V = \frac{4\pi}{3}a^3 - N_c\pi h^2\left(a - \frac{h}{3}\right) \tag{F.1}$$

Geometrically, it is possible to make a relation between h and θ (see Figure F.1).

$$h = a(1 - \cos(\theta)) \tag{F.2}$$

Take the hexagonal stack, using the fact that the grain material is incompressible, we can assume that the initial grains volume is equal to their current volume after sintering. We can also compute the contact number $N_c = 12$. Consequently,

$$V_0 = V \Rightarrow \frac{4\pi}{3}a_0^3 = \frac{4\pi}{3}a^3 - 12\pi\left(a\left(1 - \cos(\theta)\right)\right)^2\left(a - \frac{1}{3}\left(a\left(1 - \cos(\theta)\right)\right)\right) \tag{F.3}$$

Then we can obtain the equation (8.42).